Advances in Printing and Media Technology

Vol. XLVIII(VIII)

Edited by Cathy Ridgway

Darmstadt
MMXXII

Advances in Printing and Media Technology

Proceedings of the 48th International Research Conference of iarigai
Greenville, USA, 19–21 September 2022

Published by the International Association of
Research Organizations for the Information,
Media and Graphic Arts Industries
Darmstadt, Germany, 2022

Edited by Cathy Ridgway, Oftringen, Switzerland

Online edition
ISBN 978-3-948039-03-5
ISSN 2409-4021
DOI 10.14622/Advances_48_2022

Contents

SESSION 5

SESSION 6

SESSION 7

Preface

For the first time in the long history of both organizations, we welcomed iarigai and The International Circle to hold a joint conference in North America. The 2022 conferences, featuring graphic communications scientific research and education, were conducted September 19–21, 2022, in Greenville, South Carolina, USA, and were hosted by the Department of Graphic Communications, Clemson University, Clemson, SC, USA.

Although both conferences have previously occurred in the US and Canada, this marked the inaugural event where both meetings could be attended with a single registration in North America. In recent years this opportunity has only occurred in Europe, including Greece, Germany, Poland, and Switzerland.

Although global travel to the USA was quite trying for some participants, a solid group of international attendees both presented or attended, providing stimulating presentations and spirited discussions from across the graphic communication industry. This was also a rare opportunity for those from our region of the world to stay close to home to participate and present their research at these prestigious conferences.

The downtown Greenville location, in the storied American South, brought new experiences for many attendees. Likewise, the wealth of presentations and keynotes, 24 in total, over the first two days enlightened all the participants as well. On the third day, the conference traveled to nearby Clemson, SC, home of one of North America's top graphic communications research and testing facilities, the Sonoco Institute for Graphics and Packaging. There we witnessed a demonstration of cutting-edge VR technology for press education and training and a tour of the historic Godfrey Hall (c.1889), where the undergraduates learn about various technology, software, and processes.

The annual gala was the highlight of the event, where rooftop dining gave way to views of the tree-lined streets and where the winner of the top presenter award was given to Pauline Brumm, who spoke on "Creation of a comprehensive high-resolution image data set on an industrial web press to investigate hydrodynamic pattern formation in gravure printing. " She was presented a special gift box designed and printed on a flexographic press by the GC students at the Sonoco Institute. The box incorporated state-of-the-art technology to track the flow of the items it contained along the entire supply chain for sustainability and logistics.

The team of Clemson University organizers and I wish to thank all who made the long journey to attend the conference. We are happy to pass the torch to Wuppertal University in Germany and wish them a highly successful program in 2023.

Nona Woolbright, Ph.D.
Director of the iarigai and IC conferences

September 2022, Greenville, SC, USA

Link:
Clemson University
Graphic Communications
<https://www.clemson.edu/business/departments/graphics/>

DOI 10.14622/Advances_48_2022_01

Modeling and investigating the dynamic gloss of flexo printed UV-inks containing aluminum pigments

Carl Fridolin Weber, Hans Martin Sauer and Edgar Dörsam

Technical University of Darmstadt, Department of Mechanical Engineering, Institute of Printing Science and Technology, Magdalenenstr. 2, 64289 Darmstadt, Germany
E-mails: weber@idd.tu-darmstadt.de; sauer@idd.tu-darmstadt.de; doersam@idd.tu-darmstadt.de

Short abstract

Various factors affect the dynamic gloss development after printing such as the amount of ink applied, the ink viscosity or different properties of the substrate. When using metallic inks that contain aluminum leafing pigments, also these leafing properties are crucial. In this study, the micro-tri-gloss, a specular gloss meter that measures gloss at the angles of 20°, 60° and 85° is used to study the dynamic gloss of metallic inks on different substrates. The two types of inks used contain vacuum metallized pigments and cornflake pigments. It is shown how the dynamic gloss of these inks behaves differentially and how the dynamic gloss differs according to the substrate used. Further, it is shown how the dynamic gloss curves can be modelled using the Kohlrausch function or a summation of two exponential functions. Finally, it is discussed why the dynamic gloss curves measured simultaneously at different angles can behave in a contrary manner.

Keywords: gloss measurement, aluminium pigments, dynamic gloss, UV-inks, flexo printing

1. Introduction and background

In the label and package printing industry metallic embellishments can be produced with a range of different printing methods as described by Weber, Spiehl and Dörsam (2022). One of these methods is based on flexo printing with UV-curable inks containing aluminum pigments. The visual quality of a metallic embellishment is determined by various indicators. A primary one is the gloss: often metallized surfaces are targeting to have a glossy, or mirror-like appearance. This is especially the case for packaging for high quality products. The print gloss of inks is dependent on various factors. As stated by Preston, et al. (2003) who made investigations on the dynamic gloss of non-metallic printing inks, the ink formulation, paper properties such as roughness, porosity, or type of coating play a decisive role.

As stated by Rich, et al. (2017), Wheeler (1999), Wißling (2013), and Pfaff, Bartelt and Maile (2021), there are three different types of aluminum pigments used in metallic printing inks. If applied on a smooth surface, so-called cornflake pigments result in a faint or minor mirror effect. Using silverdollar pigments improves the result in terms of gloss. However, only the application of vacuum metallized pigments (VMPs), which have the highest quality and a very smooth surface can result in a mirror-like appearance. According to Wheeler (1999) and Maile, Pfaff and Reynders (2005), cornflake and silverdollar pigments typically have a thickness of about 0.1–1.0 µm. VMPs, however, can be as thin as 40 nm. It can be distinguished between leafing and non-leafing pigments. While leafing pigments float to the top of the ink film after printing, non-leafing pigments stay evenly distributed in the ink film as shown in Figure 1.

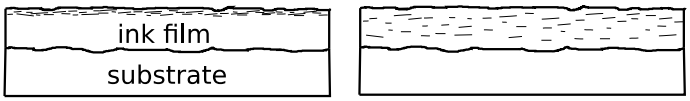

Figure 1: Distribution of leafing (left) and non-leafing (right) aluminum pigments in ink (Weber, Spiehl and Dörsam, 2022)

Beside the substrate, ink formulation and pigment type, also print settings such as the speed of the printing machine, or the amount of ink applied influence the print gloss. Another important factor is the time between application of the UV-inks on the substrate and UV-curing of the ink. After printing the ink, a change of gloss takes place, which is called dynamic print gloss or simply dynamic gloss. As stated by Koivula, et al. (2009), the measurement of dynamic gloss can be a useful tool to study paper-ink interactions after printing and can help papermakers and printers to understand why different papers lead to different print gloss. In this study, the dynamic gloss of two UV-inks containing VMPs and cornflake pigments was investigated. The metallic ink was printed on different substrates with different properties such as roughness, porosity, and pre-treatment using a laboratory flexo printing machine. A commercially available gloss meter measuring gloss continuously at three different angles was used to investigate the dynamic gloss.

2. Materials and methods

Printing trials were carried out using the laboratory flexo printing machine IGT F1. Gloss measurements were conducted using the micro-tri-gloss from Byk Gardner. As described by Weber, Spiehl and Dörsam (2021a; 2021b) in detail, this gloss meter can measure specular gloss at the specular angles of 20°, 60° and 85°. In continuous measurement mode, it measures gloss in intervals that can be adjusted from zero to nine seconds in steps of one second. For the gloss measurements made in this study, the interval was adjusted to one second. Both, the laboratory printing machine and gloss meter are shown in Figure 2.

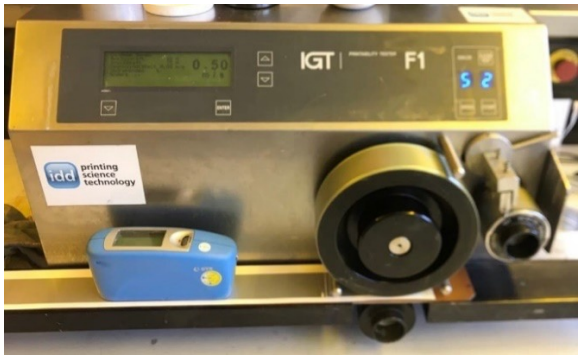

Figure 2: Laboratory flexo printing machine IGT F1 printability tester and micro-tri-gloss (in blue in the bottom left) on a printed substrate

As explained by Weber, Spiehl and Dörsam (2021b), when measuring the specular gloss, a LED flashes light that passes a lens and an aperture with an inclination of θ on the surface of a sample. There, the light is reflected and scattered and partially absorbed. A part of the reflected light passes an aperture on the receiver side of the specular angle. It is important to note that according to ASTM D523-14, the light source aperture is the same for all three angles (American Society for Testing and Materials, 2018). The receiver aperture however, differs and is larger for the receiver aperture at 60° compared to the receiver aperture at 20°. The aperture sizes are listed in Table 1. Figure 3 shows a schematic of a specular gloss meter with the angles associated to Table 1.

Table 1: Angles of the light source aperture and receiver aperture for the measurement of specular gloss at 20°, 60° and 85° after ASTM D523-14; the angles α and β correspond to Figure 1

	In plane of measurement (α)	Perpendicular to plane of measurement (β)
Light source aperture (for all angels)	0.75° ± 0.25°	2.5° ± 0.5°
20° receiver aperture	1.8° ± 0.05°	3.6° ± 0.1°
60° receiver aperture	4.4° ± 0.10°	11.7° ± 0.2°
85° receiver aperture	4.0° ± 0.30°	6.0° ± 0.3°

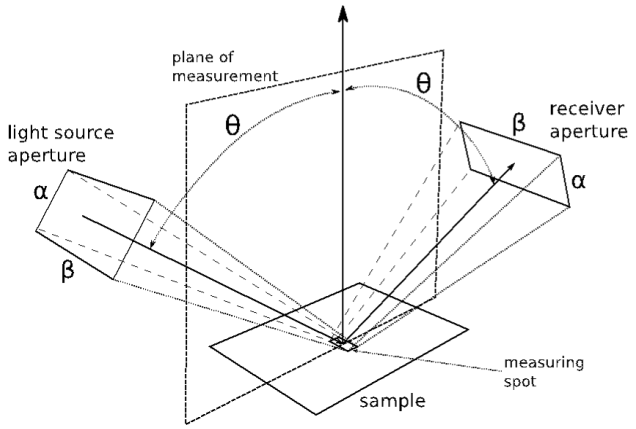

Figure 3: Schematic of a specular gloss meter with the angles associated to Table 1; after Westlund and Meyer (2001), cited from Weber, Spiehl and Dörsam (2021b)

The print settings of the printing machine as well as the anilox rollers used for the experiments are listed in Table 2. Three different substrates were used for this study. These were Chromolux paper from Zanders with a grammage of 100 g/m^2, Chromolux board from Zanders with a grammage of 400 g/m^2, and LumiArt paper from Stora Enso Oyj with a grammage of 115 g/m^2. Both Chromolux substrates are super calendered, which makes their surface extremely smooth and glossy. LumiArt paper is multicoated art paper that is rougher than the Chromolux types. The company Siegwerk produces the primer used for two series of the experiments. The metallic printing inks used for this study were UV low-migration printing inks, which were provided by the company Schlenk. According to the datasheets and additional company information, the pigments of the ink containing VMPs have a d_{50} size of 7 µm and a d_{99} size of 10–12 µm, a metal content of approximately 3 % and a viscosity of 300–900 mPas. Pigments in the ink containing cornflake pigments have a d_{50} size of 6 µm and a d_{99} size of 11–12 µm, a metal content of 15 % and a viscosity of 800–1 600 mPas.

Table 2: Print setting of the laboratory flexo printing machine IGT F1

Anilox force	60 N
Printing force	75 N
Printing velocity	0.50 m/s
Anilox roller volume for printing metallic inks	16 ml/m^2
Anilox roller volume for printing primer	8 ml/m^2

Between printing the samples with the printing machine, placing the gloss meter on the sample and starting the continuous measurement a time lag of about 2 seconds occurred, which was measured repeatedly using a stopwatch. Continuous measurements were made until no significant further change of gloss after printing was observed. Hereafter, the UV-curing of the inks was carried out. Each of the three different substrate types was printed with the two different metallic inks without prior pre-treatment using a primer.

For one series of trials, the LumiArt paper was additionally primed and then printed with the metallic inks. In total, this gave eight different combinations of substrate, pre-treatment and metallic ink.

Before the experiments were carried out, the gloss meter was checked according to its measurement stability under continuous measurement mode. To do so, the device was calibrated on a black glass calibration tile. Afterwards, 500 measurements were carried out using the continuous measurement mode with one second in between the measurements. After each 100th measurement, a measurement on the black calibration tile was taken. From the results shown in Table 3 it can be concluded that the device measurements were stable, and no internal device drift due to possible heat development during measurements could be expected. The used paper substrates were characterized in terms of gloss. The results can be seen in Table 4. Each measurement value is the average of five measurements on different positions and directions on the regarding paper substrate.

Table 3: Stability of the micro-tri-gloss at continuous measurement mode; measurement values in Gloss Units (GU); gloss$_{xx}$ denotes the specular gloss measured at the specular angle of xx°

Number of measurements	gloss$_{20}$[GU]	gloss$_{60}$[GU]	gloss$_{85}$[GU]
0 (calibration values)	92.9	95.4	99.3
100	92.8	95.3	99.3
200	92.5	95.2	99.2
300	92.6	95.2	98.9
400	92.8	95.3	98.9
500	92.8	95.3	98.6

Table 4: Gloss measured at the specular angles of 20°, 60°, and 85° with the micro-tri-gloss on the substrates used in the experiments; the average values and standard deviations are calculated from five measurements on each sample

	Chromolux board	Chromolux paper	LumiArt paper	LumiArt primed
gloss$_{20}$[GU]	57.5 ± 0.4	50.9 ± 1.0	3.4 ± 0.4	15.9 ± 0.9
gloss$_{60}$[GU]	77.9 ± 0.2	80.1 ± 0.2	29.9 ± 0.5	58.7 ± 1.6
gloss$_{85}$[GU]	97.0 ± 0.1	91.2 ± 0.4	79.9 ± 0.5	85.0 ± 0.8

3. Results and analysis

Figure 4 shows one sample of each of the eight combinations of the printing trials, which are Chromolux paper, Chromolux board, LumiArt paper and primed LumiArt paper printed with UV flexo inks containing VMPs and cornflake pigments after UV-curing. The picture was taken with samples placed in front of a checkerboard to give an impression of the glossiness and mirroring capability of the samples. It can be seen that combinations printed with inks containing VMPs give a clearer and sharper reflection of the checkerboard and have a higher gloss than the combinations printed with inks containing cornflake pigments. Further, the reflection of the printed Chromolux paper and board is superior compared to the LumiArt paper and the primed LumiArt paper. The imprint that is visible on some of the samples comes from the gloss meter that was placed on the uncured ink for dynamic gloss measurements.

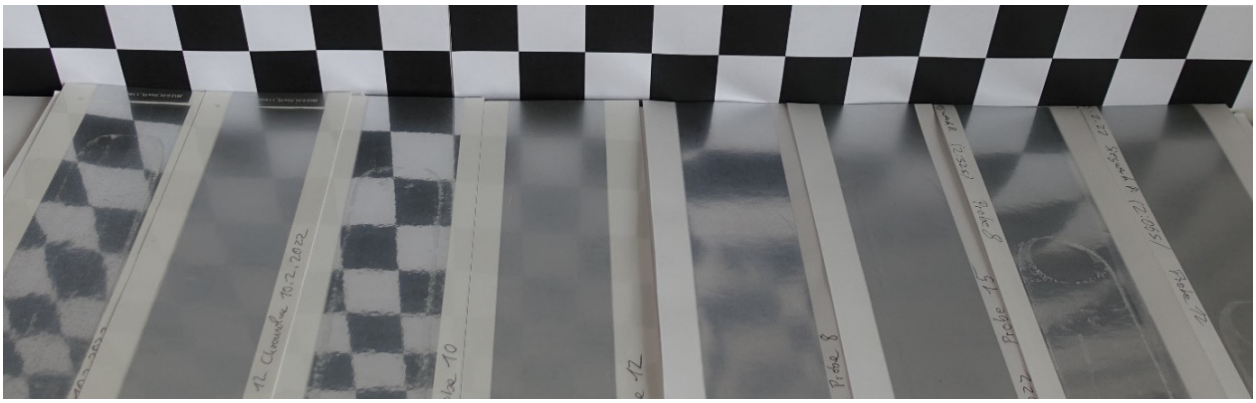

Figure 4: Collection of samples printed in the experiments photographed in front of a checkerboard; from left to right: Chromolux paper (VMP), Chromolux paper (cornflake), Chromolux board (VMP), Chromolux board (cornflake), LumiArt (VMP), LumiArt (cornflake), LumiArt primed (VMP), LumiArt primed (cornflake)

Figures 5–8 show exemplary dynamic gloss curves for each of the eight combinations. The first measurement for each trial started about two seconds after printing. Figure 5 shows the dynamic gloss measured on the uncured ink on Chromolux board. While the specular gloss of inks containing VMPs at 20° and 60° rose rapidly in the first 20 seconds, inks with cornflake pigments exhibited only minor changes in specular gloss. Figure 6 shows the dynamic gloss on Chromolux paper. Compared to all the other combinations, dynamic gloss changes can be measured for a very long time on this substrate using inks containing VMPs. It is also important to note that the specular gloss measured at 20° first decreases slightly before it goes up. Interestingly, dynamic gloss changes could be measured for a longer time on Chromolux paper compared to Chromolux board for both types of metallic inks. In Figure 7, the dynamic gloss curves for unprimed LumiArt paper can be seen. For inks containing VMPs it is interesting to see that the specular gloss measured at 60° rose for more than 60 seconds while the specular gloss measured at 20° only rose for a short instant, and then decreased. When comparing the dynamic gloss on LumiArt paper with dynamic gloss on primed LumiArt paper it is striking that the time during which the gloss rose after printing was shorter while the total gloss measured at the three angles was higher compared unprimed LumiArt paper. Overall, the rise of the gloss values measured at the three angles always took longer, and the maximum gloss levels were always higher for inks containing VMPs compared to cornflake pigments.

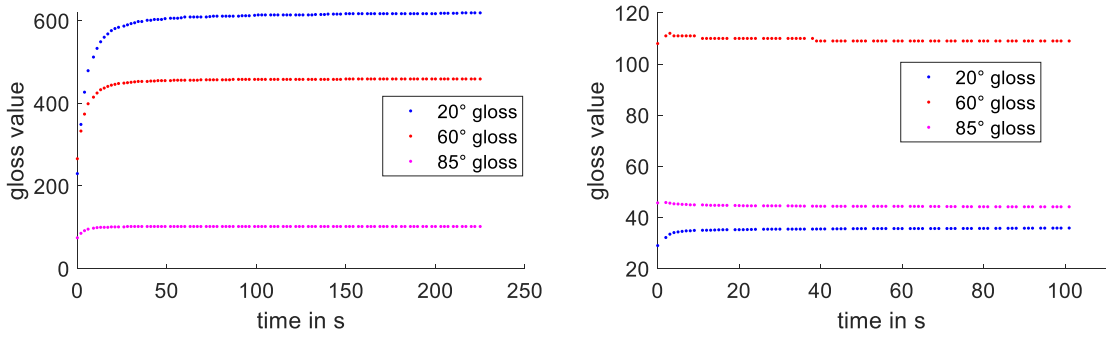

Figure 5: Dynamic gloss measured on Chromolux board with inks containing VMPs (left) and cornflake pigments (right)

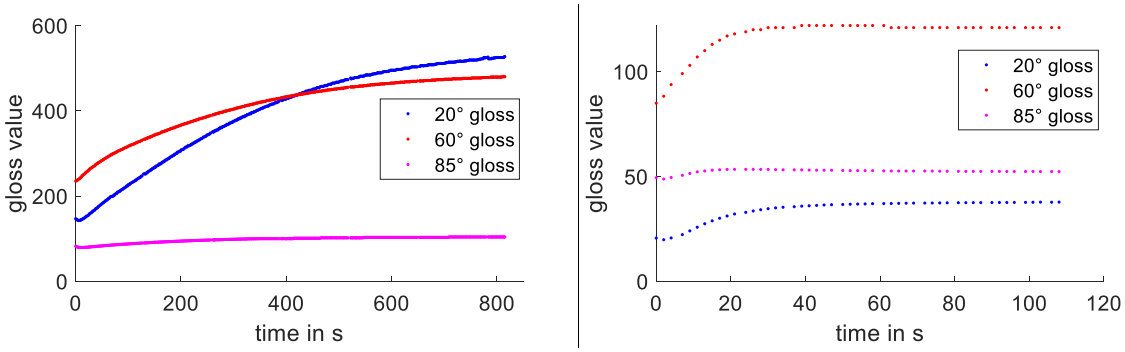

Figure 6: Dynamic gloss measured on Chromolux paper with inks containing VMPs (left) and cornflake pigments (right)

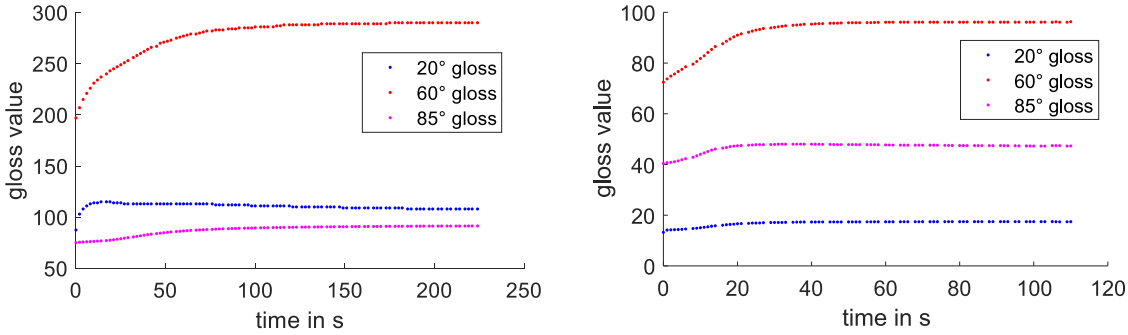

Figure 7: Dynamic gloss measured on LumiArt paper with inks containing VMPs (left) and cornflake pigments (right)

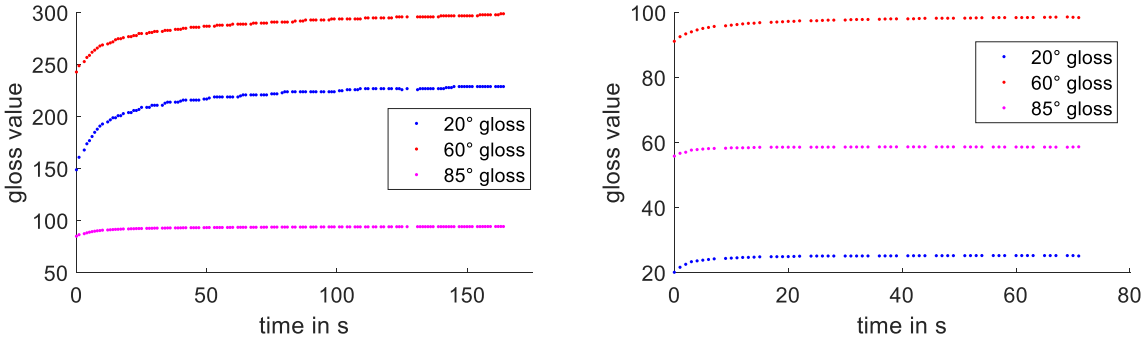

Figure 8: Dynamic gloss measured on primed LumiArt paper with inks containing VMPs (left) and cornflake pigments (right)

Figure 9 shows two microscopic images taken from metallized Chromolux board after UV-curing. On the left, VMPs and on the right Cornflake pigments of the metallic inks used can be seen. The light areas in the respective pictures are the pigments. It can be seen that the VMPs appear to align better to each other, while the cornflake pigments appear to have a greater size distribution, more edges, and a higher surface roughness. Thus, light reflection becomes more diffusive, and gloss is generally lower for substrates metallized with cornflake pigments than with VMPs.

There are three factors that could lead to a higher mobility of the VMPs in the ink compared to the cornflake pigments. First, VMPs are much thinner than cornflake pigments, second the metal content of the VMP ink is lower, and third the viscosity of the ink containing VMPs is lower. Hence, gloss changes are measurable for a longer time when using the ink containing VMPs.

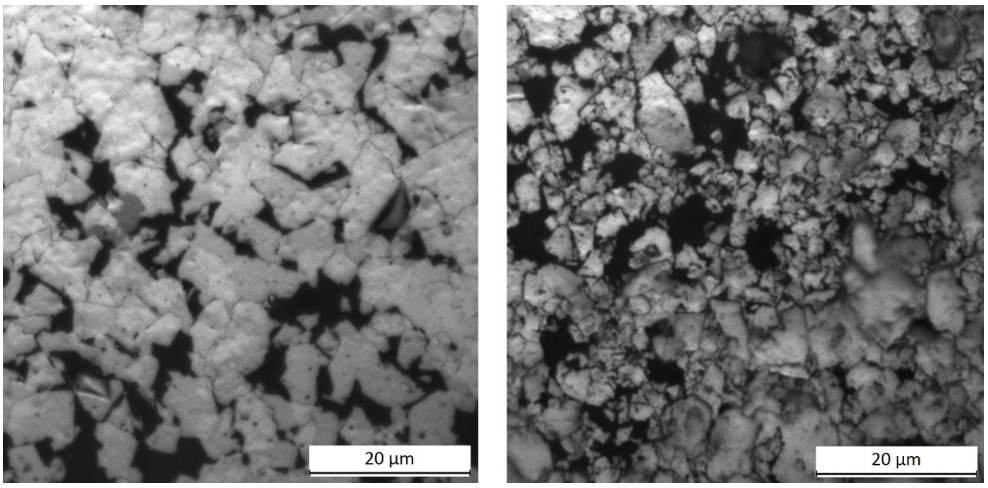

Figure 9: Inks containing VMPs (left) and cornflake pigments (right) printed on Chromolux board

In the following, only the dynamic gloss measured on Chromolux board and on unprimed LumiArt paper are analyzed in greater detail and it is shown how the dynamic gloss trends can be modeled using mathematical functions. When using inks containing VMPs, dynamic gloss curves for Chromolux board and Chromolux paper can be modeled best with a Kohlrausch function 1. The t is the time of measurement, a, b, c and d are non-negative fit parameters. $c - a$ is the gloss delta from the start of the measurement until the steady state gloss value, given by c. The b reciprocally correlates with the time needed to reach the steady state gloss value, and positively correlates with the initial incline. The d is the stretching exponent that is usually between 0 and 1.

$$f(t) = -a * exp(-(b * t)^d) + c \qquad [1]$$

This Kohlrausch function (Kohlrausch, 1854) describes the distribution of attachment energies of electric charges at the dielectric between capacitor plates. The stretching exponent d = 0…1 is characteristic for the material and its influence on the capacitor discharge process. The case d = 1 corresponds to ordinary exponential relaxation. If applied to dynamic print gloss, the stretching exponent d could describe the feature that pigments float up with size-dependent rates. For the VMP relaxation on Chromolux board, e.g., one finds d = 0.70 and 0.74 for gloss angles of 20° and 60°, as shown in Figure 10. This could describe the feature that larger pigments float up faster than smaller ones.

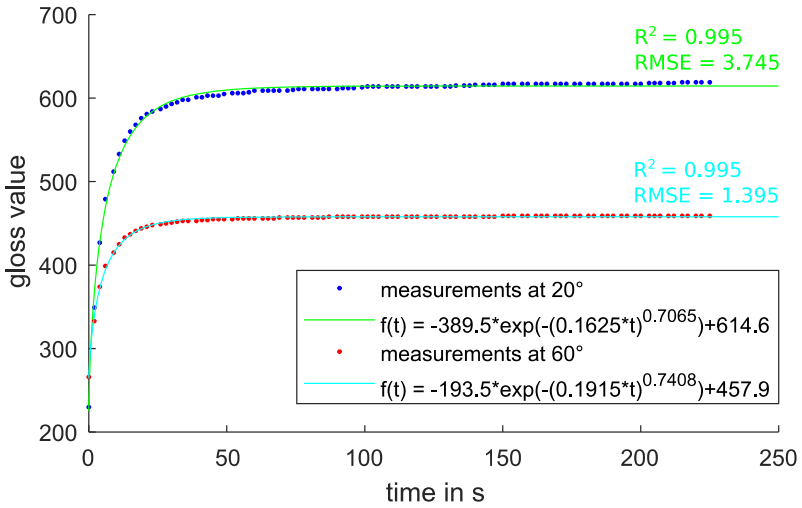

Figure 10: Fitting of function 1 on the dynamic gloss measured on Chromolux board when printing with inks containing VMPs

When fitting function 1 on the dynamic gloss trends measured at 20° and 60° resulting from unprimed LumiArt paper and inks containing VMPs, it is striking that the function does not give a good fit for the trend measured at 20°. However, for the trend measured at 60° a Kohlrausch fit with $d = 1$ appears adequate, which is shown in Figure 11. Function 2 is a better model of the gloss curve measured at 20°. It is the sum of two exponential functions. One of them describes the rising, the second one a slow and steady decrease of the gloss level.

$$f(t) = -a * exp(-b * t) + c * exp(-b' * t) + h \quad [2]$$

Where $h + c$ gives the gloss maximum that is reached, a gives the delta between the first measurement and the gloss maximum. b is the rising rate of the initial incline, and $b' << b$ describes the slow decline after the gloss maximum has been passed. The description of the dynamic gloss with the summation of the two exponential function shows that basically two different processes happen after printing, of which one is responsible for the incline of the curve and one for the decline. To explain these different behaviors of dynamic gloss measured at 20° and 60° both the process that happens after printing as well as the construction of a gloss meter has to be considered.

After printing, the gloss influencing processes are first the levelling of the ink film, the alignment of the pigments to the ink surface as well as the floating up of the pigments in the ink. Secondly, the binder of the ink penetrates into the substrate. For this reason, the ink film that is still present on the paper surface together with the pigments aligns more and more with the paper surface texture. This leads to a rising roughness of ink film. A schematic of this process can be seen in Figure 12. The decreasing interspace between the pigments leads to the effect that total amount of reflected light increases. The increasing roughness of the ink film surface caused by the comparatively slow binder penetration into the paper leads to an increasing scattering of light.

Since the receiver aperture of the gloss meter at 20° is smaller than the receiver aperture at 60°, the increasing scattering of light results in a decreasing fraction of incident light at the photodiode behind the aperture. Thus, the measurement signal decreases when scattering becomes more apparent. The larger receiver aperture at 60° however, is not so sensitive to the scattering of reflected light. From the amount of scattered light, a greater amount can pass the receiver aperture without attenuation. Hence, the amount of light passing the receiver aperture increases as the interspace between the pigments decreases.

According to ASTM D4039-09, haze that makes statements about the scattering of light can be calculated by taking the subtraction of 20° from gloss measured at 60° (American Society for Testing and Materials, 2015). For reasons unknown to the authors this is only specified for nonmetallic surfaces. However, if that is applied here not only the dynamic gloss is measured but also statements about a dynamic haze that changes with time after printing can be made.

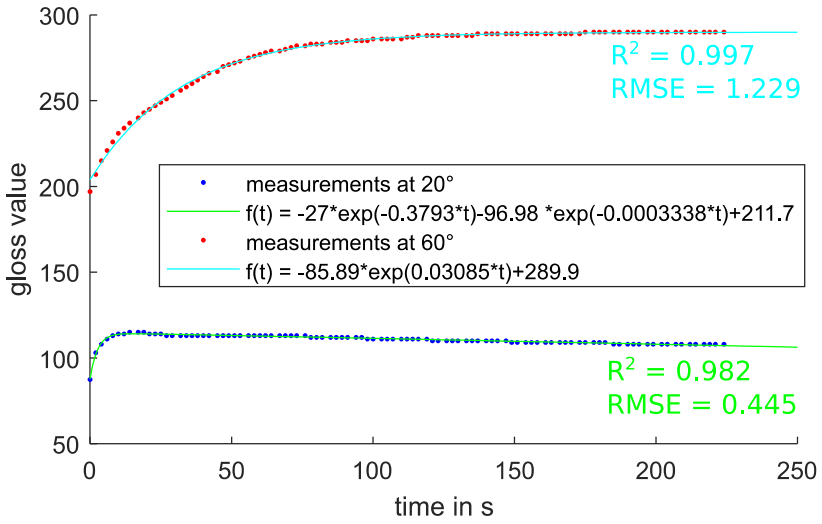

Figure 11: Fitting of function 1 and function 2 on the dynamic gloss measured on unprimed LumiArt paper when printing with inks containing VMPs, with b = 0.3793 and b' = 0.0003338 at a gloss angle of 20°

Figure 12: Schematic of ink levelling of metallic inks on a rough substrate with a relatively high porosity and roughness

4. Conclusion and outlook

In the present study, the dynamic gloss after printing metallic inks on different substrates was investigated using specular gloss measurements made at three different angles. It was shown that inks containing different sorts of aluminum pigments behave very differently, and that the substrate also has a major impact on the dynamic gloss. Further, it was shown how some of the dynamic gloss trends can be modeled using exponential functions and how the meaning of the fit parameters of these can be explained. A major finding was that the dynamic gloss trends measured at different angles can have opposite directions. An explanation of this phenomenon was given by referring to the construction of the gloss meter as well as by referring to the processes influencing the gloss and the scattering of light after printing. The difference of the trends of gloss measured at 20° and 60° can also be referred to as dynamic haze.

In further studies the process of the change of dynamic gloss will be interrupted in different time intervals. By doing so, we will be able to investigate the changing positions of the pigments and the correlating gloss in a steady state and hence in more detail. Further, we will examine the pore structure and water absorptivity of the substrates to relate them with the dynamic gloss and to find out why e.g., Chromolux paper and Chromolux board behave very different in terms of dynamic gloss. Additionally, experiments are planned using a different gloss meter that enables to make continuous gloss measurements and to make investigations on the light distribution around the specular angle and gives not only a single gloss value for every angle.

Acknowledgements

The authors would like to express their gratitude for the financial support by the Heidelberger Druckmaschinen AG. Furthermore, we kindly acknowledge Schlenk AG, Roth (Germany) for cooperation. We also acknowledge Eckart GmbH, Hartenstein (Germany) for support. Mr. Yishuo Wang is to be thanked for his pre-investigations in his master thesis with the title "Software-based evaluation of microscope images and printing parameters for the analysis of printed metallic gloss".

References

American Society for Testing and Materials, 2015. *ASTM D4039-09(2015): Standard test method for reflection haze of high-gloss surfaces*. West Conshohocken, PA, USA: ASTM.

American Society for Testing and Materials, 2018. *ASTM D523-14(2018): Standard test method for specular gloss*. West Conshohocken, PA, USA: ASTM.

Kohlrausch, R., 1854. Theorie des elektrischen Rückstandes in der Leidener Flasche. *Annalen der Physik*, 167(2), pp. 179–214. https://doi.org/10.1002/andp.18541670203.

Koivula, H.M., Juuti, M., Bousfield, D., Preston, J., Silvennoinen, R., Peiponen, K. and Toivakka, M., 2009. Comparison of dynamic print gloss measurement techniques. *Tappi Journal*, 8(2), pp. 19–28. https://doi.org/10.32964/TJ8.2.19.

Maile, F.J., Pfaff, G. and Reynders, P., 2005. Effect pigments – past, present and future. *Progress in Organic Coatings,* 54(3), pp. 150–163. https://doi.org/10.1016/j.porgcoat.2005.07.003.

Pfaff, G., Bartelt, M.R. and Maile, F.J., 2021. Metal effect pigments. *Physical Sciences Reviews,* 6(6), pp. 179–197. https://doi.org/10.1515/psr-2020-0182.

Preston, J.S., Parsons, D.J., Gate, L.F., Husband, J.C., Legrix, A. and Jones, M., 2003. Ink gloss development mechanisms after printing: part 1 – the influence of ink film thickness. *Journal of Graphic Technology*, 1(2), pp. 29–37.

Rich, D.C., Marcus, R., Lovell, V. and Kreutz, T., 2017. Modeling the appearance of metal-like packaging printing. *Color Research and Application,* 42(1), pp. 38–49. https://doi.org/10.1002/col.22035.

Weber, C. F., Spiehl, D. and Dörsam, E., 2021a. Comparing gloss meters for gloss measurements on metallic embellishments from the printing industry. In: C. Ridgway, ed. *Advances in Printing and Media Technology: Proceedings of the 47th International Research Conference of iarigai*. Athens, Greece, 19–23 September 2021. Darmstadt: iarigai, pp. 189–199. https://doi.org/10.14622/Advances_47_2021.

Weber, C.F., Spiehl, D. and Dörsam, E., 2021b. Comparing measurement principles of three gloss meters and using them for measuring gloss on metallic embellishments produced by the printing industry. In: C. Schierz and C. Vandahl, ed. *Lux junior 2021: 15. Internationales Forum für den lichttechnischen Nachwuchs*. Ilmenau, Germany, 4–6 Juni 2021. Ilmenau: Technical University Ilmenau, pp. 327–341. https://doi.org/10.22032/dbt.49339.

Weber, C.F., Spiehl, D. and Dörsam, E., 2022. Printing methods used in the label and package printing industry for producing metallic embellishments with a focus on metal effect pigments. *Journal of Print and Media Technology Research,* 11(1), pp. 29–45. https://doi.org/10.14622/JPMTR-2118.

Westlund, H.B. and Meyer, G.W., 2001. Applying appearance standards to light reflection models. In: *SIGGRAPH '01: Proceedings of the 28th annual conference on Computer graphics and interactive techniques*. New York, NY, USA: ACM, pp. 501–51. https://doi.org/10.1145/383259.383318.

Wheeler, I., 1999. *Metallic pigments in polymers*. Shawbury, U.K: Rapra Technology Ltd.

Wißling, P., 2013. *Metalleffekt-Pigmente*. 2nd ed. Hannover: Vincentz Network.

DOI 10.14622/Advances_48_2022_15

Investigation of relationships between the flexographic printing plate patterning and the anilox surface and volume in case of solid white ink printing on transparent materials

Csaba Horvath[1], *Klaudia Manurova*[2], *Edina Preklet*[3] *and Ferenc Varza*[2]

[1] Óbuda University; Institute of Media Technology and Light Industry Engineering; Hungary

[2] University of Sopron; Doctoral School of Wood Sciences and Technologies; Hungary

[3] University of Sopron; Institute of Wood Engineering; Hungary

E-mails: csaba.horvath@nyt.hu; vach.klaudia@gmail.com; joobne.preklet.edina@uni-sopron.hu; varzaf@gmail.com

Short abstract

This paper aims to explore the relationships between the flexographic printing plate surface patterning and anilox cell geometry and simultaneously searches for the solution to a genuine phenomenon in flexographic printing – to find an answer on how to achieve an optimal white underprint coverage.

Keywords: flexography, surface patterning, white inks, coverage, mottle

1. Introduction and background

Despite the massive expansion and development of digital printing techniques, the innovation is not dropped away in the branch of flexography at all. In the full width of the flexographic printing process, we can meet exciting innovations- fast, precise, more-economic printing machines, advanced ink recipes, ecofriendly materials, revolutionary aniloxes, etc.

Over the past two decades, in the production of flexographic printing plates, we could observe massive technological progress. The newest technologies in platemaking work with flat-top dots and nowadays we can choose from flat-top dots generated inherently by the plate material, or we can create them by different technologies where the absence of oxygen at the main exposure is essential for the creation of flat-top dots. Big advantages in quality can be achieved by the plate surface patterning. There exist many structures which are applicable on the plate surface helping to optimize the ink transfer and the ink laydown and supporting through that the achievement of excellent print quality.

Not only the contemporary technology is driving through changes, so do the market and the customer needs too. The market is becoming faster and faster because the customer today wants everything immediately, in good quality and cheap if possible. The technical progress aims to help printing houses fight the new trends successfully, but every step through the whole process needs to be optimized, standardized, and improved to the best possible level.

One of the challenges for the printing houses working with flexo technology is to print on different print surfaces with inks of different compositions to produce good quality prints. (Várza, Preklet and Horváth, 2021) A big part of flexible packaging materials is printed on transparent substrates, where white underprint is almost always a must. Displaying white color is a complex and difficult task itself if it is not examined in the active color display (on-screen), but from the aspect of passive (reflectional) printed colors. To reach the most optimal result during flexo printing, the coordinated operation of several elements of the process is necessary. (Várza, Preklet and Horváth, 2021; Borbély and Szentgyörgyvölgyi, 2011)

2. Materials and methods

In our research, we are examining how plate surface patterning and anilox cell geometry affect the white ink laydown, the ink coverage, and the visual ink porosity in the solvent-based and UV-based flexographic printing process.

For our research purposes, we have chosen two technologies often used in contemporary flexo printmaking practice – the Kodak Flexcel NX technology and the Pixel+ software solution from Esko combined with the DuPont™ Cyrel® Digiflow technology for flat-top dot plate making. To enable an outstanding print quality is efficient and controlled ink transfer crucial, which can maximize the color gamut and gives a great tonal range. Traditionally, for flexography was a problem to achieve pinhole-free ink laydown and a maximal color gamut and efficient ink use at the same time. The micro surface textures of flexo plates are solving this while they also transform the flexo ink transfer.

2.1 Printing plates used for the test

The Kodak Flexcel NX technology was the first of the modern techniques that came back with flat top dots in a "half-digital way". The Flexcel NXH plates can be used with a wide range of substrates and work with unique technology. The Flexcel NX Thermal Imaging Layer, utilizing unique imaging technology, and lamination: this combination provides high-resolution imagery on the plate, with 1:1 dot replication, and stable, predictable ink transfer. Digicap NX Patterning with Advanced Edge Definition enables good ink laydown control, expanding achievable color gamut and delivering better print contrast, improved tonal range, smooth solids, bright colors, and crisp text. (Miraclon, 2022) Because of more than 10 years of FNXH plate success, we have chosen this material to be one of our tested raw materials (Figure 1).

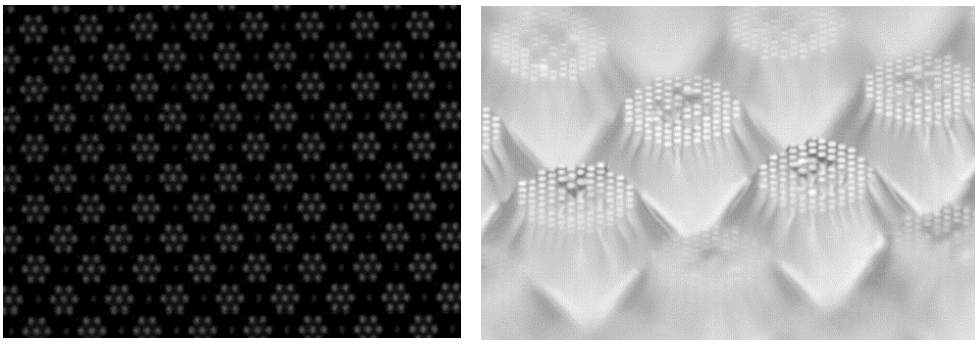

Figure 1: High magnification view of FNXH Digicap Patterning – Advanced pattern

For the case of the other technology – the Pixel+ - we had more variable possibilities. The microcell structure of Esko's Pixel + may be applicable on common digital printing plates, which need to be processed later on a specific technology to achieve flat-top dots – in our case on DuPont™ Cyrel® Digiflow or we can choose modern printing plates, where the capability of flat-top dot creation is included in the raw plate material and a classic plate making process is sufficient. In our test are 4 materials included with Pixel+ technology, two of them are classic digital plates and two have inherent flat top dot possibility (Figure 2). These five plates with different surface structures are tested in the printing process under different conditions. DuPont™ Cyrel® DPR plate is a digital solvent plate and can be used in a wide range of applications. Its durometer is 76 Shore A, and with the application of surface patterning and Digiflow technology, good results could be obtained. A similar, medium-hard printing plate is the DuPont™ Cyrel® DPN. It should have similar characteristics to the DPR plate, it has the same hardness, but according to our professional experience, this plate fits well for solid applications. Our third choice was the DuPont™ Cyrel® EASY ESXR plate. DuPont™ Cyrel® ESXR is the latest addition to the DuPont™ Cyrel® EASY platform with built-in flat-top dot technology for solvent processing. It´s a plate that is based on advancements to Cyrel® EASY

polymer, that delivers high ink transfer and resolution (DuPont de Nemours Inc., 2019). The fourth plate selected for the test was the MacDermid LUX ITP™ 60. This plate was the first to market with an inherently flat-top dot technology for flexographic photopolymer plates. It´s a hard durometer photopolymer plate with its 78 Shore A, where no additional platemaking steps or equipment are needed to take advantage of the flat-top dots provide.

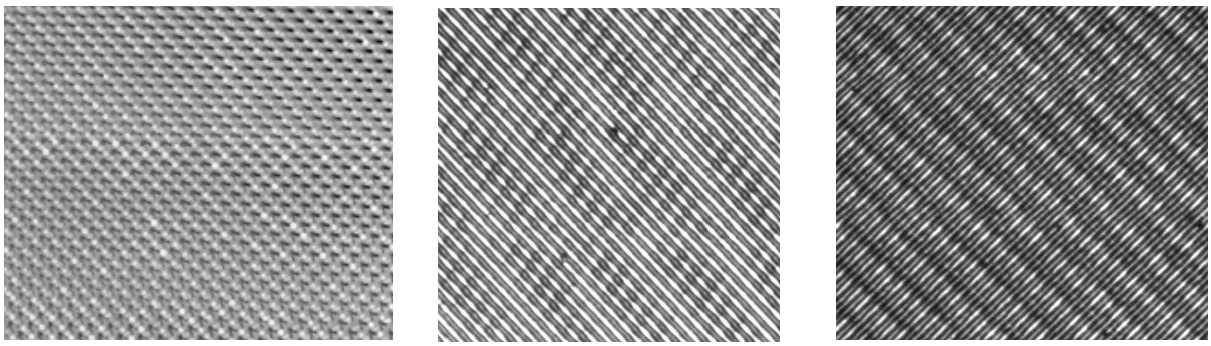

Figure 2: Photo of the MacDermid LUX ITP™ 60 plate and the MCWSI structure on the solid (left), the DuPont DPN plate with MG45 (middle) and the DuPont ESXR plate with MG34 structure (right)

Altogether, these five plates (FNXH, DPR, DPN, ESXR, ITP 60) with different surface structures are tested in the printing process under different conditions.

During our works we made a complete photography documentation of the printing plates we used in the test. All plates, all structures and all laser powers have been documented, but due to the limited space we show above a very few of them. Figure 3 illustrates the design of the printing plates.

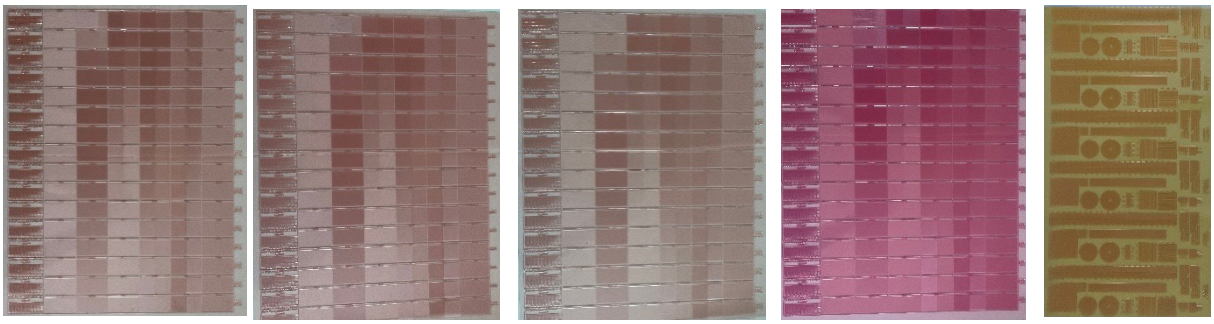

Figure 3: Photos of the printing plates used in the testing process

2.2 White ink printing in the flexography

In flexography is one of the most complicated topics the printing of the white underprint. It is no coincidence that one of the key points in improving print quality lies in the practice of using white inks, as there are many obstacles to printing in white.

The first printing problem is the coverage, the smoothness of the solid ink, which simply means the opacity and saturation of white ink. This is especially important if there are strong, contrasting colors to print, because with a poor quality white underprint on a transparent substrate the color-print will not be visible. If the white is weak, the packed product also can show through the packaging, which can spoil the imagined design and product appearance.

During our tests two types of white ink were used. The first one is a standard white UV ink for lamination and the second one is also a standard white solvent ink, where the print can be laminated in the later steps.

The sole function of the anilox is to ensure that a consistent amount of ink is delivered onto the printing plate, time after time. (Racey, 2016) For our research, we are using three types of anilox rolls – the classic 60°hexagonal, channel engraved, and high-volume process aniloxes with elongated hexagonal cells (Figure 4).

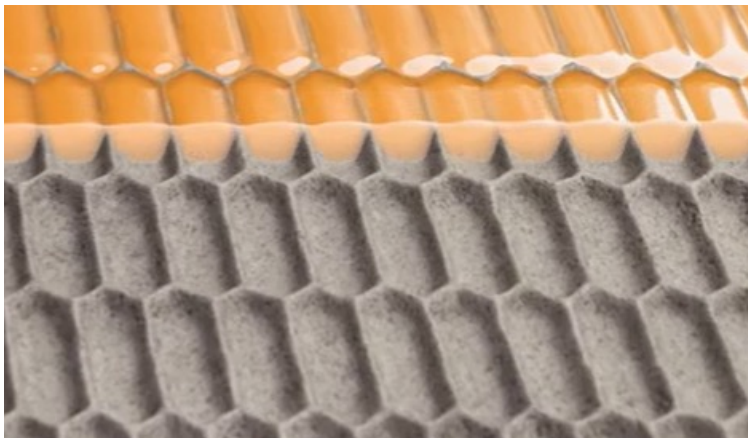

Figure 4: High volume process aniloxes with elongated hexagonal cells (Sandon, 2022)

The following anilox rollers were included in the test process:

- high-volume process with elongated hexagonal cells 200 lpcm / 12 cm^3/m^2
- high-volume process with elongated hexagonal cells 200 lpcm / 10 cm^3/m^2
- high-volume process with elongated hexagonal cells 160 lpcm / 14 cm^3/m^2
- classic hexagonal cells 60° 120 lpcm / 15 cm^3/m^2
- channel engraved (L) 10-11 cm^3/m^2
- channel engraved (XL) 13-15 cm^3/m^2
- channel engraved (M) 7-8 cm^3/m^2

Last, but not least we examined according to our possibilities the above-mentioned settings in a solvent-based printing process and in a UV-based printing process. The test for the solvent-based samples was produced on an 8-color Soma Midi Flex 2 machine and our UV-based samples were made on a 670 mm wide Bobst M6 printing machine.

3. Results and discussion

What we evaluated for the purposes of this research for both presses – the solvent-based and the UV-based – is the solid ink coverage. coverage. We carried out measurements on the test prints. During these examinations, we used an X-Rite NGH (eXact) spectrophotometer with D50/2°, M0(No) no filter conditions for measuring lightness. With our measurements we determined the coverage levels of the opaque white relative to each other. This means that we measured the achievable whiteness in CIE $L^*a^*b^*$ values after laminating onto a black base foil. Here, we examined absolute values, that is how much we could approximate the ideal colorimetric white ($L^* = 100$ $a^* = 0$ $b^* = 0$). The level of coverage always depends on the backing material. Under these conditions, we need to focus mostly only on the L^* value of the CIE $L^*a^*b^*$ measurements, and the absolute values of a^* and b^* need to remain less than 2–3. (Várza, Preklet and Horváth, 2021) We did the measurements for every printing plate and every pattern we used, to get the results on which patterning fits the best for the printing of the white underprint – we did it for solvent and UV separately. As the next step of our research, we will also evaluate the mottle effect on the printed samples, because not only the solid ink coverage is an important factor to evaluate, but it has to be examined together with the mottle – these two factors together build up the visible result of a solid. Further, we evaluated the influence of the anilox cell geometry and the ink volume that influences the quality of the white underprint.

It is not necessarily true, that a print squeaking in ink is the best solution for a white print. Moreover, if the white separation would contain vignettes, the situation would become even more complicated. For this article we don´t discuss any fades and vignettes, we are just dealing with the solids, but we plan to extend our research further to this topic too.

Based on the measurements of 2 730 measuring points, we made the following findings:

- For the solvent based flexo technology the best coverage was achieved by the DuPont DPR plate and with the high-volume process anilox with elongated hexagonal cells 200 lpcm /10 cm^3/m^2. The winning structure was the MG45 at a very low – 110 % laser power. In addition the MacDermid ITP60 plate was performed also outstandingly.
- In the UV printing process we got the best results with the DuPont ESXR plate and the channel engraved anilox (XL) 13–15 cm^3/m^2. The best surface structure performance was given also by the MG45 at 110 % laser power. We could observe very high values also in the case of the MCWSI structure on the same (ESXR) material.

In the Table 1 and Table 2 we present our measurement data (L^* values) for the winning samples.

Table 1: Data of the sample with the best results in the UV printing process

Printing plate: ESXR		Printing process: UV		Anilox: XL		
Laser power (%)	MC16P	MG25	MG45	MG34	MCWSI	Solid
100	82.04	82.37	78.75	82.89	43.57	82.04
110	82.12	82.43	82.95	82.75	81.90	82.09
120	82.08	82.38	82.85	82.51	82.65	82.06
130	82.09	82.40	82.68	82.33	82.69	82.00
140	82.12	82.42	82.63	82.24	82.67	82.04
150	82.16	82.43	82.57	82.23	82.65	82.01
160	82.17	82.44	82.56	82.03	82.55	82.03
170	82.13	82.47	82.52	82.01	82.53	82.12
180	82.20	82.52	82.46	82.04	82.50	82.10
190	82.31	82.59	82.50	82.01	82.44	82.07
200	82.23	82.56	82.44	81.96	82.44	82.24
210	82.25	82.47	82.37	81.92	82.26	82.05
220	82.23	82.48	82.41	81.97	82.28	82.11
230	82.16	82.49	82.34	81.96	82.18	82.05
240	82.24	82.45	82.27	81.92	82.09	82.16
250	82.18	82.49	82.22	82.00	82.07	82.19

Table 2: Data of the sample with the best results in the solvent printing process

Printing plate: DPR		Printing process: Solvent		Anilox: 200/10		
Laser power (%)	MC16P	MG25	MG45	MG34	MCWSI	Solid
100	75.15	76.42	75.50	76.12	68.77	76.01
110	74.87	76.40	79.96	76.29	75.23	75.94
120	74.75	76.40	76.41	76.28	75.96	75.74
130	74.72	76.41	76.35	76.26	76.61	75.74
140	74.89	76.41	76.28	76.11	76.74	75.76
150	74.90	76.38	76.28	75.94	76.72	75.77
160	74.85	76.43	76.16	75.88	76.65	75.71
170	74.82	76.37	76.06	75.91	76.56	75.57
180	75.02	76.32	76.04	75.80	76.53	75.61
190	74.87	76.21	75.99	75.58	76.26	75.72
200	74.96	76.15	75.73	75.57	76.22	75.54
210	75.87	76.08	75.83	75.75	76.19	75.62
220	74.71	75.97	75.85	75.72	76.17	75.57
230	74.94	75.96	75.85	75.75	76.10	75.56
240	74.98	76.21	75.61	75.86	76.02	75.53
250	75.11	76.12	75.76	75.92	76.20	75.59

We can overall determine, that for the conditions of the material types and equipment we used in solvent technology fits the DuPont DPR plate and for the UV technology is the DuPont ESXR plate the best solution for the coverage.

4. Conclusions

When we sum up everything, the goal of our research was to determine the configurations of the printing process with the usage of our specific technologies. We aimed to find out which of the settings can result in the most perfect product using the least possible amount of raw material.

Based on our measurements, we determined the optimal and economical white ink application options for the conditions we used and found that by using them, we can achieve a significant improvement in quality and ink savings. The high print quality is also reflected in the fact that we did not realize any ink smudging.

As a result of the last world events, increasing market and economic uncertainty encourages us all to be thrifty. In addition to all this, the role of environmental awareness is becoming more and more prominent these days, so it is important from several points of view to achieve the best results in terms of both material use (economy) and scrap production (quality) during the production of our products. We are confident that our research represents a big step forward in this regard.

Hopefully despite the crises of the last period the doors will remain open to numerous new research and development projects in the future. Thus, our plans with this research are to help to improve the quality of flexographic printing and our future research plans include the creation of new surface patterns, printability analysis of text elements, the study of prints with certain screen types, printing optimization and standardization and the examination of the possibilities of increasing ink coverage.

Acknowledgments

We would like to thank Plastex Ltd. in Nitra -Slovakia for the production of the printing plates for our research and for their technological equipment to make the measurements and photo documentation. Our thanks also belong to Pandan Ltd. in Hungary – Szombathely for their time and material, where our samples have been printed.

References

Borbély, Á. and Szentgyörgyvölgyi, R., 2011. Flexográfiai eljárással műanyag fóliákra készült nyomatok színminősége. *Óbuda University e-Bulletin*, 2(1), pp. 341–346.

DuPont de Nemours Inc., 2019. *DuPont™ Cyrel® EASY ESXR*. [online] Dupont.com. Available at: <https://www.dupont.com/content/dam/dupont/amer/us/en/cyrel/Public/documents/en/PDS-NA0096-EN_Cyrel_ESXR.PDF> [Accessed 29 March 2022].

Miraclon, 2022. *KODAK FLEXCEL NXH Plates*. [online] Miraclon. Available at: <https://www.miraclon.com/products-technology/flexcel-nx-system/flexcel-nxh-plates/> [Accessed 28 March 2022].

Racey, G., 2016. *How to Optimise the performance of your anilox rolls in 3 steps*. [online] Pamarco. Available at: <https://web.archive.org/web/20171012153042/http://www.pamarco.com/how-to-optimise-the-performance-of-your-anilox-rolls-in-3-steps/> [Accessed 13 November 2021].

Sandon, 2022. *Anilox rollers & sleeves – laser engraved ceramic coated – wide web – Sandon Global*. [online] Available at: <https://www.dksh.com/kr-en/products/ppc/sandon-global-anilox-rolls-and-sleeves-wide-web> [Accessed 28 March 2022].

Várza, F., Preklet, E. and Horváth, C., 2021. Application analysis of white flexographic printing inks on biodegradable flexible foil. In: *Proceedings of the 2nd International Conference on Circular Packaging*. Slovenj Gradec, Slovenia, 9–10 September 2021, pp. 311–320.

DOI 10.14622/Advances_48_2022_13

Angular dependent reflectance spectroscopy of RGBW pigments

Alina Pranovich[1], *Abigail Trujillo Vazquez*[2], *Daniel Nyström*[1], *Sergiy Valyukh*[1], *Jeppe Revall Frisvad*[3], *Susanne Klein*[2] *and Carinna Parraman*[2]

[1] Linköping University, Sweden

[2] University of the West of England, United Kingdom

[3] Technical University of Denmark, Denmark

E-mails: alina.pranovich@liu.se; abigail.trujillovazquez@uwe.ac.uk,

Short abstract

Traditional printing relies primarily on subtractive color mixing techniques. In this case, optical color mixing is achieved by one of the established halftoning methods that use Cyan, Magenta, Yellow and Black (CMYK) primaries on a reflective white substrate. The reason behind the subtractive color mixing in printing is the high absorbance of available pigments used in inks. A new type of mica-based pigments that exhibit high reflectivity at Red, Green, Blue and White (RGBW) spectral bands was recently introduced by Merck (Spectraval™). Printing with RGBW primaries on black background allows additive color mixing in prints. While offering excellent color depth, the reflected spectra of such pigments vary with the angles of incidence and observation. As a result, new approaches in modelling the appearance of prints as well as strategies for color separation and halftoning are needed. The prior optical characterization of the reflective inks is an essential first step. For this purpose, we have used Spectraval™ pigments to prepare acrylic based inks, which we applied on glass slides by screen printing. In this work, we measured the relative spectral bidirectional reflection distribution of Red, Green, Blue and White reflective inks. The measurements were conducted on an experimental set up consisting of a goniometer, spectrometer, and a xenon light source. Based on the measurements, we simulate the reflectance spectra under diffuse illumination and demonstrate ratios of red, green, and blue spectral components for different observation angles of individual inks and their combinations.

Keywords: RGB printing, BRDF, spectroscopy, special effect inks

1. Introduction and background

Mica minerals are widely used in the production of coloring media in a range of applications, including printing and cosmetics. The preparation process of mica-based pigments is a complicated process that depends on the desired properties. After grounding the mineral into powder, the process can include dyeing the mica particles, coating them with metallic oxide or optimizing the particles' surface structure, depending on the desired properties (Maisch, Stahlecker and Kieser, 1996). The resulting inks and coatings based on treated mica flakes can provide visual effects such as goniochromatism, or pearlescent (metallic) effects. The recently introduced Merck Spectraval™ pigments are optimized for selective light reflectivity at the RGBW bands (Merck, 2021). This property allows additive color mixing in printing, which is not possible with traditional inks according to the subtractive model. It is possible to use Spectraval™ pigments in commercial printing such as screen printing or lithography (Klein, Parraman and Voges, 2019; Parraman and Klein, 2021) however the methods have to be adapted to the size of the pigments (1–25 μm) i.e. using lower print resolution. The appearance of the prints, however, is difficult to predict, due to the optical properties of highly reflective pigments applied on their own or in combination with absorbing pigments (Trujillo-Vazquez, et.al., 2022).

In conventional color printing, the colorants (inks) are characterized by their spectral power distribution, in combination with the reflective substrate. Various color prediction models and halftoning techniques have been implemented to achieve accurate color reproduction, using subtractive color mixing of dye-based inks. As the main input, such models require the spectral reflectivity of the primary inks, as well as overlapping inks (the so called Neugebauer primaries). The spectral reflectance is assumed to be constant for all viewing and illumination directions, a property called Lambertian reflectance. For an accurate color reproduction, effects such as mechanical and optical dot gain need to be compensated for in the color separation and halftoning process.

In the case of reflective inks like Spectraval, the assumption of Lambertian surface reflectance does not hold. Furthermore, the reflective RGBW inks used in our experiment can exhibit goniochromatic properties. The main property of the inks studied here, is that the nominal pigment color (red, green, or blue) can be observed only for a specific combination of angles of illumination and observation (or specific angle of observation in case of diffuse illumination). For non-optimal observation angles, the perceived color of the inks fades towards grayish or white. The light-matter interaction leading to the color formation of these inks is therefore different from the well-characterized conventional CMYK inks. Rather than selective absorption, and high scattering at specific wavelengths, selective light interference on the pigment coating may provide an explanation for the observed visual effects (Du, et al., 2008). Thus, full optical characterization is required for accurate appearance modeling of prints made with RGBW primaries. This characterization includes but is not limited to the angularly dependent relative reflected spectral composition (Tomić, et al., 2017). Additionally, for further developments of colorant mixing and halftoning methods, the modelling of optical dot gain needs to be refined to describe the optical properties of the RGB inks more accurately (Meruga, 2014).

In our work, we measure angularly dependent reflected spectra of inks prepared with available pigments with nominal red, green, blue, and white colors. As one of possible demonstrations of the obtained results, we present calculated relative spectra for diffuse illumination. Additionally, we compare color saturation of inks prepared with low and high concentration of pigments and simulate spectra of their mixtures in case of optical mixing.

2. Materials and methods

Samples for our study were prepared by mixing (Merck Spectraval™) pigments with acrylic binder. For our experiment we prepared inks with 10 wt% (low) and 30 wt% (high) concentration of pigments. The inks were applied on glass slides by screen printing. Samples with 1 layer and 4 layers were prepared for both concentrations. Figure 1 demonstrates how the inks are perceived visually under diffuse daylight at various angles of observation. For demonstration purposes, inks prepared with a high concentration of pigments were applied on black paper and wrapped around a cylinder.

Figure 1: Photographs of inks prepared with nominal Red (left), Green (middle) and Blue (right) pigments, inks were applied on black paper and wrapped around a cylinder under diffuse daylight illumination

Visible color variations were characterized by recording spectral reflectance distributions for a set of combinations of angles of incidence and observation (reflected angles). If absolute values of reflected radiance

are known, the color of the samples can be represented in one of the CIE color spaces. We observe wavelength dependent reflectance of the samples to obtain the spectral BRDF in arbitrary units (scaled to the unknown value of solid angle):

$$R(\omega_i, \omega_o, \lambda) = \frac{dL'_o(\omega_i, \omega_o, \lambda)}{L'_i(\omega_i, \lambda) \cdot \cos\theta_i d\omega_i}, \quad [1]$$

where measured quantities L'_o and L'_i are spectrometer responses proportional to the reflected and illuminated radiances, ω_i (ω_o) are the directions of incidence (observation) and θ_i is the angle between the direction of incidence and sample normal. Measurements were made in the plane of incidence.

Our experimental set up for the spectral BRDF measurements consists of a goniometer, a xenon lamp with focusing lens and a spectrometer. Figure 2 depicts the experiment and the notation of angles of incidence, observation, and specular direction of reflectance. We set illumination angles to 15°, 20°, 30°, 40°, 50°, 60°, and 70°. Due to the limitations of the experimental measurement set up, only certain combinations of incidence and reflectance angles were feasible to measure. Reflected spectra were collected for a discrete set of observation directions with dense (1–2° step) scanning around specular reflectance direction and 5–10° step with further inclination from the direction of the specular reflection, for each angle of incidence. During the analysis of the measured results, we calculated relative reflectance of the inks by subtracting the background noise and dividing measured spectra of the samples by the measured spectral response of the light source. The measured relative spectra were scaled to the maximum value of 1. After collecting and analyzing spectral BRDF data, we simulate angular spectral reflectance distributions under diffuse illumination by calculating cosine weighted average of normalized measured reflected spectra for different observation angles, as:

$$R(\omega_o, \lambda) = \frac{\sum_{\omega_i} R(\omega_i, \omega_o, \lambda) \cdot \cos(\theta_i)}{\sum_{\omega_i} \cos(\theta_i)} \quad [2]$$

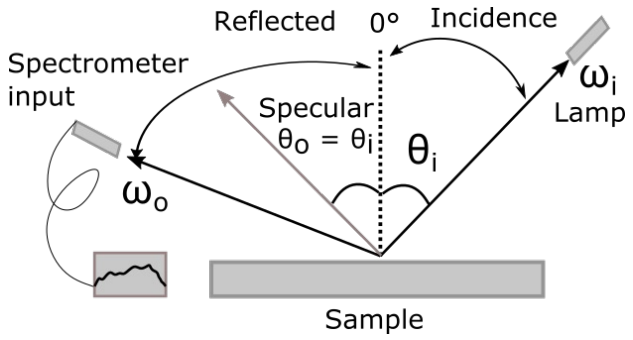

Figure 2: Experimental set up and angle notation for spectral BRDF measurements with demonstrated definition of specular reflectance direction

The perceived color saturation at different observation angles can be characterized by the relative ratio of corresponding spectral components (wavelengths in the interval) in the normalized spectrum. We defined a contrast function as follows:

$$C(\Delta\lambda) = \frac{\text{mean}(R_{\Delta\lambda})}{\text{mean}(R)}, \quad [3]$$

where mean(R) is the mean value of the intensities in the whole spectral range 380–780 nm, mean($R_{\Delta\lambda}$) is the mean value of the normalized intensities at wavelengths corresponding to the specific color. The wavelength bands Δλ were chosen as 620–750 nm for red, 526–606 nm for green, and 450–495 nm for blue.

3. Results and discussion

Figure 3 demonstrates reflectance spectra of samples prepared with high pigment concentration and 4 applied layers of inks. For demonstration purposes, spectra for the angle of incidence 40° and 70° under different observation angles are shown. For visualization purposes, all spectra in Figure 3 were rescaled with respect to the maximum value for all reflected directions, for each angle of incidence individually. Angles of observation were scaled with respect to the specular reflection direction (i.e. the reflectance at 40° for the incidence at 40° and 70° for the incidence at 70°). Varying balance between spectral components represents observed color change at different angles of observation. The presence of the blue spectral components in all inks is significant.

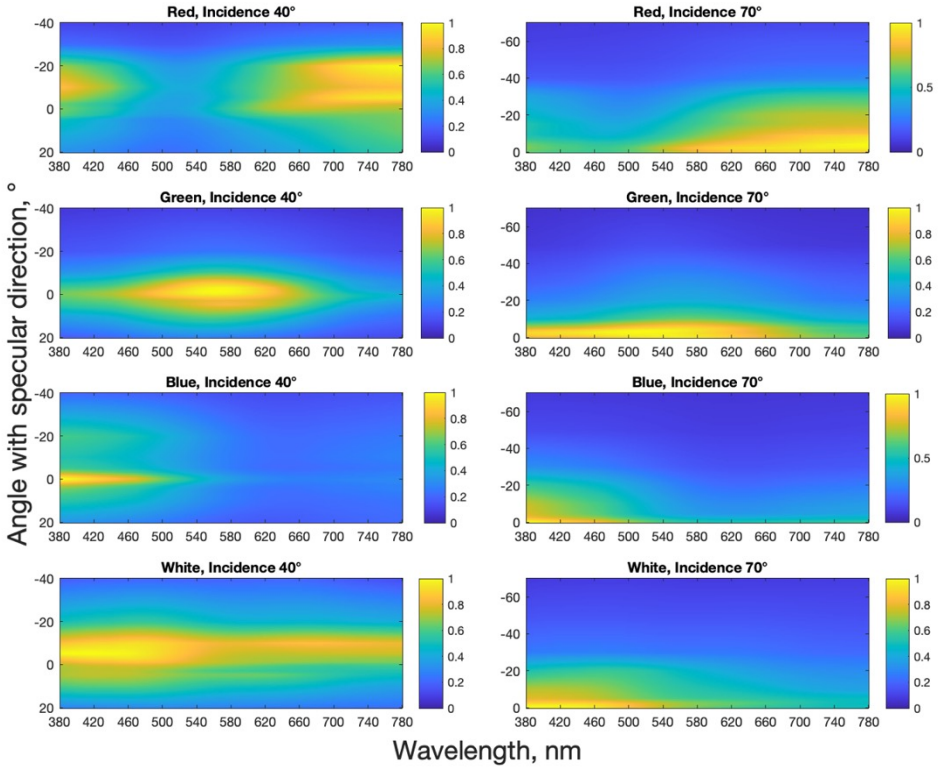

Figure 3: Scaled reflected spectra for angles of incidence (40° and 70°) for reflected angles with respect to the specular reflection direction; spectra of samples with 30% pigment concentration and 4 applied layers are demonstrated

After calculating spectral reflectance of the samples under diffuse illumination (Equation [2]), we estimated the contrast of spectral bands for the nominal colors of the pigments used (according to Equation [3]). In other words, relative contribution of the "red" wavelength band (620–750 nm) was estimated for the red ink, and for the green (526–606 nm) and blue (450–495 nm) inks, respectively. Figure 4 shows the relative color saturation with respect to different angles of observation for four types of samples: low and high concentration of pigments in the inks, as well as 1 and 4 layers of inks. These calculations were made with the spectra normalized individually for each measurement.

We simulated the result of optical mixing of two and three different ink combinations, respectively. For the two ink-mixtures, the results would correspond to the visual impression of two inks printed with 50 % area coverage, using dot-off-dot halftoning (i.e. no overlapping inks). For the three-ink mixture, the result corresponds to the visual impression of all three inks printed dot-off-dot, each with 33 % area coverage. The calculated contrasts are presented for the case of equal coverage of each pair of two colorants (Figures 4a–c), as well as an equal mixture of all three primary inks (Figure 4d). Figure 5 depicts the predicted contrast for the individual wavelength bands (corresponding to red, green, and blue) in the simulated

mixtures. On the contrary to the colorants with angular constant spectral characteristics, overlap of the contrast curves for individual inks and their mixtures is angularly dependent.

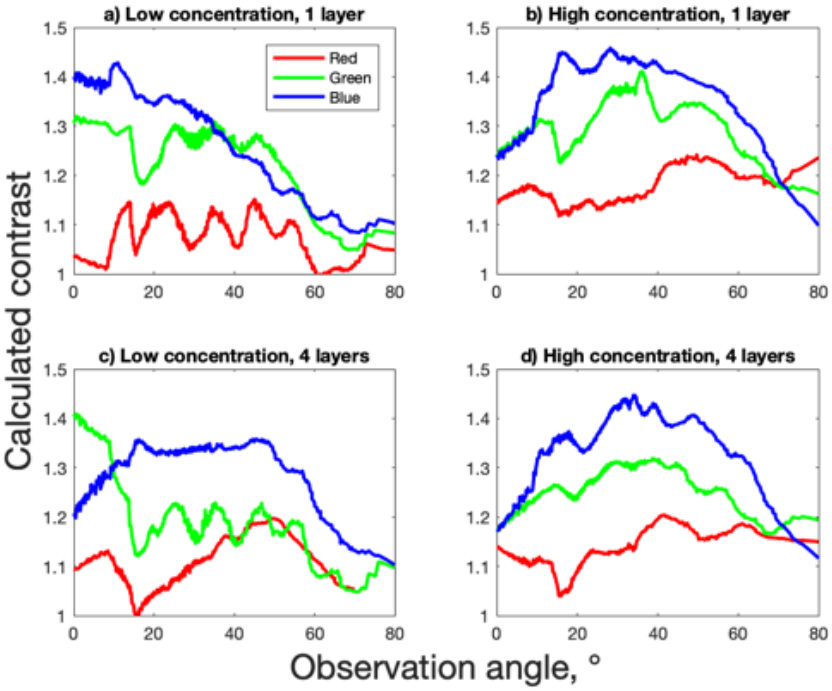

Figure 4: Calculated contrast of reflected spectra at various observation angles for red, green and blue inks after simulating diffuse illumination

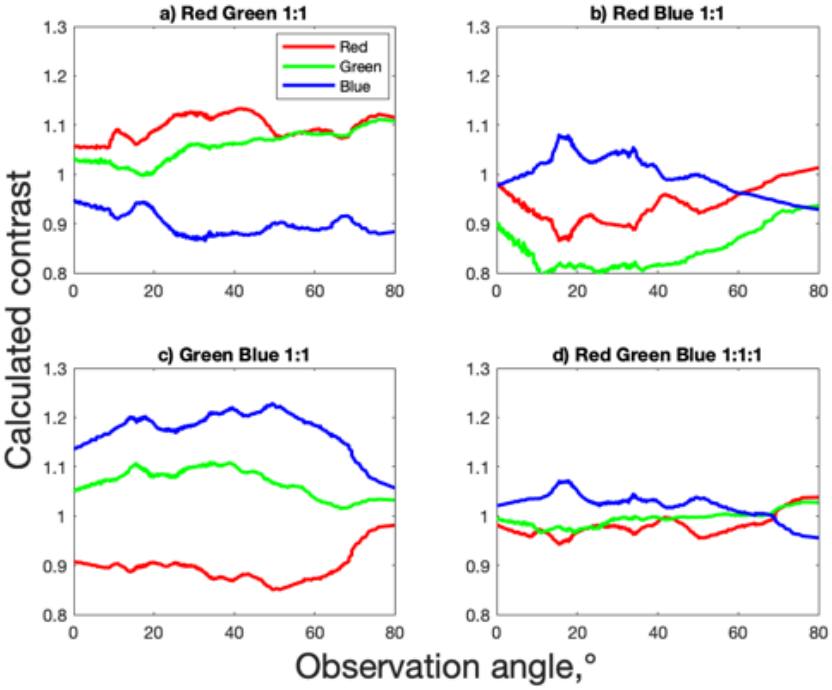

Figure 5: Calculated contrast for red, green and blue wavelength bands in the simulated mixtures of pairs of primaries and all three primary inks

The oscillations of the calculated contrast with respect to the observation angle observed at Figure 4, for the low concentration of pigments can be a result of fluctuations in measured spectra for different angles of observation and propagation of the limited measurement repeatability during the averaging over differ-

ent angles of illumination (illuminated area of the rough sample surface increases with increasing angle of illumination). On the other hand, the dip in the red wavelength band (observed around 20°) is consistent with both measured spectral distribution and can be observed in the photograph in Figure 1 (blueish color for the observation angle near specular) or spectral variations with the angle of observation (Figure 3).

4. Conclusions

Obtained measured and calculated results present relative spectral bidirectional reflectance distribution of RGBW inks prepared with selectively reflecting pigments. Demonstrated angular spectral variations and calculated contrasts of individual spectral components (red, green and blue) is angularly dependent and suggest higher presence of the blue in the inks and their potential mixtures. As expected, higher concentration of pigment in the prepared inks provides better contrast of the spectral components representing nominal colors of the pigments. Future color separation strategies for halftoning algorithms may be adjusted considering calculated contrast curves in the case of dot-off-dot halftoning.

5. Future work

Future full optical characterization of selectively reflecting inks will allow modeling of the appearance in case of ink overlapping and will include ellipsometry measurements for specular reflections.

Acknowledgements

Funded by the Horizon 2020 programme of the European Union. Grant # 814168 (ApPEARS).

References

Merck, 2021. *RGB printing*. [online] Available at: <https://www.merckgroup.com/en/expertise/effect-pigments/solutions/printing/rgb.html> [Accessed 14 April 2022].

Du, H., Liu, C., Sun, J. and Chen, Q., 2008. An investigation of angle-dependent optical properties of multi-layer structure pigments formed by metal-oxide-coated mica. *Powder Technology*, 185(3), pp. 291–296. https://doi.org/10.1016/j.powtec.2007.10.031.

Klein, S., Parraman, C. and Voges, L., 2019. How to print a rainbow. In: *NIP & Digital Fabrication Conference (NIP35).* San Francisco, CA, 29 September – 2 October 2019. IS&T, pp. 52–55.

Maisch, R., Stahlecker, O. and Kieser, M., 1996. Mica pigments in solvent free coatings systems. *Progress in Organic Coatings*, 27(1–4), pp. 145–152. https://doi.org/10.1016/0300-9440(95)00530-7.

Meruga, J.M., Baride, A., Cross, W., Kellar, J.J. and May, P.S., 2014. Red-green-blue printing using luminescence-upconversion inks. *Journal of Materials Chemistry C*, 2(12), pp. 2221–2227. https://doi.org/10.1039/C3TC32233E.

Parraman, C. and Klein, S., 2021. Printing the light*. Coloration Technol*ogy, 137(1), pp. 86–89. https://doi.org/10.1111/cote.12523.

Tomić, I., Dedijer, S., Martínez-Cañada, P., Novaković, D. and Hladnik, A., 2017. Camera characterization for colorimetric assessment of goniochromatic prints. *Journal of Imaging Science and Technology*, 61(2), pp. 20502-1–20502-15. https://doi.org/10.2352/J.ImagingSci.Technol.2017.61.2.020502.

Trujillo-Vazquez, A., Fuller, H., Klein, S. and Parraman, C., 2022. The Amber Project: a survey of methods and inks for the reproduction of the color of translucent objects. *Applied Sciences*, 12(2): 793. https://doi.org/10.3390/app12020793.

DOI 10.14622/Advances_48_2022_12

Free dispersing agent impact on latency issue for water-based inkjet inks

Amélie Brogly[1], Gilbert Gugler[2], Gioele Balestra[2], Raphaël Wenger[2], Aurore Denneulin[1] and Anne Blayo[1]

[1] Université Grenoble Alpes, LGP2, F-38000 Grenoble, France

[2] iPrint Center, HEIA-FR, HES-SO University of Applied Sciences and Arts Western Switzerland, 1700 Fribourg, Switzerland

E-mails: amelie.brogly@grenoble-inp.fr; anne.blayo@grenoble-inp.fr; aurore.denneulin@grenoble-inp.fr; gilbert.gugler@hefr.ch; gioele.balestra@hefr.ch; raphael.wenger@hefr.ch

Short abstract

The formulation of water-based pigment inkjet inks constitutes a major challenge: in addition to be perfectly stable colloidal suspensions, water-based pigment inks should strictly meet all the requirements imposed by the printhead specifications regarding flow properties, surface tension and density. The nature and the quantity of dispersing agent used to stabilize the pigment particles in suspension are crucial issues that can significantly impact the ejection phase. Inkjet inks must be stable over time and during jetting whatever the ejection duration and cycle imposed by the digital printing flow. Each nozzle can be activated according to different ejection cycles. All the nozzles are not jetting at the same time. Some idle nozzles do not jet for a certain duration which can lead to ejection disturbances when they are restarted after this period. The latency refers to this negative behaviour after periods of sitting idle in the printhead. So far, solutions for minimizing the impact of latency have been proposed by adjusting the formulation but no scientific research tried to understand precisely the causes behind this phenomenon. This paper tries to show the significant influence of the dispersing agent on the latency issue for the jetting of water-based and pigmented inks.

Keywords: water-based pigment inkjet inks, latency, dispersing agent, drop formation

1. Introduction and background

Inkjet printing is a non-impact printing method in which picoliter droplets of ink are jetted onto different substrates such as paper, textile or non-porous substrates. This method of printing allows an infinite choice of printed images. Drop on Demand (DoD) systems including a piezoelectric element are the most common in the industry for the moment. This jetting process saves ink, cleaning time and offers an excellent printing quality at high speeds. Typically, DoD systems with a piezoelectric element can jet at high frequencies (above 10kHz). The inks should meet strict requirements imposed by the printhead manufacturer in terms of physico-chemical and rheological properties such as viscosity, density and surface tension as explained by Hoath (2016).

The use of water-based and pigmented inks can induce different defect while printing such as latency of the nozzles. Latency appears when a nozzle cannot jet correctly after a certain time without jetting. This can be critical for graphical applications: unprinted zones may appear in the printed image. This phenomenon is often explained by the drying of components at the meniscus at rest, as described by Magdassi (2010). In fact, the use of water as the main solvent induces water evaporation at the meniscus and implies the rise of concentration of other components such as pigments as suggested by Thakkar and Sun (2003). This leads to an increase in viscosity and elasticity. However, this hypothesis has never been demonstrated. Another explanation is made by Jackson (2016) with the use of different counter-ions to neutralize the dispersing agent. The larger the hydration radius (or Stern layer) of those counter-ions is, the lower is the possibility of pigment particles to retract from the ink vehicle (Kabalnov and Wennerstrom, 2006) and would imply

latency. Jackson (2016) provided a solution to slow this possible drying by the addition of humectants such as glycerol or mixes of counter-ions including lithium. A higher number of patents exists on this subject as for example the work of Brust, et al. (2009).

Only the hypothesis of drying of the meniscus is raised. However, if only this drying is the reason of latency, why different inks with approximatively the same water content can show latency or not?

It is a big challenge to explain what really happens at the nozzle meniscus. In this paper, latency phenomenon for water-based and pigmented inkjet inks is highlighted through different ink formulations and printing tests. A focus is made on the role of the dispersing agent. Jackson (2016) made the hypothesis that the extra free dispersing agent contained in the initial pigment dispersion may be the cause of latency issues. Different formulations will be prepared with or without pigment and with or without dispersing agent in order to show its impact on jetting.

2. Materials and methods

2.1 Materials

Four cyan dispersions were used in the ink formulations. Those dispersions were prepared with polystyrene-acrylic dispersing agents with different molecular weights: 8 500 $g.mol^{-1}$; 11 500 $g.mol^{-1}$ and 16 500 $g.mol^{-1}$ and PB15:3 phtalocyanine blue pigment from an external supplier (dispersions respectively called D1, D2 and D3). The fourth one, Projet ADP 1000 Cyan, was provided by Fujifilm. A dye supplied by Clariant (Direct Blue 199, Duasyn Cyan FRL-SL liquid) was also used. Three different humectants including glycol(s) and diol(s) were bought from Sigma-Aldrich. A silicon surfactant was also added into the ink formulations. Deionized water was prepared in laboratories. The type of printhead used to perform the drop observations and printing tests is a non-recirculating piezoelectric printhead including more than 2 000 nozzles with a 10 µm orifice diameter and a temperature of use between 30 °C and 32 °C. In total, seven inks were implemented, and the details of their composition are presented in Table 1. No binder was added into those inks' formulations. The addition of a binder may hide the impact of the dispersing agent.

Table 1: Formulations of the pigment-based inkjet inks

Component (wt %)	Ink 1	Ink 2	Ink 3	Ink 4	Ink 5	Ink 6	Ink 7
Colourant type	D1	D2	D3	Projet ADP 1000	Projet ADP 1000	DB 199	DB 199
Colourant	3	3	3	3	3	1	1
Dispersing agent contained in the dispersion	3	3	3	?	0	0	0
Free dispersing agent at 16 500 $g{\cdot}mol^{-1}$	0	0	0	0	1	0	3
Humectant 1	24	24	24	24	24	24	24
Humectant 2	2	2	2	2	2	2	2
Humectant 3	3	3	3	3	3	3	3
Silicone surfactant	1	1	1	1	1	1	1
Deionized water	64	64	64	?	66	69	67

2.2 Methods

2.2.1 Preparation of the pigment dispersion

PB15:3 pigment (15 wt %) and a dispersing agent (15 wt %) are mixed with water (60 wt %) for one night. Then the mixture is poured into a grinder at 4 000 rpm for approximatively 6 hours. The desired mean particle size is less than 150 nm.

2.2.2 Preparation of the inkjet inks

Pigment and dye-based inks are prepared according the same procedure. Their formulations are listed in Table 1. Deionized water, humectants, silicone surfactant and free dispersing agent (if one is added) are mixed under stirring until homogenization. Then, the pigment dispersion or the dye is added. The mixture is stirred until homogenization. Finally, the ink is filtered through a WHATMAN 1 μm GF/B w/GMF filter thanks to a peristaltic pump. This step permits to avoid the presence of large particle aggregates, if necessary. The inks are directly used to do drop ejection observations and printing tests.

2.2.3 Measurement of physico-chemical properties of the inkjet inks

The particle size of the inks was measured by Dynamic Light Scattering at ambient temperature. pH measurement was made thanks to a pH-meter (Checker Portable pH Meter, Hanna Instrument) at ambient temperature. The rheological analysis was performed thanks to a TriPAV (Piezo Axial Vibrator) rheometer, provided by TriJet Limited. The measurements were made at 32 °C from 1 Hz to 10 000 Hz. In this case, measured values are valuable up to 5 000 Hz. The dynamic surface tension of the inks was measured with a bubble pressure tensiometer (BP100 from Krüss) between 10 ms and 10 000 ms at 32 °C. Static surface tension was then read at the equilibrium.

2.2.4 Drop formation observation

The observation of the drop formation is possible thanks to a JetXpert set up. The drop watcher is placed in a controlled atmosphere at 23 °C and a humidity rate between 40 % and 50 %. Drops of 4 pL targeted volume are jetted and their volume, speed and trajectory can be measured. A printing station includes a conveyor belt to allow to print on different substrates.

2.2.5 Printing test: evaluation of the latency

In order to evaluate the latency of the different inkjet inks, a printing test including a specific test form is performed on non-coated white paper with 80 gm^{-2}. The printhead is cleaned and a specific pattern (Figure 1) is printed one time at time 0. The printhead is then stopped and started again to print the same pattern 1 min after. The same process is repeated at several times: 3, 5, 10 and 30 min. The idea is to know if the ink can be printed without latency after a certain idle duration. To evaluate the latency, the index I_{latency} was defined (Equation [1]). In Figure 1, 16 lines are printed at first. The number of missing lines indicates the level of latency. If $I_{\text{latency}} = 0$, the ink can be jetted perfectly without delay, if $I_{\text{latency}} = 1$ none of the 16 lines is printed, the ink shows a latency issue.

$$I_{\text{latency}} = \frac{\text{number of missing lines}}{16} \qquad [1]$$

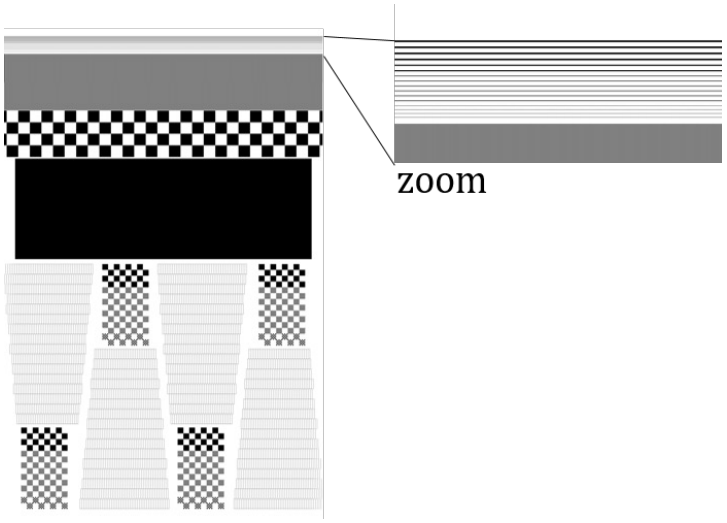

Figure 1: Printed pattern to evaluate the latency of an inkjet ink

The observations of the different printed patterns are made with the help of a Keyence numerical microscope using the objective ZS20.

3. Results and discussion

3.1 Physico-chemical properties of the inkjet inks

Different properties of the inks such as pH, viscosity, mean particle size (D_{50}), the static and dynamic surface tensions and density were characterized. Data are shown in Table 2. The dynamic surface tension was determined at 1 ms thanks to the model established by Hua and Rosen (1991). The *Z* number is also calculated in Table 2 with a nozzle diameter set at 10 µm. *Z* (Equation [2]) is used as ejectability criterion for inkjet.

$$Z = \frac{1}{Oh} = \frac{\sqrt{\rho\sigma L}}{\mu} \qquad [2]$$

With:

- ρ the density of the ink in kg·m^{-3};
- σ the static surface tension of the ink in N·m^{-1};
- μ the complex viscosity of the ink in Pa·s, at 100 Hz;
- L the diameter of the nozzle in µm.

Table 2: Physico-chemical properties of the water-based inkjet inks

Sample	Colourant type	pH	Viscosity (Pa·s)	D_{50} (nm)	Static surface tension (N·m^{-1})	Dynamic surface tension (N·m^{-1})	Density (kg·m^{-3})	*Z*
1	Home-made	7.76	9.68·10^{-3}	110	27.07·10^{-3}	48·10^{-3}	1 031	1.70
2	Home-made	8.30	5.40·10^{-3}	119	21.01·10^{-3}	-	1 060	2.76
3	Home-made	8.21	8.66·10^{-3}	134	25.61.10^{-3}	59·10^{-3}	1 025	1.87
4	Commercial	-	3.22·10^{-3}	118	26.35·10^{-3}	47·10^{-3}	1 013	-
5	Commercial	-	3.98·10^{-3}	-	23.63·10^{-3}	-	1 041	-
6	Dye	8.05	2.46·10^{-3}	-	23.19·10^{-3}	-	1 019	6.25
7	Dye	7.91	4.15·10^{-3}	-	24.02·10^{-3}	-	1 028	3.77

All the inks *Z* numbers seen in Table 2 are in the range establish by Reis and Derby (2000): $1 < Z < 10$. Which means that, according to them, all the listed inks are printable. Viscosities were measured at 100 Hz at 32 °C. The viscosity of samples 1 and 3 are above 6 mPa·s. This is certainly due to instabilities between components of the ink. In fact, the targeted viscosity is around 5 mPa·s at 32 °C. Some dynamic surface tension curves were not "S-shaped", this is why the Hua and Rosen model did not fit those measurements. In fact, S-shaped dynamic surface tension curve is needed to apply this model.

3.2 Drop watching results

Drop watching is performed for 5 out the 7 inks formulated. There are two main differences between pigment-based inks (1, 2 and 3) and dye-based inks (6 and 7). Firstly, the length of the tail when the drop comes out the nozzle seems longer for dye-based inks. Secondly, only ink 7 presents satellite drops (Figure 2). This ink is made with the addition of extra free dispersing agent. This component may disturb the jetting of the ink.

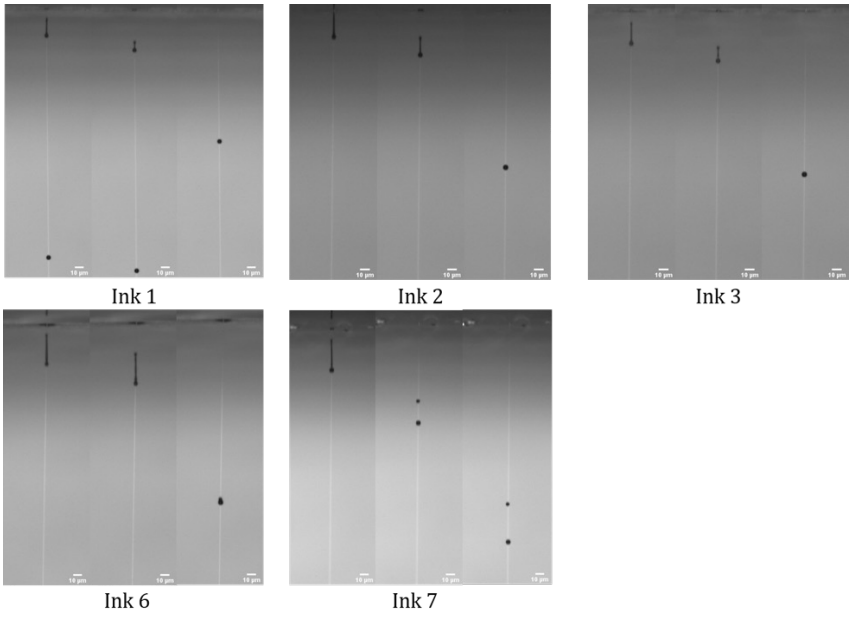

Figure 2: Images of drop watching for water-based inkjet inks

In Table 3 the different characteristics of the drops are listed. For the greyscale selected, a speed of 6 $m \cdot s^{-1}$ and a volume of 4 pL is expected. The trajectory from the nozzle plate is also measured in order to evaluate the position of the ink on the substrate. The drops for inks 1 to 3, made with dispersions, have characteristics close to the expected ones. Regarding the dye-based ink 6, volume and speed are higher than expected but there was no satellite during jetting. This is not the case for ink 7 which was impossible to analyse.

Table 3: Characteristics of drops ejected

Sample	Colourant type	Drop volume (pL)	Drop speed ($m \cdot s^{-1}$)	Drop trajectory (°)
1	Home-made	3.118	5.047	90.395
2	Home-made	4.534	5.956	90.723
3	Home-made	4.744	6.187	90.608
6	Dye	6.837	7.458	90.912
7	Dye	*unstable jetting*		

3.3 Latency test

The latency of the different inks is represented in Figure 3 thanks to the latency index described in 2.2.5.

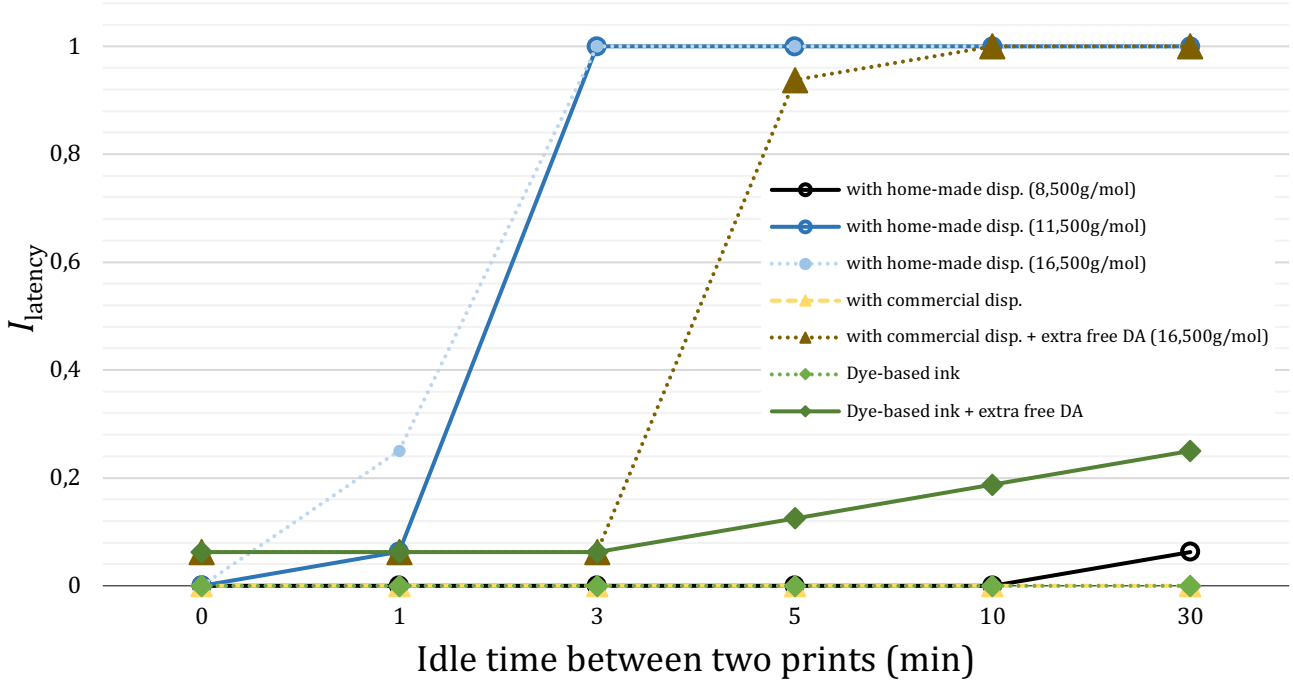

Figure 3: Latency for water-based inkjet inks for different times without printing, inks 1,2 and 3 are made with own made dispersions; inks 4 and 5 are made with a commercial dispersion and a free dispersing agent is added to ink 5; inks 6 and 7 are dye-based inks and a dispersing agent is added to ink 7

Inks 1, 2 and 3, respectively made with the dispersions D1, D2 and D3 show latency phenomenon. Latency issue increases faster with higher molecular weight of the dispersing agent. The Figure 4 shows that the first lines are not printed correctly for ink 3 after 1 min without printing. Ink 5 is the ink made with the Fujifilm dispersion. This dispersion has no excess of dispersing agent. By adding extra free dispersing agent, latency issue begins to appear distinctly after 5 min without printing. For the dye-based inks, the same observation can be made. Without free dispersing agent, the ink 6 does not show any latency. However, when a certain amount of free dispersing agent is added into the formulation, the pattern cannot be entirely printed since the time zero.

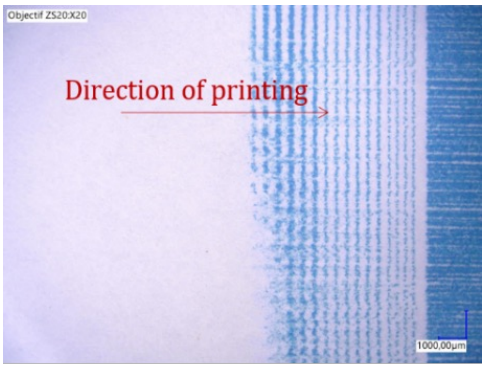

Figure 4: Photo of latency apparition for the ink made with the dispersion with molecular weight of 16 500 g·mol^{-1}, after 1 min without printing

4. Conclusions

This paper aimed to demonstrate how the extra free-dispersing agent may be involved in the latency phenomenon. All the inks prepared with home-made dispersion have this latency issue. It is assumed that all those dispersions include extra free-dispersing agent. Moreover, the latency index increases faster when the molecular weight of the dispersing agent is higher. The ink prepared with the commercial dispersion from Fujifilm does not have latency. This dispersion is prepared with the aim of removing the extra dispersing agent not anchored to the pigment particles after the grinding process. Dispersing agent with the highest molecular weight used in this study (16 500 $g \cdot mol^{-1}$) is added directly to this last ink. Surprisingly, latency appeared quite fast. To avoid any interactions between dispersing agent and pigments, dye-based inks were also tested: one without dispersing agent and another one with the addition of 3 wt% of dispersing agent with a molecular weight of 16 500 $g \cdot mol^{-1}$. The dye-based ink with no dispersing agent jetted perfectly even after 30min without printing. This was not the case of the one containing dispersing agent because the ink presented latency after few seconds without printing.

The conclusion of this study is that extra free-dispersing agent may have a strong impact on jetting and induce latency issue. Nevertheless, the hypothesis needs to be confirmed by the measurement of concentration changes at the meniscus.

References

Brust, T.B., Yacobucci, P.D., Wang, Y., Falkner, C.A. and Nguyen, T.T., Eastman Kodak Co. 2009. *Pigment-based inks with improved jetting latency*. U.S. Pat. 2009/0170986 A1.

Hoath, S.D. ed., 2016. *Fundamentals of inkjet printing*. Weinheim, Germany: Wiley-VCH.

Hua, X.Y. and Rosen, M.J., 1991. Dynamic surface tension of aqueous surfactant solutions: 3. some effects of molecular structure and environment. *Journal of Colloid and Interface Science*, 141(1), pp. 180–190. https://doi.org/10.1016/0021-9797(91)90313-W.

Jackson, C., 2016. Aspects of aqueous pigment ink formulation: latency, dynamic surface tension, and pigment volume concentration. *NIHON GAZO GAKKAISHI (Journal of the Imaging Society of Japan)*, 55(6), pp. 723–731. https://doi.org/10.11370/isj.55.723.

Kabalnov, A.S. and Wennerstrom, H., Hewlett-Packard Co. 2006. *Pigments modified with surface counter-ions*. PCT Pat. WO 2006/081299 A1.

Magdassi, S. ed., 2010. *The chemistry of inkjet inks*. Singapore: World Scientific.

Reis, N. and Derby, B., 2000. Ink jet deposition of ceramic suspensions: modeling and experiments of droplet formation. *MRS Online Proceeding Library*, 624, pp. 65–70. https://doi.org/10.1557/PROC-624-65.

Thakkar, S.R. and Sun, J.X., Lexmark International Inc. 2003. *Pigment ink formulation*. U.S. Pat. 6,585,818 B2.

DOI 10.14622/Advances_48_2022_22

Advanced print-media business models for circular economy domains

Anastasios E. Politis[1,2,3,8], *Georgios Gamprellis*[1,2,3,4,6], *Yannis Sofias*[1,2,7], *Christos Trochoutsos*[2,3,5,8] *and Marios Tsigonias*[1,2,3,6,8]

[1] University of West Attica (UNIWA), Athens, Greece
[2] GRAPHMEDLAB - The Hellenic Graphic-Media Research Lab
[3] HELGRAMED - Hellenic Union of Graphic Arts and Media Technology Engineers, Greece
[4] National Printing Office, Athens, Greece
[5] Pressious Arvanitidis SA, Greece
[6] GARDEN – Graphic Arts Research, Development and Engineering Institute, Athens, Greece
[7] Heidelberg Hellas, Athens Greece
[8] Hellenic Open University, Greece
E-mails: politismedia@gmail.com; gampgeo@gmail.com; yannis.sofias@heidelberg.com; chtrox@pressious.com; tsigonias@yahoo.gr

Short abstract

Circular Economy evolution that takes place, affects all aspects in societies and production, leading to a new view for activities in production, supply chain and consumption of goods. Within the Printing Industry and in particular the packaging printing, the current evolution includes not only the technological progress in production, but also the application of advanced concepts and systems in business models, management and workflows. The most prominent advances include the implementation of various elements ranging from continuous improvement and lean philosophies, to Industry 4.0 elements and the continuous improvement philosophy based in Lean manufacturing principles. One challenging issue for the Printing Industry, is the continuous transformation, based on the previously mentioned concepts. No matter the name used – digital transformation, digitization or digitalization, transformation is to be traced at all levels, namely at operation and business, management, technology and production. In addition to Industry 4.0, Lean philosophies and digital transformation, Circular Economy is considered as one more concept to be integrated one or the other way, in the already complex business environment of the Printing Industry. The present study investigates the current and future print-media landscape and under the scope of the integration of Circular Economy concepts in the business and operation of the printing companies. The question posed is whether and to which extend new or updated business models are required in order to facilitate this integration. As a result, the current status of the Printing Industry is to implement Circular Economy concepts, to the extent of the industry operational framework. One interesting aspect revealed, is the effort to implement these concepts, towards the "before" and the "after" in print production, which is not a part of the core printing business. Finally, the present study suggests an initial framework for the establishment of dynamic and flexible business models for the Printing Industry, where current and future innovations could be implemented.

Keywords: printing industry, circular economy, sustainability, business models, industry 4.0, digital transformation

1. Introduction

Circular Economy is nowadays the key word summarizing environmental protection, energy efficiency and sustainability. No matter the challenges created by recent global negative issues (such as COVID-19 and the pandemic, the war in Ukraine, energy and raw materials prices and shortages), Circular Economy is here to stay.

Circular Economy evolution that takes place, affects all aspects in societies and production, leading to a more generic view of all activities in production, supply chain and consumption of goods. Further, Circular Economy creates a disrupting environment, where, new ways of doing business might be required.

The Printing Industry and in particular the packaging printing sector, is advancing rapidly and continuously. The principal evolution topics for printing and finishing include not only the technological advances but also advanced systems in management and production, quality control and workflows. The most prominent developments are (among others), the application of various Industry 4.0 elements and the continuous improvement philosophy based in Lean manufacturing principles. Such developments require a "holistic", transformation in business organization, where digitization, digitalization and the so-called "digital transformation" constitute important parts. It is necessary that all the above-mentioned separate pieces of the "puzzle" need to be brought together under "one roof" in the transformation process of the Printing Industry. Therefore, the question posed is: Which can this "roof" be?

This paper aims in investigating the printing business and the required (continuous and dynamic) transformation challenged further by the Circular Economy evolution and its application in the industry and society. The objective of the study is to investigate the how, towards which direction and to what extend the already happening transformation, is further challenged by Circular Economy characteristics.

The study focuses on business models currently operating in the Printing Industry, their evolution and characteristics and the implications caused by the various elements mentioned previously (Industry 4.0, digitalization, and Lean philosophies). Business models are explored since they are considered as the "roof" under which, every implementation of new concepts can be feasible and facilitated. Circular Economy concepts are considered as an additional parameter that needs to be implemented effectively in the print business and operation. Therefore, business models are investigated in an effort to define the effective adaptation of Circular Economy concepts in the printing industrial setting and the appropriateness of the business model structure for this purpose.

1.1 Methodology

The approach for writing this paper is based on the investigation and the combination of elements considered important for the current and future print-media business and industry.

It is a step-by step investigation of the theoretical framework for printing business, following a logical sequence of arguments. Among these, one could define whether there is a future in print business, and if new technologies and other concepts are applied (such as Industry 4.0 and digital transformation).

Securing with evidence that this is the case, then the study investigates further the facilitators for doing business more effectively. These facilitators are the business models that are to be applied in the Printing Industry.

Following this step-by-step approach, additional or new concepts, such as Circular Economy are investigated. Finally, the theoretical background provided by this part of the study, is summarized as a suggestion of an initial business model structure (framework) where new concepts such as the one of Circular Economy can be affectively implemented in Printing Industry and its operation, business and production.

Based on this methodological analysis, the present study begins with the Circular Economy concept and its importance for the business of today and tomorrow, in Chapter two, which is addressing the origins and the characteristics of the Circular Economy. In Chapter 3, evidence is provided revealing that, no matter the evolution of the digital world, print is here to stay, in particular in books and packaging. The third chapter

deals with the disrupting developments which are challenging the printing and packaging industries and in particular COVID-19 and the lockdowns.

The fourth chapter refers to the latest trends regarding the technological developments and mainly those originating from the Industry 4.0 and digital transformation topics, whereas chapter five is addressing the latest trends in business models and their application in the Printing Industry.

Finally, in chapter six, the key findings are summarized, suggesting some structures of business models for the Printing Industry, and their evolution towards the implementation of Circular Economy concepts.

2. Circular economy

A lot of discussion takes place nowadays, on Circular Economy, therefore it is rather difficult to find out evidence which will be both credible and suitable for a specific industry domain, such as the one of printing and packaging production. In this part of the study effort will be given to clarify some principal issues concerning Circular Economy, towards its implementation in the Printing Industry.

2.1 Circular Economy context and definitions

At a document published by the European Parliament (2015) it is argued that unlike the traditional linear economic model based on a "take-make-consume-throw away" pattern, a Circular Economy is based on sharing, leasing, reuse, repair, refurbishment and recycling, in an (almost) closed loop, where products and the materials they contain are highly valued. In practice, it implies reducing waste to minimum. (Bourguignon, 2016)

Further, regarding the role of design science in Circular Economy, it is stated that Circular Economy is increasingly seen as a key approach to operationalising goals and supporting the transition to a sustainable society by enhancing competitiveness and economic growth. Creating a Circular Economy requires fundamental changes throughout the value chain, from innovation, product design and production processes all the way to end of life, new business models and consumption patterns. (Pigosso and McAloone, 2017)

Circular Economy is opposed to the so-called Linear Economy model. The main difference between Linear and Circular Economy is presented in Figures 1 and 2 as follows (Kholod, 2019).

Figure 1: Linear Economy (Kholod, 2019)

The Circular Economy, in contrast, has the opposite aim: to radically limit the extraction of raw materials and the production of waste. It does this by recovering and reusing as many of the products and materials as possible. The Circular Economy is a "make/remake – use/reuse" economy.

Figure 2: Circular Economy (Kholod, 2019)

Another way to describe Circular Economy is the term "Closed Loop Economy". Whether the term is Closed-loop economy, Circular Economy, Closed-loop supply chain, or Closed-loop system – it's all essentially describing the same thing. A Closed-loop economy is an economic model in which no waste is generated; everything is shared, repaired, reused**,** or recycled. What would traditionally be considered "waste" is instead turned into a valuable resource for the creation of something new.

As such, a Closed-loop economy is essentially the result of multiple companies operating on a closed-loop supply chain. This requires an intelligent reimagining of how products (and packaging) are designed, manufactured, sold, refurbished, and recycled. (Quincy Recycle, 2020). The elements of the Closed-loop economy are illustrated in Figure 3.

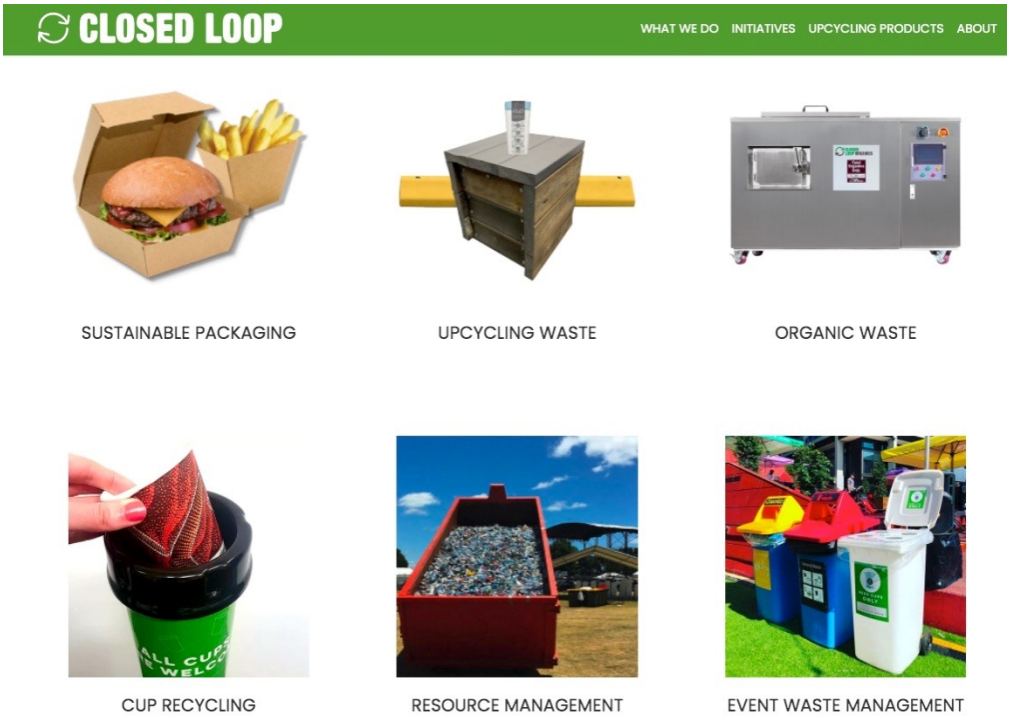

Figure 3: Elements of a Closed-loop economy (Closed loop, 2022)

Finally, in the study "On biodegradable Plastics" (Selke, 2015), it is mentioned that each possible waste management namely improper disposal (litter), landfill, incineration, composting, recycling and reuse is not in any way compatible with the use of biodegradable plastics. Packaging systems based on biodegradable plastics are not automatically more sustainable than those based on non-biodegradable plastics. This conclusion is supported strongly by the general agreement that the whole package-product system must also be considered sustainable. If this package system fails to provide adequate protection for the goods it contains it is not really sustainable at all, as in this case both package and product will be wasted. (Selke, 2015)

This argument is further enhanced if a clear distinction between Linear economy, Re-use economy and Circular Economy is made. As it is stated in a Fujifilm white paper, "the EU's Circular Economy Action Plan3 outlines a strategy to transform Europe's economy into a sustainably driven, fully Circular Economy by 2050. To achieve this goal, we must take action at all levels of society and set clear milestones. The first goal is ambitious but not unattainable: a 50 % reduction in the consumption of primary raw materials (mineral, fossil and metals) by 2030" (Fujifilm, 2022). In Figure 4, the distinction among Linear, Re-use and Circular Economy is illustrated.

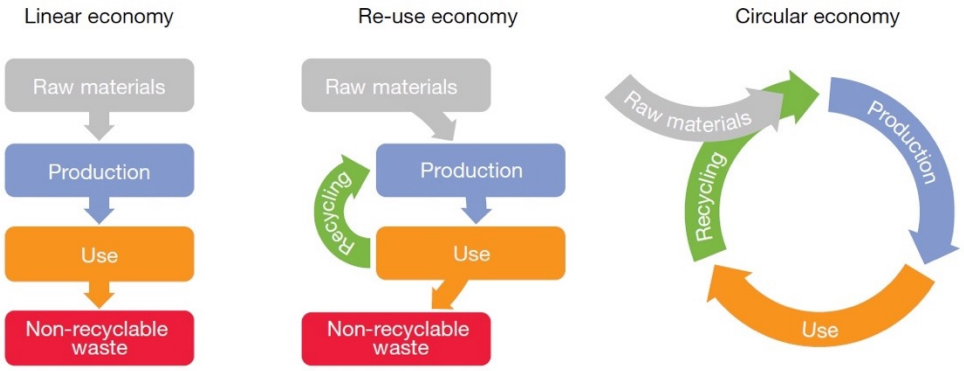

Figure 4: Linear economy, Re-use economy and Circular Economy (Fujifilm, 2022)

2.2 Sustainability and circular economy

According to Morales, et al. (2021), Circular Economy and sustainability are interrelated, without being exchangeable. While sustainability tries to reconcile the management of productive resources with their increasing consumption, Circular Economy aims to make the productive process more efficient, reducing, reusing and recycling the results of the productive process as much as possible.

A similar mindset is placed by Kuehn (2022). She defines sustainability as a principle of action according to which the conservation of resources is aimed at by means of natural regeneration to further satisfy needs. Comparing sustainability with Circular Economy she argues that "Circular Economy describes the process of optimal use of resources, optimal use of energy and, above all, the processing and reusability of used resources".

In addition, as it is pointed out by Morales, et al. (2021) sustainability is understood as the "dynamic equilibrium between the allocation of resources in the production process and consumers' behaviour patterns", whereas Circular Economy is understood as the "regenerative system that promotes the minimization of waste generation by closing and extending loops, and improving eco-efficiency technologies, while maintaining its value in the economy for as long as possible".

As Kuehn (2022) states further, "sustainability is becoming more important across all sectors, including the print industry. Niche producers are already successful with a sustainable business model, but this has not yet reached the masses. Even though products are increasingly adapting to sustainability, the incentive for companies is probably not yet great enough to incur additional costs. This will only change when ways are identified in Europe and globally and incentives are offered so that large companies voluntarily commit to finding intelligent and sustainable solutions".

2.3 Sustainability, and circular economy in the printing industry

What is applied for industry and society in general, concerns the printing and Packaging Industry. Effort is given by many, to specify the elements of Circular Economy and sustainability concepts for the Printing Industry. In this context, Sun Chemical categorizes three main product sustainability initiatives:

- The raw materials used and the manufacturing processes
- The function of Sun Chemical products and the environmental impact of this function and
- The end-of-life of Sun Chemical products and how they interact with recycling processes – to assist Sun Chemical customers in making products easier to recycle and promoting the development of circular economies. (Sun Chemical, 2020)

Intergraf (2022), defines four print product and site relevant parameters for Circular Economy. Based on Intergraf Recommendations on CO_2 emissions calculation in the Printing Industry, these are:

- Materials
- Transport
- Printing
- Distribution

The Intergraf Recommendations represent a neutral and credible approach as they cover the 3 scopes of the Greenhouse Gas Protocol. Scope 1 covers all direct emissions, scope 2 covers the indirect emissions related to energy consumption and scope 3 covers all other indirect emissions from the supply chain. Scope 3 is a key element for the carbon footprint calculation in the Printing Industry as over 70 % belong to it, with the production of substrate being the main element. The Intergraf Recommendations have received international recognition with their inclusion in the ISO 16759:2013 standard (International Organization for Standardization, 2013) on the quantification and communication for calculating the carbon footprint of print media products. In figure 5, the four product and site relevant parameters for Circular Economy are analysed. (Intergraf, 2022)

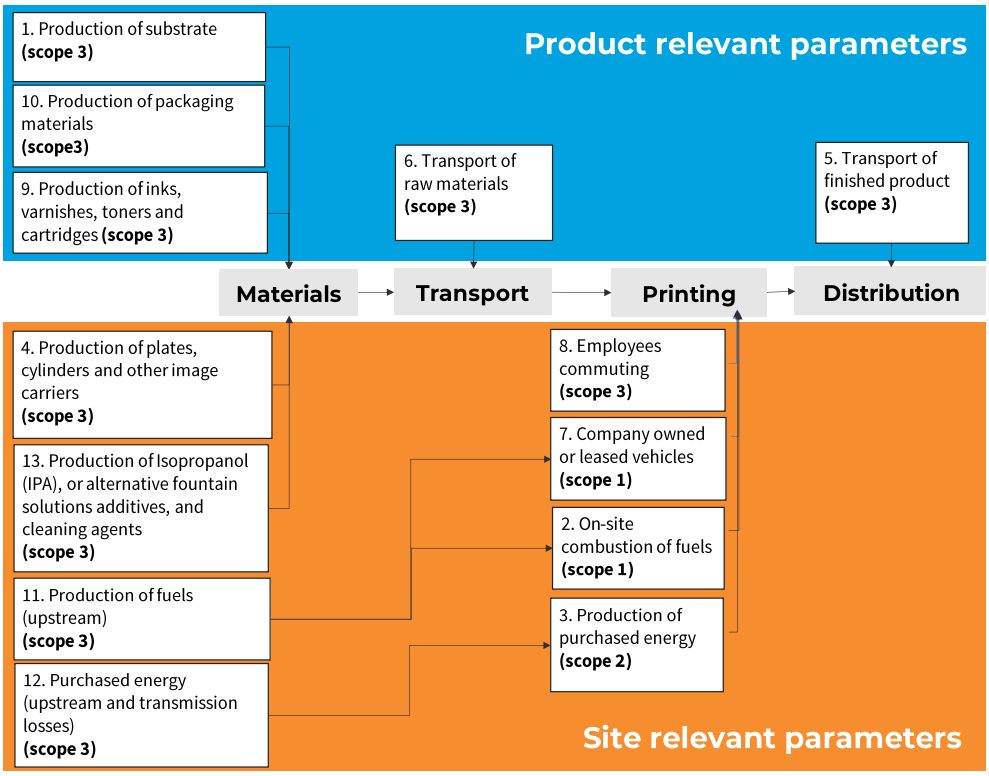

Figure 5: The four product and site relevant parameters for Circular Economy (Intergraf, 2022)

In regard with the involvement of the organizations of the printing industry, there are some initiatives that are operating. Among them, it is worthwhile to mention the Sustainable Green Printing Partnership (SGP) (Sgppartnership, 2022). According to the main message, the Sustainable Green Printing Partnership is a community of printing and packaging manufacturers, global brands suppliers, and supporting organizations working together to drive sustainability and meet the demands of today's customers. Their objective is to "make up the industry's leading supply chain certification authority and to set standards, advocate best practices and promote innovation toward a more accountable, sustainable supply chain". Moreover, as it is stated by SGP, "SGP certification is a multi-attribute endorsement created specifically for graphic communications facilities to be recognized by brands worldwide. To achieve certified SGP Facility status, companies must meet or exceed strict sustainability criteria in their manufacturing process, facility, product and social areas. Certification is offered to printers in the United States and Canada, as well as suppliers to the printing industry" (Sgppartnership, 2022).

A far more complete structure of Circular Economy elements in the Printing Industry, presented by Two Sides Australia (2022), emphasizes the complexity of Graphic Communications Supply Chain, which is "distinct from other sectorial or single issue corporate responsibility initiatives because it aims to promote responsible and sustainable business practices across every step of the AUS Graphic Communications Supply Chain, no matter how large or small the business". (Two Sides Australia, 2022). In Figure 6, this complexity is illustrated.

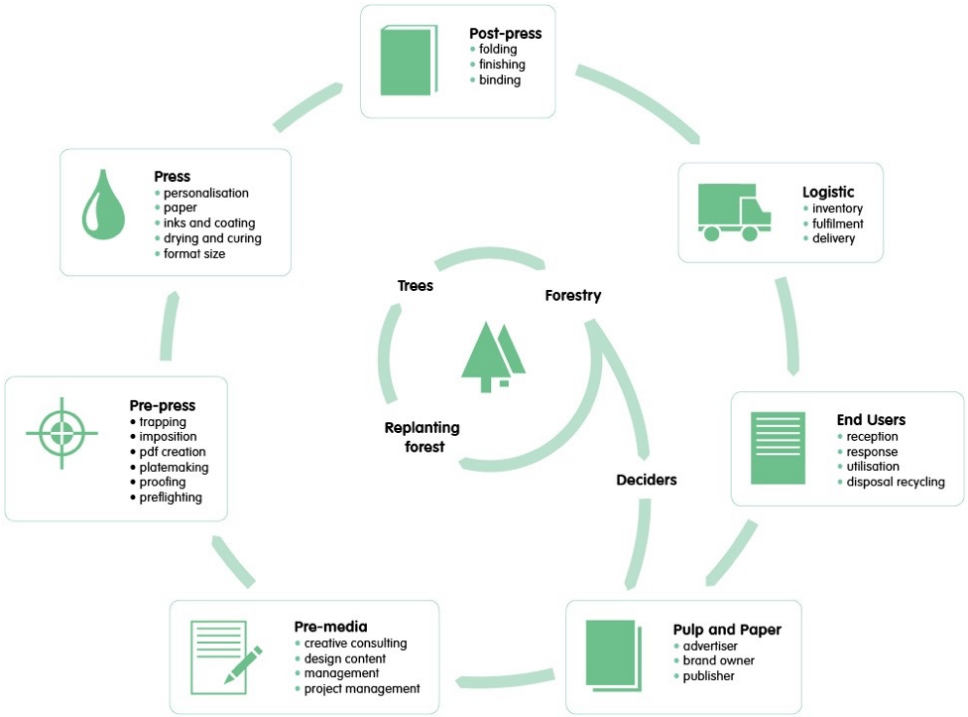

Figure 6: Graphic Communications Supply Chain (Two Sides Australia, 2022)

3. Disrupting developments and challenges

Prior to the investigation to the actual research fields, it is important to examine the current development of the Printing Industry and the issues occurred by the disruptions. Such issues are the print production for various segments (newspapers, books, packaging), the COVID-19 pandemic and the lockdowns, the energy and raw material prices as well as the war in Ukraine. The crisis plaguing the global economy from the late 2000s (2008–2009) to the present in conjunction with the COVID-19 pandemic has created an economic environment that cannot be described as easy for economic activity. (Gamprellis, et al., 2021)

3.1 The printing industry by (some) numbers

What can be considered as a fact is the expansion of digital communication and in particular the use of internet, social media, the enormous expanding of mobile devices, apps, and the web. However, the characteristics and in particular the nature of printed substrates combined with advanced technologies, such as finishing technologies reveal the strength of printing world and enhance the added value for a better communication. Haptic communication for example, is the principal driver for this enhancement (Politis, 2018). Also, despite the digital transformation, printed newspapers and magazines will continue to be a basic business segment for publishing companies in order to maintain a strong media brand across all channels. (Scherzer cited in Muller Martini, 2018)

Regarding print production, it is generally accepted that in recent years the Printing Industry has shrunk over the past few decades. The global print market is shrinking in volume but growing in value over the period 2014–2024. Output measured in billions of A4 prints (or equivalents) was 49 973 in 2014 and forecast to decline very slightly to 49 654 by 2024. In value terms, print output grows from a total of USD 767.4 billion in 2014 to USD 862.7 billion in 2024 – a Compound Annual Growth Rate (CAGR) of +1.18 % (Smithers, 2021). However, this contraction, although significant in some sectors of the Printing Industry, such as newspaper publishing, is non-existent in others, such as packaging, digital printing, screen printing, book production and label printing. (Gamprellis, et al., 2021)

Books are a quite interesting and influential segment in printing business. Some years ago, some have predicted that printed books would be dramatically limited and replaced by digital devices for reading. Hence, recent data provide evidence of a completely opposite picture, on reading books. According to several studies (PrintMonthly, BookMap Study – the Economist, Statista and Kurtz in Muller Martini in Panorama magazine 2019), printed book production is constantly increasing, reaching 122 USD billion sales in 2017. In the USA the number of hard and soft-cover books rose to a total of 695 million copies and sales of USD 10.3 billion in 2018 compared to 591 million copies in 2012. The same image appears for book sales in the UK and in Europe (Panorama, 2019).

In addition, according to Tsigonias (2018), and Adroit Market Research (2021) shows that the printed book production will be constantly increasing at least until 2028 (Figure 7)

Figure 7: Global Book Market (2018-2028) (Politis, 2022; Adroit Market Research, 2021)

This can be compared with the e-books in market growth of USD 6.93 billion from 2020 to 2025, at a 7 % CAGR (Maida, 2022; Technavio, 2022). As it is stated in Maida (2021) and Technavio (2022), the e-book

market is fragmented and the vendors are deploying growth strategies such as mergers and acquisitions and collaborating with schools and educational institutions to compete in the market. Finally, compared to printed books, e-books possess a percentage of 6–7 % in France and Germany (Panorama, 2019).

3.2 Printing industry and the COVID-19 pandemic

The global economic environment still remains in a challenging position due to the COVID-19 pandemic and it was perfectly reasonable and expected that the Printing Industry would be influenced like any other activity. (Gamprellis, et al., 2021: Whattheythink, 2020)

As Byström (2020) points out, during the COVID-19 pandemic crisis, there was a dramatic growth in online shopping that drove ten years of e-commerce growth in an eight-week period. Today, 38 % of UK consumers are now buying online at least once a week – in the US it is 26 %, Benelux 22 %, Australia 21 %, Germany 20 % and Sweden 20 %. (Byström, 2020)

Furthermore, during the COVID-19 pandemic, states and local municipalities are practicing extreme caution to avoid the spread of the corona virus. Healthcare products, such as syringes, vials, and cartridges, are required on a large scale amidst this pandemic to fulfill the increasing global demand (Wood, 2020a). There will be an increase in the demand for packaging printing solutions for food & beverage and pharmaceutical applications, during COVID-19 pandemic. (MarketsandMarkets, 2021)

These facts created a huge consumption growth that led to a growth of the packaging Printing Industry. The global packaging market size during the COVID-19 pandemic is projected to grow from USD 909.2 billion in 2019 to USD 1 012.6 billion by 2021 (Wood, 2020b).

According to Wassermann (2020), during the lockdown (due to COVID-19 pandemic), losses were still at −66.8 %. Since the stores reopened, however, the figures have turned significantly positive. During the initial restrictions, revenues then collapsed by more than half in some cases and were not yet able to recover fully in the post-lockdown phase (Wassermann, 2020).

Table 1: The estimated annual growth of the sectors of the Printing Industry (Gamprellis, et al., 2021)

Printing Industry Sectors	2020	2025	Estimated Annual Growth (%)
Press – Newspapers (millions)	157.57	149.15	−1.00
Publications – Books (billions)	117.07	122.44	+0.90
Commercial Prints (billions)	409.40	460.28	+2.24
Packaging Printing (billions)	352.10	433.40	+4.20
Labels Printing (billions)	42.70	51.89	+4.00
Security Printing (billions)	29.50	36.00	+4.10

As Gamprellis points out most of the Printing Industry segments will be expected to show an annual growth in the years coming (Table 1) despite the COVID 19 pandemic. The estimated annual growth for some of these Printing Industry segments will be higher than other, but in the end only the Press – Newspapers segment is expected to decrease (Figure 8) (Gamprellis, et al., 2021)

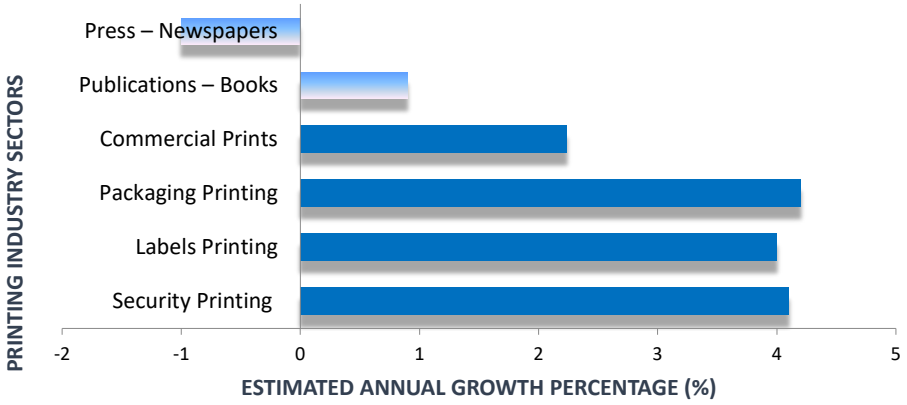

Figure 8: The estimated annual growth of the sectors of the Printing Industry 2020–2025 (Gamprellis, et al., 2021)

It seems that up to today, statements and predictions on the "decreasing" of print do not seem to be a reality. The printing field and the related sectors show a rather stable condition in terms of turnover and production, at least in Europe and North America, whereas in other continents, such as Asia, print is booming. (Politis, 2018)

3.3 Energy crisis and cost of materials

As mentioned in the previous section, the impact from the COVID-19 pandemic on the global economy is very significant. The Printing Industry, although initially was hit hard, could have overcome the difficulties caused by the COVID-19 pandemic if it had not presented a huge new economic challenge, which is nothing more than a rapid energy crisis which increases the cost of materials used by the Printing Industry.

From 2008 to 2021 the price of energy on the world market shows a slightly upward trend. This upward trend in energy price during these 14 years is also recorded by Eurostat (2021) (Figure 9).

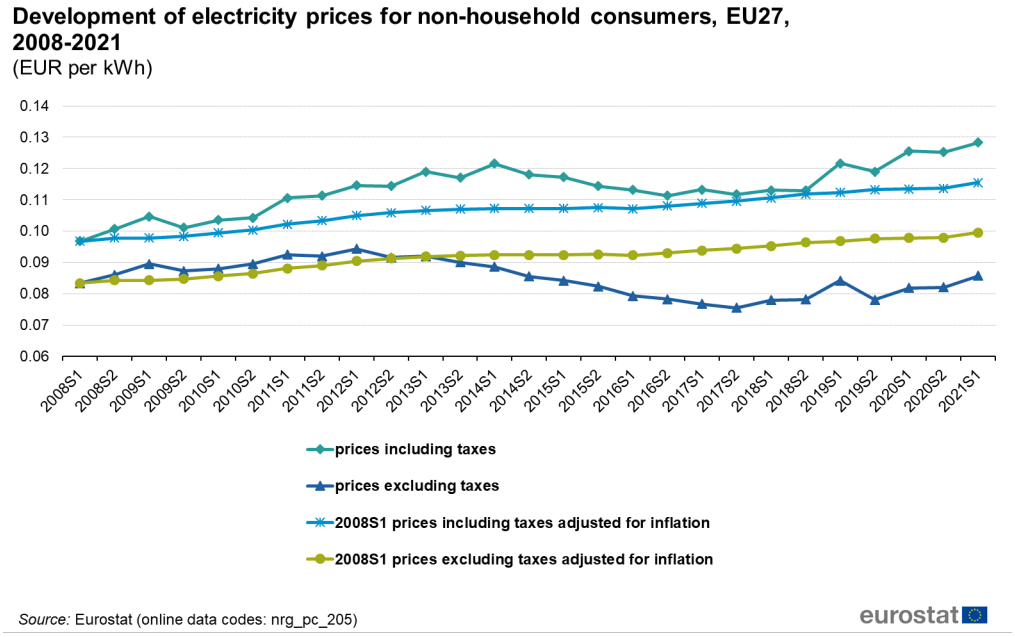

Figure 9: Development of electricity prices for non-household consumers, EU27, 2008–2021 (Eurostat, 2021)

Energy prices are expected to continue increasing, especially in 2022. The increase in energy price is accelerating significantly due to difficult geopolitical conditions, mainly in Europe (Russian invasion in Ukraine).

For delivery in March 2022, the gas price goes up 40 %, to about € 125 per megawatt-hour (MWh). The price for the supply of electricity is also rising some 40 %, to € 300 per MWh (taxes included) (The Brussels Times, 2022). Meanwhile, natural gas prices in the U.S. are approximately 60 % higher than a year ago. (McHugh, 2022). This increase of energy prices seems to be very high, as it is a reflection of very depressed energy prices in 2020 and 2021 due to the COVID-19 pandemic. If someone compares a longer historical period (2008–2021) average to the 2022 energy prices (March 2022) in order to soften the anomaly of the COVID-19 pandemic, he will find out that electricity prices for household consumers in the EU since the first half of 2008, (without taxes, i.e. the energy, supply and network), increased slightly faster than the overall inflation rate (HICP) until the second half of 2013 when it was € 133.8 per MWh. From 2014 to 2019, it remained relatively stable. In the second half of 2021, the highest ever price observed in the collection is recorded (Eurostat, 2020; 2021)

The European association representing the paper industry (CEPI) points out that the paper industry is an energy-intensive industry and, for that reason, current energy prices are a concern. The EU Commission's Green Deal and the carbon net-neutrality 2050 target, which is supported by CEPI, will lead to higher energy prices and carbon costs. The war in Ukraine and the related sanctions will add to this trend and further increase energy prices, which have reached very high levels already today (Packaging Europe, 2022).

Locally, energy prices and availability might be further impacted by the fact that some regions in the EU are highly dependent on the supply of Russian natural gas. To compensate for this, access to clean and affordable energy should be one of the EU's top priorities. The paper industry expects concrete and prompt support measures from the EU and national authorities (Packaging Europe, 2022)

Furthermore, Russia exports more or less the same amount to the EU every year (mostly kraftliner, newsprint and uncoated wood free). If we assume trade restrictions will result in the elimination of paper and board coming from Russia, the EU could suffer short-term paper shortages in some segments – particularly kraftliner. Russia usually sends some 180 000–200 000 tones of kraftliner to Europe each year. (Mata Lopez, 2022)

4. Evolution in the printing industry in technology and automation

4.1. Digital transformation, digitization and digitalization

Digital technologies play today a quite significant role in the media and graphic arts domain. However, digital transformation, digitalization or digitization have various interpretations and different meanings. The terms "digital transformation", "digitization" or "digitalization" are often confused and in many cases, they are used as they have had the same meaning. Hence there are differences in their conceptual context which need to be mentioned.

As Irving (2021), argues a lot of people have been talking about digital transformation (again). It sounds pretty cool and sophisticated. And it is. But what many of them were actually discussing was digitization (or digitisation, for those in the UK).

Irving provides an explanation regarding the term of digital transformation, stating that digital transformation is less about technology and more about people. The ability to adapt to an even more digital future depends on developing the next generation of skills, closing the gap between talent supply and demand, and future-proofing human capitals' potential. Therefore, digital transformation is a state of mind and a way of working and it is about learning and knowledge transfer. As such it is a holistic approach. (Irving, 2021)

In addition, as it is stated by Irving (2021), "Digital transformation is the process of using digital technologies to create new – or modify existing – business processes, culture, and customer experiences to meet changing business and market requirements. This reimagining of business in the digital age is digital transformation. As such, digital transformation begins and ends with how you think about, and engage with, customers. And as we move from paper to spreadsheets to smart applications for managing our business, we have the chance to reimagine how we do business – how we engage our customers – with digital technology on our side". (Irving, 2021)

Furthermore, according to Saleforce (2022), "digitization is most often mistaken for transformation. Digitization is the process of taking an existing process and digitizing, however this is not transformational. Therefore, digitization is an essential stepping stone to start digital transformation. In addition, there is a difference between digitization and digitalization; Digitization means to convert something into a digital format, and usually refers to encoding of data and documents whereas Digitalization means to convert business processes over to use digital technologies."

A more concrete distinction is presented by Thisisthelatest.news (2022). According to Thisisthelatest.news, digitization focuses on converting analogue information into digital formats. This is an important part of digital transformation. It is the process of transferring information from analogue to a digital format that can be accessed through computer systems and mobile devices. It can also be applied in business settings. In contrast, digitalization focuses more on processes and business models. It is the conversion of physical things to digital formats. Finally, digital transformation is more a holistic strategy in transforming the totality of doing business with digital tools and elements (such as Industry 4.0 settings and technologies), enabling organizations and businesses to adapt to changing market conditions and reimagine business processes and be more responsive to market changes and better serve their customers.

The interrelation of these three terms is presented in Figure 10.

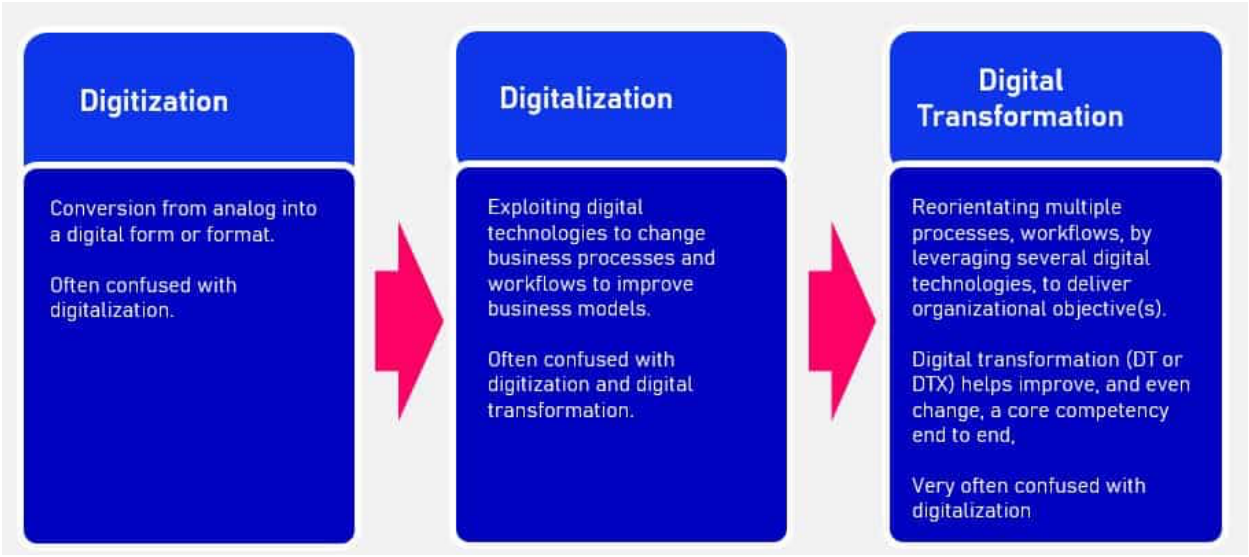

Figure 10: Digitization Vs Digitalization Vs Digital Transformation (Thisisthelatest.news, 2022)

Based on previous data, Digital transformation can be defined as a holistic development strategy. As it is argued by ionology.com (2022), "Digital transformation describes how an organization must evolve in the age of digital disruption; continually changing, innovating and reinventing rather than simply enhancing or supporting the traditional methods of its industry". Ionology organization, suggests five crucial steps for the development of a digital transformation strategy as presented in Figure 11.

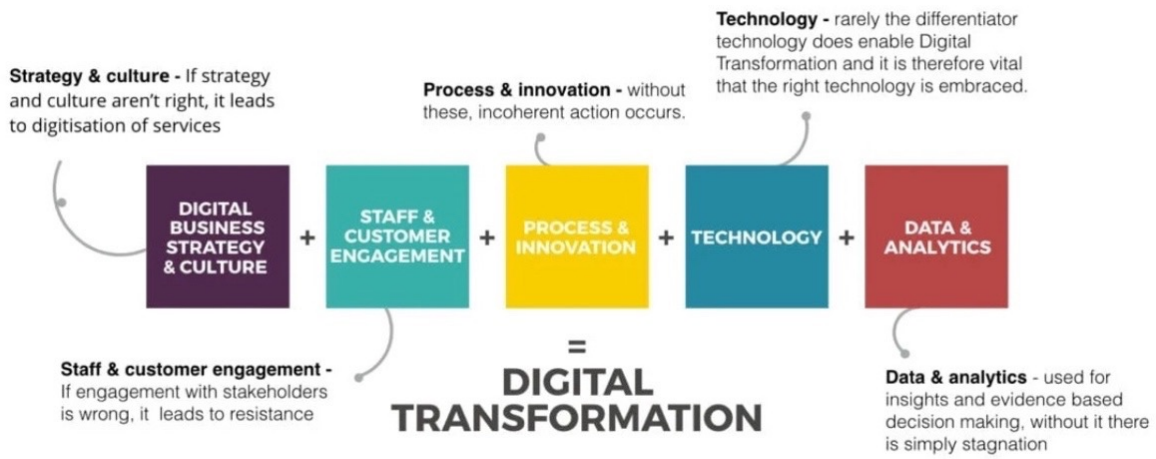

Figure 11: Five steps for a digital transformation strategy according to ionology.com (Irving, 2021)

The analogy of all three terms to the printing business and industry can be structured at the following example:

- Digitization: Inventory of printed jobs from paper to a digital file
- Digitalization: Automation of print management with the application of an MIS and use of digital data
- Digital Transformation: Integration of management, production workflows and business models in digitized platform(s) following a specified strategy.

Such classification provides evidence to clarify strategies for the printing business with the application of advanced technologies and Industry 4.0 is the most prominent step towards a new era for printing in the digital domain.

4.2 Industry 4.0 in the printing industry

Industry 4.0 is described as the 4th industrial revolution. Industrial revolution is an old term, used principally to classify the various steps of evolution in industrial operations and processes. However, the concept of Industry 4.0 appears as a global trend regarding the evolution in industrial manufacturing in the years to come. As such, it seems as a necessity for all industrial and manufacturing sectors to take under consideration the evolution that this concept brings. Hence, the term consists of several elements, which need to be carefully addressed and analyzed. This analysis should lead to the determination of potential benefits for manufacturing operations and processes in various sectors. (Drexler, 2016)

As it concerns the graphic/media, printing and packaging industries, the generic Industry 4.0 trend is applied with the combination of certain elements that fit better to the nature of processes and operations in the industry. As such, vendors, scientists and manufacturers are taking position within Industry 4.0 which is interpreted as Print 4.0, Finishing 4.0, Packaging 4.0 and Paper 4.0 (Politis, 2017).

A clear message from the investigation in the Printing Industry sector is that not all Industry 4.0 elements are applicable at all sectors. The investigation for the graphic arts and related industries (printing, packaging, paper and finishing) show that generic elements of Industry 4.0 are adapted into specific applications in a more concrete manner by the industry. (Politis, 2017, 2018)

According to Blogdrupa (2021a) quite recently, system integration and workflow automation were a top priority for printers and manufacturers. The truth is that in the Printing Industry there are a lot of repeatable tasks and processes, even though each job ticket is unique, and each printing job might be completely different than the previous or the next one. To keep the cost price as low as possible, many software

solutions offer automated workflows with the use of JDF files. The advantages of these include "increased production efficiency as well as profitability, raising the output, an increase of volume of shorter run work and avoiding bottlenecks". (Blogdrupa, 2021a)

Hence, Industry 4.0 is not only about automation of processes, use of robotics and big data. It's also about the use of cloud computing in all kinds of industries. And Printing Industry is not an exception of this rule. Newest technologies and developments include web2print, online file checking, color management and more print cloud solutions. These solutions aim of developing comprehensive AI based software solutions that aid printers in becoming more efficient, profitable and automated. Other focus on eliminating the burden on IT teams, reduce operating costs and accelerate digital transformation. (Blogdrupa, 2021b)

The current trend is the moving from many different aspects to as much as possible integrated systems, like ERP and MIS functionality with collaboration tools, web-to-print, cloud services and so on. The more the integrated systems, the less time is needed on the user's side. Following this, IoT devices and sensors make available for organizations to have access to greater insights from new analytics capabilities, which enables them to make faster, more knowledgeable business choices connected to their print ecosystem.

Cloud can also be used as a central service platform for remote maintenance and other remote services. This way, efficient and comprehensive support for machine operations, productivity improvements and troubleshooting can be provided and the whole print management of a printing company can move nowadays to cloud. (Blogdrupa, 2021b)

4.3 Robotics

A significant trend is the application of artificial intelligence and robotics into manual jobs. Although the news often puts humanoid robots and artificial intelligence (AI) in the spotlight, there's no shortage of exciting innovations in industrial robotics. From medicine and agriculture to production and printing, robotics plays a vital role in various industries, helping businesses become more efficient and cost effective.

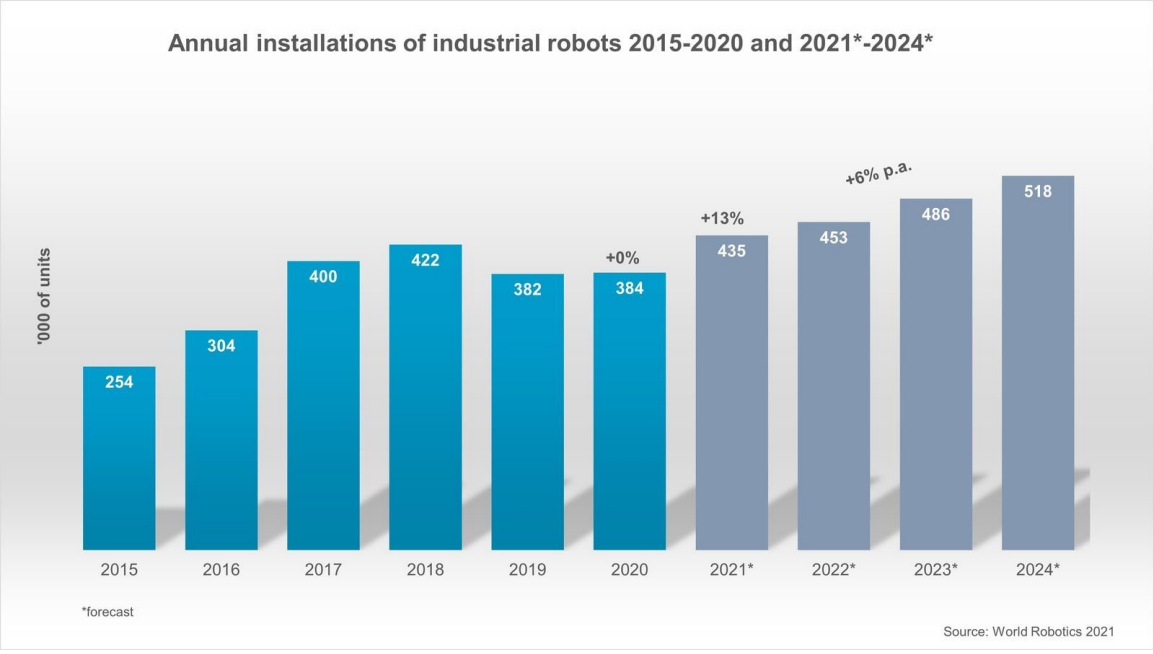

Figure 12: Annual installation of industrial robots (IFR, 2021)

Although robots have been used in industry since the 1960s in manufacturing, new technological capacities have made them versatile. New technologies like drones, collaborative robots with sensors and the incorporation of artificial intelligence and automation have opened the doors for robotics. As robotics and automation technology develop, we expect to see increased innovative uses applied to various industries (Figure 12). From medical robotics to automation in transport, we can expect to see the automation and robotics sector expand and grow. In fact, the World Robotics 2021 Industrial Robots report shows a record of 3 000 000 industrial robots now operate in factories around the world. (IFR, 2021)

In printing business, there is an increased use of robotic functions to improve precision and productivity and reduce time, while the use of automation and artificial intelligence help to coordinate and optimize production and operation (Heidelberg, 2022). Furthermore, according to Frey and Osborn (2013), print finishing and bindery operatives have a 95 % probability of a robot doing their job, ranked as 618 most likely out of 702 occupations. It is certainly feasible that manual loading and unloading operations could be replaced, and in many cases automatic palletization has replaced manual labor while robotic hoists are commonplace in loading logs of printed sections into gatherers for binding.

Relevant robots in the Printing Industry (Frey and Osborn, 2013)

- Collaborative robots
- Loading and unloading of machine
- Service and communication robots
- Transport and logistics
- Transport and service

The application of Industry 4.0 elements within a Circular Economy is a matter of high importance. An example on the relation of Circular Economy with industry 4.0 in an industrial setting, is presented in Figure 13.

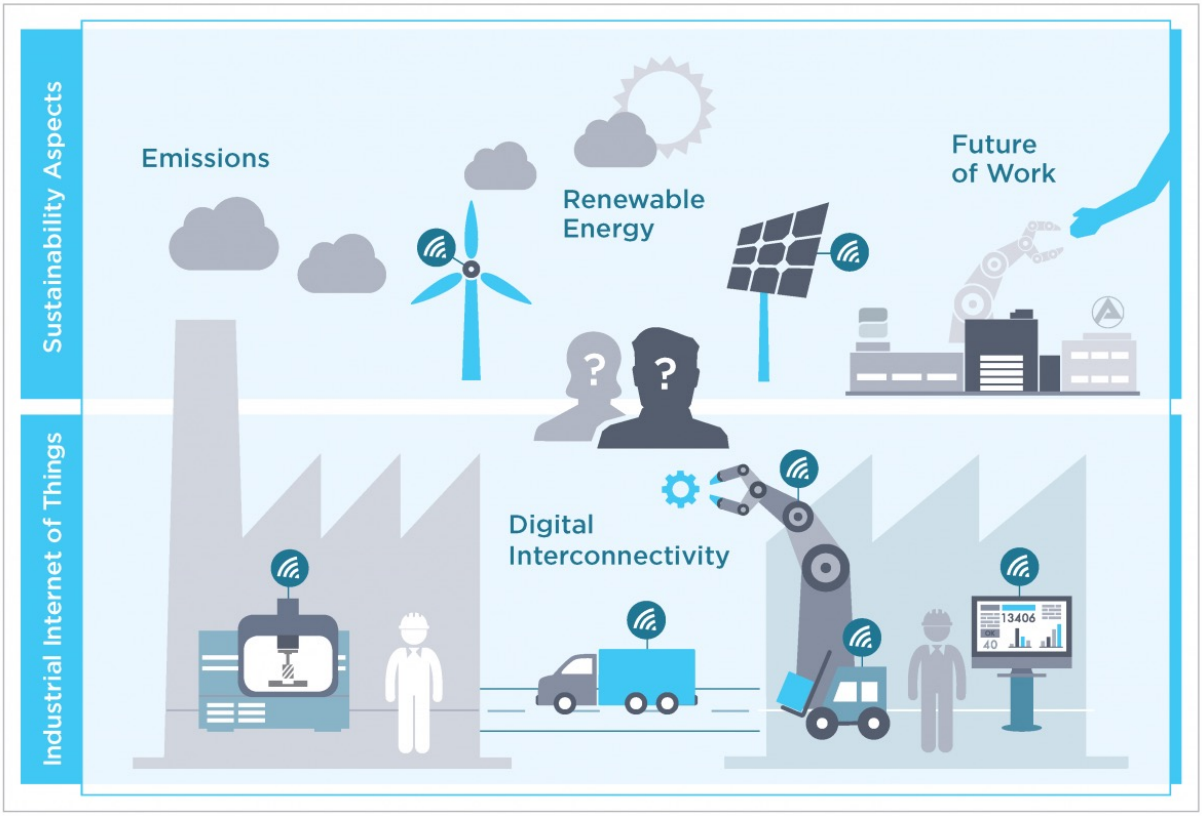

Figure 13: Convergence of Circular Economy with industry 4.0 in an industrial setting (UNIDO, 2017)

5. Print-media business models – advances and evolution

5.1 Business models – definitions and classifications

What is a business model? An answer is not easy to be given, since business models constitute purely conceptual frameworks. In other words, everyone can interpret the term by his/her own and unique way. Searching in the literature provided efforts by numerous scientists, in an attempt to define business models. For example, a look through Harvard Business Review - HBR's archives shows that "business thinkers use the concept of a "business model" in many different ways, potentially skewing the definition" (Ovans, 2015).

As it can be derived from Ovans (2015), the meaning of the term, can be described as an interplay of various concepts and opinions by many, such as "business strategy", "assumptions about what a company gets paid for" or "better business model into an existing market is the definition of a disruptive innovation".

Regarding the definition, it is argued that the business model concept is a particularly helpful unit of strategic analysis tailored to today's competitive business environment. It helps executives as well as entrepreneurs increase their capacity to manage continuous change and constantly adapt to rapidly changing business environments by injecting new ideas into their business model. Hence, there is often a lack of a more precise and shared understanding of what a business model is. Yet, such a common understanding is required if we want to have high quality discussions of one's business model and make important business model decisions.

A more concrete definition has been provided by Osterwalder (2005). According to Osterwalder "A business model is nothing other than a representation of how an organization makes (or intends to make) money". This definition is further implemented as follows: "A business model is a conceptual tool that contains a set of elements and their relationships and allows expressing the business logic of a specific firm. It is a description of the value a company offers to one or several segments of customers and of the architecture of the firm and its network of partners for creating, marketing, and delivering this value and relationship capital, to generate profitable and sustainable revenue streams". (Osterwalder, Pigneur and Tucci, 2005)

According to e=mc^3 (n.d.), "if managers want to overcome past barriers and experiment with alternative business models, they must construct maps of business models, to clarify the processes underlying them, which then allows them to become a source of experiments considering alternate combinations of the processes. One example of a mapping approach comes from Alex Osterwalder who, following his dissertation at Lausanne, has consulted, and spoken widely on business models and business model innovation (Osterwalder, 2005). His empirical focus utilizes a 9-point decomposition that characterizes a business model, namely the Business Model Canvas – BMC. The nine key elements, comprising the basis for any business model, can be viewed in Figure 14.

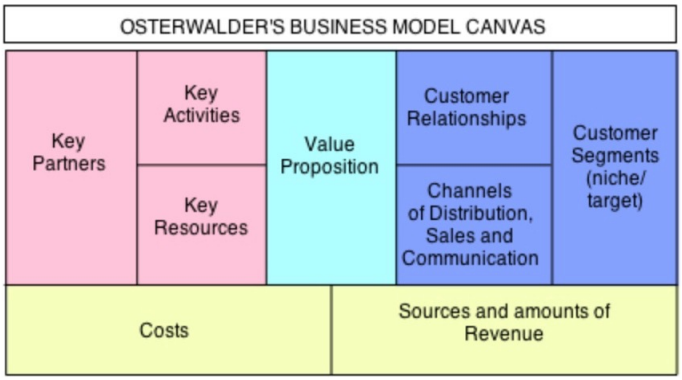

Figure 14: Osterwalders' Business Model Canvas – BMC (e=mc^3, n.d.)

The Business Model Canvas, can be considered as the basis for the conceptualization of the rather vague ter. According to e=mc^3 (n.d.), "although, like other models it is a simplified description and representation of a complex real world object, it describes the original in a way that we understand its essence without having to deal with all its characteristics and complexities. In the same line of thought we can define a business model as a simplified description of how a company does business and makes money without having to go into the complex details of all its strategy, processes, units, rules, hierarchies, workflows, and systems".

What is essential and highly innovative from the work of Osterwalder, as it regards the context of business models, is the introduction of "blocks" or "pillars" or "elements" in the form of a canvas, which immediately changes the process of conceptualizing a model of a business, or any other type of organization public or private, profit or non-profit. The canvas just happens to fit perfectly with the principles of the Lean Startup process, especially the emphasis it lays on experimentation, hypothesis testing, and systematic learning. (Fielt, 2014; e=mc^3, n.d.)

Regarding business models classification, Elearnmarkets (2022), suggest a different approach in defining and classifying business models; "Every business or companies makes a plan for generating profit. They create a model for identifying products and services to sell, the market they want to target and also take into account anticipated expenses. This is known as business models. Even if the business is already established or even if it is a new business, plan needs to be made. Businesses need to regularly update their plans and strategy as they need to take into accounts the challenges and trends for the future models. (Elearnmarkets, 2022)

Elearnmarkets classify four types of business models as follows:

- Business to Business Model − B2B
- Business to Consumer Model – B2C
- Subscription based Business Model
- On Demand Business Model (Elearnmarkets, 2022)

Regarding conceptualization of business models, Fielt (2014), suggests that "a business model describes the value logic of an organization in terms of how it creates and captures customer value and can be concisely represented by an interrelated set of elements that address the customer, value proposition, organizational architecture and economics dimensions". Field (2014) suggests further the following conceptualization of business models based on his analysis of business model definitions, elements, and archetypes and constructed by the following 5 main fields:

- explicitly including the customer value concept in the business model definition and focussing on value creation
- presenting the core dimensions that business model elements need to cover
- arguing for flexibility by adapting and extending business model elements to cater for different purposes and contexts (e.g. technology, innovation, strategy)
- stressing a more systematic approach to business model archetypes by using business model elements for their description, and
- suggesting to use business model archetype research for the empirical exploration and testing of business model elements and their relationships.

5.2 Business models in the printing industry

As it is stated by Bohan (2017), printing companies today have to navigate the requirements of shorter run lengths, faster turnaround times and increasing costs, all while facing relatively stable print prices and higher consumables prices. With all of these challenges, it's virtually impossible to maintain, yet alone increase, profitability without making changes to current business model or operations. According to Bohan,

the key to profitability and the solution to current challenges may be no further than workflow. An advanced workflow, should consider whether or not it drives positive impact on six key areas of printing business:

- Enhancing Customer Interaction
- Reducing Touchpoints
- Driving Productivity and Uptime
- Reducing Waste and Inventory
- Optimizing Consistency and Repeatability
- Providing Business Intelligence

Furthermore, as it is stated by Bondy, Peterson and Webb (2015), numerous management methods are deeply ingrained in the Printing Industry. Unfortunately, many no longer apply in the current market and environment. The development of "UnSquaring The Wheel", introduced the concept of a generic overview of the print management and workflow, designed to create a new and durable competitive advantage for graphic communications firms (printing companies). The approach, examines the entire business, not just one department at the expense of others. There is no one aspect of a company that can be changed and by itself create a sustainable advantage without this generic approach. (Bondy, Peterson and Webb, 2015)

Another concept under the name "Digital Supply Chain – New ideas for more efficient procurement of pharmaceutical packaging" has been introduced by Faller Packaging (2020). According to Faller Packaging white paper, "The digitized supply chain turns an order-driven process into a data-driven one that continuously monitors and optimizes itself. The basis for this is the fullest possible exchange of relevant information between pharmaceutical and packaging manufacturers. Analysis and segmentation of this item-related data makes it possible to select the best possible supply chain strategy for each product and to derive recommendations for action to improve specific process steps along the entire value creation chain".

More over, according to Salwin, et al. (2020), in the light of intensifying competition, growing customer needs and requirements, and bigger awareness of environmental impact, entrepreneurs are looking for new ways to improve and develop their operations. Therefore, seeking new business models seems extremely important as they may improve customer satisfaction and experience with the way products are offered to them and, at the same time, bring a number of benefits to entrepreneurs. Product-Service System (PSS) is a combination of products and services to meet specific customer needs and a concept that allows companies to build a competitive edge and supports sustainable development. The created PSS model provides the printing house with tools in the form of services that will eliminate production problems, improve production efficiency, minimize the adverse impact of printing production on the environment and affect the extension of the machine life cycle. (Salwin, et al., 2020)

In addition, Couckuyt (2019) in his analysis on the Printing Industry trends from the Graphics Canada 2019 trade show in Toronto suggested seven trends impacting the business models in the Printing Industry as the "impactful trends percolating into the business world in general and into the Printing Industry more specifically of those key trends that'll remake our (printing) business over the next five years". The trends are presented below:

- Accelerated Convergence of Technology and Business Verticals
- Increasing Consolidation Levels
- Increased Automation
- Shorter Run Lengths and Faster Turnaround Times
- Shift of Skill Set Requirements
- Increased Level of Machine Learning and Artificial Intelligence (AI)
- Management Sophistication

Couckuyt argues further that "in the last decades, the print industry has gone through accelerated technological changes that have fundamentally changed the conventional business model. The digitization of production processes has shifted the pendulum from Graphic Arts to Graphic Science and it is now very common for the printing model to be expanded by adding upstream and downstream services. Upstream, printers are adding web-to-print, design, and data management services. Downstream, printers are adding kitting, fulfillment, and distribution services. Couckuyt concludes his analysis by stating that "The print industry has grown into a complex, sophisticated business. Successfully managing such a diverse and sophisticated business model requires highly skilled teams. Navigating the challenges created by rapid technology changes, increasing environmental demands and a shift in human resources requirements will continue to put pressure on the management skills within the industry". (Couckuyt, 2019)

Finally, Roos (2016), claims that printing industries all over the world have to find new successful strategies and business models. The reason for the necessary changes is based on the ongoing shift from analog to digital production technologies and media products, bringing about new business opportunities on the supply side in combination with changes in the media use on the demand side. The task for printers is to understand which technologies, processes and markets fit best to implement successful business.

Roos (2016) suggests the following direction for consideration as it regards business models in the Printing Industry:

- New successful business models are individual, not limited to new technologies.
- There is an increasing field of printing technology applications outside media.
- IT – Innovations are the strategic key for most of the new business models.
- Profit is often related to the control of larger parts of the value chain.
- The work force in the printing industries needs new IT – skills for designing processes, skills for global operations and management skills – such as Lean Printing.

6. Discussion and conclusions: from the theoretical to the conceptual framework for implementing circular economy in printing industry business models

Trying to transform various theoretical and mostly generic frameworks into specific conceptual structures in a particular industrial setting such as the Printing Industry is a rather challenging task. Such study as the one in the present paper is by default a difficult task.

In the paper effort has been given in order to investigate the various concepts that affect printing business and the way that their application influences the business strategies and creates new requirements for business models.

Therefore, a step-by step procedure has been selected for presenting data and evidence on the topic of the characteristics of business models by the application of Circular Economy concepts. Given the limitations of space and time, the present study has been based on a step-by-step procedure. This methodological procedure revealed that printing business is alive and it is evolving not only in traditional fields such as book and packaging despite the digital environment in communication, but it is also expanding into new segments such as industrial and functional printing.

Research conducted, provided evidence that the Printing Industry is already rapidly transforming, with the implementation of various elements ranging from continuous improvement and lean philosophies, to industry 4.0 and the so-called digital transformation at all levels, namely at operation and business, management, technology and production. The current roadmap of the industry is to implement new / advanced business models.

Furthermore, the study concluded that indeed Circular Economy is nowadays the key word summarizing environmental protection, energy efficiency and sustainability. No matter the challenges created by recent global negative issues, Circular Economy is here to stay. The study revealed further that the effective implementation of innovative concepts such as those of Circular Economy in the printing and Packaging Industry, can reach a certain degree of implementation that concerns the print production itself. Cooperation with suppliers (the "before") and end-customers (the "after"), is a prerequisite for an effective implementation of a Circular Economy structure in printing business and production.

Further, the study provided evidence that such business strategies, should be based on the further and dynamic evolution of business models, suitable to accept and enhance the production under the Circular Economy setting. The study revealed that the current evolution of other concepts such as continuous improvement, Industry 4.0 and digitalization / digital transformation, should be considered as parts of a holistic transformation of the printing business and operation. Circular Economy should be considered as an additional parameter in the already complex business environment of the printing, finishing and packaging production industries.

One of the difficulties / obstacles is that, by its nature, Circular Economy needs to be applied from the beginning to the end of a product life-cycle. As a result, it is much more difficult to be implemented in an advanced business model in the Printing Industry in its full dimension. Quite obviously, the reason is that print production is an intermediate part in the life-cycle of a printed matter. And it is true that it was much easier to manage, adapt and implement recycling and energy efficiency policies in the printing and finishing processes.

What Couckuyt (2019) stated in his analysis with his "Upstream and Downstream" structures, can be the way towards Circular Economy integration in the Printing Industry and the transformation of its business models. Circular Economy integration demands efforts from the industry, towards the "before" and the "after" in addition to the core print production.

In other words, companies need to consider materials used in production such as printing substrates, inks and glues and the printed matter after its production in the printing, finishing and packaging production steps, in a totally new mindset, within the Circular Economy structure. Cooperation with suppliers (the "before") and end-customers (the "after"), is a prerequisite for an effective implementation of a Circular Economy structure in printing business. Here ideas should be derived by Two Sides Australia (2022) and the diagram, illustrated in Figure 6.

This mindset provides a roadmap from the theoretical to the conceptual framework for business models on the improvement of business operations. One critical aspect is the possibility of incorporating any new concept that may arise in the future.

Moreover, it is obvious that innovative trends will continue to influence the industry. Such trends can be summarized as follows:

- The Printing Industry is evolving further despite the evolution of the digital world.
- Digitization, digitalization and digital transformation are applied throughout the design, management and production settings of the industry.
- Digitalization is applied in many ways, and the key-issue nowadays is the efficient digital transformation, as a part of the holistic business transformation.
- New technologies and philosophies (such as Industry 4.0 and continuous improvement) are present in the holistic transformation of the printing business.
- Circular Economy and sustainability are definitely key-parameters in present and future evolution of the Printing Industry.

- Business models applied, require a constant restructuring in order to coop with new / additional concepts that need to be integrated in printing business.

As a result, the present study suggests that new/advanced, dynamic and flexible business models are certainly required for the printing, finishing and packaging industries. A first attempt to describe the parameters regarding the characteristics of an appropriate business model for the Printing Industry where future innovations and concepts could be implemented, is presented in Table 2.

Table 2: A suggested multilevel framework for an advanced business model in the Printing Industry

Characteristics of business models development for the Printing Industry in relation with the integration of new concepts such as Circular Economy	
Procedure	System / field to be explored, customized and applied
Operation, leadership, strategy,	Lean Manufacturing / Continuous Improvement
Technology, design, management, workflow, production	Digitalization / Digital Transformation pplication of Specific Industry 4.0 elements
Customer, Product, Supplier, Materials, Consumer, End-user	Life Cycle and Characteristics of Printed products
Circular Economy	Resources, Energy efficiency, Sustainability, Recycling, Waste management
People and the Human Capital Development	Enhancement of Knowledge with Education and Training, Improvement of Competences and Skills A timeless – ongoing procedure

Given the elements presented in Table 2, it is fully understood that there is a particularly high degree of complexity. This occurs because the various fields need to interact smoothly in order to achieve an efficient business operation at all levels and activities.

This framework is by far not complete. Intensive further research is required in an effort to bring all the pieces of the puzzle together – such as continuous improvement, industry 4.0, digital transformation and Circular Economy. Additional parameters need to be considered, such as the various segments of the industry – namely commercial or packaging printing, and paper, carton and flexible printing production. Different specific production segments in the printing companies require a high degree of customization at all fields mentioned in the framework. Last but not least, the it is of high consideration the people and the human capital that should be capable to work in such complex environments. it is suggested that further research should focus in transforming the concepts applied in the Printing Industry with specific elements of advanced business models.

As a final comment, this framework can be considered as a starting point only for printing companies that they want to transform their business and operation with new tools and integrate new concepts such as Circular Economy in their business models.

References

Adroit Market Research, 2021. *Books market size & share | industry growth report analysis, 2021–2028*. [online] Available at: <https://www.adroitmarketresearch.com/industry-reports/books-market> [Accessed April 2022].

Blogdrupa, 2021a. How far we've come! Workflow automation in 2021. *drupa blog,* [blog] 27 July. Available at: <https://blog.drupa.com/de/workflow-automation-2021-2> [Accessed 25 May 2021].

Blogdrupa, 2021b. Cloud-based print solutions by Kodak and Ricoh. *drupa blog*, [blog] 23 November. Available at: <https://blog.drupa.com/de/cloud-based-print-solutions-kodak-ricoh> [Accessed 25 May 2021].

Bourguignon, D., 2016. *Closing the loop: new circular economy package, Briefing January 2016*. Brussels, Belgium: European Parliamentary Research Service.

Bohan, M., 2017. How Prinect production manager will reshape your business. *heidlebergusa* [online] Available at: <https://newsheidelbergusa.com/author/bohanmar> [Accessed 30 May 2021].

Bondy, C., Peterson, W. and Webb, J., 2015. Breakthrough business model for the printing industry, "Unsquaring The Wheel" introduced by Webb, Bondy, Peterson. *WhatTheyThink,* [online] 20 August. Available at: <https://whattheythink.com/news/75047-breakthrough-business-model-printing-industry-unsquaring-wheel-introduced-webb-bondy-peterson/> [Accessed 25 June 2022].

Byström, M., 2020. COVID-19: From impact to action in the packaging industry. In: *COVID-19: From impact to action in the packaging industry*. [pdf] Gent, Belgium: ESKO. Available at: <https://www.esko.com/en/lp/ebooks/follow-up/covid-19-download> [Accessed July 2022].

Closed loop, 2022. *Pioneering the circular economy*. [online] Available at: <https://closedloop.com.au> [Accessed April 2022].

Couckuyt, A.G., 2019. *7 trends impacting the business models in the printing industry*. [Linkedin] 14 April. Available at: <https://www.linkedin.com/pulse/7-trends-impacting-business-models-printing-industry-alec-g-couckuyt> [Accessed 23 July 2022].

Drexler, S., 2016. The 5 Factors of Industry 4.0. *ARC Advisory Group*, [blog] 15 August. Available at: <https://www.arcweb.com/blog/5-factors-industry-40> [Accessed 23 April 2022].

e=mc^3, n.d. *Alex Osterwalder's business model canvas*. [online] Available at: <https://e-equalsmc3.com/alex-osterwalders-business-model-canvas/> [Accessed April 2022].

Elearnmarkets, 2022. Business models – example, types, importance & advantages. *Elearnmarkets,* [blog] 25 June. Available at: <https://www.elearnmarkets.com/blog/what-are-business-models/> [Accessed 25 July 2022].

European Parliament, 2015. Circular economy: definition, importance and benefits. *News European Parliament*, [online] 2 December. Available at: <https://www.europarl.europa.eu/news/en/headlines/economy/20151201STO05603/circular-economy-definition-importance-and-benefits> [Accessed April 2022].

Eurostat, 2020. Digital economy and society statistics – households and individuals. [online] *Eurostat*. Available at: <https://ec.europa.eu/eurostat/statistics-explained/index.php/Digital_economy_and_society_statistics_-_households_and_individuals> [Accessed 5 February 2021].

Eurostat, 2021. Electricity price statistics: electricity prices in purchasing power standard. [online] *Eurostat*. Available at: <https://ec.europa.eu/eurostat/statistics-explained/index.php?title=Electricity_price_statistics#Electricity_prices_for_non-household_consumers> [Accessed 16 April 2022].

Faller Packaging, 2020. *Digital supply chain: new ideas for more efficient procurement of pharmaceutical packaging*. [pdf] Available at: <https://www.faller-packaging.com/fileadmin/user_upload/user_upload/Dokumente/Whitepaper/2021-04-21_WP_Digital_Supply_Chain_EN_FINAL.pdf > [Accessed 25 May 2022].

Fielt, E. 2014. Conceptualising business models: definitions, frameworks and classifications, *Journal of Business Models*, 1(1), pp. 85–105. https://doi.org/10.5278/ojs.jbm.v1i1.706.

Frey, C.B. and Osborn, M.A., 2013. *The Future of employment: how susceptible are jobs to computerization?* Oxford, UK: Oxford Martin School. [pdf] Available at: <https://www.oxfordmartin.ox.ac.uk/downloads/academic/The_Future_of_Employment.pdf> [Accessed April 2022].

Fujifilm, 2022. *Digital print technology for a circular economy*. [online] Available at: <https://print-emea.fujifilm.com/resource/digital-print-for-a-circular-economy/> [Accessed 22 January 2022].

Gamprellis, G., Politis, A.E., Sofias, Y., Tsigonias, A., Vonitsanos, G., Tsigonias, M. and Macro, K.L., 2021. Challenges for the printing industry in the modern digital and meta-pandemic era. In: C. Ridgway, ed. *Advances in Printing and Media Technology: Proceedings of the 47th International Research Conference of iarigai.* Athens, Greece, 19–23 September 2021. Darmstadt: iarigai. https://doi.org/10.14622/Advances_47_2021.

Heidelberg, 2022. *Robotics & automation by Heidelberg*. [online] Available at: <https://www.heidelberg.com/global/en/other_business_areas/robotics_by_heidelberg/robotics_automation.jsp> [Accessed 27 April 2022].

IFR, 2021. IFR presents World Robotics 2021 reports: robots sales rise again. *International Federation of Robotics*, [online] Available at: <https://ifr.org/ifr-press-releases/news/robot-sales-rise-again> [Accessed 23 April 2022].

Intergraf, 2022. *Print's carbon footprint: assessing carbon footprint in the printing industry*. [online] Available at: <https://www.intergraf.eu/about-print/print-carbon-footprint> [Accessed 29 April 2022].

International Organization for Standardization, 2013. *ISO 16759:2013 Graphic technology – Quantification and communication for calculating the carbon footprint of print media products*. Geneva: ISO.

Ionology.com, 2022. *What is digital transformation?* [online] Available at: <https://www.ionology.com/digital-transformation> [Accessed 24 July 2022].

Irving, K., 2021. Digital transformation vs digitization: what's the difference? *+UP*, [blog] 26 August. Available at: <https://www.upthereeverywhere.com/blog/digital-transformation-vs-digitization-whats-the-difference> [Accessed 22 July 2022].

Kholod, D., 2019. 4 principles of the circular economy: do you know them all? *We share ventures,* [blog] 18 March. Available at: <https://medium.com/@we_share_ventures/4-principles-of-the-circular-economy-do-you-know-them-all-2c4619b83df6> [Accessed 21 April 2022].

Kuehn, L., 2022. *Intergraf young talent award 2022: sustainability in the print industry*. [online] Available at: <https://www.intergraf.eu/image/young-talent-award> [Accessed 25 July 2022].

Maida, J., 2022. E-book market: 6.04 % Y-O-Y growth rate in 2021 | market size, share, facts & factors. *CISION PR Newswire,* [online] 20 January. Available at: <https://www.prnewswire.com/news-releases/e-book-market-6-04-y-o-y-growth-rate-in-2021--market-size-share-facts--factors-301463965.html> [Accessed 27 May 2022].

MarketsandMarkets, 2021. *Packaging printing market*. [online] Available at: <https://www.marketsandmarkets.com/Market-Reports/packaging-printing-market-153207109.html?gclid=CjwKCAjw8ajcBRBSEiwAsSky_ecQnTHgr4mN972nMDuCrB1C2b4npfF9cDby3B1AvIbF4UwiwTxc_BoC_scQAvD_BwE> [Accessed 2 February 2021].

Mata Lopez, A., 2022. How Russia's invasion of Ukraine impacts the European pulp and paper industry. *Fastmarkets,* [blog] 7 March. Available at: <https://www.fastmarkets.com/insights/how-russias-invasion-of-ukraine-impacts-the-european-pulp-and-paper-industry> [Accessed 16 April 2022].

McHugh, D., 2022. What does Ukraine invasion mean for energy bills? *USA Today,* [online] 27 February. Available at: <https://eu.usatoday.com/story/money/2022/02/27/ukraine-invasion-russia-energy-bills/6964171001/> [Accessed 8 April 2022].

Morales, M.E., Batlles-delaFuente, A., Cortés-García, F.J. and Belmonte-Ureña, L.J., 2021. Theoretical research on circular economy and sustainability trade-offs and synergies. *Sustainability,* 13(21): 11636. https://doi.org/10.3390/su132111636>.

Muller Martini, 2018. Why is print still the anchor for strong media marketing? *Muller Martini,* [online] 11 December. Available at: <https://mullermartini.com/en/newsroom-en/mm-blog/market-trend/why-is-print-still-the-anchor-for-strong-media-marketing/> [Accessed 10 February 2021].

Osterwalder, A., 2005. What is a Business Model? *Strategyzer,* [blog], 5 November. Available at: <https://www.strategyzer.com/blog/what-is-a-business-model#:~:text=Written%20by%20Alexander%20Osterwalder%20on,or%20intends%20to%20make)%20money> [Accessed 25 July 2022].

Osterwalder, A., Pigneur, Y. and Tucci, C.L., 2005. Clarifying business models: origins, present and future of the concept. *Communications of the Association for Information Systems*, 15, pp. 1–25. https://doi.org/10.17705/1CAIS.01601.

Ovans, A., 2015. What is a business model? *Harvard Business Review, 23.* [online] Available at: <https://hbr.org/2015/01/what-is-a-business-model> [Accessed 24 July 2022].

Packaging Europe, 2022. How will the war in Ukraine affect the paper and pulp industry? *Packaging Europe,* [online] 4 March. Available at: <https://packagingeurope.com/comment/how-will-the-war-in-ukraine-affect-the-paper-and-pulp-industry/7947.article> [Accessed 15 April 2022].

Panorama, 2019. Momentum on the book market. *Panorama: Muller Martini Magazine*, Fall 2019, pp 6–7.

Pigosso, D. and McAloone, T., 2017. How can design science contribute to a circular economy? In: *Proceedings of the 21st International Conference on Engineering Design (ICED17).* Vancouver, Canada, 21–25 August 2017. Technical University of Denmark.

Politis, A., 2017. The graphic-media communication science – fields, trends and the contribution of research organizations. In: *Scientific conference Evolution Innovation in Graphic-media Science: Research, Industry Innovation and the Role of Education*. Athens, Greece, 22 March 2017. Athens, Greece: HELGRAMED.

Politis, A., 2018. Industry 4.0: what does it mean for the graphic arts industry? In: C. Ridgway, ed. *Advances in Printing and Media Technology: Proceedings of the 45th International Research Conference of iarigai.* Warsaw, Poland, October 2018. Darmstadt: iarigai.

Politis, A.E., 2022. The print-media science and technology in the modern era. Trends and evolution. *8th ICTVC Conference.* Thessaloniki, Greece, 5–9 July 2022.

Quincy Recycle, 2020. Closed loop economy: what does it mean and how does it work? *Quincy recycle,* [online] 2 December. Available at: <https://www.quincyrecycle.com/closed-loop-economy-what-does-it-mean-and-how-does-it-work/#:~:text=A%20closed%2Dloop%20economy%20is,the%20creation%20of%20something%20new> [Accessed 25 May 2022].

Roos, A., 2016. Business models and strategy finding for the printing industries. *International Circular of Graphic Education and Research*, 9, pp. 71–82.

Saleforce, 2022. *What is digital transformation?* [online] Available at: <https://www.salesforce.com/eu/products/platform/what-is-digital-transformation> [Accessed 1 May 2022].

Salwin, M., Santarek, K., Kraslawski, A. and Lipiak, J., 2021. Product-service system: a new opportunity for the printing industry. In: V. Tonkonogyi, V. Ivanov, J. Trojanowska, G. Oborskyi, A. Grabchenko, I. Pavlenko, M. Edl, I. Kuric and P. Dasic, eds. *Advanced manufacturing processes II*. Cham: Springer, pp. 83–95.

Selke, S., 2015. On biodegradable plastics. *Packaging World*, [online] 27 September. Available at: <https://www.packworld.com/issues/sustainability/blog/13368637/on-biodegradable-plastics2939> [Accessed 10 February 2022].

Sgppartnership, 2022. *Sustainable Green Printing Partnership*. [online] Available at: <https://sgppartnership.org/> [Accessed 28 July 2022].

Smithers, 2021. *How Smithers forecasts the global security printing market to reach $36 billion in 2024*. [online] Available at: <https://www.smithers.com/resources/2020/april/smithers-forecasts-global-security-printing-market> [Accessed 20 July 2021].

Sun Chemical, 2020. *Guide to sustainable packaging*. [online] Available at: <www.sunchemical.com> [Accessed 20 June 2020].

The Brussels Times, 2022. European electricity and gas prices rise 40 % due to Russian invasion of Ukraine. *The Brussels Times*, [online] 24 February. Available at: <https://www.brusselstimes.com/208157/european-electricity-and-gas-prices-rise-40-due-to-russian-invasion-of-ukraine> [Accessed 10 May 2022].

Thisisthelatest.news, 2022. *Digital transformation vs digitalization*. [online] Available at: <https://thisisthelatest.news/digital-transformation-vs-digitalization/> [Accessed 24 July 2022].

Two Sides Australia, 2022. *From tree to page*. [online] Available at: <https://twosides.org.au/from-tree-to-page/> [Accessed 29 April 2022].

UNIDO, 2017. New UNIDO report explores potential of Industry 4.0 to accelerate transition towards sustainable energy. *United Nations Industrial Development Organization*, [online] 30 August. Available at: <https://www.unido.org/news/new-unido-report-explores-potential-industry-40-accelerate-transition-towards-sustainable-energy> [Accessed April 2022].

Wassermann, K., 2020. The book market fights back. *Muller Martini,* [online] Available at: <https://mullermartini.com/en/newsroom-en/mm-blog/solutions-processes/the-book-market-fights-back/> [Accessed 16 January 2021].

Whattheythink, 2020. European Print Industry Snapshot: Spain. *WhatTheyThink* [online] 3 November. Available at: <https://whattheythink.com/data/103158-european-print-industry-snapshot-spain/> [Accessed 3 February 2021].

Wood, L., 2020a. Global commercial printing market report 2020–2025 assessed by type, application and region. *CISION PR Newswire*, [online] 25 June. Available at: <https://www.prnewswire.com/news-releases/global-commercial-printing-market-report-2020-2025-assessed-by-type-application-and-region-301083732.html> [Accessed 8 February 2021].

Wood, L., 2020b. $1 billion global packaging industry to 2021 – growing demand for FMCG and pharmaceutical packaging presents opportunities. *Globe Newswire* [online] 12 May. Available at: <https://www.globenewswire.com/news-release/2020/05/12/2031745/0/en/1-Billion-Global-Packaging-Industry-to-2021-Growing-Demand-for-FMCG-and-Pharmaceutical-Packaging-Presents-Opportunities.html> [Accessed 3 February 2021].

DOI 10.14622/Advances_48_2022_10

Effects of synchronousness in online learning experiences and the level of social presence in the pandemic 2021

Hocheol Yang[1], Jihyun Kim[2], Stephanie Kelly[3] and Ryan Goke[4]

[1] California Polytechnic State University

[2] University of Central Florida

[3] North Carolina A&T State University

[4] North Dakota State University

E-mails: Hyang25@calpoly.edu; jihyun.kim@ucf.edu; sekelly@ncat.edu; ryan.goke@ndsu.edu

Short abstract

This study examines the differences between synchronous and asynchronous online courses on students' social presence and learning experiences during the COVID 19 pandemic 2021. The final sample included 170 undergraduate students who took both synchronous and asynchronous online courses in the United States. The results of two sets of one-way repeated measures Multivariate Analysis of Variance (MANOVA) indicated synchronous online courses significantly lead to more positive learning experiences than asynchronous courses, at least when the emergency remote teaching was implemented in the COVID 19 pandemic 2021, supporting for the expanded Instructional Beliefs Model (IBM). Specifically, students reported significantly higher levels of *course satisfaction, affective learning, cognitive learning, and motivation to learn* for synchronous online courses than asynchronous online courses. Students also report experiencing significantly higher levels of social presence, such as *social richness, co-presence, passive interpersonal, actor within a medium, community within a medium* for synchronous online courses than asynchronous online courses.

Keywords: distance learning, quality of education, synchronousness, social presence, COVID 19

1. Introduction

Online learning became a central interest among educators and students when Emergency Remote Teaching (ERT) (Hodges, et al., 2020) took place due to the COVID-19 pandemic. Specifically, both synchronous and asynchronous modalities were offered as means to replace in-person instruction (Marinoni, van't Land and Jensen, 2020; Fabriz, Mendzheritskaya and Stehle, 2021). It has been considered that the differences in synchronousness are not the influential factors of online learning experiences and asynchronous courses are as effective as synchronous courses depending on the course implementations (Lew and Nordquist, 2016); educational institutions adopted these modalities to offer a more flexible schedule to students (Marinoni, van't Land and Jensen, 2020). But by the end of the pandemic, studies started to find that many students found themselves dissatisfied with their learning experiences, partly because faculty were not able to effectively use distance learning technology, leaving them with little motivation to try to overcome their professors' technological limits in ERT (Frey, 2021; Garland and Violanti, 2021), yet it is still unclear if it is just impacting students' satisfaction or their overall learning experiences.

Synchronous online learning experiences are those in which students meet at a designated, recurring time with their teacher and peers through an online platform (Amiti, 2020). Asynchronous learning environments are those in which students can access the materials at their convenience from anywhere at any time (Chen, Sun and Jin, 2019), providing them with a more flexible learning environment that can be tailored by the student to their needs. For both online structures, student learning can be enhanced through active

participation (Khotimah, 2020). Some experiments of synchronous vs. asynchronous lecturing have found no difference in students' academic achievement, satisfaction, sense of community (Olson and McCracken, 2015), or conceptual understanding (Dahlstrom-Hakki, Alstad and Banerjee, 2020) in one-time learning experiences. However, students require time to adjust to the online platform and step into their online learner identity (Yamagata-Lynch, 2014), which means these variables may change over the course of a semester.

Students who prefer asynchronous learning often prefer that modality because they have the option to engage with the course material when it works best for their schedule (Kelly and Westerman, 2016). In performance-based courses such as public speaking, asynchronous courses are often preferred because they give students the opportunity to record multiple takes and submit their best effort rather than having only one shot in real-time (Nurwahyuni, 2020). Another advantage of asynchronous online learning is that, when lectures are provided, students have the option to review them as many times as they wish, stop and take a break when needed, and even use closed caption features to ensure understanding (Foutz, 2021). Yet, those benefits of rewatching lectures and preparing multiple assignment submissions take time and motivation. As such, students who are successful in asynchronous online courses need more internal motivation than those in synchronous courses (Giesbers, et al., 2014) and must spend more time reasoning through the course material on their own (Guo, 2020). Therefore, the below hypotheses were established and tested.

H1a–d. Students will report increased online learning experiences for synchronous classes than asynchronous classes, such as (a) Course Satisfaction, (b) Affective Learning for Course Evaluation, (c) Perceived Cognitive Learning, and (d) Motivation To Learn.

Because of the interactive component of synchronous learning, students are likely to perceive more social presence with both their instructor and peers (Moallem, 2015; Rockinson-Szapkiw and Wendt, 2015; Yang, et al., 2022) and have a stronger attachment to the course material (Peterson, Beymer and Putnam, 2018; Rockinson-Szapkiw and Wendt, 2015). The Instructional Beliefs Model (IBM) (Weber, Martin and Myers, 2011) also predicts a strong association between social presence and students' learning experiences in cognitive, affective, and behavioral learning. Therefore, the following hypothesis is proposed:

H2. Students will report higher levels of social presence toward synchronous classes than asynchronous classes.

2. Methods

The final sample included 170 undergraduate students in the United States. Initially, 398 undergraduate students responded to the research survey. To ensure the eligibility of the study participants and to maximize the good quality of the data, a series of data cleaning processes were performed. First, because the purpose of the study is to compare one's learning experiences of asynchronous and synchronous online courses, responses from 210 individuals who reported taking only one type of online course (either asynchronous or synchronous) were removed. Second, 7 individuals who failed an attention check in the middle of the questionnaire were eliminated from the data. Lastly, 9 individuals reported that they have taken the survey more than once; thus, the duplicated responses from these individuals were removed from the data.

Data collection occurred via an online survey tool in April 2021, near the end of the Spring semester. After IRB's approval, one of the primary researchers contacted several instructors at multiple universities in the U.S. and asked them to share a research participation opportunity with their students. Then, a recruitment message was distributed to students through their instructors.

3. Results

This study applied two sets of one-way repeated measures Multivariate Analysis of Variance (MANOVA). The ordering effects were controlled by the study design's counter-ordering and did not find significant differences between ordering groups. Before the test, Shapiro-Wilk's *p-values* did not indicate a violation of normality. Mauchly's χ^2 significance test of sphericity was used to check this assumption but none of the results showed a statistically significant level of the *Chi-square* indicating the violation of the sphericity assumption ($p \leq .001$).

H1: The effects of synchronousness on online learning experiences

The first set of one-way repeated measure MANOVA tested the effects of synchronousness on online learning experiences. The test result indicated significant effects of effects of synchronousness on students' learning experiences [Wilks' Lambda = .884, F (5, 167) = 3.64, $p \leq .01$], explaining 11.6 % of total variances. The result supported H1, as well as all the sub hypotheses of it, as described in Table 1.

Table 1: Descriptive statistics of learning experiences

Laerning experience		Sync		A-Sync	
	N	*M*	*SD*	*M*	*SD*
CS (Course Satisfaction) ***	172	4.53	1.68	3.99	1.82
ALCE (Course Evaluation) **	172	5.65	1.40	5.33	1.53
ALEOC (Enroll in another Online Course) *	172	5.28	1.66	4.88	1.91
ALIE (Instructor Evaluation) ***	172	6.03	1.34	5.52	1.62
PCL (Perceived Cognitive Learning) *	172	5.08	1.12	4.77	1.28
MTL (Motivation To Learn) **	172	5.04	1.45	4.77	1.57
Note: $^{*}p \leq .05$, $^{**}p \leq .01$, $^{***}p \leq .001$					

Students reported that they experienced a significantly higher level of CS for synchronous online courses than asynchronous online courses [F (1, 171) = 16.03, $p \leq .001$], explaining 8.6 % of total variances. Students reported that they experienced a significantly higher level of ALCE for synchronous online courses than asynchronous online courses [F (1, 171) = 7.51, $p \leq .01$], explaining 4.2 % of total variances. Students reported that they experienced a significantly higher level of ALEOC for synchronous online courses than asynchronous online courses [F (1, 171) = 5.81, $p \leq .05$], explaining 3.3 % of total variances.

Students reported that they experienced a significantly higher level of ALIE for synchronous online courses than asynchronous online courses [F (1, 171) = 14.38, $p \leq .001$], explaining 7.8 % of total variances. Students reported that they experienced a significantly higher level of PCL for synchronous online courses than asynchronous online courses [F (1, 171) = 9.61, $p \leq .01$], explaining 5.3 % of total variances. Students reported that they experienced a significantly higher level of MTL for synchronous online courses than asynchronous online courses [F (1, 171) = 6.82, $p \leq .01$], explaining 3.8 % of total variances.

H2: The effects of synchronousness on social presence

The second set of one-way repeated measure MANOVA tested the effects of synchronousness on social presence. The test result indicated significant effects of the influence of synchronousness on the dimensions of social presence [Wilks' Lambda = .362, F (5, 167) = 58.90, $p \leq .001$], explaining 63.8 % of total variances. The result supported H2, as well as all the sub hypotheses of it, as described in Table 2.

Table 2: Descriptive statistics of social presence

Social presence		Sync		A-Sync	
	N	*M*	*SD*	*M*	*SD*
Social Richness *	172	5.76	1.50	5.01	1.84
Co-presence *	172	4.42	1.65	3.10	1.57
Passive interpersonal *	172	4.23	1.66	1.84	1.26
Actor within a medium *	172	3.94	1.66	2.16	1.77
Community within a medium *	172	4.72	1.67	3.34	1.78
Note: *$p \leq .001$					

Students reported that they felt a significantly higher level of social richness for synchronous online courses than for asynchronous online courses [F (1, 171) = 20.57, $p \leq .001$], explaining 10.7 % of total variances. Students reported that they felt a significantly higher level of co-presence for synchronous online courses than asynchronous online courses [F (1, 171) = 72.84, $p \leq .001$], explaining 29.9 % of total variances. Students reported that they felt a significantly higher level of passive interpersonal for synchronous online courses than for asynchronous online courses [F (1, 171) = 269.25, $p \leq .001$], explaining 61.2 % of total variances.

Students reported that they felt a significantly higher level of the actor within a medium for synchronous online courses than asynchronous online courses [F (1, 171) = 158.56, $p \leq .001$], explaining 48.1 % of total variances. Students reported that they felt a significantly higher level of community within a medium for synchronous online courses than asynchronous online courses [F (1, 171) = 91.19, $p \leq .001$], explaining 34.8 % of total variances.

4. Discussion

First, the study results showed significantly enhanced online learning experiences in synchronous classes than in asynchronous classes. Students reported that they experienced a significantly higher level of course satisfaction, affective learning, cognitive learning, and motivation to learn for synchronous online courses than asynchronous online courses. The results imply the current problem of implementing asynchronous online courses (Kunin, Julliard and Rodriguez, 2014) or its inherent limitations of it. At least during the pandemic's Emergency Remote Teaching (ERT) (Hodges, et al., 2020), the result of this study supports arguments that asynchronous online courses didn't do well for students learning experiences when it is not their preferred modality option (Rippé, et al., 2021). Most of the students may not be wanted to have asynchronous courses but they can also learn better with asynchronous courses during the pandemic. Based on the results, it looks like allowing the implementation of asynchronous courses widely in the pandemic was not a good decision. It also suggests more careful curriculum development and implementation guides are necessary for further use of asynchronous online courses to enhance students' online learning experiences in the post-pandemic and ERT era.

For example, in teaching a printing process management topic using a specific technique, the asynchronous only approach may not provide sufficient instruction to students. Because it is difficult to supply an optimized learning environment by standardizing students' distance learning technology and varying degrees of prior experience. As an extreme case, to incorporate such variability, the best way would be simply to let students read through the manufacturers' manual. Instead, having a short synchronous hands-on time with instructors synchronous or having group appointments that could alleviate impacted online learning experiences. Therefore, it is advised to avoid a single modality approach, especially the asynchronous one,

and consider more flexible modality options, such as mixed and hybrid modalities. Also, the results suggest that educational institutions need to spend more resources and time inventing and implementing classes with an asynchronous only modality.

Second, the study results showed a significantly enhanced level of social presence (Yang, et al., 2022) in synchronous classes than in asynchronous classes. Students also reported that they experienced a significantly higher level of social richness, co-presence, passive interpersonal, actor within a medium, community within a medium for synchronous online courses than asynchronous online courses. As predicted by IBM (Weber, Martin and Myers, 2011) and supported by the results of this study, when we design and implement online courses, it is important to consider the aspects that can enhance social presence. Although asynchronous online courses could offer higher flexibility in scheduling online courses that allow globalized and inclusive course offerings (Garland and Violanti, 2021), it is important to consider having some elements that can enhance social presence is recommended.

For example, having a small portion of synchronous meetings in asynchronous online courses would be helpful to enhance students' learning experiences. Not just because it can accommodate unpredictable differences among students, as discussed earlier, but because the results suggest the association between social presence and online learning experiences. Students may find it easier to be socially motivated and engaged in the course activities when they are synchronously working together. Also, when instructors are working on developing educationally effective implementation methods, having considerations regarding the effects of social factors would be helpful (Yang, et al., 2022). Therefore, further investigations regarding the mediating associations, as proposed in IBM (Weber, Martin and Myers, 2011), between the dimensions of social presence and online learning experiences are important to develop more educationally effective asynchronous online courses.

5. Limitations and future research directions

Although the present study revealed meaningful findings, there are a few limitations that should be considered when interpreting the results. First, the study collected data using a convenience sampling method, which may not fully reflect the nature of the population. Although the sample consisted of participants from multiple universities across the United States, it cannot guarantee the representativeness of the population. To further enhance external validity, future research should consider using a nationally representative sample through a random sampling procedure.

Second, the study did not consider the varying degrees of technology affordances in online courses. Each course or instructor may utilize different technology features in their courses. For example, the results showed the amount of gap in learning experiences is smaller than the gap in social presence. Thus, the range of learning tools and technology options to engage in communication and/or learning might influence student learning experiences. To better understand which aspects of technology features and how they influence student learning experiences in synchronous and asynchronous courses, follow-up research is needed.

Third, given that data were collected during COVID-19, there is a possibility that the nature of the pandemic may have partially affected the pattern of the results. For example, students did not have any other option but to take online courses because of the lockdown and/or restricted physical gatherings in a classroom. Some students may not have had the flexibility to choose a particular type of online course (synchronous or asynchronous); rather, they may have taken whatever option that is available for them. The popularity of online education has continuously increased (Allen and Seaman, 2017), and it will likely continue to do so. To fully understand how different types of online courses affect student learning experiences when

students take those courses based on their interests and choices, researchers are encouraged to replicate this study during non-pandemic times.

Lastly, although the simple study design of this study is best to clarify the impact of synchronousness, it is known that both students' success and satisfaction with online learning rests heavily on their traits and capabilities as well (Kauffman, 2015). For example, student self-efficacy tends to predict learning satisfaction through students' interactions with classmates, instructors, and technology (Shen, et al., 2013). Simply put, the students who are more confident in their ability to communicate and learn online, who have a clear understanding of the course expectations, and who believe they are performing well tend to have higher satisfaction with the course (Palmer and Holt, 2008). Additionally, students report higher satisfaction with the course when they perceive more instructional, peer, and technical support (Lee, et al., 2014). While students have diverse needs that vary on an individual basis (Croxton, 2014), some of their biggest frustrations with online courses include technological issues and the instructor being unavailable (Elshami, et al., 2021). However, support from the institution and its instructors can give students a more positive outlook on the course (Almusharraf and Khahro, 2020).

References

Allen, I.E. and Seaman, J., 2017. *Digital learning compass: distance education enrollment report 2017*. [pdf] Babson Survey Research Group, e-Literate, and WCET. Available at: <https://onlinelearningsurvey.com/reports/digtiallearningcompassenrollment2017.pdf> [Accessed June 2022].

Almusharraf, N. and Khahro, S., 2020. Students satisfaction with online learning experiences during the COVID-19 pandemic. *International Journal of Emerging Technologies in Learning,* 15(21), pp. 246–267. https://doi.org/10.3991/ijet.v15i21.15647.

Amiti, F., 2020. Synchronous and asynchronous e-learning. *European Journal of Open Education and E-learning Studies,* 5(2), pp. 60–70. https://doi.org/10.46827/ejoe.v5i2.3313.

Chen, Y., Sun, X. and Jin, Y., 2019. Communication-efficient federated deep learning with layerwise asynchronous model update and temporally weighted aggregation. *IEEE Transactions on Neural Networks and Learning Systems,* 31(10), pp. 4229–4238. https://doi.org/10.1109/TNNLS.2019.2953131.

Croxton, R.A., 2014. The role of interactivity in student satisfaction and persistence in online learning. *Journal of Online Learning and Teaching*. 10(2), pp. 314–324.

Dahlstrom-Hakki, I., Alstad, Z. and Banerjee, M., 2020. Comparing synchronous and asynchronous online discussions for students with disabilities: the impact of social presence. *Computers & Education*, 150: 103842. https://doi.org/10.1016/j.compedu.2020.103842.

Elshami, W., Taha, M.H., Abuzaid, M., Saravanan, C., Al Kawas, S. and Abdalla, M.E., 2021. Satisfaction with online learning in the new normal: perspective of students and faculty at medical and health sciences colleges. *Medical Education Online*, 26(1): 1920090. https://doi.org/10.1080/10872981.2021.1920090.

Fabriz, S., Mendzheritskaya, J. and Stehle, S., 2021. Impact of synchronous and asynchronous settings of online teaching and learning in higher education on students' learning experience during COVID-19. *Frontiers in Psychology*, 12: 733554. https://doi.org/10.3389/fpsyg.2021.733554.

Foutz, B., 2021. Instructor misbehavior: when instructors online are naughty; not nice. In: S. Kelly, ed. *Online instructional communication.* Newcastle upon Tyne, UK: Cambridge Scholars Publishing. pp. 97–106.

Frey, T.K., 2021. Overcoming technological barriers to instruction: situating Gen Z students as reverse mentors. *Frontiers in Communication*, 6: 630899. https://doi.org/10.3389/fcomm.2021.630899.

Garland, M.E. and Violanti, M.T., 2021. Rock my world: rewind to a better transition to remote learning. *Frontiers in Communication*, 6: 641873 23. https://doi.org/10.3389/fcomm.2021.641873.

Giesbers, B., Rienties, B., Tempelaar, D. and Gijselaers, W., 2014. A dynamic analysis of the interplay between asynchronous and synchronous communication in online learning: the impact of motivation. *Journal of Computer Assisted Learning*, 30(1), pp. 30–50. https://doi.org/10.1111/jcal.12020.

Guo, S., 2020. Synchronous versus asynchronous online teaching of physics during the COVID-19 pandemic. *Physics Education*, 55(6): 065007. https://doi.org/10.1088/1361-6552/aba1c5.

Hodges, C., Moore, S., Lockee, B., Trust, T. and Bond, A., 2020. The difference between emergency remote teaching and online learning. *Educause Review*, [online] Available at: <https://er.educause.edu/articles/2020/3/the-difference-between-emergency-remote-teaching-and-online-learning< [Accessed June 2022].

Kauffman, H., 2015. A review of predictive factors of student success in and satisfaction with online learning. *Research in Learning Technology*, 23; 26507. http://dx.doi.org/10.3402/rlt.v23.26507.

Kelly, S.E. and Westerman, D.K., 2016. New technologies and distributed learning systems. In P.L. Witt, ed. *Communication and learning*. Boston/Berlin: DeGruyter Mouton. pp. 455–480.

Khotimah, K., 2020. Exploring online learning experiences during the Covid-19 pandemic. In: *Proceedings of the International Joint Conference on Arts and Humanities (IJCAH 2020*). Surubaya, Indonesia, 3–4 October 2020. Atlantic Press. https://doi.org/10.2991/assehr.k.201201.012.

Kunin, M., Julliard, K.N. and Rodriguez, T.E., 2014. Comparing face-to-face, synchronous, and asynchronous learning: postgraduate dental resident preferences. *Journal of Dental Education*, 78(6), pp. 856–866. https://doi.org/10.1002/j.0022-0337.2014.78.6.tb05739.x.

Lee, S.J., Srinivasan, S., Trail, T., Lewis, D. and Lopez, S., 2014. Examining the relationship among student perception of support, course satisfaction, and learning outcomes in online learning. *The Internet and Higher Education*, 14(3), pp. 158–163. https://doi.org/10.1016/j.iheduc.2011.04.001.

Lew, E.K. and Nordquist, E.K., 2016. Asynchronous learning: student utilization out of sync with their preference. *Medical Education Online*, 21(1): 30587. https://doi.org/10.3402/meo.v21.30587.

Marinoni, G., van't Land, H. and Jensen, T., 2020. *The impact of Covid-19 on higher education around the world*. [pdf] International Association of Universities. Available at: <https://www.iau-aiu.net/IMG/pdf/iau_covid19_and_he_survey_report_final_may_2020.pdf> [Accessed 18 June 2021].

Moallem, M., 2015. The impact of synchronous and asynchronous communication tools on learner self-regulation, social presence, immediacy, intimacy and satisfaction in collaborative online learning. *The Online Journal of Distance Education and e-Learning*, 3(3), pp. 55–77.

Nurwahyuni, R., 2020. An analysis of students' perception on synchronous and asynchronous learning in speaking skill during pandemic Covid-19. In: M. Zini Miftah, ed. *Proceedings of International Conference on English Language Teaching (INACELT).* Palangka Raya, Indonesia, 19 September 2020, pp. 189–201.

Olson, J.S. and McCracken, F.E., 2015. Is it worth the effort? The impact of incorporating synchronous lectures into an online course. *Online Learning*, [e-journal] 19(2). Available at: <https://eric.ed.gov/?id=EJ1062939> [Accessed June 2022].

Palmer, S.R. and Holt, D.M., 2008. Examining students satisfaction with wholly online learning. *Journal of Computer Assisted Learning*, 25(2), pp. 101–113. https://doi.org/10.1111/j.1365-2729.2008.00294.x.

Peterson, A.T., Beymer, P.N. and Putnam, R.T., 2018. Synchronous and asynchronous discussions: effects on cooperation, belonging, and affect. *Online Learning*, [e-journal] 22(4), pp. 7–25. Available at: <https://eric.ed.gov/?id=EJ1202382> [Accessed June 2022].

Rippé, C.B., Weisfeld-Spolter, S., Yurova, Y. and Kemp, A., 2021. Pandemic pedagogy for the new normal: fostering perceived control during COVID-19. *Journal of Marketing Education*, 43(2), pp. 260–276. https://doi.org/10.1177/0273475320987287.

Rockinson-Szapkiw, A. and Wendt, J., 2015. Technologies that assist in online group work: a comparison of synchronous and asynchronous computer mediated communication technologies on students' learning and community. *Journal of Educational Multimedia and Hypermedia*, 24(3), pp. 263–279.

Shen, D., Cho, M.-H., Tsai, C.L. and Marra, R., 2013. Unpacking online learning experiences: online learning self-efficacy and learning satisfaction. *The Internet and Higher Education*, 19, pp. 10–17. https://doi.org/10.1016/j.iheduc.2013.04.001.

Weber, K., Martin, M.M. and Myers, S.A., 2011. The development and testing of the instructional beliefs model. *Communication Education*, 60(1), pp. 51–74. https://doi.org/10.1080/03634523.2010.491122.

Yamagata-Lynch, L.C., 2014. Blending online asynchronous and synchronous learning. *International Review of Research in Open and Distributed Learning,* 15(2), pp. 189–212. https://doi.org/10.19173/irrodl.v15i2.1778.

Yang, H., Kim,, J., Kelly S. and Merrill Jr, K., 2022. Learning in the online classroom: exploring the unique influence of social presence dimensions. *Communication Studies,* 73(3), pp. 245–262. https://doi.org/10.1080/10510974.2022.2074491.

DOI 10.14622/Advances_48_2022_05

A gate-to-gate life cycle analysis of wide-format flatbed inkjet printing

Zuha Waqar and Jonghun Park

Graphic Communications Management of The Creative School, Toronto Metropolitan University
E-mails: zwaqar@ryerson.ca; jaypark@ryerson.ca

Short abstract

Life cycle analysis (LCA) studies of ultra-violet (UV) inks used for inkjet printing systems are an emerging field of research and development within the print and packaging industries. This study conducted a life cycle inventory analysis on four process UV light-emitting diode (LED) inks throughout the production of a plastic point-of-purchase (POP) display. Furthermore, this study considered the inventories of expendable consumable materials used for the set-up and cleaning processes of a wide-format flatbed inkjet printer and its total electricity consumption. The study found that electricity consumption from the wide format printing press contributed the most to human health, ecosystems, and resources endpoint indicators. Conversely, the UV LED inks' environmental contributions, and consumable inventory amounted to < 0.1, with most of the environmental impact stemming from the production of the polypropylene body of the lint-free microfiber cleaning swabs. In addition, the process contribution analysis per impact category indicated that the most significant environmental impacts contributed to (1) human health, global warming, (2) fine particulate formation, (3) human carcinogenics, and (4) human non-carcinogenics impact categories. The significant limitations of the study consisted of a lack of a controlled printing environment that affected ink consumption values. Likewise, this study only considered the environmental impact of the inkjet printer following the production of a plastic POP display. Hence, the results of this study are specific to the final product and its characteristics. This study also substituted ink ingredients based on relevant literature due to a lack of available inventories on SimaPro v9.0. Therefore, future studies are recommended to explore additional methods to model UV ink inventories, calculate ink consumption, and measure emissions for UV LED inks for multiple print applications. The study results further indicated that future research is needed to optimize the electrical consumption of inkjet printing systems to decrease environmental contributions.

Keywords: inkjet, ultra-violet ink, sustainability, LCA

1. Introduction and background

The graphic communications industry embraces ultra-violet (UV) curable ink technology as an environmentally sustainable alternative to traditional ink for many print and packaging applications. For example, UV ink technology provides applications for flatbed printers and novel applications in coating and labelling (Magdassi, 2009). The choice to adopt UV curable inks primarily lie within its function to remain as solid after curing processes and hence are affordable and energy-efficient (Magdassi, 2009). A significant research area of UV curable inks within the print industry includes the recent formulation of light-emitting diode (LED) UV ink technology for inkjet printing (Magdassi, 2009).

A variety of studies have been conducted on the environmental impacts of selected components of inkjet printing and UV ink printing, including a comparison of solvent-based, water-based, UV curable, and soy-based inks used in flexographic printing (Piluso, et al., 2009; Kozake, et al., 2021). In addition, a comprehensive review of typical formulas for UV printing inks is described in 'The Chemistry of Inkjet Inks' by Magdassi (2009) that states inkjet printing must be considered as a system to evaluate UV ink tech-

nology, such as the hardware, ink components, facility requirements (power). Furthermore, Piluso, et al. (2009) evaluated the environmental impact of an improved printing system (including UV curable ink) in comparison to several printing inks such as solvent-based and water-based inks. However, few life cycle assessment (LCA) studies have been conducted on Canada's UV inkjet printing system. Moreover, LCA studies focus on ink cartridge and toner-based ink printing systems (Pollock and Coulon, 1996; Kara, 2010; Krystofik, Babbitt and Gaustad, 2014), and solvent-based inks (Egawa and Kozake, 2019), but only finds a few recently published studies that analyze the impact of water-based solvents (Robert, 2015; Kawaguchi, et al., 2020), soy-based solvents (Tolle, et al., 2000), and UV ink technology (Piluso, et al., 2009; Liao, et al., 2012; Seipel, et al., 2018). This project aims to obtain a detailed life cycle inventory analysis and impact assessment of the UV LED flatbed digital printer system. This study uses a functional unit of UV ink (g), electricity (KWh), and other consumables (g) consumed for the digital printing of 10 000 plastic point-of-purchase (POP) products.

2. Materials and methods

This study conducted a LCA of a wide-format flatbed inkjet printing system in collaboration with an imaging and electronics company and a Toronto Metropolitan University-based creative technologies lab. This study complied with ISO 14040 and ISO 14044 (International Organization for Standardization, 2006a; 2006b) and used SimaPro v9.0, a LCA software, to model life cycle inventories and analyze their environmental impacts.

2.1. Goal and scope

The goals of this LCA were (1) to build a life cycle inventory for UV LED inks and (2) to analyze the environmental impacts of the intermediate processes involved in the inkjet printing of a plastic consumer packaged goods (CPG) point-of-purchase (POP) display (18-inch by 30-inch (457.2 mm by 762 mm)) using UV LED inks. In particular, the intermediate processes included raw material extraction and production of the UV inks, expendable consumables, and electricity consumption. First, the LCA began constructing a life cycle inventory for four UV bottle inks (CMYK) comprised of oligomers, monomers, photoinitiators, phenolic sensors, and additives based on primary data sourced from the ink manufacturer and secondary sources (Magdassi, 2009). Second, the LCA analyzed the environmental contribution of the ink, electricity, and expendable consumables using a gate-to-gate system boundary. Transportation and disposal were not considered for all inventories. The use of raw materials and processes to produce energy for the electricity consumption of the print system was not considered. The functional unit used for this study was the printing of 10 000 products. In Table 1, we see the material inventories under assessment.

2.2. Life cycle anventory analysis

2.2.1 CMYK UV inks

The first phase considers the raw materials and air emissions from the production of UV inks, consisting of oligomers, monomers, type I photoinitiators, and additives, as noted from primary and secondary sources. The goal of this inventory was to estimate the total amount of UV ink components, from a gate-to-gate perspective, for 10 000 products. Due to limitations of available inventories on SimaPro, the study substituted most ink components mentioned in the safety data sheets (SDS) as noted from secondary sources (Magdassi, 2009). However, this study used primary data to gather information about the POP product characteristics (e.g., substrate type, dimensions, ink percentage breakdown, ink coverage percentage), expendable consumables, and total time spent completing set-up procedures as noted from the structured interviews with the Toronto Metropolitan University-based lab. The specific ink ingredient and percentage

of ingredients for each UV bottle ink inventory used the information listed on the corresponding SDS and was calculated using the formula below (Equation [1]).

$$Process\ Ink\ Consumption\ (g) = Process\ Ink\ Weight \times Material\ \% \quad [1]$$

2.2.2 Expendable consumables used for set-up and cleaning

The second inventory considered the raw materials and intermediate processes used to produce the expendable consumables (see Table 1). The goal of this inventory was to estimate the consumption of the expendable consumables used for cleaning and maintenance, such as cleaning liquid, lint-free microfiber cleaning swabs, expendable plastic bags, and expendable nitrile gloves. Likewise, this inventory also considered the consumables to complete makeready materials, including painter's tape and recycled pulp paper, as observed from the Toronto Metropolitan University-based lab visitations. The cleaning materials were used once every 20 print runs, assuming the print runs are of average print size and ink consumption, whereas the makeready materials were used after each run.

At the beginning of each press run, the print operators use paper (recycled pulp) and painter's tape (Kraft Paper; Synthetic Rubber) to conduct a quality assurance test of the print nozzles and ink output. For cleaning and maintenance of the printer, cleaning solution (butyl diglycol acetate), lint-free cleaners (HDPE; polystyrene), expendable bags (LDPE) and gloves (LDPE) are used at the end of the printing process at end of every twenty runs.

2.2.3 Electricity consumption

The third inventory focused on the electricity consumption generated from the UV LED flatbed inkjet printer (see Table 1). The Toronto-based lab estimated the approximate time spent for set-up and printing was 12.50 minutes and 2 minutes, respectively. This study also calculated inventories for the computer monitors. The average computer monitors energy consumption for a typical 17-inch (431.8 mm) LCD monitor was 35 W, and the average computer energy consumption for a desktop computer was between 60 W and 250 W (Northwestern University, 2018). The study used the following formula [Equation [2]) to calculate the total energy consumption of the flatbed printer and the LCD monitor for 10 000 products:

$$Total\ Energy\ Consumption\ (KWh) = \frac{\text{Watts (W)}}{1\,000} \times \left(\frac{\text{Set–up Time (min)}}{60} + \frac{\text{Total Print Time (min)}}{60}\right) \times 10\,000 \quad [2]$$

2.2.4 Limitations and assumptions

The following limitations and assumptions could affect the results of this LCA.

- It was assumed that the electrical power required to the set-up process and the printing process were the same. Thus, the electrical power used for them were not separately calculated.
- The transportation between manufacturers and the printing facilities was excluded from the scope of this study.
- The secondary and tertiary packaging used to ship the consumables from their manufacturers to the printing facility are excluded from the scope of this study.

2.3. Life cycle impact assessment

The life cycle impact assessment used an endpoint-oriented life cycle impact assessment methodology called ReCIPe 2016 (Huijbregts, 2016). The ReCIPe model was selected for this study due to the use of a North American geographical scope. The model analyzes three endpoint impact categories: human health, ecosystems, and resources.

3. Results and discussion

3.1. Life cycle inventory results

In Table 1, we see the life cycle inventory for UV LED bottle inks. The material column lists the ingredients extracted from the SDS supplied by the ink manufacturer. However, many ink ingredients were unavailable on SimaPro v9.0. Hence, some materials were substituted based on secondary sources (Magdassi, 2009). Furthermore, the inventories as described in sections 2.1.1 and 2.1.2 were combined to form one overall inventory, whereas the second and third inventories consisted of the electrical consumption of the printing press and desktop devices, respectively.

Table 1: Life cycle inventory analysis of the UV LED bottle inks

Ink Component	Material	Material (Substituted)	LCI	LCI Type	Pedigree score
A[a]	Additives, unspecified	Additives	Pigment, paper production, unspecified, at plant/US-US-EI U	US LCI	(1,3,1,1,2,3)
O[b]	4-(1-oxo-2-propenyl)-morpholine	Bisphenol A	Bisphenol A epoxy-based vinyl ester resin, {GLO}| market for | APOS, S	US LCI	(1,3,1,1,2,3)
M[c]	2-phenoxyethyl acrylate	Ethoxylated (4) phenol acrylate	Ethoxylated alcohols, unspecified, at plant/US-US-EI U	US LCI	(1,3,1,1,2,3)
	Isobornyl acrylate	2-Ethylhexyl Acrylate	2-Ethylhexyl Acrylate/EU-27	Inventory Data 2.0	(1,3,1,1,2,3)
	(5-Ethyl-1-1,3-dioxan-5-)methyl acrylate	Methacrylic Acid	Methyl Methacrylate/ EU-27	Industry Data 2.0	(1,3,1,1,2,3)
	Tricyclo decane dimethyl diacrylate	Diethylene Glycol	Diethylene glycol, at plant/US- US-EI U	US LCI	(1,3,1,1,2,3)
PI[d]	Diphenyl(2,4,6-trimethylbenzoyl)phosphine oxide	Acetophenone	Acetophenone Airborne emission	SimaPro v9.0	(1,3,1,1,2,3)
	2-Phenoxyethanol	Benzophenone	Benzophenone Airborne emission	SimaPro v9.0	(1,3,1,1,2,3)
	Phenyl bis(2,4,6,-trimethylbenzoyl)-phosphine oxide		N/A		
PS[e]	4-Methoxyphenol	P-Nitrophenol	P-nitrophenol {GLO}| market for | APOS, S	Ecoinvent 3.0	(1,3,1,1,2,3)

[a]= additives, [b] = oligomers, [c] = monomers, [d] = photoinitators, [e] = phenolic sensor

In Table 2, we see the complete life cycle inventory analysis for the complete life cycle inventory analysis to produce 10 000 POP products.

Table 2: Life cycle inventory analysis of the UV LED flatbed printing system for 10 000 products

Inventories	Components	Materials	Inventory name	Values/functional Unit	Inventory type	Pedigree Score
UV Bottle Inks[a]	UV Ink Bottle Magenta UV Ink Bottle Cyan UV Ink Bottle Yellow UV Ink Bottle Black		See Tables 2 - 5	2.36 kg	See Tables 2 - 5	
Electricity[b]	Printer	Electricity	Electricity, medium voltage, at grid/Ontario CA US-EI U	15,600 kWh	US-EI 2.2	(1,2,1,2,2,5)
	17" Dual LCD Monitors	Electricity	Electricity, low voltage, at grid/Ontario CA US-EI U	400 kWh	US-EI 2.2	(1,3,1,3,2,5)
Expendable Consumables[c]	Cleaning Liquid	Butyl diglycol acetate	Butyldiglycol acetate {GLO} butyldiglycol acetate production | APOS, S	10 g	Ecoinvent 3.0 allocation at point of substitution – system	(1,2,1,2,2,5)
	Lint-free Microfiber Cleaning Swabs	PP Process Polyester Process	Polypropylene, granulate, at plant/US- US-EI U Injection moulding, at plant/US- US-EI U Unsaturated polyester, resin, at plant/US- US-EI U Injection moulding, at plant/US- US-EI U	163.8 g	US-EI 2.2	(1,2,1,2,2,5)
	Painter's Tape	Kraft Paper Synthetic Rubber	Kraft paper, bleached, at plant/US US-EI U Synthetic rubber, at plant/US US-EI U	114.2 kg	US LCI US-EI 2.2	(1,3,1,2,2,3) (2,3,1,3,2,5)
	Expendable LDPE Bags	LDPE Process	Low density polyethylene granulate, at plant/US- US-EI U Extrusion, plastic film, at plant/US US-EI U	97.2 g	US LCI US-EI 2.2	(1,3,1,2,2,3) (2,3,1,3,2,5)
	Expendable Nitrile Gloves	Synthetic Rubber Process	Synthetic rubber, at plant/US- US-EI U Extrusion, plastic film, at plant/US US-EI U	53.4 g	US LCI US-EI 2.2	(1,3,1,2,2,3) (2,3,1,3,2,5)
	Paper	Recycled Pulp	Graphic paper, 100% recycled {RoW}| production | Conseq, U	219 kg	Ecoinvent 3.0 allocation at point of substitution – system	(1,3,1,3,2,5)

[a] = ultra-violet ink production and consumption, [b] = electricity consumption of printer and desktop, [c] = expendable consumables used for makeready and cleaning

3.2. Results of contribution analysis

Figure 1 shows normalized results of the contribution analysis of the UV flatbed printing.

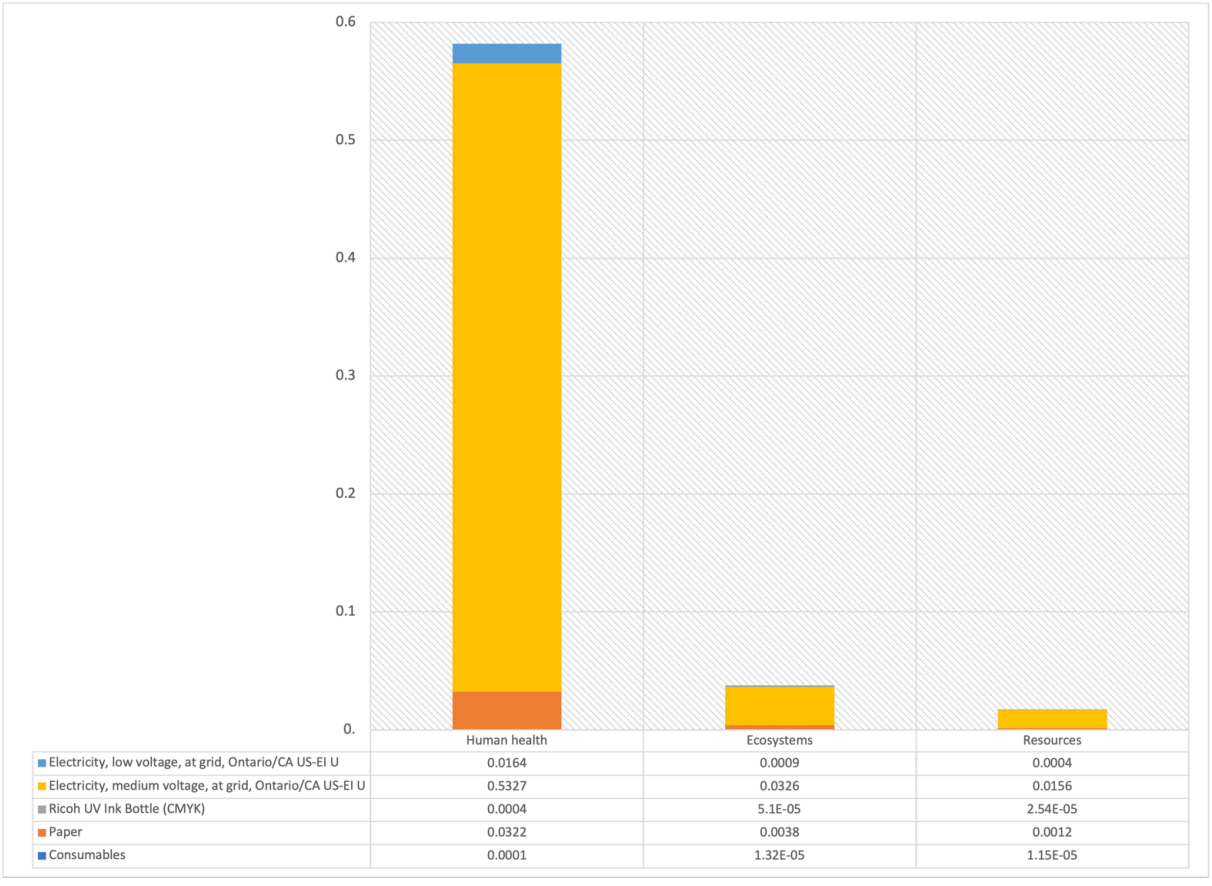

Figure 1: Results of contribution analysis of the UV LED flatbed printing (normalized values)

The results indicates that the electricity consumption of the printing process had the greatest environmental impact in all three endpoint environmental impact categories including human health (91.6 % of the total impact), ecosystems (87.2 % of the total impact), and resources (90.1 % of the total impact). Specifically, diesel burned in the power plant contributed the most to human health and ecosystems, while natural gas burned in the power plant had the most contribution to resources.

Paper production generated the second largest environmental burden for all environmental impact categories (5~10 % of the total impact). In particular, the electricity used for the recycling process to manufacture recycled paper had the greatest contribution to human health. The natural gas consumed during the pulping process contributed most to ecosystems and resources.

The electricity consumption of the computer monitor had the third largest environmental impact for all environmental impact categories. It accounted for approximately 2 % of the total environmental burden for those impact categories.

The environmental impact of the ink was nearly negligible as it only accounted for 0.07 %, 0.14 %, and 0.15 % of the total environmental impact for human health, ecosystems, and resources, respectively. The consumables used for the printing process including cleaning liquid, lint-free microfibre cleaning swabs, LDPE bags, gloves, and painter's tape contributed the least to all environmental impact categories (less than 0.1).

The greatest environmental impact was generated by printer hardware similar to the findings of relevant literature that concluded inkjet printer systems were energy-intensive machinery. For example, Viluksela, Kariniemi, and Nors (2010) stated that digital printing methods consumed greater amounts of energy and ink consumption when compared to other methods. For the UV bottle inks and consumables inventories, it was expected that the environmental impact generated would be negligible in comparison to the electrical consumption of the print system. Similarly, the subsequent results indicated some impact on the degradation of human health, such as in the categories of human carcinogenics and non-carcinogenics, although the specific amounts were approximately 0.1.

4. Conclusions

The environmental contributions of the overall inkjet printing system largely stemmed from the electrical consumption of the printing press (medium voltage). Hence, the inkjet printing system was energy intensive. Despite the lack of LCA studies on the environmental impacts of UV LED inkjet presses, there is a general understanding that digital methods consume greater energy than traditional printing presses (Viluksela, Kariniemi, and Nors, 2010). However, the degree to which the energy consumption offsets the environmental contributions of other printing systems is underexplored. Future studies are recommended to compare multiple printing systems including UV inkjet printers to gain a thorough understanding of printing ink sustainability implications.

This study analyzed the environmental impact of a UV LED flatbed inkjet printing system with a focus on the materials and intermediate processes inventories based on a case study. First, the study found the electricity generated from the UV flatbed inkjet printer (medium voltage) contributed the most to all impact categories in comparison to all three material inventories. Second, the production of the polypropylene body of the lint-free microfiber cleaners contributed the most to the human health and ecosystem categories, whereas the production of recycled pulp contributed the most environmental impact to the resources category when analyzing the UV bottle ink and consumables inventory. Third, the study found that the ink ingredients did not contribute to the overall environmental impact in either of the three impact categories.

However, the UV LED ink inventories were difficult to assess due to the lack of available inventories. More research is needed to obtain a better and more reliable understanding of the UV LED inks. These include input and output figures like materials consumption, emissions, and waste output. The suitable functional units are the mass and the surface area of ink coverage, i.e., one square meter of ink coverage. This study also did not consider the environmental impact of transportation or disposal. Future studies are encouraged to examine the environmental impact of digital printing systems by optimizing electricity consumption processes. Likewise, the results of this study are only applicable to the production of the product under study. For this reason, it is encouraged to conduct similar studies of different print products.

Acknowledgements

This research acknowledges the contributions of Orit Zewge-Abubaker and Alda Escareno at the Design + Technology Lab located at Toronto Metropolitan University for their assistance in material and process data collection, and Begum Walji for sharing her expertise in UV inkjet printing.

References

Egawa, T.; Kozake, K., 2019. Development of eco-friendly water-based inkjet ink for flexible packaging film. *Soft Drink Gijyutsusiryou*, 188, pp. 111–118.

Huijbregts, M.A.J., Steinmann, Z.J.N., Elshout, P.M.F., Stam, G., Verones, F., Vieira, M.D.M., Hollander, A, Zijp, M. and van Zelm, R., 2016. *ReCiPe 2016 v1.1: a harmonized life cycle impact assessment method at midpoint and endpoint level*. [pdf] Bilthoven, The Netherlands: National Institute for Public Health and the Environment. Available at: <https://pre-sustainability.com/legacy/download/Report_ReCiPe_2017.pdf> [Accessed February 2022].

International Organization for Standardization, 2006a*. ISO 14040:2006 Environmental management – Life cycle assessment – Principles and framework*. Geneva: ISO.

International Organization for Standardization, 2006b. *ISO 14044:2006 Environmental management – Life cycle assessment – Requirements and guidelines*. Geneva: ISO.

Kara, H., 2010. *Comparative carbon footprint analysis of new and remanufactured inkjet cartridges*. Centre for Remanufacturing & Reuse. https://doi.org/10.13140/RG.2.2.32313.19040.

Kawaguchi, F., Egawa, T., Kunii, S., Kozake, K., Okada, T., Shibata, M. and Itsubo, N., 2020. Environment assessment of water-based inkjet printing for flexible package. In: *Proceedings of the 15th Meeting of the Institute of Life Cycle Assessment*. Tokyo, Japan, 10–12 March 2020; pp. 160–161.

Kozake, K., Egawa, T., Kunii, S., Kawaguchi, H., Okada, T., Sakata, Y., Shibata, M. and Itsubo, N., 2021. Environmental impact assessment of flexible package printing with the "LUNAJET®" aqueous inkjet ink using nanodispersion technology. *Sustainability*, 13(17): 9851. https://doi.org/10.3390/su13179851.

Krystofik, M., Babbitt, C.W. and Gaustad, G., 2014. When consumer behavior dictates life cycle performance beyond the use phase: case study of inkjet cartridge end-of-life management. *The International Journal of Life Cycle Assessment*, 19(5), pp. 1129–1145. https://doi.org/10.1007/s11367-014-0713-6.

Liao, S., Tai, M., Lin, S.-C. and Lin, C.-K., 2012. A study of print quality of UV ink-jet printing on glass. *Applied Mechanics and Materials*, Vol. 262, pp. 287–290. https://doi.org/10.4028/www.scientific.net/amm.262.287.

Magdassi, S. ed., 2009. *The chemistry of inkjet inks*. Singapore: World Scientific Publishing.

Northwestern University, 2018. *Computer energy consumption (average user).* [online] Available at: <https://www.it.northwestern.edu/hardware/eco/stats.html> [Accessed 29 March 2022].

Piluso, C., Serafano, J., Kloock, L.M., Grandke, R. and Bradlee, C.A., 2009. Eco-efficiency analysis demonstrates the environmental and economic benefits of flexographic printing inks in film applications. *Ink World*, 15(6), pp. 66–73.

Pollock, D. and Coulon, R., 1996. Life cycle assessment: of an inkjet print cartridge. In: *Proceedings of the 1996 IEEE International Symposium on Electronics and the Environment. ISEE-1996*. Dallas, TX, USA, 6 August 2002. IEEE, pp. 154–160.

Robert, T., 2015. "Green ink in all colors" – printing ink from renewable resources. *Progress in Organic Coatings*, 78, pp. 287–292. https://doi.org/10.1016/j.porgcoat.2014.08.007.

Seipel, S., Yu, J., Periyasamy, A.P., Viková, M., Vik, M. and Nierstrasz, V.A., 2018. Inkjet printing and UV-LED curing of photochromic dyes for functional and smart textile applications. *RSC Advances, 8(50),* pp. 28395–28404. https://doi.org/10.1039/C8RA05856C.

Tolle, D.A., Evers, D.P., Vigon, B.W. and Sheehan, J.J., 2000. Streamlined LCA of soy-based ink printing. *The International Journal of Life Cycle Assessment,* 5(6): 374. https://doi.org/10.1007/BF02978677.

Viluksela, P., Kariniemi, M. and Nors, M., 2010. *Environmental performance of digital printing: VTT Research Notes 2538*. Espoo, Finland: VTT.

DOI 10.14622/Advances_48_2022_18

Revising our thinking on tone value increase

John Seymour

John the Math Guy, LLC, and Clemson University
E-mail: john@johnthemathguy.com

Short abstract

The equation for tone value increase (TVI) is based on two things: 1) a simplistic mathematical model relating reflectance of a halftone and the area coverage, the Murray-Davies (MD) equation, and 2) the assumption that "dots get bigger" is an adequate explanation for the decrease in reflectance between plate and substrate. The TVI has proven a useful metric for process colors, but it has numerous drawbacks. It fails miserably for some spot colors. The calculated TVI depends on the wavelength. There is not a one-to-one correspondence between CIELAB values and TVI. The MD equation produces a poor estimate the spectrum of a halftone. These deficits all stem from the fact that MD is a simplistic mathematical model. Improvements to the MD mathematical model have been developed which add the effects of light scattering into the paper, and which account for the thinning of dots as they spread in the print process. A complete mathematical model would take both of these effects into account but since the two effects are similar numerically, either equation could be used as a stand-in for the combined effect of the two. This paper posits that the dot squish mathematical model could be used to generate a process control parameter that behaves similar to TVI. This parameter would work equally well with process and spot colors. Since it is based on a reasonably accurate mathematical model, it could be used to predict the spectra of halftones and hence there would be a one-to-one correspondence between this parameter and CIELAB values.

Keywords: tone value increase, TVI, Murray-Davies, Noffke-Seymour, process control metrics

1. History

1.1 The Murray-Davies equation

The computation of apparent tone value is based on an equation originally published by Alexander Murray in 1936 (Murray, 1936; Gamm, 2020). In this paper, he attributes the equation to Edward Davies – hence the equation has been named the Murray-Davies (MD) equation.

$$D = \log\left(\frac{1}{1 - a(1 - r)}\right) \qquad [1]$$

where D is the density of the halftone, a is the relative amount of paper covered with ink, and r is the reflectance of the solid.

A practical issue with this equation is that the reflectance of the paper is ignored. This was corrected in a 1941 paper by Yule (Yule, 1941; Dorst, 1943).

A didactic issue with Equation [1] is that it is obtuse. There is an underlying mathematical model, but that model is obscured by the math. A simpler form, first stated by Dorst, expresses the absorbance value of the halftone as a function of the dot area, and absorbance values of the paper and solid. Equation [2] shows Dorst's version, but in terms of reflectance rather than absorbance.

$$R_t = (1 - A)R_p + AR_s \quad [2]$$

where R_p is the reflectance of the substrate (the paper), R_s is the reflectance of the solid, A is the area of the halftone, and R_t is the predicted reflectance of the halftone (the tint).

In his equation, it is seen that the reflectance of the halftone is a weighted average of the solid and the paper, with the weighting being the area of the dots and the uncovered paper, respectively. The underlying assumption is that a photon will either hit the ink (and reflect as if it were a solid) or hit paper (and reflect accordingly).

As an aside, the so-called Murray-Davies equation is an example of Stigler's law, which states that no scientific finding is named after the original inventors. Instead of Murray-Davies, the equation should be called Davies-Dorst.

1.2 Murray-Davies as a metric

The Murray paper is widely recognized as the source for the MD equation, but there was another contribution of this paper that is less well known. A large portion of this paper is devoted to understanding "dot spreading". Murray recognized that dots grew between the plate and the print, and that this growth led to changes in the density of the print. He proposed that, rather than use the actual size of the dot for process control, density would be a suitable proxy.

"For control of daily production, micrometry [direct measurement of dot size] is too laborious. As the object of the measurements is to secure data for the calculation of density, it seems more efficient to measure densities directly."

Murray planted the idea for a metric for dot gain, but did not provide a means to determine dot area from density measurements. This can readily be derived from the prediction provided by Equation [2]. Inverting this equation gives us a process control metric.

$$A_{out} = \frac{R_t - R_p}{R_s - R_p} \quad [3]$$

If the reflectance values are all known from measurements of a press sheet, then A_{out} represents the *apparent dot area* of the halftone on the substrate. The difference between the dot area on the plate, A_p, and the apparent dot area from Equation [3] became known as the *dot gain*, A_Δ.

$$A_\Delta = A_{out} - A_{in} \quad [4]$$

More recently, the terms were renamed *apparent tone value* and *tone value increase* (TVI) to incorporate technologies where the dots were less distinct or absent. Thus, we have an indirect means to estimate the growth of halftone dots.

1.3 Deficiencies of Murray-Davies

The simplifying assumptions in the MD model have had some repercussions. Three of the repercussions are described here.

1.3.1 Wavelength dependence

According to the MD assumptions, it should be possible to compute the TVI at any wavelength where there is at least some absorption. The size of a dot should not depend on wavelength. The plot (Figure 1) shows

the TVI of a cyan halftone, computed at each individual wavelength. In this case, the TVI ranges from about 3 % to 18 %.

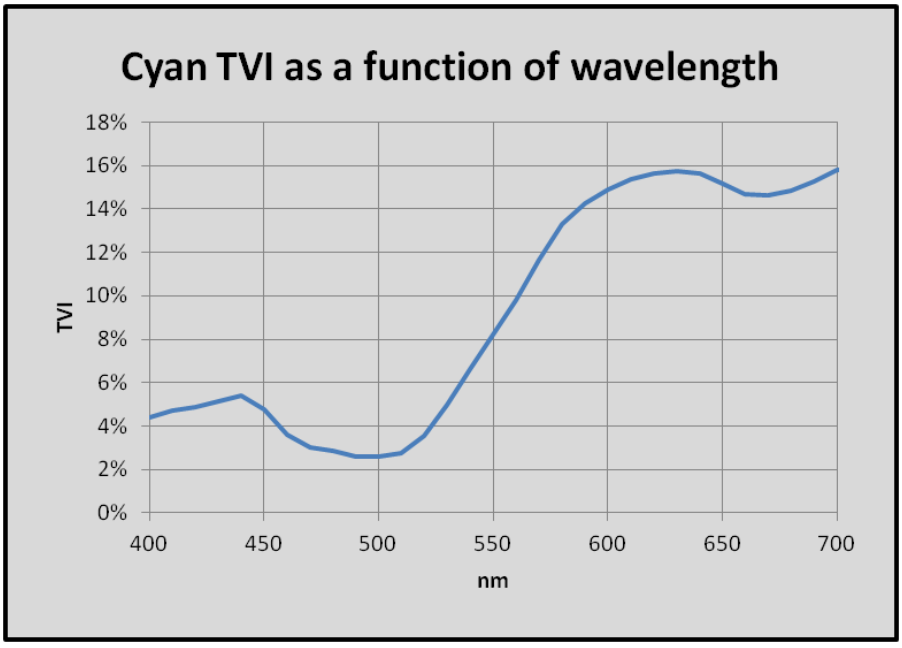

Figure 1: The TVI computed at each wavelength (Seymour, 2013c)

If the TVI were the same or nearly the same at all wavelengths, then it would not matter whether TVI were calculated with a Status T or E filter, or from *X*, *Y*, or *Z* values, or from narrowband reflectance. The numbers would be nearly the same. The choice of wavelength range would be a largely academic matter, rather than a potential source for miscommunication when TVI is computed from different parts of the spectrum.

From a theoretical standpoint, this serves as proof that MD does a poor job of simulating the reflectance of halftones. The size of a dot should not depend on what part of the spectrum you look at. Further, it is incorrect to refer to any of these measures of TVI as being a more accurate estimate of the "true TVI", since it is the model itself that is inaccurate.

From a practical standpoint the graph demonstrates that it is important to be consistent in the choice of wavelength range. Any of the wavelength ranges have been demonstrated to work in practice. For CMYK inks, TVI Status T/E broadband filters, Status I narrowband filters, and *XYZ* filters have all been demonstrated to work well for creation of plate curves and for process control.

1.3.2 Inability to predict spectra and color

If halftones followed the assumptions embedded in the MD equation, then it would be possible to reliably predict the spectrum of a given halftone from the spectra of the paper and the solid, along with the TVI. Figure 2 shows the problem with this.

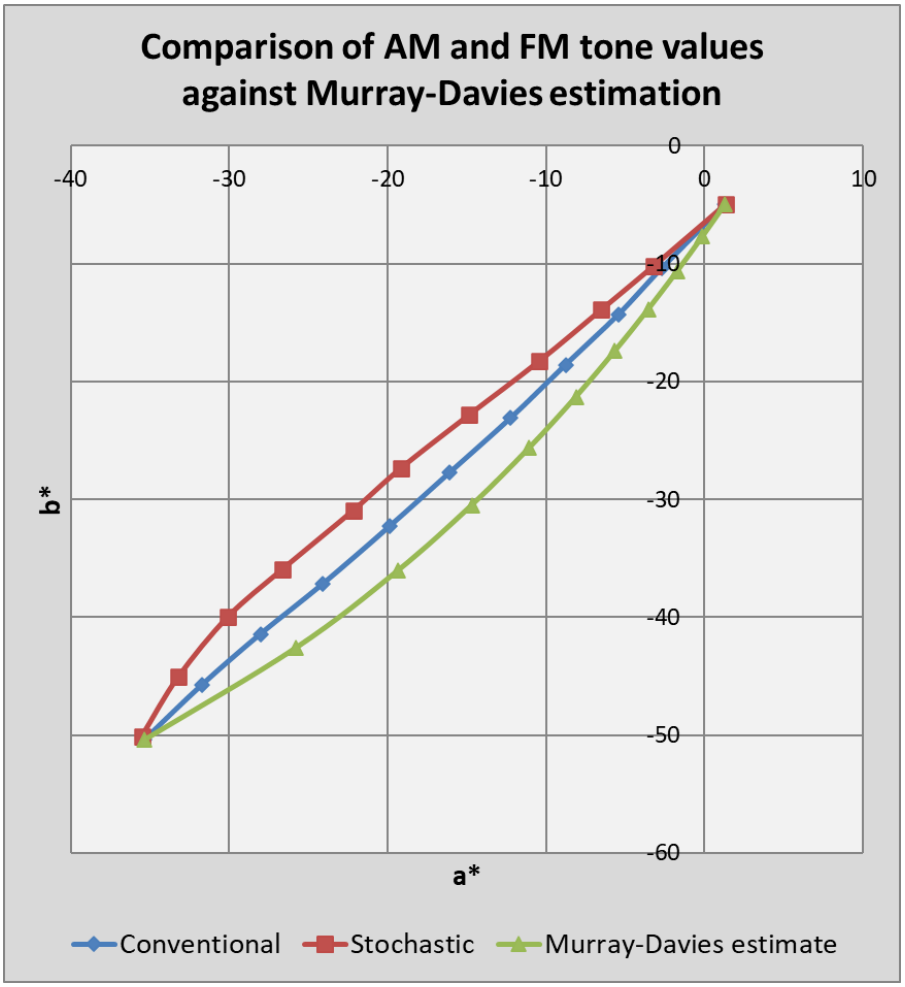

Figure 2: Murray-Davies predictions of halftones versus reality (Noffke and Seymour, 2012)

The plot shows the *a*b** values of three cyan tone ramps. The green curve traces the halftone trajectory of a hypothetical ink/press that follows the MD equation. The blue and red curves are actual data from cyan halftone ramps using conventional screening and stochastic screening on the same sheet. If we could rely on the MD equation to predict spectra, then we could rest assured that specifying a TVI would provide a reasonable color match.

1.3.3 Application to spot colors

In 2013, there was a growing awareness that TVI did not work well for spot colors. For certain inks, the attempt to linearize tone ramps using TVI failed abysmally. The lower bar graph in Figure 3 illustrates a tone ramp that is linear according to the MD equation. "That first step is a doozy!" The awareness of this problem led to the formation of the Spot Color Halftone Metric Optimization committee to find a better metric.

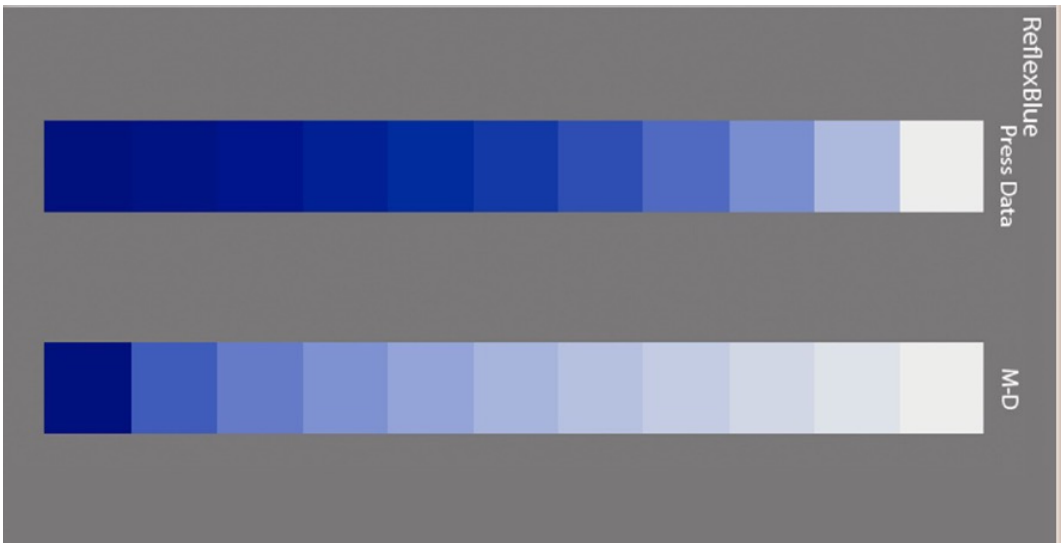

Figure 3: Reflex blue tone ramps, native (top) and after "linearizing with TVI" (below) (Smiley, 2015)

Many different equations were proposed and tested against real data. One of the equations was selected and has been formalized in ISO 20654 (International Organization for Standardization, 2017) under the name Spot Color Tone Value (SCTV). This new metric satisfied the immediate need for a way to construct linear tone ramps for spot colors. It was also found to be an acceptable replacement for TVI of process colors (Strickler, 2018).

SCTV does not, however, have an underlying mathematical model. As such, it cannot be used to estimate spectra of halftones (Seymour, 2013a; 2013b; 2013c; 2013d; 2014). Further, SCTV is only remotely related to colorimetry, so it cannot be counted on to provide perceptual linearity. Aside from the work done by the committee, there is no research that says that equal steps in SCTV are equal steps in perception.

It is the contention of this paper that the failure of MD TVI on spot colors is a direct consequence of the underlying simplistic mathematical model.

1.4 Improvements to the theory

Yule and Nielsen (1951) published a paper that showed that there were significant systematic differences between the actual dot area on a printed sheet and the apparent dot area as computed with the MD equation. For some reason, the dots on a printed sheet absorbed more light than would be expected from their size.

To explain the difference between theory and reality, Yule and Nielsen eliminated the second assumption in the MD equation, that the reflectance of the substrate in between the dots was the same as the bare substrate. They posited that some light entered through a halftone dot, scattered in the paper, and then exited outside of the halftone dot. In this way, the substrate between the dots was tinted toward the color of the solid. There would thus be an apparent increase in the area of the halftone dots. They called this *optical dot gain* (as opposed to *physical* dot gain), and provided an equation to predict this. The Yule-Nielsen (YN) model included a parameter *n* which related to the amount of light scattered in the substrate.

$$R_t^{1/n} = (1 - A)R_p^{1/n} + AR_s^{1/n} \quad [5]$$

While this paper received much academic interest, it had little practical impact. The Yule-Nielsen *n* factor could have been used as a process control parameter in place of the dot gain parameter derived from the Murray-Davies equation. Two issues kept this from happening. The first issue was that their equation is

unfortunately not invertible, so determining *n* for a given halftone would have required computers and iterative methods.

The second issue was that the paper ingrained the theoretical concept that "dot gain = physical dot gain + optical dot gain". Ostensibly, physical and optical dot gain needed to be determined separately. It is likely that any idea of using the *n* factor to account for both optical and physical dot gain was squelched by the theoretical concept. And since physical dot gain was at best cumbersome to measure, the use of the YN equation was deemed impractical for common use.

So, industry continued to use the MD equation to determine the process control parameter that they called dot gain, largely oblivious to the fact that the control parameter might more accurately be called "increase in physical dot area plus the error caused by the use of the MD equation which neglects important physical phenomena in the mathematical model".

The combination of MD and YN mathematical models is ineffective at predicting reflectance of midtone dots on a gravure press with very low viscosity inks. A midtone thus printed may spread to cover the entire area. MD would predict that the midtone has the same reflectance as the solid. Since there is effectively no paper showing through, there is no YN correction.

Noffke and Seymour (2012) provided a third mathematical model. Their model eliminated the assumption that the halftone dots have the same reflectance as the solid. They theorized that halftone dots are initially the same thickness as the solids, but as they transfer from plate to substrate, they spread out. Since the ink volume per dot must remain the same, there is a corresponding decrease in thickness corresponding to the increase in area.

Equation [5] is a restatement of the Noffke-Seymour (NS) equation from the original paper. This restatement is algebraically equivalent, but restates it in a way that the parameter A_Δ can be seen as analogous to TVI from the MD equation.

$$R_t = (1 - A_{in} - A_\Delta)R_p + (A_{in} + A_\Delta)R_p\left(\frac{R_s}{R_p}\right)^{(A_{in}+A_\Delta)/A_{in}} \quad [6]$$

It was shown that this mathematical model could be used to predict a variety of types of print, including ink jet printing and soft dot gravure which do not necessarily follow the intended model.

To summarize the three models, MD assumes that the reflectance of the paper between the dots is the same as the paper away from the dots and that the reflectance of the halftone dot is the same as that of the solid. YN eliminates the first assumption, and NS eliminates the second.

It would therefore seem reasonable that the most accurate model would eliminate both simplifying assumptions. The new definition of dot gain is "dot gain = NS dot gain + optical dot gain". However, one of the findings in the Noffke-Seymour paper was that the YN and NS models produced very similar results. Because of this, it would be very difficult to look at a set of spectra and differentiate between the two effects. On the other hand, it is not generally necessary to determine which of the two effects dominates. Either one can be used to account for the effects of both.

Unfortunately, like the YN equation, the NS equation cannot be algebraically solved for A_Δ. An iterative algorithm must be used to determine the dot squish TVI.

2. To be demonstrated

The thesis of this paper is to demonstrate the following points:

1. The NS mathematical model can be used as a metric very similar to TVI computed from MD, but which is based on a more accurate mathematical model of the reflectance of halftones.
2. The NS TVI metric is less dependent on choice of wavelengths than is the MD model.
3. The NS TVI metric can provide a reasonable estimate of the spectrum of a halftone of a given dot area from the spectrum of the substrate and solid and the NS TVI.
4. The NS TVI metric will accurately predict the hue shift between stochastic and conventional halftones.

References

Dorst, P.W., 1943. Halftone densities. *Journal of Optical Society of America*, 3(8), pp. 436–439. https://doi.org/10.1364/JOSA.33.000436.

Gamm, B., 2020. The Murray-Davies equation: an origin story. *CMYK History* [blog], 18 October. Available at: <https://cmykhistory.com/murray-davies-equation-origin-story/> [Accessed February 2022].

International Organization for Standardization, 2017. *ISO 20654:2017 Graphic technology – Measurement and calculation of spot colour tone value*. Geneva: ISO.

Murray, A., 1936. Monochrome reproduction in photoengraving. *Journal of the Franklin Institute*, 221(6), pp. 721–744. https://doi.org/10.1016/S0016-0032(36)90524-0.

Noffke, P. and Seymour, J., 2012. A universal model for halftone reflectance. In: *64th TAGA Annual Technical Conference*. Jacksonville, FL, USA, 18–21 March 2012. Sewickley, PA: TAGA.

Seymour, J., 2013a. *Measuring TVI of a spot color* (unpublished). [pdf] Available at: <http://johnthemathguy.com/files/pdf/MeasuringTVIOfASpotColor.pdf> [Accessed February 2022].

Seymour, J., 2013b. The color of a bunch of dots, part 1. *John the Math Guy* [blog], 19 June. Available at: <https://johnthemathguy.blogspot.com/2013/06/the-color-of-bunch-of-dots-part-1.html> [Accessed February 2022].

Seymour, J., 2013c. The color of a bunch of dots, part 3. *John the Math Guy* [blog], 3 July. Available at: <https://johnthemathguy.blogspot.com/2013/07/the-color-of-bunch-of-dots-part-3.html> [Accessed February 2022].

Seymour, J., 2013d. The color of a bunch of dots, part 4. *John the Math Guy* [blog], 31 July. Available at: <https://johnthemathguy.blogspot.com/2013/07/the-color-of-bunch-of-dots-part-4.html> [Accessed February 2022].

Seymour, J., 2014. The color of a bunch of dots, part 5. *John the Math Guy* [blog], 25 June. Available at: <https://johnthemathguy.blogspot.com/2014/06/the-color-of-bunch-of-dots-part-5.html> [Accessed February 2022].

Smiley, S., 2015. *Managing spot colour tints*. FTA Forum 2015.

Strickler, M., 2018. Measuring CMYK Halftones: the case for spot color tone value formula. In: *70th TAGA Annual Technical Conference*. Baltimore, MD, 18–21 March 2018. Sewickley, PA: TAGA.

Yule, J.A.C., 1941. *Journal of the Franklin Institute*, 231(1), pp. 23–38. https://doi.org/10.1016/S0016-0032(41)90356-3.

Yule, J.A.C. and Nielsen, W.J., 1951. The penetration of light into paper and its effect on halftone reproduction. In: *Proceedings of the 3rd annual technical meeting.* Columbus, OH, 7–9 May 1951. TAGA, pp. 65–76.

DOI 10.14622/Advances_48_2022_17

A visualization tool for paper compression in a rolling nip

Emanuele Zeni[1,2], *Cecilia Rydefalk*[3] *and Li Yang*[3]

[1] School of Electrical Engineering and Computer Science, Royal Instititute of Technology (KTH), Stockholm, Sweden

[2] Department of Information and Communication Engineering, Università di Trento, Trento, Italy

[3] Department of Pulp, Paper, and Packaging, RISE - Research Institutes of Sweden, Stockholm, Sweden

E-mails: zeni@kth.se; cecilia.rydefalk@ri.se; li.yang@ri.se

Short abstract

Rolling nip consisting of two rotational cylinders is an essential element of a conventional printing device, flexography, gravure, and offset. Running at a speed up to ten(s) of meters per second, material behaviour inside a printing nip is not only complex but also hard to be accessed or studied. Quantitative knowledge on the materials behaviours has been shallow. We have thus proposed to use scientific visualisation technology to bring clear details of the dynamic processes inside the nip. As an example, dynamic behaviour of a model material (like a paperboard) has been studied and demonstrated.

Keywords: printing dynamics, viscoelasticity, graphic representation, scientific visualisation

1. Introduction and background

Rolling nip consisting of two rotational cylinders is an essential element of a conventional printing device, e.g., flexography, gravure, and offset. These cylinders are often called print cylinder and compression cylinder, respectively. The surface of the print cylinder is either covered by a print plate or engraved in case of gravure. When entering the nip, a paperboard undergoes compressive deformation governed by soled nip pressure. Texts and graphics are created by transferring inks from the print plate onto the paperboard surface with the help of mechanical contacts / compressions between the printing plate, the ink, and the paperboard.

Packaging printing is complex and multidisciplinary. With a modern printing press running at a printing speed up to ten(s) of meters per second, the duration time that the substrate is compressed in the nip is very brief, e.g., in a few or even a fraction of milliseconds. On the other hand, the materials involved in the compression process, print plate made of either polymer or rubber, foam materials, and paper substrate etc, are very often viscoelastic. Their responses to the nip compression depend not only on the nip geometry, but also on their mutual interactions between these materials, and even printing speed. Thus, experimental studies have been very difficult and rare. Apart from qualitative knowledge accumulated in the field, there are a lot of unknowns about what is happening inside the nip.

Simulation and visualization may fill the knowledge gap. There are two major types of visualization techniques: scientific visualization and information visualization. Scientific visualization provides graphical representations of numerical data that help qualitative and quantitative analysis (Hansen and Johnson, 2004). It has found applications in a broad scientific research and industrial applications, e.g., fluid-flow simulations, molecular dynamics, digital pathology, material sciences, astronomy, space missions, and many medical topics. There is plenty of visualization software available on the market, from general purpose numeric programs MATLAB and IDL to more specialized and powerful ones provided by VTK and ParaView software, OpenGL för graphics programming, and OpenSceneGraph, a higher-level programming

library built on top of OpenGL, etc. (BU TechWeb, n.d.). However, to our best knowledge, there has been no work reported on printing related topics.

The goal of this project is to introduce and demonstrate the usefulness of scientific visualisation in printing related applications. In the present study to visualize the dynamic interactions involved in printing nip, based on a physical model and simulation.

2. Methods

Rather than a genuine printing situation, we limit our study to compression dynamics of a paper board which is known as being viscoelastic. The rolling nip is formed by two rigid cylinders, like the case of hard calendering.

2.1 Physics model of compression dynamics

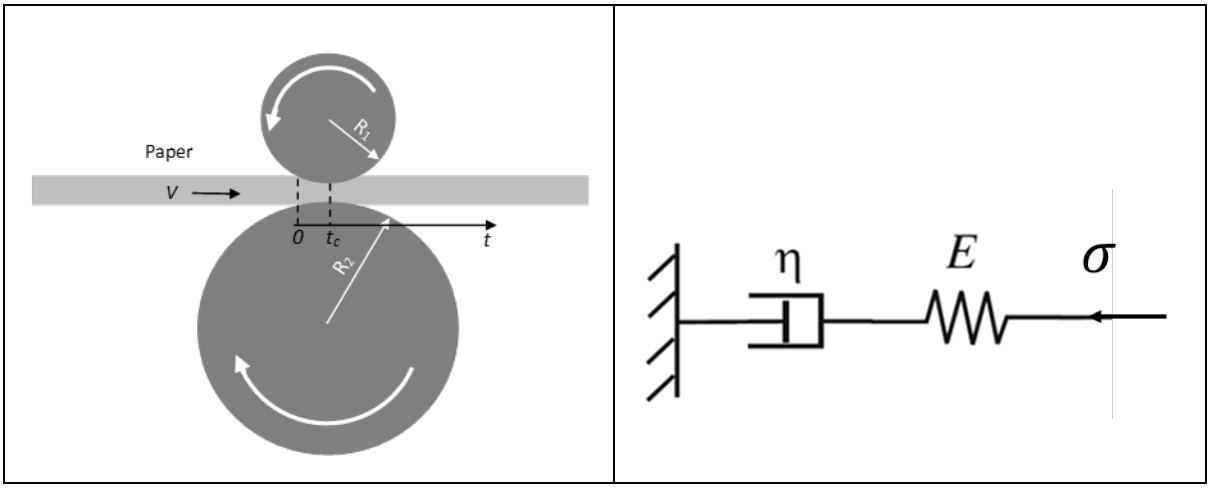

Figure 1: Illustration of the rolling nip between two rigid cylinders (left), t_c is the time duration from entering the nip to reaching the nip center; and the material model of the paper (right)

In the rolling nip shown in Figure 1 (left), the paper is subjected to compressive stress of the nip. To simulate the viscoelastic response of paper in creep and relaxation experiments spring and dashpot elements are frequently used (Roylance, 2001; Sperling, 1992). Similar treatment has been applied in fast compression situation like printing or calendaring (Litvinov and Farnood, 2010; Yang, 2020). Figure 1 (right) depicts the material model of the paper, known as Maxwell model, in which the string and the dashpot is connected in series. The mathematical expression for the model is (Yang, 2020),

$$\sigma(t) = 2\frac{\eta \cdot \Phi}{D_0}t + 2\frac{\eta \cdot \Phi}{D_0}\left(t_c + \frac{\eta}{E}\right)\left[exp\left(-\frac{E}{\eta}t\right) - 1\right] \quad [1]$$

where E and η stand for the elastic and viscos modulus, respectively, while σ for the correspondent stress. The quantity Φ is dependent of the nip geometry and the printing speed, as given below

$$\Phi = \frac{V^2}{2}\left(\frac{1}{R_1} + \frac{1}{R_2}\right) \quad [2]$$

Hence, for a given nip geometry, R_1 and R_2, the nip pressure can be determined by the following parameters, E, η, and V, or the elastic and viscos modulus of the material and the print speed, respectively. The pressure data with respect to the material properties and print settings are generated by employing these equations.

2.2 Visualisation of the dynamic compression

The visual representation has been built following a very specific process derived from Munzner's work (Munzner, 2009) using a high-level, general-purpose programming language, Python. The user interface is shown in Figure 2. By sliding the bar(s), one can change the input parameters of the simulation and visualisation, e.g., the print speed, the viscos and elastic modules of the paper substrate.

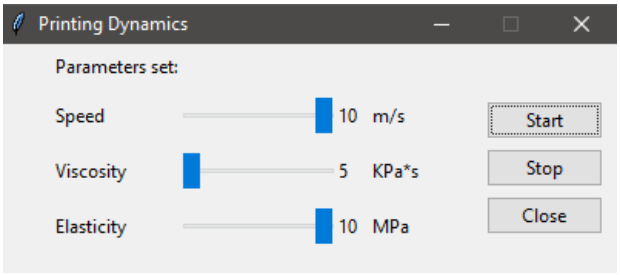

Figure 2: The user interface of the visualisation tool

3. Results and discussion

Figure 3 shows six or three pairs of examples of pressure distributions in the nips. The two circular disks with the arrow are the printing rollers where the arrow shows the direction of rotation. The ratio of the cylinders' radius is 1:2. The blue rectangle represents the substrate or paper in the present case. The pressure distribution inside the nip is represented by colour code, blue for low pressure and red for high pressure, as denoted by the vertical pressure-scale bar on the right. The input parameters of the three pairs of the simulations, e.g., the elastic and viscos components and the printing speed are listed in Table 1. For an easy reading, the parameters that are different are highlighted in the table.

Table 1: Material properties and printing speed used in the six simulation cases; the highlighted areas are the parameters different in each pair

Case	Elastic component E (MPa)	Viscos component η (KPa·s)	Speed V (m/s)
1	7	12	5
2	7	198	5
3	7	198	1
4	7	198	10
5	3	198	5
6	10	198	5

In the first two cases, the model materials have the same elastic modulus but different viscos modulus. These model materials were compressed in the same speed. As seen from the images, the pressure was low at the position of entering or exiting the nip. The nip pressure became higher when approaching the nip center denoted by the dashed lines. There are some obvious differences between the images. First, the maximal pressure in the left image is lower than that in the right. Second, the pressure distribution in the left image is much more asymmetric with respect to the nip geometry i.e., the major part lies towards the nip entrance side. Third, the model material didn't recover its full thickness when exiting the nip in the left image.

The second pair of the simulation (cases 3 and 4) illustrates the influence of the elastic component on the nip pressure. As seen from the images, when the elastic increased from 3 MPa to 10 MPa, the nip pressure was drastically increased.

The third pair of the simulation (cases 5 and 6) demonstrate the influence of the printing speed. As seen from the images, at V = 1 m/s only the positions in the vicinity of the nip center gain somewhat yellow tone while at V = 10 m/s, the width of the yellow band is significantly extended and the yellow tone more saturated. This indicates that for the same material and the same nip geometry, the nip pressure increased with the increasing printing speed.

These observations can be attributed to the viscoelastic nature of the model materials as earlier reported (Yang, 2020).

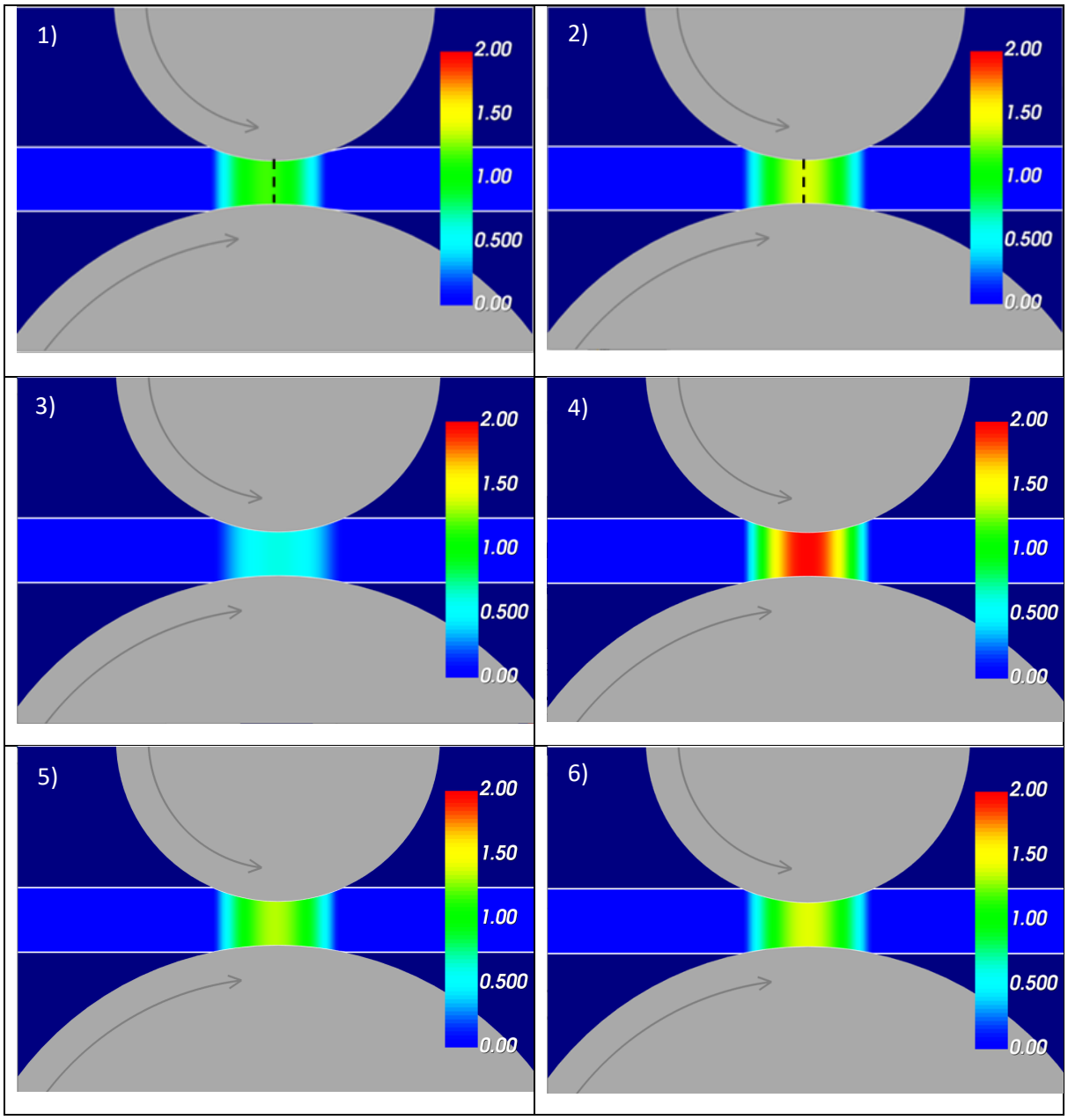

Figure 3: Three pairs of examples of nip pressure distribution; the material properties and the printing speed used in the simulations are given in Table 1, the dashed lines in images 1 and 2 stand for the position of the nip center

4. Conclusion remarks

Compression process in a printing nip is complex and highly dynamic. For an easy understanding of paper's response towards the compression from a rolling nip, a visualisation tool for the dynamic compression has been developed. This can be utilized to promote understanding and communication about complex dynamic processes. For instance, the impacts of the viscoelastic properties of the material as well as printing speed can be easily captured / perceived from the colour coded zone in the nip.

In the present work Maxwell model was used because of its simplicity. In this material model, a few assumptions were made as listed below.

The paper is a linear viscoelastic material, whose mechanical properties (both elastic and viscos components) remain constant during the compression, or independent of compression rate. For a paper material, its elastic modulus gradually increases with the increasing strain-rate as the mass density increases.

The compression is modest or within the elastic range of the paper, namely neither fibre nor its network structure is damaged during the compression.

The material distribution is uniform in x–y plane and in the thickness (z) direction. Variations of the paper structure can be ignored in the model.

With these assumptions in mind, the material model is probably most applicable to a paper having a single-ply fibre structure. For paper of multiply structure having different mass densities and viscoelastic properties or the densification effect is no negligible, a non-linear material model has to be considered which is beyond the scope of this work. Even though a simplified material model was used in the simulation, here Maxwell model, the concept of using visualisation as an aid for understanding and research is rather general. Extension of this framework to a more complex material model is more straight forward.

Acknowledgements

The project was financed by STFI:S INTRESSEFÖRENING.

References

BU TechWeb, n.d. *Scientific visualization software packages*. [online] Available at: <https://www.bu.edu/tech/support/research/training-consulting/online-tutorials/introduction-to-scientific-visualization-tutorial/software-packages/> [Accessed February 2022].

Hansen, C.D. and Johnson, C.R. eds., 2004. *Visualization handbook.* San Diego, CA: Academic Press.

Litvinov, V. and R. Farnood., 2010. Modeling of the compression of coated papers in a soft rolling nip. *Journal of Materials Science*, 45(1), pp. 216–226. https://doi.org/10.1007/s10853-009-3921-x.

Munzner, T., 2009. A nested model for visualization design and validation. *IEEE Transactions on Visualization and Compuer Graphics*, 15(6), pp 921–928. https://doi.org/10.1109/TVCG.2009.111.

Roylance, D., 2001. *Engineering viscoelasticity.* [pdf] Massachusetts Institute of Technology. Available at: <https://web.mit.edu/course/3/3.11/www/modules/visco.pdf> [Accessed February 2022].

Sperling, L.H., 1992. *Introduction to physical polymer science.* 2nd ed. London: Wiley Interscience.

Yang, L. 2020. Printing dynamics: nip pressure and its relationship with materials viscoelasticity, *Journal of Packaging Technology and Research*, 4(2), pp. 145–156. https://doi.org/10.1007/s41783-020-00091-z.

DOI 10.14622/Advances_48_2022_07

Evaluation of measurement methods for compression, re-swelling and material thickness through the embossing process of cardboard

Ulrike Kaeppeler[1,2], *Jennes Huenniger*[1,2] *and Lutz Engisch*[1,2]

[1] Leipzig University of Applied Science, Faculty of Media and information Science, Karl-Liebknecht-Str. 132, 04277 Leipzig

[2] iP[3] Leipzig – Institute for Printing, Processing and Packaging Leipzig, Karl-Liebknecht-Str. 132, 04277 Leipzig

E-mail: ulrike.kaeppeler@htwk-leipzig.de

Short abstract

The subject of the present study is the detection and measurement of the material thickness after embossing, the compressibility and the re-swelling on embossed board samples using various methods. Knowledge of these aspects is relevant for the production of high-quality embossed structures. One aspect is to achieve the highest possible deformation in the process, with little shrinkage even after the samples were pressure relieved. In addition to the forming effect, densification and the degree of re-swelling also play a decisive role in the quality of the product. Furthermore, it is important to gain such an understanding of the material in order to be able to model the material in FEM simulations. Studies on the forming behavior of paper and board are well known from the field of deep drawing. These experimental studies mainly look at the wrinkle distribution in the product. Other researchers have not yet found out which is the best method to analyze the thickness of the material after the sample has been relieved of force in order to obtain efficient and reliable results. Therefore, this study focuses on finding a suitable analysis method to detect material compaction and thus measure the different material thicknesses of embossed paperboard samples. In order to validate different analytical methods, they need to be tested experimentally. In addition, the results are related to the compressibility and the re-swelling after deflating the material. It was found that the material thickness within the embossing geometry can be measured most efficiently with a digital cross section. Furthermore, it can be assumed that the re-swelling is related to the degree of forming. So far, the compressibility in the embossing gap still differs from that of the single measurement.

Keywords: embossing, material compression, re-swelling

1. Introduction

1.1 Material

Embossing is used as optical and haptical effect for packaging such as cardboard folding boxes. For example, the embossing highlights a logo on folding boxes or braille letters on medical products. Embossing is an important part of print finishing. Especially with regard to the sustainability debate, embossing is a very sustainable finishing process without the use of additional raw materials such as foils, varnishes, etc.

Paper and cardboard are single- or multilayer fiber composites. Fibers generally consist of three main components: 40 % cellulose, 30 % hemicellulose and 20 % to 30 % lignin (Bayerl and Pichol, 1986; Ek, Gellerstedt and Henriksson, 2009).

These multiple layers of cardboard are not glued. The fibers are only linked together by intermolecular forces in form of hydrogen bonds (Radzanowski, 2017; Brenner, 2016).

The layers may have the same or varying compositions. Thus, it is one of the important aspects of material properties besides the bonding within the layers as well as the fibers (Blechschmidt, 2013). Because of this, different materials show different mechanical behavior during forming.

1.2 Process

During the embossing process, the material is shaped between the male and the female die. First, the roughness peaks of the fiber composite are equalized (Schaffrath and Göttsching, 1992). Then the compression of the fibers as well as the eliminations of hole structures follows until the complete compaction of the material. The pore volume decreases close to zero (Hauptmann, 2013).

The embossing process stretches the material. This is due to the fact that the projected area is always larger than the initial area, depending on the embossing height. Initially, the material withstands the stretching. Especially on the outside of the embossing, the impact of stretching is very high. In addition, there are many material tensions which are indicated by an uneven base surface after embossing. If the material is stretched too much, it cracks. Fibers remain connected via hydrogen bonds, but those forces decrease with increasing distance. If the material is stretched too much, the distance increases and the fiber structure breaks.

There are studies on deep drawing of cardboard but the analysis is focused on the wrinkle distribution. The differences between deep drawing and embossing are the lack of a blank holder in embossing, the dimensions are different and folding is undesirable in embossing (Meyer, 2015; Oehm, 2010; Wallmeier, 2018; Weber, 2017). To analyze crack formation during embossing, different methods of analysis such as coloring with safranin and with carbon, embedding and cross sections are examined.

The quality of the embossing depends among other things on the degree of shaping. Too little shaping leads to blurred contours. As the embossing path increases, the material becomes more compressed and the material thickness in the flanks get smaller. Too much shaping, though, leads to crack formation. These cracks are unwanted because they interfere with the appearance of the embossed product.

1.3 Compression and compression areas

During material forming, the cardboard is compressed between the male and female die. The remaining gap between the two tools determine the maximum material thickness at each embossing path. The more embossing path covered, the less gap is between the tools. If the distance between the tools falls below the material thickness in the initial state, the material is inevitably compressed. The degree of compressibility is material-specific.

In order to analyze different compression areas distributed over one embossing geometry, the test geometry truncated pyramid has proven to be useful. Due to the geometric conditions, the truncated pyramid can be divided into three areas of interest: Outer area, flank area, top area. Within the area, further parameters can be defined, which are described in chapter 2.3.

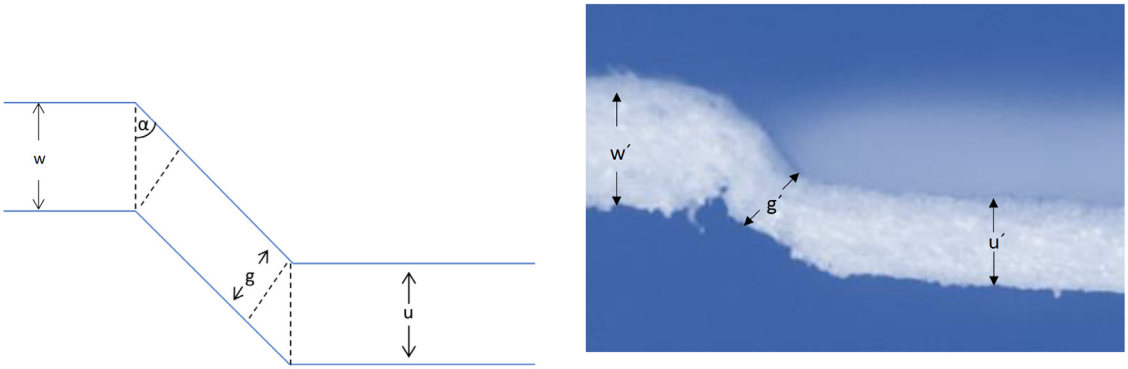

Figure 1: Measurement of material thickness at different compression areas

Figure 1 shows a cross section of an embossed cardboard. Three parameters describe the material thickness in each of the three areas.

w: Area outside the embossing geometry
g: Area within the flank of the embossing geometry
u: Area in top of the embossing geometry

From various specifications of tool, material and embossing path, the gap distances can be calculated according to Equations [1] and [2].

$$u = Element\ height - (Embossing\ path - Material\ thickness) \quad [1]$$

$$g = \sin(\propto) * u \quad [2]$$

The stress-strain behavior of paper and board in the tensile test shows that elastic and subsequent plastic deformation takes place until failure (Hauptmann, 2013). In case of the compression, the viscoelastic component has to be taken into account as well. Due to the re-swelling, the deformation of the material under load differs from the subsequent state after load release of the embossed sample.

1.4 Research questions

The resulting material thickness from the shaping processes has not been analyzed in depth so far. Knowledge of the distribution of material thickness within an embossing geometry is important for the understanding of the material behavior during the process. The material is formed three-dimensionally and compressed. The compression does not take place equally at all points. The material thickness is a characteristic value for the quality of the representation of the interaction properties, especially for the understanding of re-swelling processes.

A measurement of the material thickness according to DIN EN ISO 534 is obsolete for three-dimensional formed materials (Deutsches Institut für Normung, 2011). Three-dimensional shaping results in flanks, i.e. areas that are not parallel to the actual original cardboard grade. Thus, the measuring device should either have to be mounted at right angles to the surface of the flanks or this should be taken into account within the measuring analysis. Figure 2 shows the different measured values for measurements at right angles to the zero line and at right angles to the material surface. The gray sketch is the embossed material (truncated pyramid).

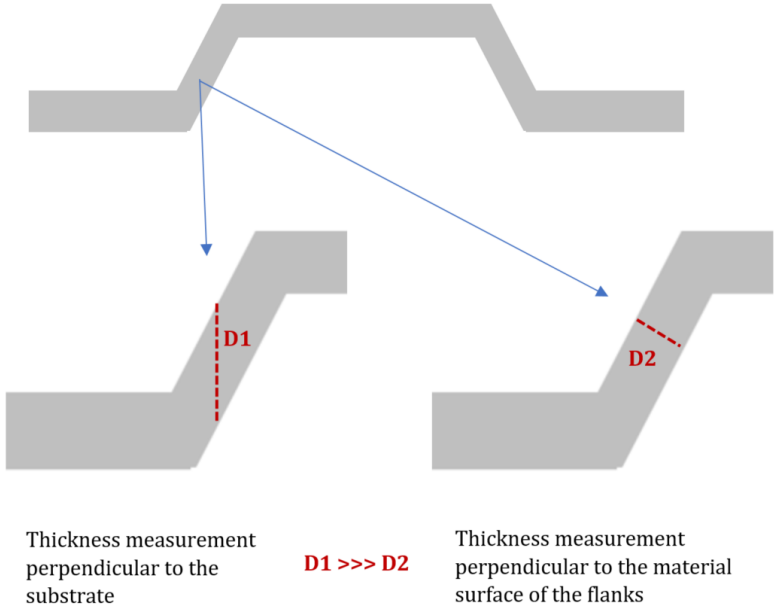

Figure 2: Comparison of the material thickness measurements in relation to the surface of the zero line and the material surface

1.5 Existing studies on the measurement of the material thickness of the embossed board sample after the embossing process after load release

There are some approaches for determining the material thickness of fiber composite materials. In a former study, the samples were placed between two pieces of metal and foam rubber and fixated with a Hofmann screw clamp. This clamp has two plano-parallel elements that can be shifted against each other. Thus, they are good to fix the sample in place. The rubber avoids the compression of the material due to internal forces (see Figure 3).

A sharp razor blade was used to create an almost artefact-free cross-section of the sample (Käppeler, 2019; Schuhmann, Hodes and Engisch, 2016). For this method it is not analyzed yet, if the samples get damaged through cutting. If so, for example, the measured material thickness by fanning out the sample could be higher than the real sample thickness.

In addition, another method known from botanical objects and microtome examinations was used. The samples were embedded in a block of different natural or synthetical resins or paraffin waxes (Schrödel, 2011; Scheuter, 1980). Schuhmann, Hodes and Engisch analyzed printed paper and used methacrylate- and epoxy-resins to prepare the samples. The paper samples were put in a hexagonal container. The samples were embedded in the resins and hardened by ultraviolet radiation. Afterwards, the block was fixed into a microtome cutter to produce thin microtome cuts (Schuhmann, Hodes and Engisch, 2016).

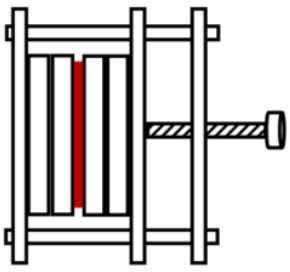

Figure 3: Method of the Hoffman screw clamp for preparing the cross sections (Käppeler, et al. 2020)

This method is quite laborious and time-consuming due to the small-scale embedding process. In addition, there is a high risk that the sample is not ideally vertical in the embedding or shift during the sample preparation. Then the sample would not be cut exactly perpendicular to the plane. Furthermore, it cannot be clarified whether the resins have an influence on the forming, for example due to penetration into the sample.

In both analytical methods, the material thicknesses of the samples would be measured with a microscope.

2. Materials and methods

2.1 Materials and embossing process

Cardboard is a typical material for folding boxes used for packaging products. The examined cardboard has three layers made from fibers. The three types of cardboard used are shown in Figure 4.

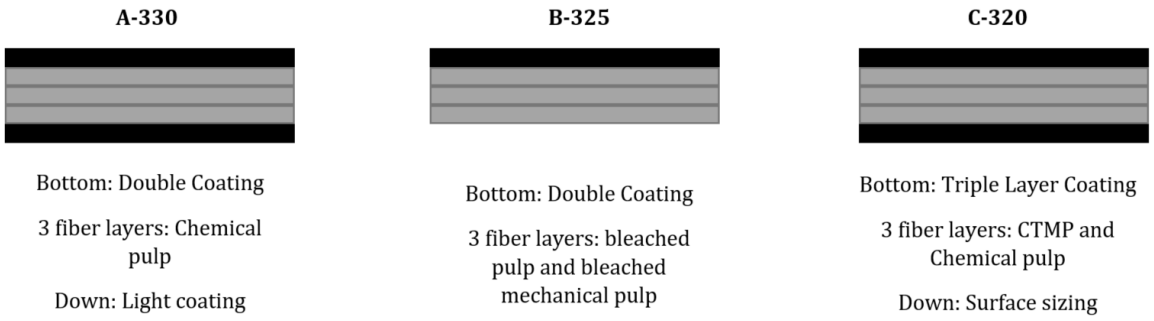

Figure 4: Three different types of cardboard used

The material thickness in the initial state is measured with a Frank thickness device (FRANK-PTI GmbH, Birkenau, Germany) according to DIN EN ISO 534. 10 samples per cardboard type are measured and the mean is reported with two-sided confidence interval (alpha = 5 %, *t*-distribution).

A truncated pyramid is used as embossing geometry. The edge length of the truncated pyramid is 5 mm. The angles are 45° and the height is approximately 620 µm. The geometry is shown in Figure 5. Due to the dimensions and angles, the geometry is designated with the abbreviation PS45-5.

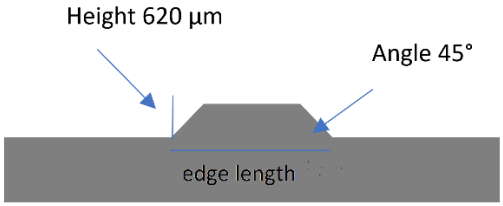

Figure 5: Schematic dimensions of the embossing geometry (PS45-5)

In the process, the embossing tools are moved into each other by two guided parallel tools. The material in between is pushed into the mold, where it is shaped and pressed (see Figure 6). The process ends when no change of the embossing path is longer detected while the force still increases. The experiments were carried out with a Tensile-Compression Testing- Machine (Zwick Roell, Ulm, Germany).

Figure 6: Schematic representation of the embossing process (flat embossing, relief embossing) – left side: wide spacing of the embossing tools, no material contact; middle: first material contact without shaping; right: material shaping, embossing tools move into each other

2.2 Compression behavior

The approaches were carried out on three different cardboards shown in Figure 4. The thickness of the samples was measured in the initial state according to DIN EN ISO 534. The samples were subsequently compressed in a compression test rig (Käppeler, et al, 2022). This was used to determine the compressibility of the material under maximum load.

The three materials were compressed. From the geometric considerations it can be seen that compression of the material occurs during the embossing test, particularly in the flanks of the truncated pyramid. At the end of the process, the distance between the flanks is less than the actual material thickness; consequently, the material must have been compressed. The end of the process is reached when the compression force increases exponentially, but almost no more increase in the embossing path can be observed. This process end differs from carton type to carton type. A correlation between material compressibility, distance in the embossing gap of the flanks and process end is still to be found.

The compression behavior of the material is determined by an equivalent test. For this purpose, a circular punch with a diameter of 10 mm is pressed into the material against a plane-parallel plate. It is measured how far and with how much force the punch can be pressed into the material. The compression process ends when the material is completely compressed. Complete compression is shown in the path–force-diagram by an exponentially increasing force with hardly any increasing compression displacement.

After compression is completed, the sample is relieved. The material in the relieved state swells back. This means that the compressing depth in the relieved state is lower than pressure relieved. Therefore, the compressed contours in the relieved state are less pronounced, i.e. less sharp and rich in contours, than in the loaded state within the process. This is measured by imaging the sample with a Keyence 3D VR-3000 Macroscope (Keyence, Neu-Isenburg, Germany) stripe light macroscope. In the virtual cross-section through the sample, the resulting compression indentation depth is determined.

2.3 Compression areas within the embossing process

A scale sketch was created to gain a better understanding of the process. Figure 7 shows the male and the female die as well as the material in between. The sketch shows the end of the process, i.e. when the forming end is reached. The shaded sections show the areas where the material is compressed. The compression range depends on the material and its specific compressibility. The material is compressed in the top area, but especially in the flanks.

The following characteristic values are measured:

(1) The embossing path: The distance covered by the machine from the start time, when the pre-force is reached until the maximum force is reached.
(2) Tool gap flank: The distance between the male and the female die in the area of the flanks.
(3) Tool gap inside: The distance between the male and the female die in the area of the top.
(4) Material thickness: The original material thickness of the board without forming.

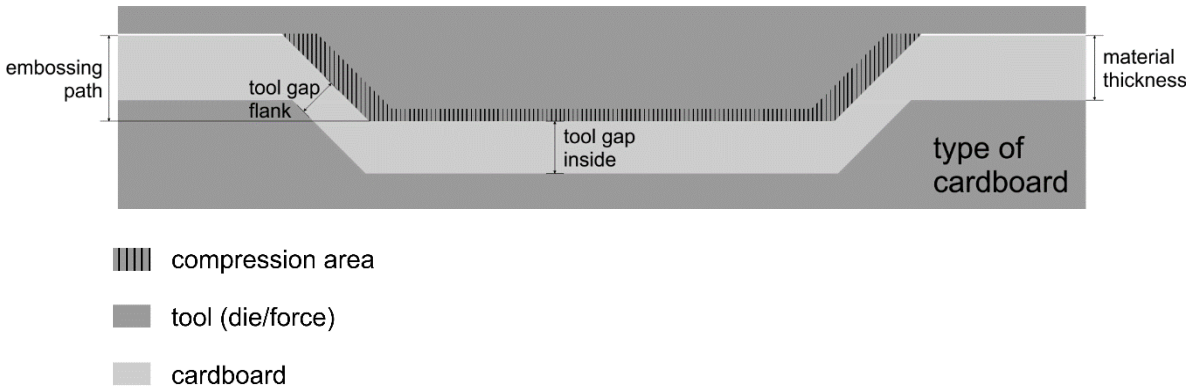

Figure 7: Effect Pairing analysis for calculating the material thickness under load (Hünniger, 2020)

2.4 Material re-swelling

A test method was developed for investigating the re-swelling behavior of the board materials. The process is shown in Figure 8. For this purpose, the compression test tool is pressed into the material. The force and the associated compression path are detected. The resulting impression is recorded with a Keyence VR-3000 macroscope (Keyence, Neu-Isenburg, Germany). A virtual cross-section is placed in the center of the circular indentation and the remaining indentation depth is measured.

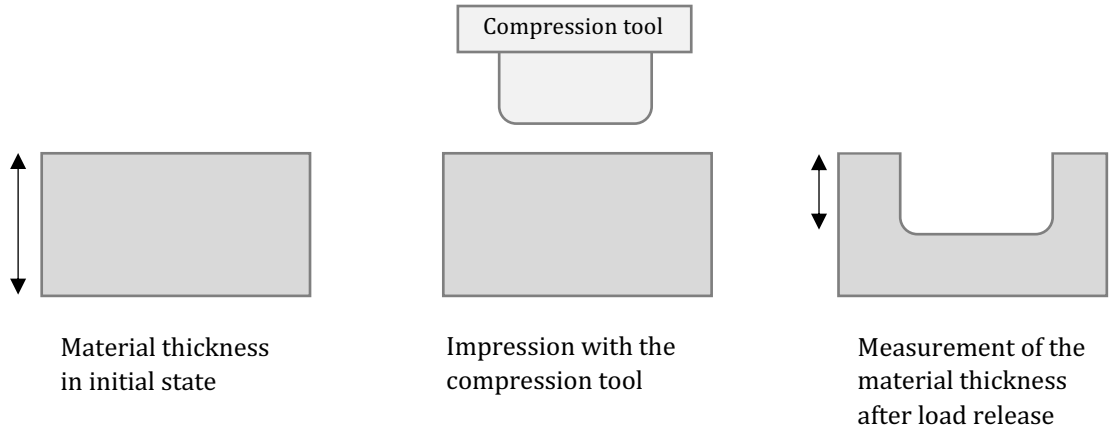

Figure 8: Test sequence for measuring the indentation depth after compression of the material

2.5 Methodology for determining the material thickness of embossed samples after load release

2.5.1 Real cross sections

Cross-sections are to be created in order to measure the material thicknesses in the material cross-section. Similar to the described sample cutting with the hose clamps, the samples were cut by using a cutting mat and a sharp razor blade (Figure 9). The results of these two cutting methods do not differ significantly. Therefore, the cutting method without any clamps was used for the following experiments.

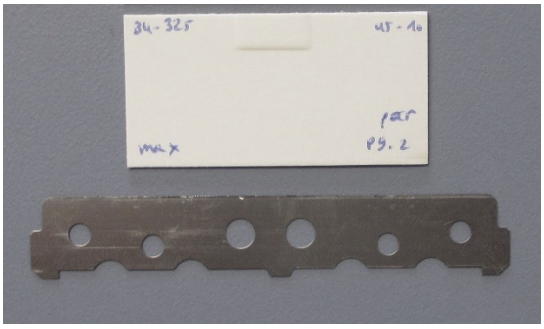

Figure 9: Sharp razor blade for making cuts without clamping

The cross-sections were examined with a macroscope measurement device Keyence VR-3000 (Keyence Deutschland GmbH, Neu-Isenburg, Germany). The measurement technique is stripe light projection which can be used to create three-dimensional surface scans. The material thickness of the samples was detected at the cross-section of the embossed samples.

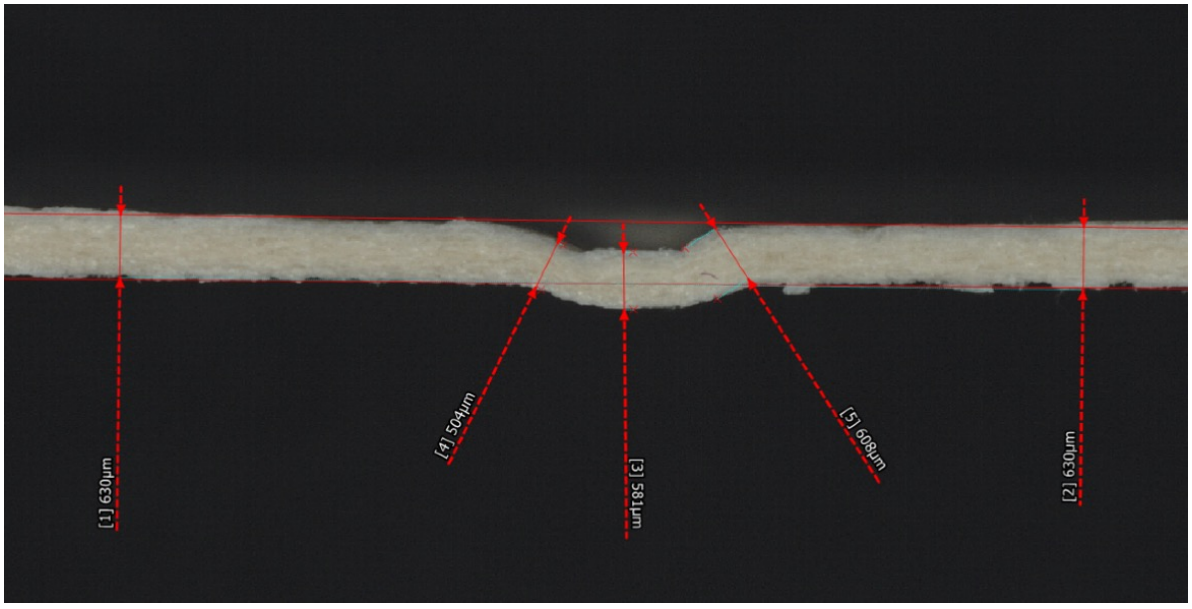

Figure 10: Measurement of material thickness in cross section with embossing geometry PS45-5

Figure 10 shows the results of a measured sample. The positions [1] and [2] were not compressed during the embossing process, because they are located outside the embossing element and therefore present the original material thickness. The positions [3] in the center and [4]; [5] in the flank areas were compressed during the embossing process and show the compressed areas after load release of the sample.

2.5.2 Virtual cross section

To combine the measurement results of the upper and the bottom side of embossed samples, the analysis tool “Measurement Comparision” is used. The device detects the surface topographies of the samples (Figure 11, left) and the data is visualized as a 3D-plot (Figure 11, middle).

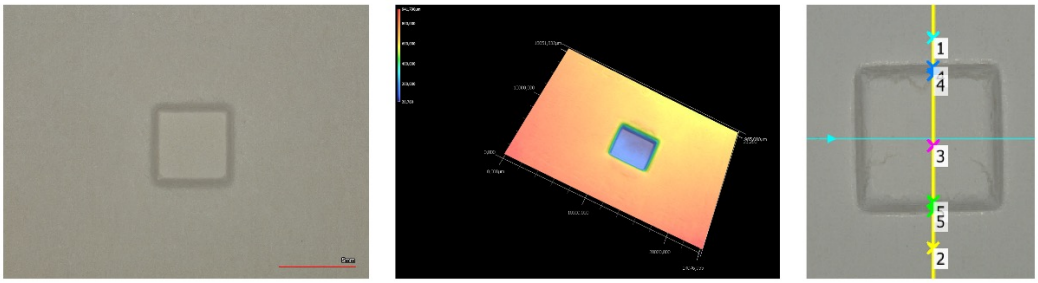

Figure 11: Measured 3D-topography of the samples and the virtual cross sections placed in the middle of the sample

The measurement data of the upper and the bottom side are positioned relative to each other so that the measured material thickness of the cross-section analysis (Figure 11) is achieved outside the embossing element (Figure 12).

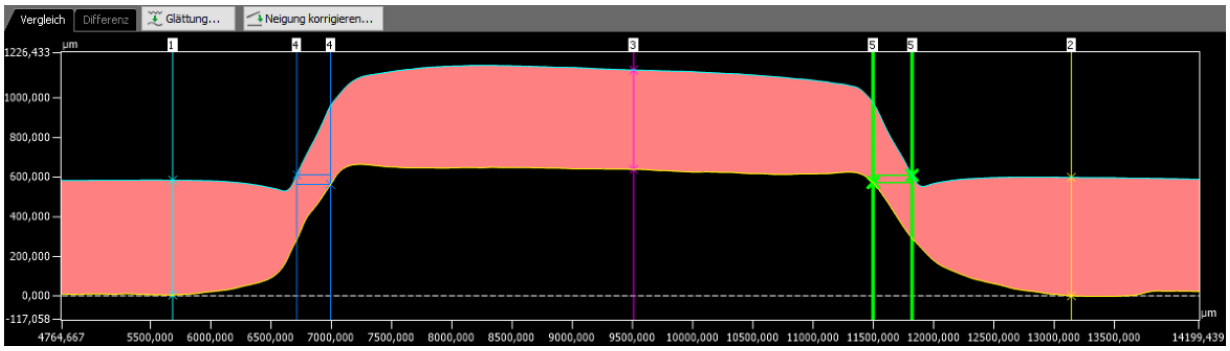

Figure 12: Digital measurement comparison for determining the material thickness of an embossed cardboard sample (PS45-5)

To calculate the material thickness in the embossing area, the cross-sections were put above each other with a definite gap (Figure 12, point 1). This gap was considered as a region far off the embossing area where no deformation took place. Thus, it represents the original thickness of the sample. All the other gap sizes between the upper and the bottom sample cross section were related to that present gap size. Besides the original material thickness (Figure 12, points 1 and 2), the thickness of the middle of the element (Figure 12, point 3) as well as of the flanks (Figure 12, points 4 and 5) were measured.

2.5.3 CT-cross section

Another method is the analysis of the compression with computer tomography (CT) measurements.

The following CT-parameters were chosen: 1 800 pictures, 4 ms measuring time for one shot, temperature 23 °C, current 120 ampere, power 80 volt, 4.8 µm voxel size. Figure 13 shows a cross-section within the embossing geometry of several samples. The samples were all of the same material; they just differ in the chosen embossing paths.

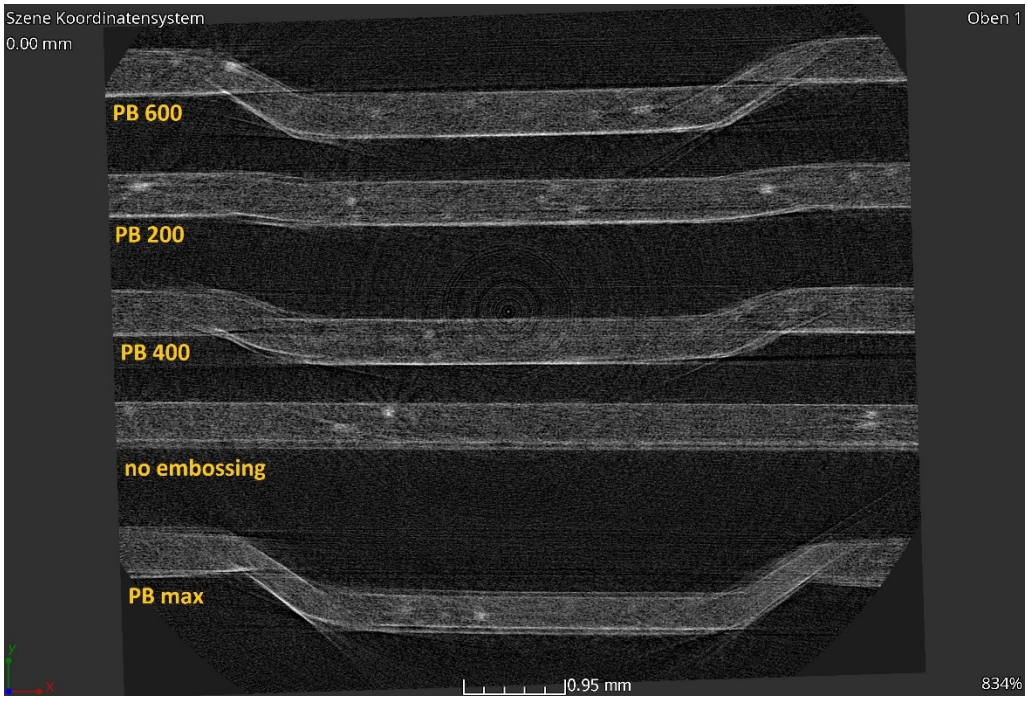

Figure 13: X-ray CT measurement of embossed board samples with different embossing paths, embossing geometry PS45-5

For the first sample from above (PB600) an embossing path of 600 µm was set, for the next one 200 µm (PB200), then 400 µm (PB400). Sample "no embossing" is without embossing and the last is one with maximum embossing path until total compression (approximately 700 µm).

The different material compression of the samples within the different embossing paths is well shown. The higher the degree of embossing is, the stronger is the compression of the material. The degree of embossing is defined by the embossing path. Furthermore, not all areas within the embossing area are compressed to the same extent. The detailed thicknesses of the samples were measured with the software ImageJ.

3. Results and discussion

3.1 Material thickness initial state

The material thickness of the boards was measured. The measurement results are shown in Figure 16 on the right hand side.

3.2 Compression behavior of the paperboards

Diagram in Figure 14 shows the percentage of compressibility of the three board materials. Material A-330 shows a compressibility of nearby 57 %, materials B-325 and C-320 over 60 %. The compressibility is thus related to the material thickness. Thus, the compressibility data are comparable. The compressibility of materials B-325 and C-320 are similar, while A-330 differs significantly.

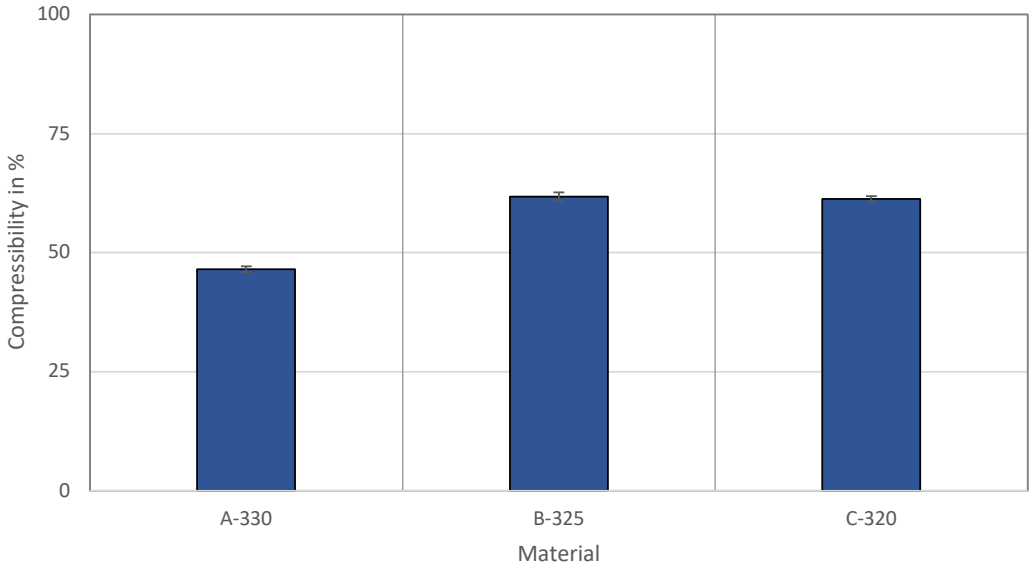

Figure 14: Comparison of compressibility of materials A-330, B-325 and C-320

3.3 Material thickness of embossed samples under pressure

Figure 15 shows the 3 materials under load at maximum compression. The material is thus compressed to the maximum. The material thicknesses in the three areas of interest are indicated in each case.

It is noticeable that the ratio between embossing path and material thickness is higher for cardboard A-330 than for the two cardboard B-325 and C-320. As shown in Figure 14, Material A-330 is less compressible. The material thickness in the flanks is higher compared to the other two materials in relation to the respective material thickness.

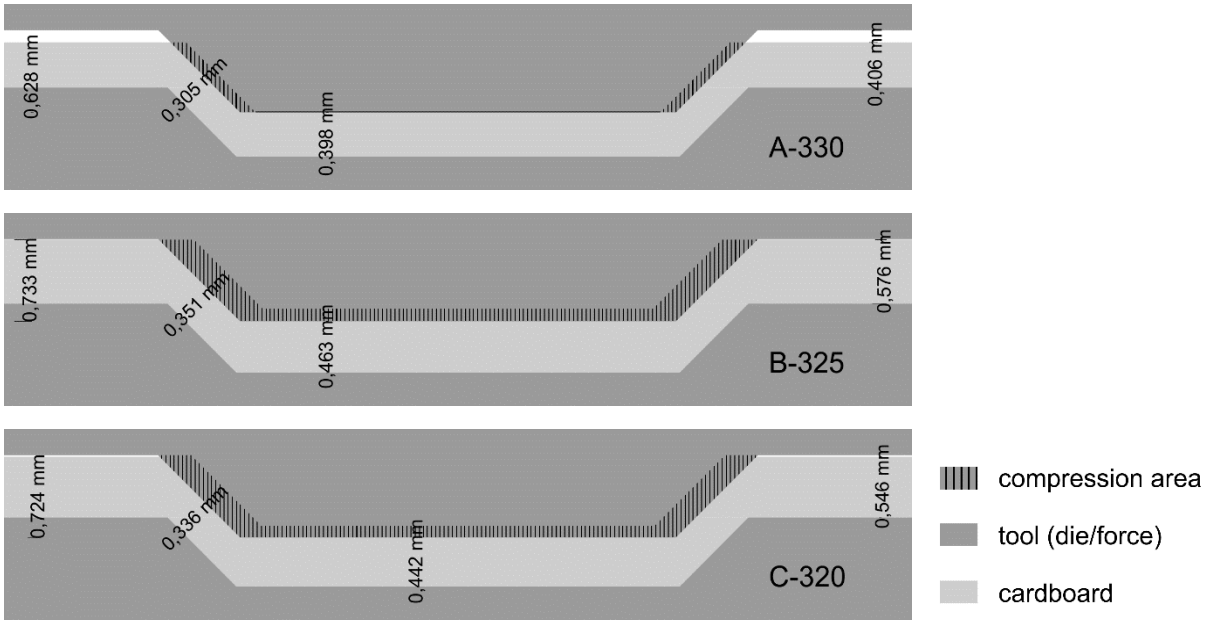

Figure 15: Effect Pairing analysis for calculating the material thickness under load for the used card materials A-330, B-325 and C-320

3.4 Re-swelling of the cardboards

It can be seen that the compressed material swells back. The depth of the indentation is thus greater in the loaded state than after load release. Figure 16 schematically shows the material behavior.

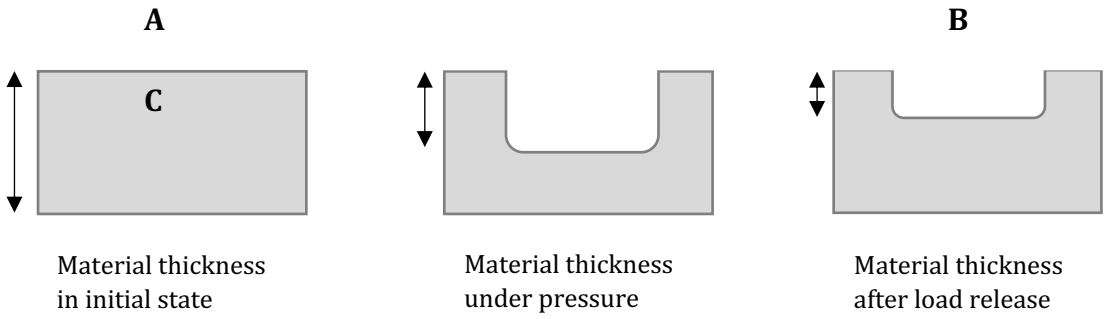

Figure 16: Material behavior re-swelling

Figure 17 shows an example of how the re-swelling affects the compression result. The compressing depth under load is significantly higher than the compression height after load release. In comparison, the resulting compression height is approximately 50 % of the compression height under load. In relation to the material thickness in the initial state, this results in a re-swelling of about 25 %.

These results show that the re-swelling has a decisive influence on the material thickness within the compression geometry. Furthermore, it influences the embossing quality, i.e. how good the impression is.

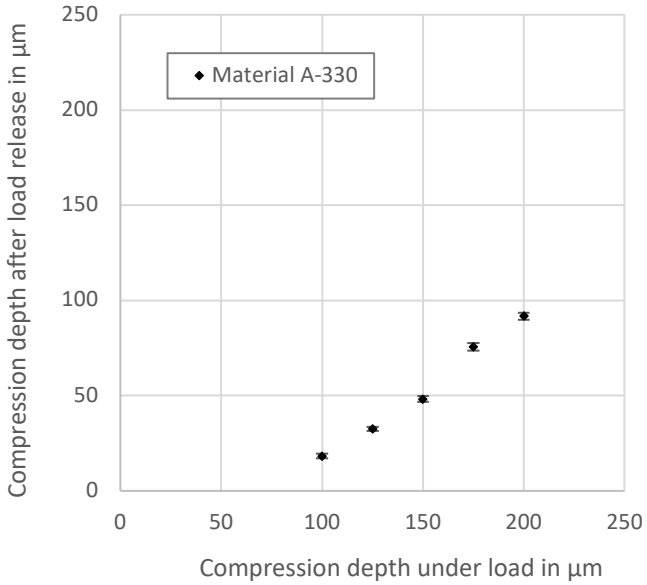

Figure 17: Comparison of the indentation depth of the compressibility stamp in the carton in the loaded state and after load release

3.5 Material thickness of the cardboard materials after load release

Figure 18 compares the different measuring methods for the material thickness in different areas of the samples after maximum compression.

It is obvious that the sample thickness on the right and left side, far off the embossing area, is the highest.

The three measurement methods *real cross section, virtual cross section* and *CTcross sections* show different results. It is noticeable that the material thicknesses seem to be highest for the real cross sections. The difference to the two preparation methods virtual cross-section and CT cross-section is about 100 µm. Both methods show sample thicknesses of about 400 µm. These values seem more realistic, compared with the material thickness of the material in uncompressed state (402 µm). Regarding the other areas, the material thickness measured with the CT cross section is always higher than the calculated material thickness with the virtual cross-section.

The measurement values of the real cross section and the virtual cross-section differ within factor 1.2 up to 1.5. The values in the highly compressed flanks differ even more (up to 2.0).

The CT-cross sections show that the material thickness in the area right and left beside the embossing area are uncompressed after the process. The thickness of the material is approximately 400 µm. In the middle (top of the truncated pyramid), the sample thickness is about 335 µm. Thus, in this area the material was compressed within the embossing process.

The highest compression is in the flanks of the truncated pyramid with a material thickness of approximately 250 µm.

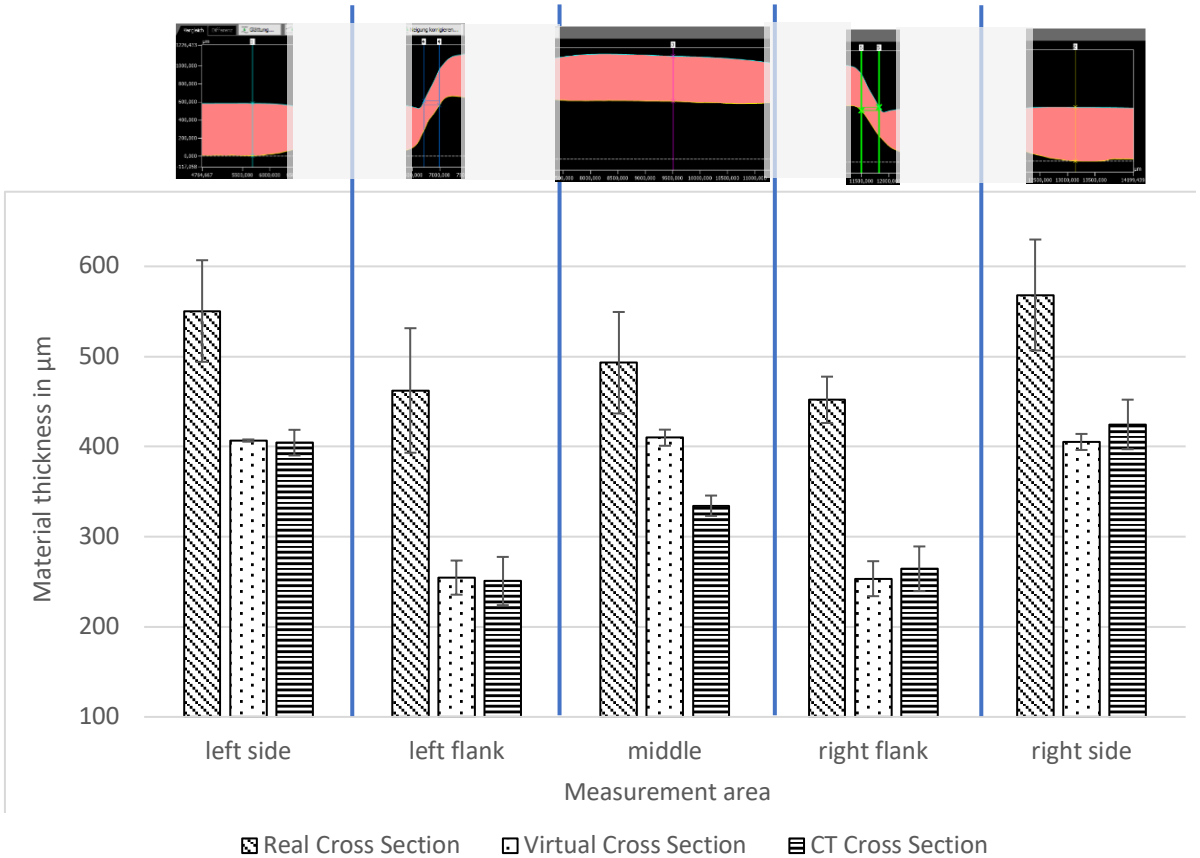

Figure 18: Comparison of the material thicknesses measured with different methods, material A-330 and assignment of the measurement data to the areas within the embossing

It can be assumed that cutting the samples physically changes the material thickness due to material damage like a delamination of the layers or the plucking of fibers. In addition, it is suspected that the cross-sectional images vary due to misplacement and mismeasurement. The images should be optimized with a modified specimen preparation and a comparative measurement procedure. Therefore, the contactless measurement methods should be preferred at the moment.

Comparing the contactless methods, the values are roughly the same. The differences between them are not significant (two sided *t*-test, $p = 0.975$) except in the middle of the embossing area.

Regarding results and effort, the measurement comparison has equivalent results with less effort in comparison to the CT-cross section.

3.6 Relationship compression within the compression test, compression within the embossing geometry and after load release

Figure 19 shows the material thicknesses for different loading scenarios. The material thickness in the initial state is highest at about 400 µm.

The material can be compressed to about 220 µm during compression and expands back to about 300 µm during unloading. There is thus de-compression of the material during compression.

During the embossing process, the material is also formed and compressed in the embossing nip. After unloading, the compression is also less than in the compression test alone. This suggests that tensions occur in the process that hinder perfect re-swelling. However, this would need to be investigated further.

It must always be taken into account that the forming process during coining is much more complex than when determining material compression. Energy is used not only for compression, but also for tensile and shear stresses and layer displacements. The material behavior needs to be further investigated.

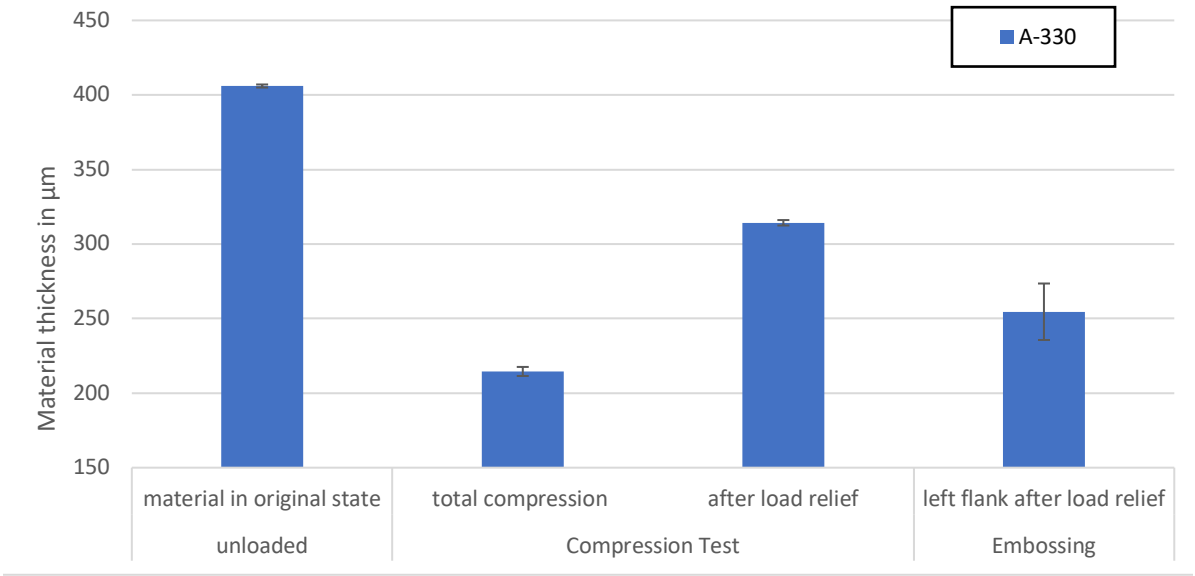

Figure 19: Comparison of the material thicknesses by different loading scenarios

4. Conclusion

The effect pairing analysis shows that compression occurs within the embossing geometry during the process. In addition, it can be seen within which partial areas compression occurs. It also allows conclusions to be drawn as to which areas are subject to particularly high or low compression.

The highest compression occurs in the area of the flanks in the case of the truncated pyramid embossing geometry.

Due to the three-dimensional forming, the virtual cross-section proved to be the most suitable substitute thickness measurement method.

The material thickness at full compression in the embossing gap and the substitute test method produce deviating results. This must be checked again.

Initial findings suggest that there tends to be less swelling back at a higher degree of forming. However, this would have to be investigated more extensively.

Acknowledgements

This work was supported by the European Social Fund and the Federal Ministry of Economic Affairs and Energy (BMWI) by funding the 100382159 research project ''SmartKMU".
The authors thank Thomas Wagner of Fraunhofer IWMS for the CT-measurements.

References

Bayerl, G. and Pichol, K., 1986. *Papier: Produkt aus Lumpen, Holz und Wasser*. Reinbek bei Hamburg: Rowohlt-Taschenbuch Verlag.

Blechschmidt, J., 2013. *Taschenbuch der Papiertechnik*. 2nd ed. München: Hanser Verlag.

Brenner, T., 2016. *Anwendung von Ultraschall zur Verbesserung der Papierfestigkeit durch Beeinflussung der Fasermorphologie*. Dresden: TU Dresden, Institut für Naturstofftechnik, Professur für Papiertechnik.

Deutsches Institut für Normung, 2011. *DIN EN ISO 534 Papier und Pappe – Bestimmung der Dicke, der Dichte und des spezifischen Volumens (ISO 534:2011)*. Berlin: DIN.

Ek, M., Gellerstedt, G. and Henriksson, G. eds., 2009. *Pulp and paper chemistry and technology: volume 1 – wood chemistry and wood biotechnology.* Berlin: de Gruyter.

Hauptmann, M., 2013. *Die gezielte Prozessführung und Möglichkeiten zur Prozessüberwachung beim mehrdimensionalen Umformen von Karton durch Ziehen*. Dr.-Ing. Dissertation. Technische Universität Dresden.

Hünniger, J., 2020. *Charakterisierung des Umformverhaltens von Karton im Reliefprägeprozess*. ZINT Doktorandenkolloquium.

Käppeler, U., 2019 *Charakterisierung physikalisch-chemischer Veränderungen im Karton im ultraschallunterstützten Prägeprozess*. Dissertation. Hochschule für Technik, Wirtschaft und Kultur Leipzig.

Käppeler, U., Hünniger, J., Hofmann, A., Berlich, A. and Engisch, L., 2020. Thermal influence on the mechanical properties of cardboard during an ultrasonic-assisted embossing process. *BioResources,* 15(3), pp. 5110–5121. https://doi.org/10.15376/biores.15.3.5110-5121.

Käppeler, U., Schneller, K., Wallburg, F., Engisch, L. and Schoenfelder, S., 2022. (in press) Analysis of the compression behavior of different cardboard materials during embossing. In: *Tagungsband Nachwuchswissenschaftler*Innen Konferenz 2022*. Brandenburg, 11–13 May 2022. Technischen Hochschule Brandenburg.

Meyer, M., 2015. *Entwicklung und Umsetzung eines Moduls zur Inline-Faltenauswertung an Kartonziehteilen.* Diplomarbeit. Technische Universität Dresden.

Oehm, L., 2010. *Untersuchung des Einlaufverhaltens beim Tiefziehen von Papier und Karton*. Studienarbeit. Technische Universität Dresden.

Radzanowski, G., 2017. *Untersuchungen zu Strukturveränderungen in Karton im ultraschallunterstützten Prägeprozess*. Master thesis. Hochschule für Technik, Wirtschaft und Kultur Leipzig.

Schaffrath, H.-J. and Göttsching, L., 1992. Modellierung der Kompression von Papier in z-Richtung bei niedriger Flächenpressung. *Das Papier,* 46(7), pp. 350–355.

Schrödel, A., 2011. Schnittherstellung mit dem Mikrotom. *Biologie in unserer Zeit*, 41(6), p. 368. https://doi.org/10.1002/biuz.201190099.

Schuhmann, K., Hodes, A. and Engisch, L., 2016. Migrations- und Penetrationsprozesse im Druckprozess, Charakterisierung von Druckfarben, Papieren und Druckproben im Querschnitt. Deutsch. *Wochenblatt für Papierfabrikation – Fachzeitschrift für die Papier-, Pappen- und Zellstoffindustrie*, 30 November 2016. pp. 742–747.

Wallmeier, M., 2018. *Experimental and simulative process analysis of deep drawing of paperboard*. Dr.-Ing. Dissertation. Technische Universität Dresden.

Weber, P., 2017. *Entwicklung einer grafischen Benutzeroberfläche zur Erprobung von Wechselwirkungen zwischen den Prozessparametern des Tiefziehprozesses*. Studienarbeit. Technische Universität Dresden.

DOI 10.14622/Advances_48_2022_20

Optimization of PEDOT:PSS layers for hole transporting layers of organic photodetectors

Tomáš Syrový[1], František Josefík[2], Lucie Syrová[1], Ignasi Burgués Ceballos[3], Petr Janíček[4], Jhonatan Rodriguez Pereira[5], Lubomír Kubáč[2] and Laura López Mir[3]

[1] Department of Graphic Arts and Photophysics, Faculty of Chemical Technology, University of Pardubice, Technological Pavilion Doubravice 41, 53353 Pardubice, Czech Republic

[2] Center for Organic Chemistry s.r.o., Rybitví 296, 53354 Rybitví, Czech Republic

[3] Eurecat, Av. Ernest Lluch 36, 08302 Mataró, Spain

[4] Institute of Applied Physics and Mathematics, Faculty of Chemical Technology, University of Pardubice, Studentská 95, 53210 Pardubice, Czech Republic

[5] Center of Materials and Nanotechnologies, Faculty of Chemical Technology, University of Pardubice, Cs. Legií square 565, 53002 Pardubice, Czech Republic

E-mail: tomas.syrovy@upce.cz

Short abstract

The study focuses on the optimization of PEDOT:PSS ink for the preparation of a hole transport layer. The ink was developed for the spiral bar coating technique and for subsequent organic photodetector preparation. In this study, the effect of various variables such as secondary dopant, surfactant, PEDOT:PSS complex ratio, and ink composition on selected characteristics such as conductivity, work function, charge carrier mobility, etc. is demonstrated.

Keywords: PEDOT:PSS, secondary dopant, hole transport layer, organic photodetectors, conductivity

1. Introduction

Conducting polymers are one of the most commonly used materials in printed or organic electronics. They can be used in a wide range of functional structures, such as photovoltaic cells, organic electrochemical transistor (OECT), organic field effect transistors (OFET), electroluminescent displays, and others. Conducting polymers can be used where their properties – semiconductivity and transparency are beneficial as in the case of hole transport layer (HTL). This group of conductive polymers includes, the poly(3,4-ethylenedioxythiophene) polystyrene sulfonate (PEDOT:PSS), which is often used in the field of organic photovoltaics (OPV) or organic photodetectors (OPD) for either HTL preparation or transparent conductive layer (TCL). In the research of PEDOT:PSS-based inks for the OPD field, our study is directed to develop an ink for the spiral bar coating technique for the preparation of PEDOT:PSS HTL and TCL layers.

OPD, similar to conventional OPV, consists of several layers – TCL, electron transport layer (ETL), photoactive layer (PAL), HTL, and top electrode (Figure 1). All layers have a significant effect on the performance of OPD. In our study, we focused specifically on optimizing and characterization of the HTL layer as one of the components of the OPD. In general, for optimal OPD performance, parameters such as high charge carrier mobility of holes are required for HTL to ensure efficient and selective hole transport into the PAL layer. Furthermore, an optimum value of the work function (WF) of the PEDOT:PSS layer is needed, which is optimized in its value with respect to the preceding and following layers. Last but not least, relatively high conductivity of the PEDOT:PSS layers is required, which will contribute positively to the low internal resistance of the OPD. In addition to the physical parameters mentioned above, high homogeneity of the layers, with no craters/pinholes present, and low thickness are also important. For the preparation of TCLs

based on PEDOT:PSS, high conductivity of the layers and high transparency and homogeneity of the layers are important. The aforementioned parameters can be modified by different approaches, especially by modifying the ink composition but also by choosing specific conditions for the synthesis of the PEDOT:PSS or by selection of complex ratios, where PSS- serves as the primary doping counterion.

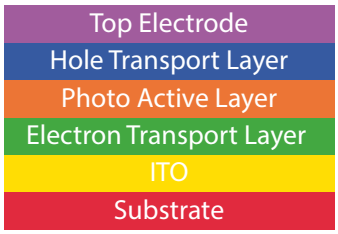

Figure 1: Schematic cross section of the layers structure of OPD, Indium Tin Oxide (ITO)

Several studies in the literature have been focused on determining the effect of secondary dopants on the conductivity of the PEDOT:PSS layer. It has been found that PEDOT:PSS layers additionally treated with ethylene glycol exhibited conductivity up to 1 418 S/cm, which has been attributed to the removal of some PSS^- from PEDOT:PSS layers (Kim, et al., 2011). Ouyang (2013) published that PEDOT:PSS film can reach 3 000 S/cm when post-treated with sulfuric acid. Ouyang, et al. (2004) achieved conductivities of 200 S/cm and 143 S/cm using secondary dopants ethylene glycol and dimethyl sulfoxide, respectively, which they attributed to increased interaction between the chains. When ethylene glycol was used as a secondary dopant, a conductivity of 160 S/cm was determined by Ouyang, et al. (2005). This was attributed to conformational changes. In another study, the authors obtained a conductivity of 966 S/cm, due to the addition of dimethylsulfoxide (DMSO) (Gasiorowski, et al., 2013). Kim, et al. (2002) added tetrahydrofuran to PEDOT:PSS which gave a specific conductance of 4 S/cm, 30 S/cm using dimethylformamide, and 80 S/cm using DMSO. Increases in conductivity up to 48 S/cm attributed to morphological changes caused by various secondary solvents were published by Jönsson, et al. (2003). There are some new approaches to doping or posttreatment of PEDOT:PSS layers, where Khasim, et al. (2022) published posttreatment by camphor sulphonic acid, resulting in 1 826 S/cm. Tang, et al. (2020) used for secondary doping various oxoammonium salts (TEMPO+X–) which enhanced conductivity and allowed to tune work function of PEDOT:PSS layers. Mineral acids were used by Zhang, et al. (2020) into PEDOT:PSS ink formulations resulting to high conductivity up to 2 244 S/cm.

The aim of our study is to investigate ink for the preparation of the HTL layer for the OPD. The investigated inks were prepared from synthesized PEDOT:PSS dispersions with different ratios, ranging from the 1:1 to the 1:5 complex ratio. The composition and other properties of the inks were modified by various solvents, which served as secondary dopants and by surfactants, which enabled high-quality wetting of the printing substrate or the underlying film.

2. Materials and methods

In the study, layers of the PEDOT:PSS conductive polymer were prepared from its modified water-based dispersions. PEDOT:PSS dispersions synthesized with complex ratios of 1:1, 1:1.4, 1:2.5, 1:3.5 and 1:5 were used to prepare the layers. Spiral bar coating technique (TQC AB3120) and corona (Alhbrandt) treated PET substrates (Melinex ST506 125 µm or 175 µm) substrate were used for layers fabrication.

In the case of experiments where the effect of solvents on the electrical conductivity of PEDOT:PSS layers was studied, inks were prepared using a PEDOT:PSS 1:2.5 pristine dispersion with a dry solid content of 0.8 wt.%. Secondary dopant (5 wt.%) was added dropwise to the dispersion while stirring with a magnetic stirrer at 600 RPM. Stirring was carried out for 6 hours at 600 RPM. The prepared ink formulations were

filtered through a polytetrafluoroethylene (PTFE) syringe filter (0.45 μm). The solvents used as secondary dopant included the glycol family, amides, and some other aprotic solvents with high dielectric constants up to 180 (Table 1).

Table 1: Types of solvents used as secondary dopants of PEDOT:PSS 1:2.5 layers

Secondary dopant SD #	Sample
Pristine dispersion	Pristine dispersion
SD 1	Amide I
SD 2	Amide II
SD 3	Amide III
SD 4	Amide IV
SD 5	DMSO
SD 6	Glycol I - EG
SD 7	Glycol II
SD 8	Glycol III
SD 9	Organic amine
SD 10	Sulfone I

In the case of the study of the effect of surfactants on the conductivity of layers, the formulations consisted of a pristine dispersion of PEDOT:PSS 1:2.5, 5 wt.% ethylene glycol as a secondary dopant and 0.5 wt.% surfactant (Table 2).

Table 2: Types of surfactant for the improvement of the surface tension of PEDOT:PSS 1:2.5 inks

Surfactant Surf #	Chemical type of surfactant
Pristine dispersion	Pristine dispersion
Surf 1	acetylenic diol
Surf 2	polyether siloxanecopolymer
Surf 3	polyether-modified polydimethylsiloxane
Surf 4	polyethylene glycol phenylether I
Surf 5	polyethylene glycol phenylether II
Surf 6	polyoxyethylene alkyl ether
Surf 7	polyoxyethylene sorbitan oleate
Surf 8	siloxane-based gemini surfactant
Surf 9	tetramethyl decynediol

In the study of the influence of secondary dopant on the conductivity and WF of PEDOT:PSS layers, 5 different solvents were studied (Table3). Ink based on PEDOT:PSS 1:1.4 dispersion consisted of 0.1 wt.% Surf 5, 10 wt.% 2-propanol and 5 wt.% solvents.

For all experiments, inks were coated with an automated spiral bar coater (50 μm spiral bar) at a speed of 100 mm/s. The deposited layers were dried first at 95 °C for 10 min, then at 120 °C for 30 min in a Memmert UF75 hot-air oven.

The electrical properties of PEDOT:PSS layers were measured using the four-point method (digital multimeter Rigol DMM 3068 6 ½) at laboratory temperature in an air-conditioned laboratory at 20 °C and 35 % relative humidity. Geometrical characteristics of the measured samples were determined by optical

microscopy (Nikon). The thickness of the prepared layers was measured by mechanical profilometry (KLA Tencor P-7). UV-VIS spectra were measured on a Specord 210 UV-VIS spectrophotometer.

Table 3: Types of secondary doping solvents for improving work function and conductivity of PEDOT:PSS 1:2.5 layers

Secondary dopant SD #	Sample
Pristine dispersion	Pristine dispersion
SD6	Glycol I
SD1	AMIDE I
SD11	AMIDE V
SD12	AMIDE VI
SD13	organic acid

The work function was determined by ultraviolet photoemission spectroscopy (UPS) performed in an UHV apparatus (ESCA 2SR, Scienta-Omicron). XPS spectra were determined at X-ray photoelectron spectroscope (ESCA 2SR, Scienta Omicron).

3. Results and discussion

3.1 Influence of the type of secondary dopant on PEDOT:PSS conductivity

The influence of secondary doping solvents on the conductivity of layers was investigated in the first part of the study. In general, the influence of the solvents can be evaluated in terms of better/worse morphology adjustment of the PEDOT:PSS layer compared to the condition of setting the layer for pristine dispersion. The addition of given secondary dopants often improves the conductivity as well. In some cases, conductivity improvements of up to 3 orders of magnitude are observed. In the experiments, 5 wt% of secondary dopant was added to the pristine dispersion based on our previous experience. In total, 10 different solvents were compared, including a pristine PEDOT:PSS 1:2.5 dispersion.

The amide solvent group has a decreasing value in the terms of permittivity in row Amide I to Amide IV. The overall decreasing trend in the series from Amide I to Amide IV is also at the boiling point. For glycols, Glycol I is ethylene glycol, and the series Glycol I to Glycol III has an increasing trend in terms of the boiling point and molecular weight. In the series Glycol I to Glycol III, the permittivity has a decreasing trend.

Ethylene glycol is used as the standard solvent for secondary doping because of its very good compatibility with PEDOT:PSS dispersions and good secondary doping performance. It is used as a baseline, and the solvent is generally used in further development because of its relatively low toxicity, good conductivity-enhancing properties, does not cause precipitation in combination with many ink additives, and its improvement of the film forming and leveling properties of ink formulations.

From the determined conductivities (Figure 2), it can be concluded that there is a strong correlation between the conductivity of PEDOT:PSS films and the permittivity of the solvents. With increasing solvent permittivity, PEDOT:PSS films generally exhibit higher conductivity. This trend is evident for all solvents considered, but also for a number of amides or glycols. From Figure 2, it can be seen that the layers prepared from ink with SD1 – Amide I solvent (highest permittivity) show the highest conductivity of 78 S/cm. This conductivity is higher than that of the commonly used DMSO.

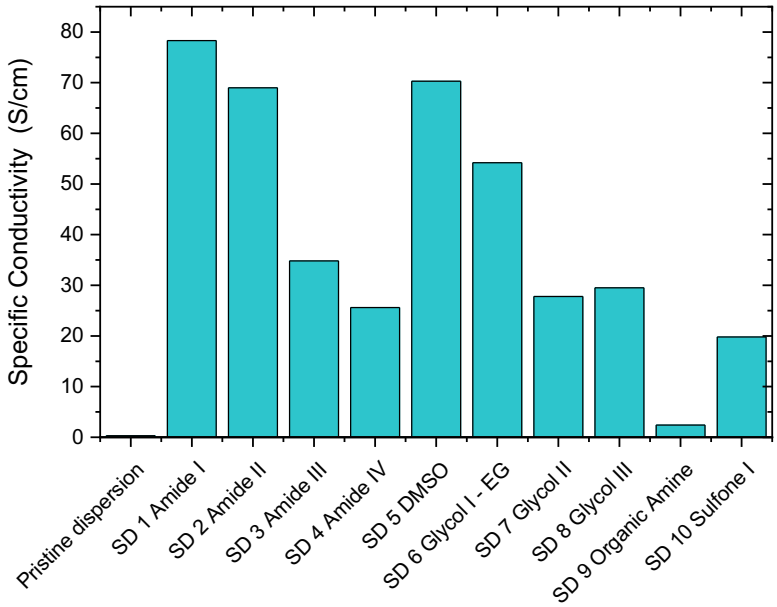

Figure 2: Dependence of conductivity of PEDOT:PSS 1:2.5 layers on the secondary dopant (solvent)

3.2 Influence of the type of surfactant on conductivity and overall layer quality

Nine non-ionic surfactants of different types were used to improve the surface tension of the PEDOT:PSS-based waterborne ink. The effect on the ink wetting capabilities of the print substrate, the appearance of the layers after application, and the conductivity of the layers themselves were investigated.

Because the composition of all of the inks was analogous, all of the layers were compared using the relative conductivity of the layers, which were normalized to the most conductive PEDOT:PSS layer. Figure 3 shows that the layers prepared from inks based on Surf 5 and Surf 7 surfactants had the highest conductivity.

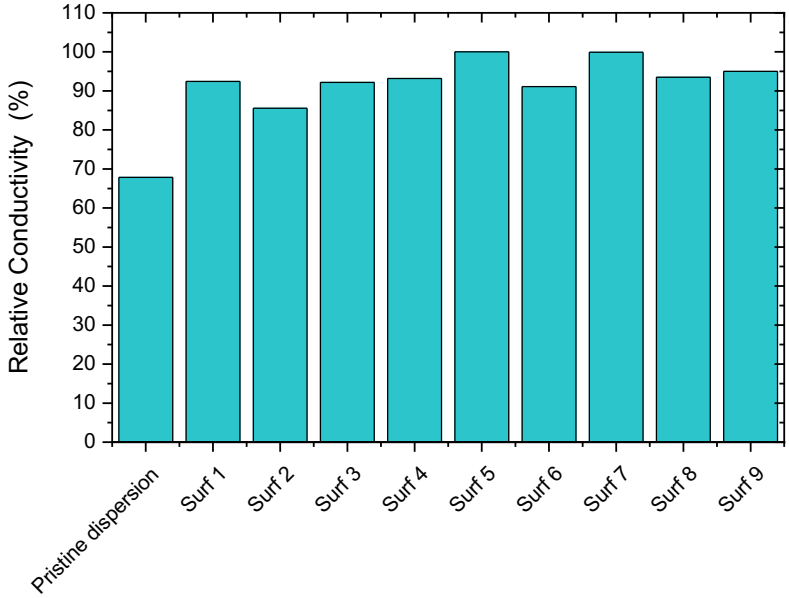

Figure 3: Dependence of relative conductivity of PEDOT:PSS layers on the surfactant

Alongside the evaluation of layer conductivity, the quality/appearance of the layer was evaluated too, because HTL requires high quality/homogeneity imperfection free surface/layer. The evaluation of appear-

ance quality was subjective, assessing the quality of the layer both wet, immediately after coating, and the quality of the layer after drying. The homogeneity of the wet layer and the wetting quality of the PET substrate were observed. For the dry layer, the homogeneity of the layer, the gloss of the layer, the presence of craters, agglomerates, or surfactant residues on the surface of the layer were observed too. Layers with the highest quality of surface appearance had generally the smoothest surface with high surface gloss and without defects (mottling, pinholes, rough surface, etc.). A relative scale was determined from 1 to 5, where the samples with the highest surface quality having a number of 5 (Figure 4). From the given perspective, it was the PEDOT:PSS layers based on ink with Surf 5 that showed high performance - high layer quality and also the highest conductivity.

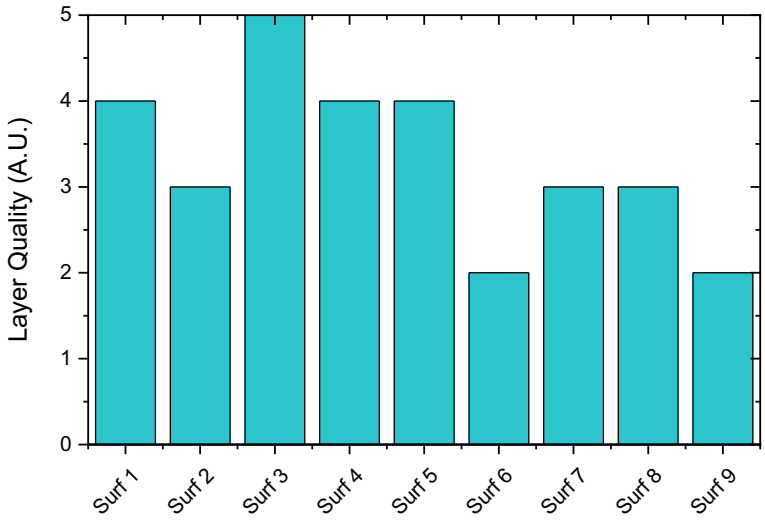

Figure 4: Dependence of layer quality of PEDOT:PSS layer on the surfactant

Based on conductivity and layer quality, Surf 5 (polyethylene glycol phenyl ether II) surfactant was used for further research of ink composition. The surfactant shows excellent film-forming behavior, achieves high film uniformity, high gloss, and no surface defects. The film-forming properties of the ink were very good for the PAL used for the OPD.

3.3 Influence of the complex ratio of PEDOT:PSS to the layer conductivity

In a study of the effect of primary dopant (PSS-) on the conductivity of PEDOT:PSS layers, 5 different complex ratios were studied. Two sets of inks were prepared, where the first set of inks did not contain secondary dopant, whereas the second set of inks contained 5 wt.% SD6 - ethylene glycol. In all inks, 0.5 % Surf 5 surfactant was used to improve the wetting behavior of the inks.

Table 4: Estimated characteristics of PEDOT:PSS films with various ratios of PEDOT:PSS complex

Conductive polymer	Ratio	Without secondary dopant	With 5 % of SD6 Ethylene glycol	
		Conductivity [S/cm]	Conductivity [S/cm]	Conductivity ratio
PEDOT:PSS	1:1	23.98	122.9	6
PEDOT:PSS	1:1.4	9.87	140.7	13
PEDOT:PSS	1:2.5	1.75	85.8	59
PEDOT:PSS	1:3.5	0.42	30.5	64
PEDOT:PSS	1:5	0.24	11.2	47

From Table 4, it can be seen that the most conductive layer is based on PEDOT:PSS with a complex ratio of 1:1.4 improved by secondary dopant SD6. Given ink also exhibited very good film-forming behavior. It is also evident that for samples without SD6, PEDOT:PSS with a ratio of 1:1 is the most conductive. Layers with PEDOT:PSS ratios of 1:3.5 and 1:5 showed the highest surface quality (smoothness, transparency, gloss), although they provide much lower conductivity than the PEDOT:PSS layer with 1:1.4 ratio. These results were confirmed for both sets of inks – with and without secondary dopant. Comparing the analogous dispersion with/without SD6, the improvement in conductivity is more pronounced for the dispersion with a higher PEDOT:PSS ratio. The effect of the secondary dopant solvent is lowest for the PEDOT:PSS complex with a 1:1 ratio.

3.4 Influence of various solvents on the conductivity and work function of PEDOT:PSS layer

Influence of various types of solvents/secondary dopants with specific properties on conductivity and WF were tested. The results in Figure 5 show the significant effect of the selected solvent types on the WF and also on the conductivity of the PEDOT:PSS layers.

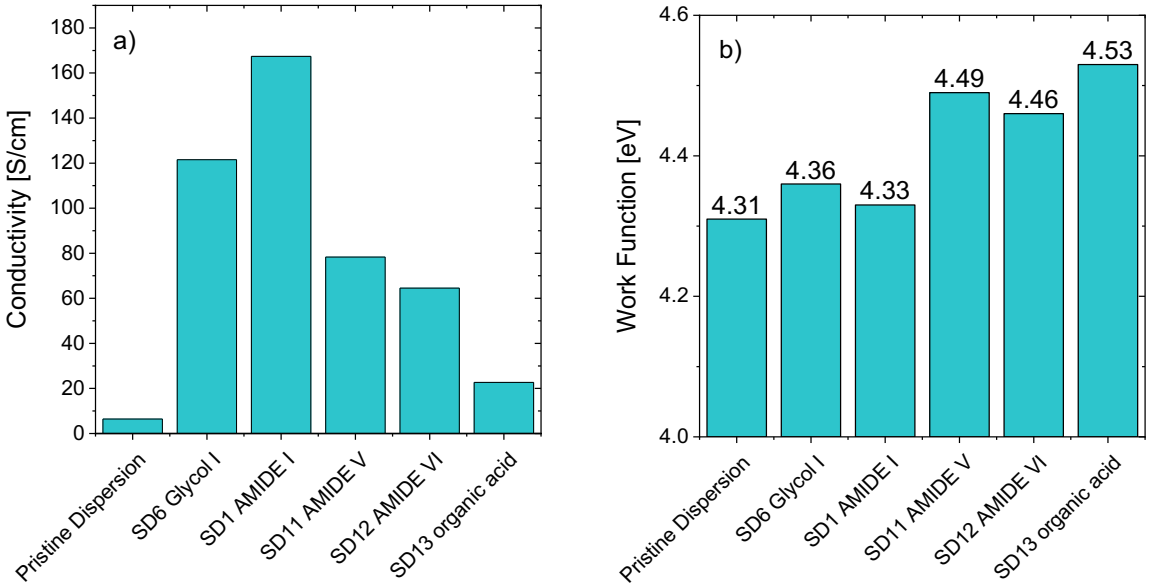

Figure 5: Dependence of conductivity (a) and WF (b) of PEDOT:PSS 1:1.4 layers on type of secondary doping solvent

The best conductivity was achieved for the layers prepared from ink containing SD1 – AMIDE I, whereas the higher WF value of PEDOT:PSS layer was achieved by the SD11 – AMIDE V solvent based ink. The effect of SD13 – organic acid on the high WF value of PEDOT:PSS layer is also interesting in terms of optimizing the energy levels in the OPD and tuning its performance.

4. Conclusion

It has been demonstrated that various characteristics of PEDOT:PSS films can be tuned by a number of the variable parameters of inks. One of the most influential is the PEDOT:PSS complex ratio. It has shown that the highest conductive films can be prepared for a 1:1.4 complex ratio, while the least conductive films are based on a 1:5 complex ratio. The conductivity of PEDOT:PSS layers can also be affected by the addition of solvents/secondary dopants with a high dielectric constant. These additives allowed us to increase the conductivity up to two orders of magnitude, where for PEDOT:PSS 1:1.4 layers a specific conductivity of 167 S/cm was achieved in the case of SD1 – AMIDE I solvent based ink. The choice of surfactant also has a significant influence on not only the conductivity but also on the quality of the prepared PEDOT:PSS layer.

In the case of HTL layer formation with a thickness of about 40 nm, the high homogeneity of the layer is essential for the preparation of high-performance multilayer structures such as OPVs or OPDs. Finally, it can be stated that the specific solvents/secondary dopants can be used to effectively influence the work function of PEDOT:PSS layers. This is a strong tool for enhancing the performance of various multilayer structures too. Further findings from our research related to PEDOT:PSS layers will be presented at the iarigai conference.

Acknowledgement

This work was supported by the MADRAS project funded from the European Union Horizon 2020 research and innovation programme under grant agreement No. 862492.

References

Gasiorowski, J., Menon, R., Hingerl, K., Dachev, M. and Sariciftci, N.S., 2013. Surface morphology, optical properties and conductivity changes of poly(3,4-ethylenedioxythiophene):poly(styrenesulfonate) by using additives. *Thin Solid Films*, 536, pp. 211–215. https://doi.org/10.1016/j.tsf.2013.03.124.

Jönsson, S.K.M., Birgerson, J., Crispin, X., Greczynski, G., Osikowicz, W., van der Gon, A.W.D., Salaneck, W.R. and Fahlman, M., 2003. The effects of solvents on the morphology and sheet resistance in poly(3,4-ethylenedioxythiophene)–polystyrenesulfonic acid (PEDOT–PSS) films. *Synthetic Metals*, 139(1), pp. 1–10. https://doi.org/10.1016/S0379-6779(02)01259-6.

Khasim, S., Pasha, A., Lakshmi, M., Chellasamy, P., Kadarkarai, M., Darwish, A.A.A., Hamdalla, T.A., Al-Ghamdi, S.A. and Alfadhli, S., 2022. Post treated PEDOT-PSS films with excellent conductivity and optical properties as multifunctional flexible electrodes for possible optoelectronic and energy storage applications. *Optical Materials,* 125: 112109. https://doi.org/10.1016/j.optmat.2022.112109.

Kim, J.Y., Jung, J.H., Lee, D.E. and Joo, J., 2002. Enhancement of electrical conductivity of poly(3,4-ethylenedioxythiophene)/poly(4-styrenesulfonate) by a change of solvents. *Synthetic Metals,* 126(2–3), pp. 311–316. https://doi.org/10.1016/S0379-6779(01)00576-8.

Kim, Y.H., Sachse, C., Machala, M.L., May, C., Müller-Meskamp, L. and Leo, K., 2011. Highly conductive PEDOT:PSS electrode with optimized solvent and thermal post-treatment for ITO-free organic solar cells. *Advanced Functional Materials,* 21(6), pp. 1076–1081. https://doi.org/10.1002/adfm.201002290.

Ouyang, J., 2013. "Secondary doping" methods to significantly enhance the conductivity of PEDOT:PSS for its application as transparent electrode of optoelectronic devices. *Displays*, 34(5), pp. 423–436. https://doi.org/10.1016/j.displa.2013.08.007.

Ouyang, J., Xu, Q., Chu, C.W., Yang, Y., Li, G. and Shinar, J., 2004. On the mechanism of conductivity enhancement in poly (3, 4-ethylenedioxythiophene): poly (styrene sulfonate) film through solvent treatment. *Polymer,* 45(25), pp. 8443–8450. https://doi.org/10.1016/j.polymer.2004.10.001.

Ouyang, J., Chu, C.W., Chen, F.-C., Xu, Q. and Yang, Y., 2005. High-conductivity poly (3, 4-ethylenedioxythiophene): poly (styrene sulfonate) film and its application in polymer optoelectronic devices. *Advanced Functional Materials,* 15(2), pp. 203–208. https://doi.org/10.1002/adfm.200400016.

Tang, H., Liu, Z., Hu, Z., Liang, Y., Huang, F. and Cao, Y., 2020. Oxoammonium enabled secondary doping of hole transporting material PEDOT:PSS for high-performance organic solar cells. *Science China Chemistry,* 63(6), pp. 802–809. https://doi.org/10.1007/s11426-020-9729-y.

Zhang, L., Yang, K., Chen, R., Zhou, Y., Chen, S., Zheng, Y., Li, M., Xu, C., Tang, X., Zang, Z. and Sun, K., 2020. The role of mineral acid doping of PEDOT:PSS and its application in organic photovoltaics. *Advanced Electronic Materials,* 6(1): 1900648. https://doi.org/10.1002/aelm.201900648.

DOI 10.14622/Advances_48_2022_08

Creation of a comprehensive high-resolution image data set on an industrial web press to investigate hydrodynamic pattern formation in gravure printing

Pauline Brumm[1,2], Thomas Sprinzing[3], Thorsten Euler[1], Matthias Galus[3], Armin Weichmann[3] and Edgar Dörsam[1,2]

[1] Technical University of Darmstadt, Department of Mechanical Engineering, Institute of Printing Science and Technology, Magdalenenstr. 2, 64289 Darmstadt, Germany

[2] Collaborative Research Center (CRC) 1194 – Interaction between Transport and Wetting Processes, Project C01, Germany

[3] Hochschule der Medien Stuttgart, Institut für Angewandte Forschung (IAF), Nobelstr. 10, 70569 Stuttgart, Germany

E-mails: brumm@idd.tu-darmstadt.de; sprinzing@hdm-stuttgart.de; euler@idd.tu-darmstadt.de; galus@hdm-stuttgart.de; weichmann@hdm-stuttgart.de; doersam@idd.tu-darmstadt.de

Short abstract

Hydrodynamic pattern formation in gravure printing is not yet fully understood, but a deep insight into the fluid transfer process is crucial for process control and for high-quality printed layers. Therefore, a large-scale gravure printing trial was conducted on an industrial-scale web press to analyze pattern formation phenomena on the printed samples using various complementary methods: deep learning for pattern classification, Fourier analysis of ribbing patterns, gradation measurements, mottle index measurements and missing dots analysis. The printing form layout was especially developed for use with these analyzing methods. From over 23 km of printed foil and paper, over 4 000 printed sheets were extracted and cut into pieces, from which over 1 200 were scanned at a resolution of 2 400 dpi (10.58 µm per pixel), resulting in images of size 20 400 × 28 080 pixels. Thus, a comprehensive, versatile high-resolution image data set larger than three terabytes was created which can be used to investigate the influence of printing parameters on pattern formation. During the printing trial, the following printing parameters were varied systematically: printing velocity (15–240 m/min), type of ink (solvent-based, water-based), ink viscosity (base, high, medium, low), type of substrate (foil, paper), electrostatic assist (ESA) (on, off) and doctor blade angle (high, medium, low). First analysis results are presented in this article.

Keywords: rotogravure, fluid transfer, ink splitting, parameter study, quality control, dynamic wetting

1. Introduction and background

Understanding hydrodynamic pattern formation during fluid transfer in gravure printing is crucial for the fabrication of homogeneous ultra-thin functional layers as e.g. used in printed electronics, for large-throughput high-quality graphical printing applications, as well as for special applications like printed security features or biomedical printing. Numerous researchers like Kunz (1975), Hübner (1991), Kumar (2015), Grau, et al. (2016) and Schäfer, et al. (2019) have contributed to a deeper understanding of fluid transfer in gravure printing in the last decades. However, pattern formation dynamics are still only partially understood and the printing industry often relies on the practical experience of professional printers. Therefore, the aim of our large-scale gravure printing trial was to systematically investigate the influence of selected major printing parameters (printing velocity, type of ink, ink viscosity, type of substrate, electrostatic assist (ESA) and doctor blade angle) on hydrodynamic pattern formation. Various pattern formation phenomena can be observed in the dried ink layer, such as (missing) dots, ribbing and more complex patterns (Brumm, et al., 2021a). Depending on the printing application, a certain pattern is desired or even required. For halftones in graphical applications, typically dot patterns are desired, whereas for functional coatings or printed electronics, closed homogeneous layers of ink with the least amount of pattern formation possible are generally needed.

2. Materials and methods

2.1 Gravure printing trial

2.1.1 Design of experiments

We conducted a 3-day printing trial on an industrial-scale gravure printing machine Bobst Rotomec MW 60 (Bobst, Mex, Switzerland) with a printing form cylinder of 700 mm circumference and 700 mm face and a maximum printing speed of 300 m/min. On day one we printed with solvent-based ink (NC 133-15, magenta, Siegwerk, Siegburg, Germany) on foil (WSS 20 BoPP solid white film, both sides heat sealable, treated, Taghleef Industries, Dubai, United Arab Emirates), on day two with solvent-based ink (NC TOB, magenta, Siegwerk, Siegburg, Germany) on two different paper substrates (UPM Smart G 60 g/m^2, super-calendered, UPM, Augsburg, Germany and Sigmakraft RTC Green 70 g/m^2, coated, Mosaico Specialty Papers, Altavilla Vicentina, Italy) and on the third day with water-based ink (R0001235761, red bluish, Sun Chemical, Niedernhausen, Germany) again on the Sigmakraft paper.

The design of experiments is based on ascending velocity ramps with the printing velocities 15, 30, 60, 90, 120, 180, and 240 m/min as target velocities. ESA was always turned off for 15 and 30 m/min and was turned both off and on for the other printing velocities. Furthermore, the ink viscosity and the angle of the doctor blade (Swedcut MicroKote G, RG10530, coated carbon steel blade, 40 mm × 0.15 mm Standard Lamella, Swedev, Munkfors, Sweden) were varied in three steps (high, medium, low). The water-based ink was even prepared using four different viscosities (base, high, medium, low). For diluting the solvent-based inks, a nearly azeotropic mixture of ethanol (30 %) and ethyl acetate (70 %) was used. The water-based ink was diluted with tab water. The ambient temperature and humidity were recorded and the ink temperature was monitored during the printing trial. Printing ink viscosity was measured with a 4 mm ISO flow cup (DIN EN ISO 2431) as well as a 4 mm DIN flow cup (DIN 53211) (Deutsches Institut für Normung, 2019; 1987) and was controlled with a Fasnacht Viscopoint IL CPS viscosity sensor in combination with a viscosity control system Fasnacht pentasmart (Fasnacht Dynamics AG, Worb, Switzerland). After the printing trial, ink viscosities were measured using a rotational rheometer Kinexus Lab+ (NETZSCH-Gerätebau GmbH, Selb, Germany). Doctor blade pressure (1.5 bar), impression roller pressure (1.5 bar) as well as impression roller hardness (80 Shore A) were kept constant. In total, 17 velocity ramps were performed with 12 parameter combinations each. For each parameter combination, 20 sheets (each 600 mm × 700 mm) were manually cut out, which results in over 4 000 sheets in total. The sheets were post-processed according to the chosen analyzing method which mostly required further cutting as well as digitization steps.

2.1.2 Printing form layout

We used an electromechanically engraved, chrome-plated printing form (circumference 700 mm, engraving width 590 mm, pyramid shaped cells). The printing form was engraved on a Hell K500 engraving system (Hell Gravure Systems GmbH & Co. KG, Kiel, Germany). Several raster angles (Hell engraving angles 0, 2, 4), raster frequencies (60, 70, 80, 100 lines/cm) and tonal values (0, 1, 2, 3, 4, 5, 8, 10, 15, 20, 25, 30, 35, 40, 45, 50, 55, 60, 65, 70, 75, 80, 85, 90, 93, 95, 98, 100 %) were realized on the same printing form with constant stylus angle 120°. Hell engraving angles 0 (2, 4) equal a raster angle of 36.87° (59.35°, 40.16°). The printing form layout was especially developed for use with the analyzing methods as described in Section 2.3. Five defined parts (A, B, C, D, E) of the printing form layout are directly dedicated to the five different analyzing methods, see Figure 1. Part A is especially used for classification of patterns with deep learning, part B for Fourier analysis of ribbing patterns, part C for gradation measurements, part D for mottle index measurements and part E for missing dots analysis. In Figure 1 in part C, D and E, Hell engraving angle 0 is displayed as cyan and Hell engraving angle 4 as black, both with a nominal raster frequency of 80 lines/cm. In part A and B, where the raster angle is always Hell engraving angle 2, the color black stands for a nominal raster frequency of 60 lines/cm, yellow for 70 lines/cm, magenta for 80 lines/cm and cyan for 100 lines/cm.

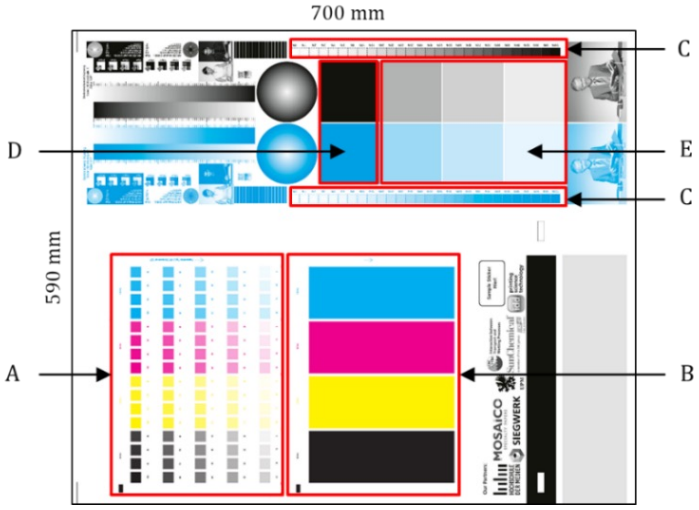

Figure 1: Printing form layout: part A is used for classification of patterns with deep learning, part B for Fourier analysis of ribbing patterns, part C for gradation measurements, part D for mottle index measurements and part E for missing dots analysis

2.2 Sample digitization and post-processing

Parts A and B of the printing form layout (Figure 1) were digitized using two Epson Perfection V850 Pro flatbed scanners (Seiko Epson Corporation, Suwa, Japan) operated with the professional scanning software Silverfast Ai Studio 9 (LaserSoft Imaging AG, Kiel, Germany). The scanner was color-calibrated before each use with a reflected light Kodak IT8-Target. The nominal scanning resolution was chosen as 2 400 dpi (10.58 µm per pixel) and the scanned images were saved as uncompressed TIF files with 16-bit lightness values per R, G and B color channel. All filters and retouching options were turned off. In total, over 1 200 images of size 20 400 × 28 080 pixels were scanned. For further processing of the scanned images, a source code in the programming language Python was developed which automatically identifies and cuts out the 13 mm × 13 mm squares in part A and the 64 mm × 179 mm rectangles in part B. This leads to over 48 000 cut-out squares and over 2 400 cut-out rectangles. Parts D and E were scanned together with an Epson Perfection 4870 Photo flatbed scanner (Seiko Epson Corporation, Suwa, Japan) at a nominal resolution of 1 200 dpi (21.17 µm per pixel) in 8-bit grayscale. The scanner was calibrated that the brightest substrate delivered lightness values above 240 but less than 255 (no overexposure) and the darkest patch, the solid black patch of area D, had values between 5 and 50.

2.3 Sample analysis

2.3.1 Classification of patterns with deep learning

The cut-out squares that were derived from part A after post-processing shall be classified using trained convolutional neural networks (CNNs) from Brumm, et al. (2021b), a common method in deep learning. These CNNs were trained to distinguish between three classes of pattern formation: dots, fingers and mixed. Fingers are also known as 'ribbing' patterns and derive from Saffman-Taylor instabilities at the ink-air-interface (Saffman and Taylor, 1958). The classified images shall be used to create regime maps, see Brumm, et al. (2021a), in which two or more printing parameters are displayed on the axes, e.g., printing velocity and tonal value, and data points including the pattern class are plotted. Regime maps visualize the cause-effect-correlations between printing parameters and printed pattern class and shall help the operators of a printing press to choose the correct set of printing parameters for their intended application. We assume that these regime maps are especially useful for developing innovative printed products, for operating the printing press at uncommon process parameters and for process scaling.

2.3.2 Fourier analysis of ribbing patterns

The cut-out rectangles from part B shall be analyzed with a 1-dimensional fast Fourier transformation algorithm in the programming language Matlab which was developed and already approved for the analysis of ribbing patterns in flexographic printing by Brumm, Sauer and Dörsam (2019). The Fourier analysis yields dominant frequencies of the ribbing patterns which are plotted in double-logarithmic scale over printing velocity. From the plots, scaling behavior of pattern formation in form of scaling exponents can be extracted. These scaling exponents help the operator of the printing press to tune the printing parameters in order to obtain a certain ribbing pattern, e.g., for the fabrication of capillary networks for biomedical applications (Fritschen, et al., 2021), or to reduce the ribbing pattern as much as possible as it is mostly the case in graphical printing and printed electronics.

2.3.3 Gradation measurements

Gradation measurements shall be performed on the tonal value wedges over the whole tonal range (28 steps, see Section 2.1.2) in part C of the printing form layout. The spectral values will be measured by a Techkon SpectroDens spectro-densitometer (TECHKON GmbH, Königstein im Taunus, Germany), converted into CIE *L*a*b** values and then the spot color tonal values (SCTV) (according to ISO 20654:2017) will be calculated and evaluated (International Organization for Standardization, 2017).

2.3.4 Mottle index measurements

Mottle index measurements shall be performed on the two 100 % tonal value fields in part D. The overall mottle index is determined within a 300 dpi grid calculated by downscaling the 1 200 dpi image. The evaluation program is written in Java by Weichmann (2015) basically using the algorithm by Rosenberger (2002). It works on an area of 512 x 512 pixels (43.34 mm × 43.34 mm), calculates the mean of the absolute differences of the mean of the gray values of the four sub-squares in a circumscribing square, takes the standard deviation of these means of all squares in the area multiplied by the mean of the grey values of the squares multiplied by the standard deviation of the mean of the grey values of the squares. The size of the squares increases over eight steps: 85, 170, 340, 680 µm, 1.34, 2.68, 5.42, 10.84 mm. The values for the different sizes show the inhomogeneity of the solid ink layer in the respective space frequency areas. It can be assumed that some of these correlates better to the finger structures than others, because of the pattern of the fingers being of similar size to these squares. The final mottle index is the mean of the eight values. The greater the value the more mottle is detected. An overall mottle index greater than 10 indicates well visible structures. Even lower numbers are associated with mottle, however, less visible.

2.3.5 Missing dots analysis

In part C, the tonal values of 75 %, 50 % and 25 % in two Hell engraving angles shall be used to count the missing dots per area. The evaluation program is written in Java by Weichmann (2015) and works with the 1 200 dpi images. It utilizes edge filtering and adaptive dot size filtering to count the number of missing dots in these fields and normalize them to $1/cm^2$. As missing dots distort the image and decrease the image quality, the less missing dots the better.

3. Results and discussion

3.1 Printing trial protocol

In total, we consumed over 23 km of foil and paper for printing. We extracted over 4 000 printed sheets from the printed rolls. The printing trial without preparatory work but including subsequent cutting of the sheets from the printed rolls took over 140 hours. The sorting, labeling and cutting of the sheets into smaller pieces consumed over 200 hours and over 350 hours were needed for scanning of over 1 200 images of only part A and B of the samples.

3.2 Data set characteristics

To the best of our knowledge, our high-resolution image data set is by far the largest industrial-scale scientific data set for gravure printing compared with earlier studies. The over 1 200 scanned images of part A and B alone provide high-quality uncompressed image data of gravure printed patterns with a total size of over three terabytes. If applicable, the cut-out rectangles and squares can be saved in a compressed and downscaled data format during post-processing to save memory capacity. The scanned images of part D and E will provide another several gigabytes of image data. The data set helps to gain a deeper understanding of pattern formation in gravure printing.

Cut-outs from two exemplary samples are shown in Figure 2. Sample #1 (identification number: B2-03_ECPvmam_V240_ESA1) was printed at 240 m/min on the Sigmakraft paper with the NC TOB ink of medium viscosity (20 s with ISO flow cup) with ESA turned on and medium blade angle of nominal 55°. Sample #2 (B3-05_WCPvlam_V015_ESA0) was printed at 15 m/min, on Sigmakraft paper with water-based ink of low viscosity (17 s with ISO flow cup) with ESA turned off and medium blade angle 55°.

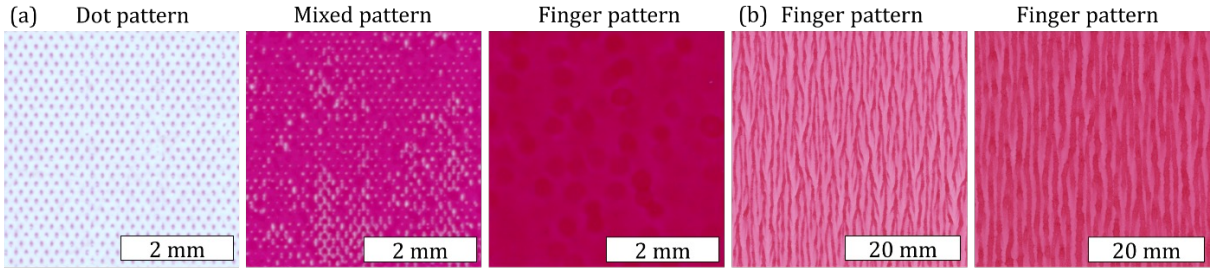

Figure 2: Exemplary cut-outs from samples #1 (a) and #2 (b) show various types of patterns

3.3 First analysis results of pattern formation

For sample #1, we calculated the spot color tonal values (SCTV) and plotted them over the tonal value from the data for Hell engraving angle 0 and 4, see Figure 3a. The curves of the two Hell engraving angles differ slightly but are both relatively close to a linear curve with a slope of 1, which would be the ideal behavior. For sample #2, we observed strong finger patterns (Figure 2b), which we analyzed using the Fourier analysis approach. Figure 3b shows four Fourier spectra for the four different raster frequencies. The global peaks at frequencies around 5 cm^{-1} to 7 cm^{-1} reveal the dominant frequencies of the ribbing patterns, which are much lower than the underlying raster frequencies of 60 cm^{-1} to 100 cm^{-1} measured along the raster angle. The raster frequency is visible in the right half of the Fourier spectra in form of small local sharp peaks at 55 cm^{-1}, 65 cm^{-1}, 75 cm^{-1} and 94 cm^{-1} since the Fourier analysis is performed perpendicular to the printing direction and not along the raster angle. In conclusion, the ribbing patterns span 11 to 13 raster dots on average and thus are clearly visible to the human observer as printing defects.

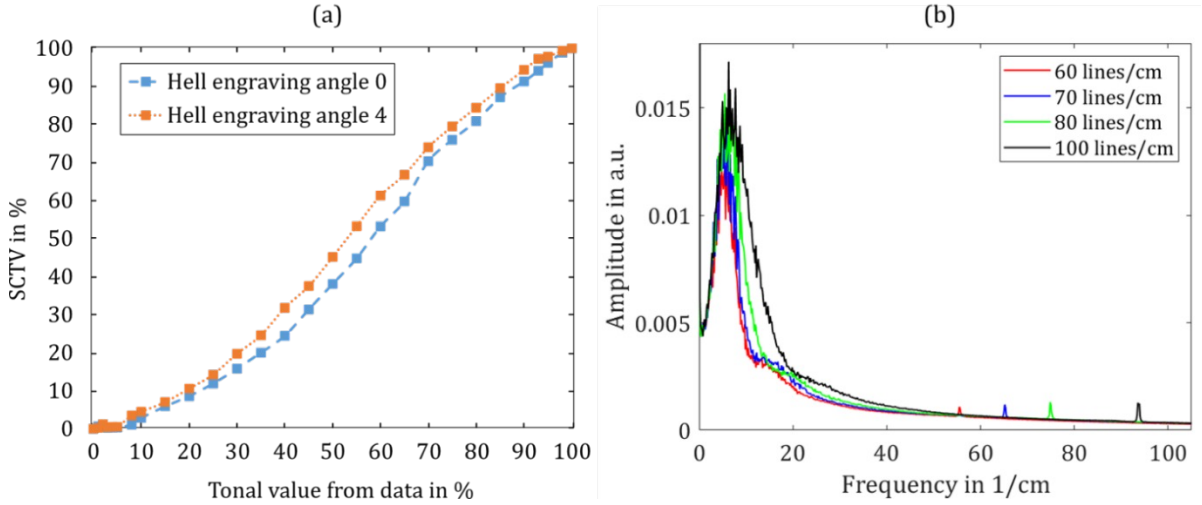

Figure 3: Exemplary SCTV curves for two Hell engraving angles for sample #1 (a) and exemplary Fourier spectra for four raster frequencies at Hell engraving angle 2 for sample #2 (b)

Exemplary mottle index measurements can be found in Table 1 and an exemplary missing dots analysis is depicted in Table 2.

Table 1: Exemplary mottle index measurements for sample #1 for two Hell engraving angles

Hell engraving angle	Mottle 1	Mottle 2	Mottle 3	Mottle 4	Mottle 5	Mottle 6	Mottle 7	Mottle 8	Mottle index
0	143.970	98.434	16.344	1.603	0.207	0.043	0.012	0.015	32.579
4	56.479	29.139	4.821	0.865	0.220	0.115	0.204	0.138	11.498

Table 2: Exemplary missing dots analysis for sample #1 for two Hell engraving angles

Hell engraving angle	0			4		
Tonal value	25 %	50 %	75 %	25 %	50 %	75 %
Missing dots per cm^2	1 228.0	3.2	8.5	4 836.0	191.0	257.0

Based on visual evaluation, the image quality of our high-resolution data set is very satisfactory for pattern analysis. Further evaluations are currently being carried out.

4. Conclusions and outlook

We were able to create a comprehensive, high-resolution image data set and showed first exemplary results of the pattern formation analysis. Further analyzing methods can be applied to the printed samples or the data set. At this point we would like to emphasize the versatility of the data set, which we plan to make available to the public under creative commons license and use as a benchmark for the comparison between classical electromechanically engraved printing forms and recently developed polymeric printing forms. Besides, we plan to compare pattern formation phenomena and their scaling behavior as observed on different printing machines. Another future investigation shall be focused on the correlation of mottle index and ribbing pattern frequency.

Acknowledgements

We kindly acknowledge the financial support by the Deutsche Forschungsgemeinschaft (DFG, German Research Foundation) – Project-ID 265191195 – SFB 1194 'Interaction between Transport and Wetting Processes', project C01. We kindly thank CAPA Crummenerl & Albers and UPM for providing paper substrates and Siegwerk and Sun Chemical for providing printing inks.

References

Brumm, P., Sauer, H.M. and Dörsam, E., 2019. Scaling behavior of pattern formation in the flexographic ink splitting process. *Colloids and Interfaces*, 3(1): 37. https://doi.org/10.3390/colloids3010037.

Brumm, P., Weber, T.E., Sauer, H.M. and Dörsam, E., 2021a. Ink splitting in gravure printing: localization of the transition from dots to fingers. *Journal of Print and Media Technology Research*, 10(2), pp. 81–93. https://doi.org/10.14622/JPMTR-2016.

Brumm, P., Lindner, N., Weber, T.E., Sauer, H.M. and Dörsam, E., 2021b. A deep learning approach for the classification task of gravure printed patterns. In: C. Ridgway, ed. *Advances in Printing and Media Technology: Proceedings of the 47th International Research Conference of Iarigai.* Athens, Greece, 19–23 September 2021, pp. 2–9. Darmstadt: iarigai. https://doi.org/10.14622/Advances_47_2021.

Deutsches Institut für Normung, 2019. *DIN EN ISO 2431 Paints and varnishes – Determination of flow time by use of flow cups (ISO 2431:2019, Corrected version 2019-09*). Berlin: DIN.

Deutsches Institut für Normung, 1987. *DIN 53211 Paints, varnishes and similar coating materials: Determination of flow time using the DIN flow cup*. Berlin: DIN.

Fritschen, A., Brumm, P., Doss, L., Dörsam, E. and Blaeser, A., 2021. Fabrication of vascular network mimicking pattern using flexographic printing technology. In: *TERMIS 6th World Congress*. Maastricht, the Netherlands, November 15–19, 2021.

Grau, G., Cen, J., Kang, H., Kitsomboonloha, R., Scheideler, W.J. and Subramanian, V., 2016. Gravure-printed electronics: recent progress in tooling development, understanding of printing physics, and realization of printed devices. *Flexible and Printed Electronics*, 1(2): 023002. https://doi.org/10.1088/2058-8585/1/2/023002.

Hübner, G., 1991. *Ein Beitrag zum Problem der Flüssigkeitsspaltung in der Drucktechnik.* Dr.-Ing. Dissertation. Technische Hochschule Darmstadt. https://doi.org/10.25534/tuprints-00013550.

International Organization for Standardization, 2017. *ISO 20654:2017 Graphic technology – Measurement and calculation of spot colour tone value*. Geneva: ISO.

Kumar, S., 2015. Liquid transfer in printing processes: liquid bridges with moving contact lines. *Annual Review of Fluid Mechanics*, 47, pp. 67–94. https://doi.org/10.1146/annurev-fluid-010814-014620.

Kunz, W., 1975. Ink transfer in gravure process. In: *TAGA Proceedings 1975: Annual meeting of the Technical Association of the Graphic Arts*. Toronto, Ontario, 1975. Rochester, NY, USA: TAGA, pp. 151–176.

Rosenberger, R.R., 2002. *Mottle measurement of wet trap, back trap and other motley images*. [pdf] VERITY IA. Available at: <https://www.verityia.com/_files/ugd/c4e5fa_efd8667d40f44c45a0187b99b2fb7559.pdf> [Accessed 22 March 2022].

Saffman, P.G. and Taylor, G.I., 1958. The penetration of a fluid into a porous medium or Hele-Shaw cell containing a more viscous liquid. *Proceedings of the Royal Society A: Mathematical, Physical and Engineering Sciences*, 245(1242), pp. 312–329. https://doi.org/10.1098/rspa.1958.0085.

Schäfer, J., Roisman, I.V., Sauer, H.M. and Dörsam, E., 2019. Millisecond fluid pattern formation in the nip of a gravure printing machine. *Colloids and Surfaces A: Physicochemical and Engineering Aspects*, 575, pp. 222–229. https://doi.org/10.1016/j.colsurfa.2019.04.085.

Weichmann, A., 2015. *GravureQ: commercially available software for mottle and missing dots analysis*. Hochschule der Medien Stuttgart, Germany.

DOI 10.14622/Advances_48_2022_11

Comparison of the performance of DLC to chromium as wear resistance layer on a gravure cylinder for printing fine line structures

Laura Cirstea, Anna Kolesova, Hammad Khan, Mohamed Abouelmagd, Swapnil Patel, Thomas Sprinzing, Matthias Galus and Armin Weichmann

Hochschule der Medien Stuttgart, Institut für Angewandte Forschung (IAF), Nobelstr. 10, 70569 Stuttgart, Germany
E-mails: lc035@hdm-stuttgart.de; ak280@hdm-stuttgart.de; hk060@hdm-stuttgart.de; ma120@hdm-stuttgart.de; p099@hdm-stuttgart.de; sprinzing@hdm-stuttgart.de; galus@hdm-stuttgart.de; weichmann@hdm-stuttgart.de

Short abstract

For many decades in rotogravure electro plating a chromium layer on top of the copper surface which holds the cells was used as wear protection for the print form cylinder. Recently, coating the copper with a layer of diamond like carbon (DLC) presents an alternative with even higher wear protection. The price of a DLC coating is significantly higher, so further advantages would be beneficial to justify its application. There were indications that the ink accepting and releasing properties of the DLC are superior to chromium. This would be especially useful for micro structures and fine lines. Therefore, we designed a print form including many different small structures and manufactured two identical cylinders by laser mask etching, one electro plated with chromium, one coated with DLC. A print trial was conducted on our industrial-scale gravure printing machine. We compared the two surfaces with black ink on a white biaxially oriented polypropylene (BoPP) film under varying ink viscosities, doctor blade materials and doctor blade angles. Analysis of print gradation, missing dots and mottle was made, a visual assessment of a fine line star pattern was conducted and 15 µm, 20 µm, and 50 µm lines in and across the print direction were measured according to their average width and homogeneity. Almost every evaluation shows the micro structures printed were significantly better with the DLC surface. The influence of the surface surpassed by far the other parameters. The ink viscosity had surprisingly low influence. This indicates that the difference of the surfaces in respect to print quality indeed is based on their different ink releasing capabilities, constituting DLC superior to chromium.

Keywords: rotogravure, diamond like carbon, micro structures, quality control

1. Introduction and background

One of the challenges that the global gravure printing industry is facing is its homologation in line with the requirements of sustainable printing. Finding environmentally friendly alternatives to electro plating of the rotogravure cylinders with Chromium(IV) is an urgent matter of research, mainly due to the environmental hazard of this element in its ionic state. The Green Gravure project aims exactly at this, and one solution developed by the Roto-Hybrid Group is coating of the copper with a layer of Diamond like Carbon (DLC). The Roto Hybrid Process® was already part of various pilot studies in Europe and USA, at Mondi Group and Western Michigan University. This new technology presented even better properties in wear protection of the cylinder, print quality and surface smoothness. Moreover, among the advantages are a reduction in ink usage of up to 10 %, an increase in the cylinders' lifetime of 500 %, a decrease in storage space for the print jobs of 80 %, a reduction in time of cylinder readiness to print of 50 %, and the elimination of the chromium oxide layer. Due to its high production cost, the sector that would benefit the most from the change to DLC coating is security printing (European Commission, 2022). In fact, the reproduction quality

of micro structures and fine lines, along with wear protection, is the main aspect that interests this sector. This paper investigates if DLC can satisfy or even exceed these requirements compared with chromium.

2. Materials and methods

Fluid transfer in gravure printing is a complex process. In the last decades, researchers like Kunz (1975), Hübner (1991), Kumar (2015), Grau, et al. (2016) and Schäfer, et al. (2019) have contributed to a deeper understanding. More recently, Brumm, et. al. (2021a; 2021b) tried to classify transfer patterns on the basis of a neural network. This paper uses a design of experiments (DoE) to compare the performance of the DLC surface versus the standard hard plated chromium surface with a specific focus on very fine structures.

2.1 Printing form layout

The company GRT (GRT GmbH, Hamm, Germany) used two identical gravure cylinders with a basic copper roughness of r_z = 0.37 µm (r_z is defined as the average of the difference between the tallest "peak" and the deepest "valley" in the surface within 5 traces of 0.25 mm length) to produce the print form with the Think Laser process (Think Laboratory, Kashiwa, Japan). This process utilises a laser generated mask with a laser spot size of 2 µm to etch the micro structures into the copper. The etching depth was 9 µm. The print form was designed to contain various small structures and patterns in a total format of 700 mm × 590 mm (Figure 1). The chrome plating (layer thickness 5–7 µm) was also performed by GRT, and the DLC coating (layer thickness 5–7 µm) was performed by RotoHybrid (Roto-Hybrid Gravure Technologies, Wuppertal, Germany).

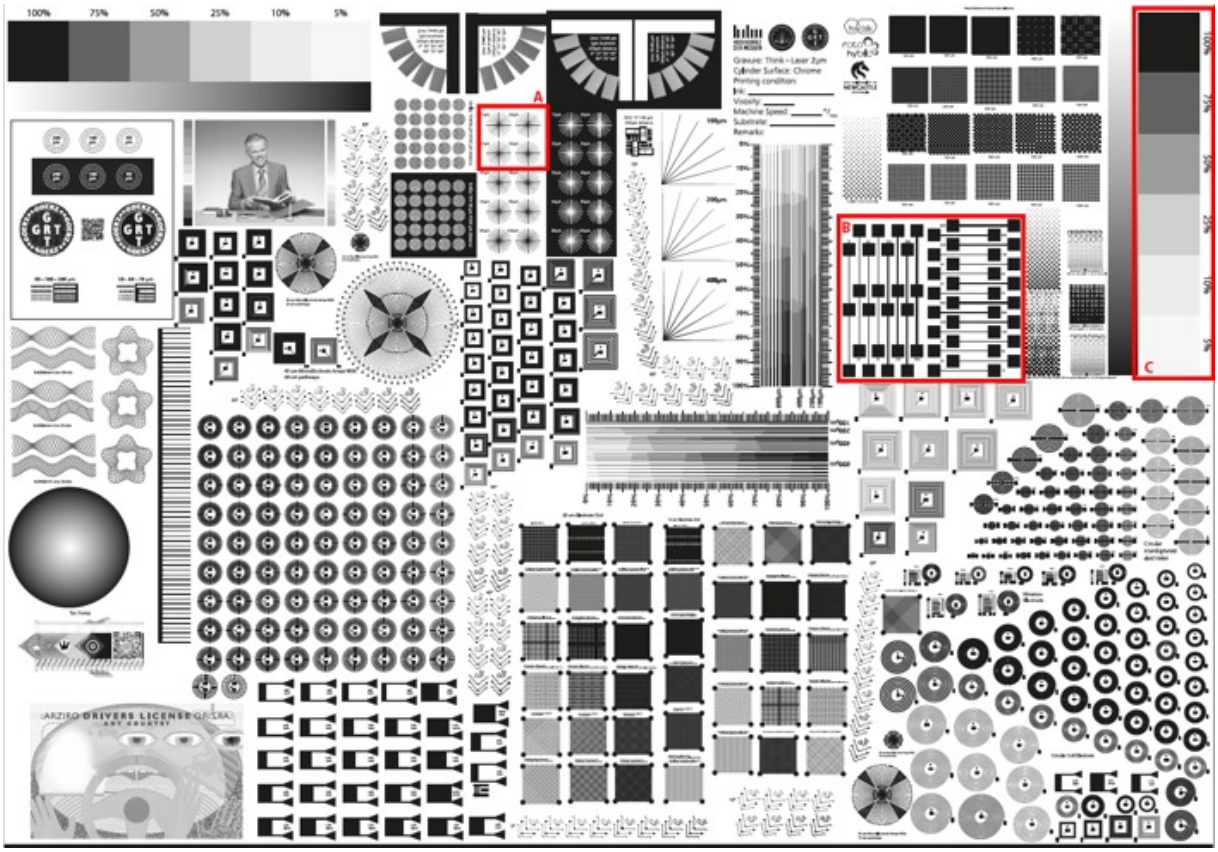

Figure 1: Upper half of printing form layout (350 mm × 590 mm); the complete form (700 mm × 590 mm) consists of the upper part and the lower part, the lower part uses a 180° rotation of the upper part

2.2 Gravure printing trial

The print trial was conducted on an industrial-scale gravure printing machine, with black ink on white biaxially oriented polypropylene (BoPP) film. The following print conditions apply for the trial:

- *Gravure press*: BOBST ROTOMEC MW 60, press speed: 150 m/min, cylinder circumference: 700 mm, cylinder bale width: 700 mm, pressure roller hardness: 75 shore A, pressure roller pressure: 1.5 bar, doctor blade pressure: 1.5 bar, dryer temperature: 60 °C with 10 % recirculation, corona treatment: 20 W·min/m^2. No electrostatic assist (ESA) was used during the DoE, except for one additional trial point.
- *Substrate*: WSS 20 BoPP solid white film, both sides heat sealable, treated (Taghleef Industries, Dubai, United Arab Emirates)
- *Ink*: Siegwerk series NC 133-4, black (Siegwerk Druckfarben, Siegburg, Germany) used together with extender NC 133-15 Extender Varnish G0 (Siegwerk Druckfarben, Siegburg, Germany) in a blend of two parts basic ink, one part extender.
- To dilute to print ready ink a solvent mixture of ethyl acetate CAS 141-78-6 (70 %) and ethanol CAS 64-17-5 (30 %) was used.
- *Doctor blades*: Two different doctor blades were used – Swedcut MicroKote G, 40 mm × 0,15 mm Standard Lamella (Swedev AB, Munkfors, Sweden) and MDC 40 mm × 0.150/0.065 mm × 1.3 mm, type No. 01040001500.02534, Roll #16 1 003110.01 (Daetwyler SwissTec, Bleienbach, Switzerland).

2.3 Design of experiments

The print trial was started by determining a good print quality with good adhesion to the BoPP substrate. This was used as the reference quality and determined the medium setting of the DoE: doctor blade Swedcut MicroKote G, doctor blade angle 55°, ink viscosity 19.8 s/ISO#4, cylinder type chromium.

The following DoE variables resulted in a total count of 36 trial points:

- *Cylinder surfaces*: chromium (Cro), diamond like carbon (DLC)
- *Ink viscosities*: 17.1 s, 19.8 s, 23.1 s measured with a 4 mm ISO flow cup (DIN EN ISO 2431, No. 322 Erichsen, Hemer, Germany)
- *Doctor blade types*: Swedcut MicroKote G, MDC Type No. 01040001500.02534
- *Doctor blade angles*: 48°, 55°, 60°

2.4 Sample analysis

The target functions of the DoE were print gradation, mottle of the solid, number of missing dots per area, line homogeneity and line width of fine lines, and quality assessment of a fine line star pattern.

2.4.1 Gradation measurements

Density measurements were performed on the tonal values (100 %, 75 %, 50 %, 25 %, 10 %, 5 %; screen frequency 100 lines/cm) in part C of the printing form layout with a Techkon SpectroDens Spectro-Densitometer (TECHKON GmbH, Germany).

2.4.2 Mottle index measurements

Mottle index measurements were performed on the 100 % tonal value field in part C. The overall mottle index is determined within a 300 dpi grid calculated by downscaling the 1 200 dpi image. The evaluation program is written in Java by Weichmann (2015) based on the algorithm by Rosenberger (2002).

It works on an area of 256 × 256 pixels, resp. 21.67 × 21.67 mm. It segments this area into squares that subsequently increase in size over 7 steps: 85 µm, 170 µm, 340 µm, 680 µm, 1.34 mm, 2.68 mm, 5.42 mm

edge length. For each size it calculates the mean of the absolute differences of the means of the grey values of the four sub-squares contained in each of these squares. Then it takes the mean of these means, multiplied by the standard deviation of these means, and multiplied by the standard deviation of the mean of the grey values of the squares. This results in a value for each size of squares. Finally, the mottle index is the mean over these 7 values.

The greater the value of the mottle index the more mottle is detected. An overall mottle index greater than 10 indicates well visible structures. Lower numbers but above 1 are associated with less severe mottle, however visible. Values below 1 indicate a nice homogeneous ink surface.

2.4.3 Missing dots analysis

In part C the tonal values of 50 %, 25 % and 10 % in a screen frequency of 100 lines/cm were used to count the missing dots per area. The evaluation program is written in Java by A. Weichmann (2015) and works with 1 200 dpi images. It utilizes edge filtering and adaptive dot size filtering to reliably count the number of missing dots in these fields and normalise them to cm^2. As missing dots distort the image and decrease the image quality, fewer missing dots are better.

2.4.4 Fine line analysis

In part B fine lines with a nominal width of 15 µm, 20 µm and 50 µm in-web and in cross-web direction were measured according to their width and homogeneity and additionally evaluated for their difference in the two directions. The evaluation program "Line Analysis for Printed Lines" is written in Java by A. Weichmann (2021). It utilizes an USB microscope (TOOLCRAFT USB Microscope, 2 592 × 1 944 pixels, magnification factor 200), with which a single line is captured. For analysis, the line is rotated into a horizontal position, then in every pixel column the upper and lower border is determined by a threshold operation (66 % of the brightness between darkest pixel and substrate white). After calculating the regression line of all pixels of a border, to exclude dents in the border or small holes within the line, 30 % of the pixels which have the greatest distance to the regression line are eliminated. With the residual 70 % the final regression line is calculated and determines this border of the line (Figure 2). The distance between the regression lines of the upper and the lower border defines the measured line width.

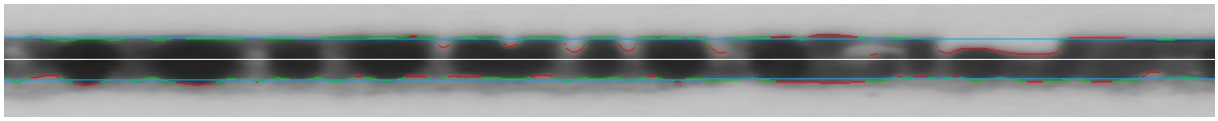

Figure 2: Fine line with nominal width 20 µm analysed in "Line Analysis for Printed Lines"; blue pixels: regression lines for borders, green pixels: border pixels for final regression (70 %), red pixels: 30 % of border pixels too far from regression line and therefore not used for final regression, white line: centre line between the two border lines

From the pixels of the middle area of the line (± 2 pixels around the centre line between the two border lines) the standard deviation is calculated. This number serves as the measure for homogeneity, i.e. the higher its value the less homogenous the reproduction of the line.

Figure 3 shows all lines measured for chromium and DLC for the trial point with viscosity 19.8 s #4, doctor blade Swedcut, angle 55°. Every line of chromium alternates with its counterpart of DLC surface. As expected, the cross-web lines reproduce much better than the in-web lines. Clearly the DLC lines are more defined. Especially the in-web direction lines are much better reproduced. The chromium 15 µm (3) line is not reproduced at all and the 20 µm line (7) is printed as fragments only, while the DLC lines are not perfect but recognizable as lines. The line DLC 50µm cross-web (10) is overly wide, as the high ink volume with this line depth leads to smearing.

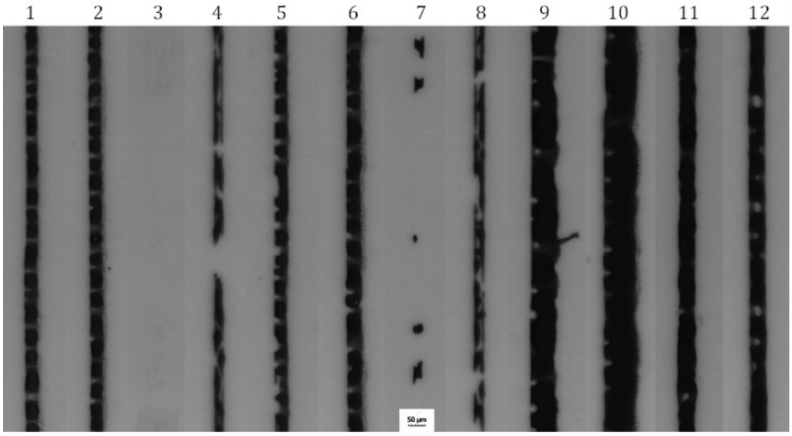

Figure 3: Example of lines, trial point with viscosity 20 s #4, doctor blade Swedcut, angle 55°, no ESA; 1: Cro 15 µm cross-web, 2: DLC 15 µm cross-web, 3: Cro 15 µm in-web (no line at all), 4: DLC 15 µm in-web, 5: Cro 20 µm cross-web, 6: DLC 20 µm cross-web, 7: Cro 20 µm in-web, 8: DLC 15 µm in-web, 9: Cro 50 µm cross-web, 10: DLC 50 µm cross-web, 11: Cro 50 µm in-web, 12: DLC 50 µm in-web

2.4.5 Visual assessment of fine line star pattern

The star pattern from area A of the print form (Figure 1) was cut out for every trial point and collected on one sheet to visually assess the quality of the fine line printing. The star pattern reproduces fine lines (15 µm, 20 µm, 25 µm, 30 µm) under many different angles and is especially sensitive to the homogeneity of the line and varying widths of the printed lines. The more homogeneous and uniform the widths of the lines under different angles, the better the quality. A scale was defined from 1 to 5 (Figure 4), where:

1. All lines are reproduced homogeneously
2. Some lines of 15 µm are fading away
3. Some lines of 15 µm are not printed and some lines of 20 µm are fading away
4. Some lines of 15 µm and 20 µm aren´t printed, some lines of 30 µm are fading away
5. All lines have some disruptions and are not homogeneous

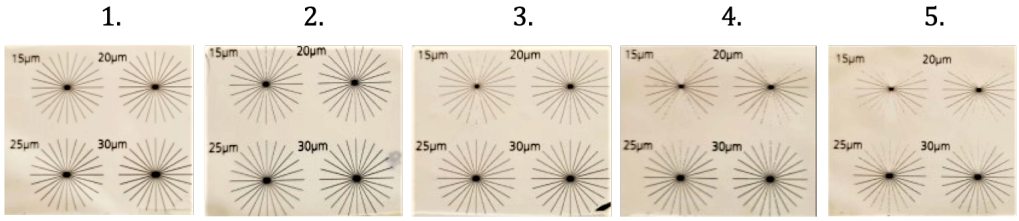

Figure 4: Examples of the five grades of star patterns with fine lines of 15 µm, 20 µm, 25 µm, and 30 µm from area A of the print form

The patterns were presented to 6 people, 3 with and 3 without printing background. Every person graded every trial point from 1 to 5 by looking at them with the help of a magnifying glass. The mean of all evaluators' gradings was used as a measure of the line quality.

3. Results and discussion

The density of the solids, the mottle, the missing dots and the fine line star patterns were analysed in MiniTab version 21.1.1 (Minitab, LLC, State College, Pennsylvania, USA). The Pareto diagram of the standardized effects and the main effects plot were used to graphically display the results.

3.1 Gradation measurements

The Pareto chart of the standardized effects for the solid density (Figure 5a) shows very clearly that the surface is by far the strongest factor of the DoE. Figure 5b shows that the DLC leads to a higher solid density than chromium. This is attributed to better cell emptying, and therefore more ink being transferred to the substrate. With DLC an average density of 2.26 was achieved, while chromium achieved only 1.91. The next relevant factor is the viscosity, where the best solid density was achieved with the lowest viscosity. The blade angle and its combination with the other factors, as well as the doctor blade on its own have a smaller influence, but they can still be considered significant. In fact, all the 4 factors, A, B, C, D, namely, surface, ink viscosity, doctor blade and blade angle, respectively, are over the significance threshold. The lower tonal values showed very similar results and are not detailed in this paper.

a)

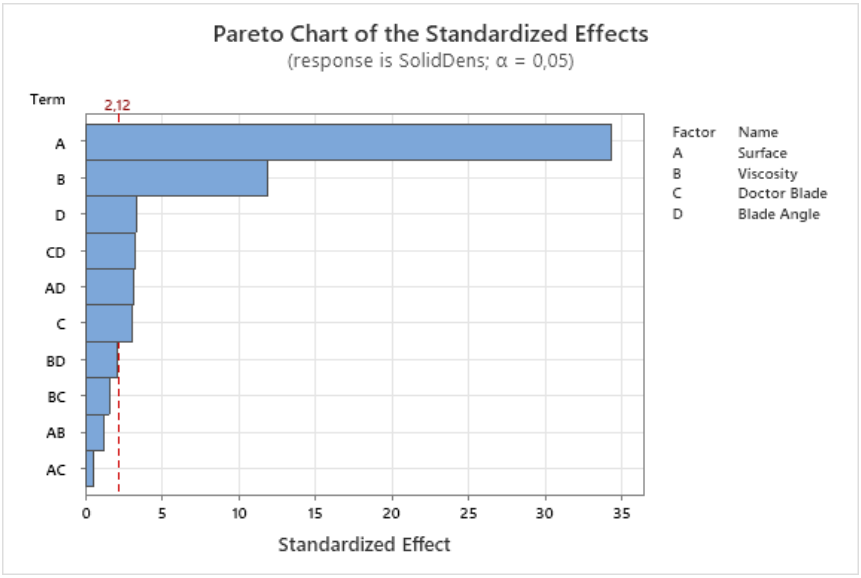

b)

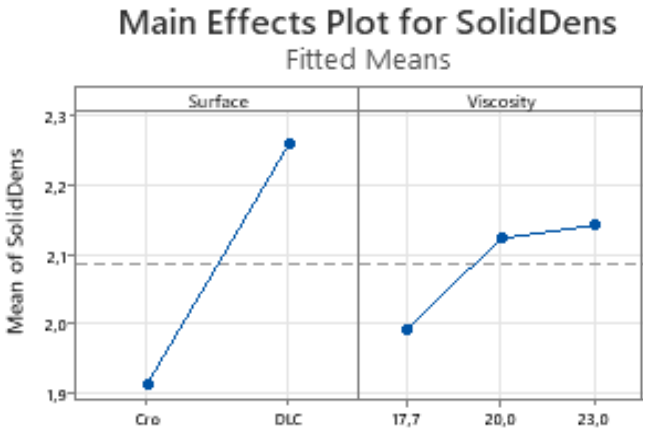

Figure 5: Pareto diagram of the standardized effects (a), and surface and viscosity plot (b) for the gradation measurements of the solid density, the red dotted line represents the significance level of 95 %

3.2 Mottle index measurements

The mottle index measurements show that the surface and its combination with ink viscosity are the most significant effects (Figure 6a). All the other parameters (viscosity, doctor blade and blade angle) and their combinations are quite far below the threshold. Indeed, the drying patterns depend on the amount of solvent in the ink. The best results were achieved with the highest viscosity and the chromium surface

(Figure 6b), the MDC doctor blade and the 55° blade angle. The DLC surface resulted worse for mottle, but this apparently negative result is caused by better cell emptying, that as mentioned above results in higher solid density, meaning that more ink volume was transferred. This increases the micro flow of the inks and the drying time and therefore these artefacts-related formations are facilitated. This effect, however, can be overcome easily by reducing the cell volume. In fact, 2.26 solid density is a high value (maximum was 2.44), and with smaller or more shallow cells a satisfying value of around 2.0 for the density can be achieved and consequently mottle reduced.

a)

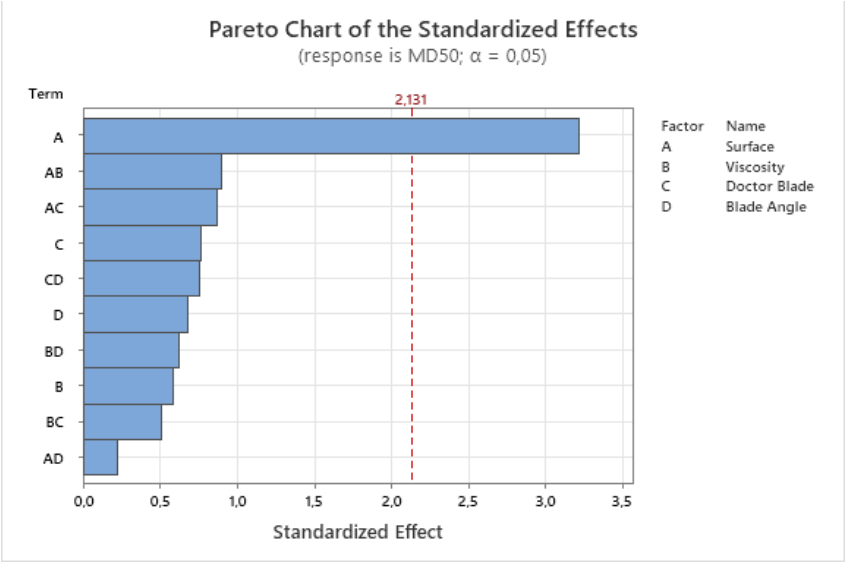

b)

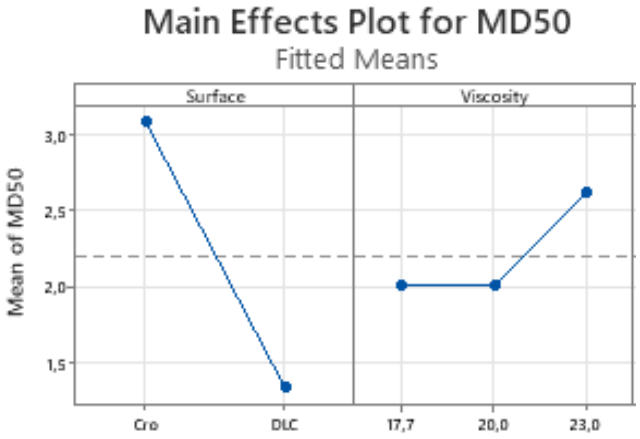

Figure 6: Pareto diagram of the standardized effects (a), and surface and viscosity plot (b) for mottle

3.3 Missing dots analysis

The average numbers of missing dots over all trial points normalised to cm² are shown in Table 1. The number of missing dots is higher for a lower tonal value, i.e. the smaller the dots printed.

Table 1: Average number of missing dots over all trial points normalised to cm²

Coating	50 %	25 %	10 %
Chromium	3.1	200	1 524
DLC	1.3	64	296

The missing dots per area at the tonal value of 50 % have a similar behaviour as at 10 %. In both cases the only significant parameter was the cylinder surface applied (Figure 7a). The other aspects could be neglected. The DLC surface performed clearly better, while the low and medium viscosity appeared to be favourable at the same level, for 50 % (Figure 7b), while for 10 % the best result was the opposite, i.e. with the highest viscosity the smallest dots could be reproduced better with less solvent, and, thus, more pigment and binder. For both 50 % and 10 % the Swedcut doctor blade and 48° blade angle provided the optimal choice.

a)

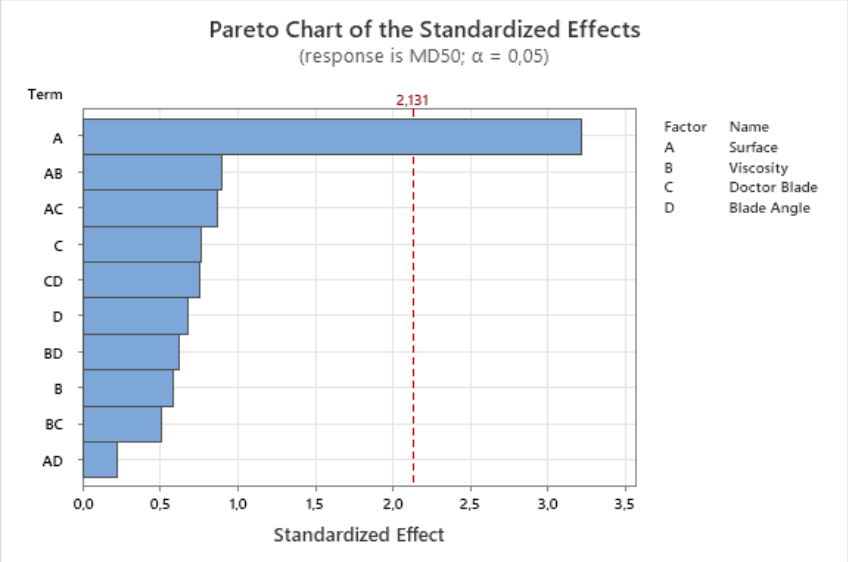

b)

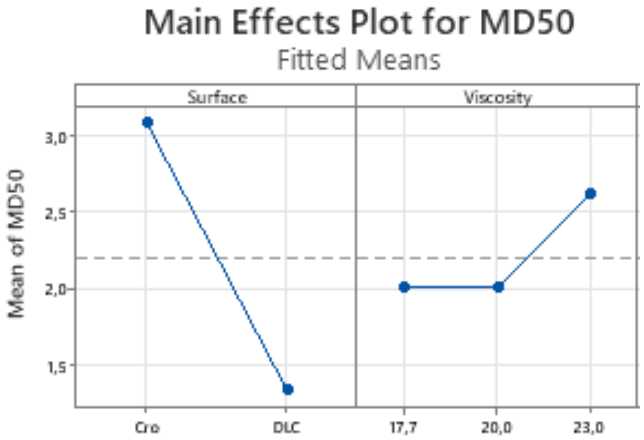

Figure 7: Pareto diagram of the standardized effects (a), and surface and viscosity plot (b) for missing dots in a patch of tonal value of 50 %

For the tonal value 25 % the most important parameter was the surface. In this case the viscosity was significant as well, though at a much lower level (Figure 8a). The missing dots per area at the tonal value of 25 % were counted least with the DLC surface and with the highest viscosity (Figure 7b). The Swedcut doctor blade had only slightly better values than the MDC, while the 48° blade angle was ideal.

a)

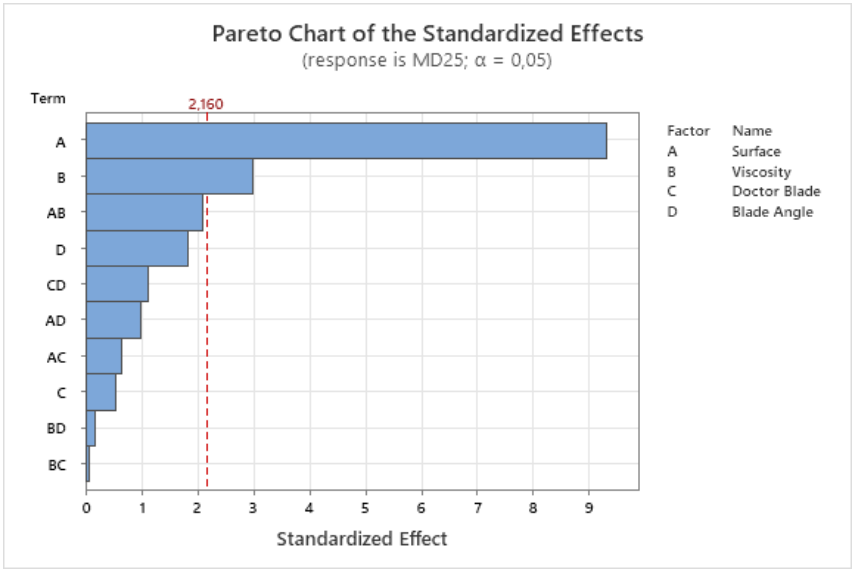

b)

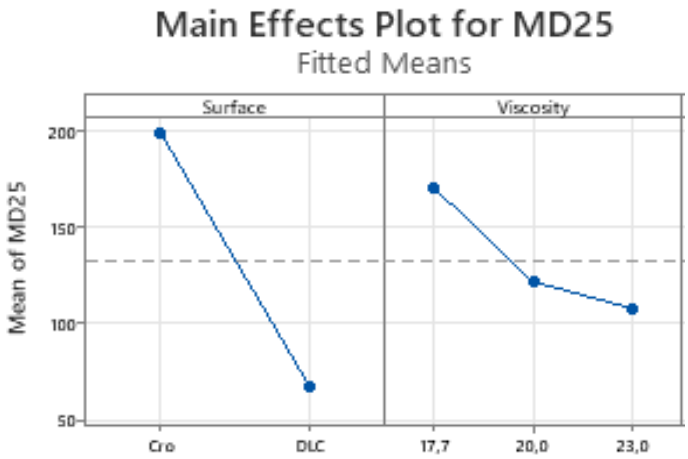

Figure 8: Pareto diagram of the standardized effects (a), and surface and viscosity plot (b) for missing dots in a patch of tonal value 25 %

3.4 Fine line analysis

Table 2 shows the average line width for 15 µm, 20 µm and 50 µm lines in in-web and in cross-web direction. The line analysis was not possible at all for the in-web 15 µm lines with chromium surface, as they did not print well enough to be analysed, in contrast to the DLC, where the lines were clearly defined. The lines appear reasonably spread with the DLC significantly wider than chromium. The cross-web lines are more than 10 µm wider than the vertical ones, which is to be expected with the gravure printing process. As mentioned with Figure 3 the excessive spreading of the cross-web 50 µm DLC line is due to smearing.

Table 2: Average line widths in µm over all trial points for chromium (Cro) and DLC for 15 µm, 20 µm and 50 µm lines in in-web and in cross-web direction

Lines	Cro 15 µm	DLC 15 µm	Cro 20 µm	DLC 20 µm	Cro 50 µm	DLC 50 µm
cross-web	33.1	37.3	36.0	43.2	76.7	93.7
in-web	---	25.6	26.9	30.0	46.1	47.1

The homogeneity of the lines is also significantly better with DLC. As an example, the Pareto diagram and main effects plot of homogeneity of the cross-web 20 µm line are shown in Figure 9.

Viscosity plays an important role as well. Surprisingly, higher viscosity results in better results. A 60° blade angle is preferred for cross-web line width and cross-web homogeneity. For in-web homogeneity the 48° is better. Swedcut is slightly preferred over MDC.

a)

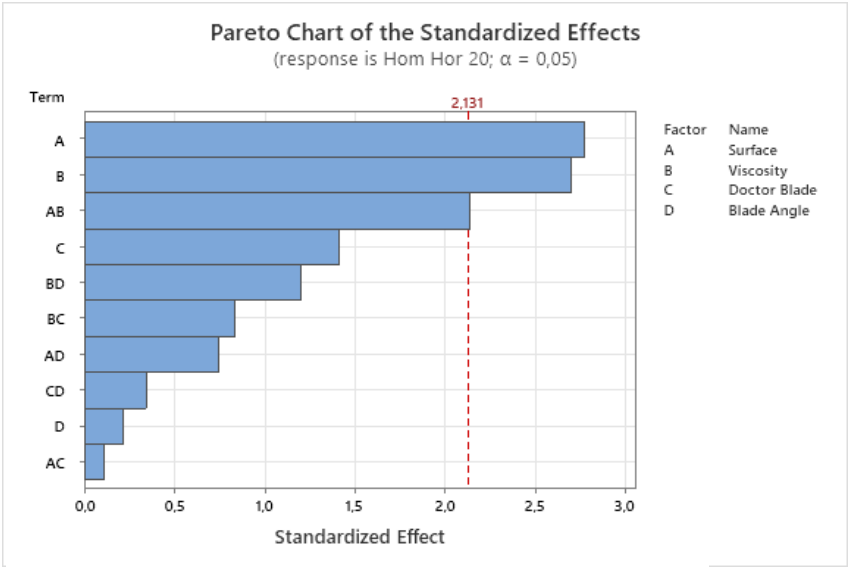

b)

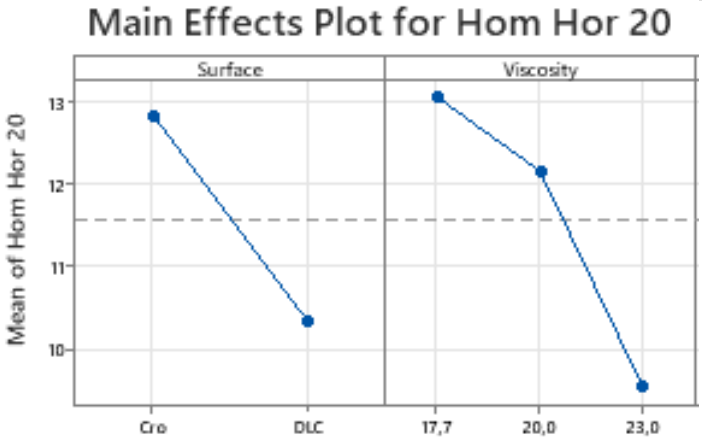

Figure 9: Pareto diagram of the standardized effects (a), and surface and viscosity plot (b) for homogeneity of the cross-web direction 20 µm lines

3.5 Visual assessment of fine line star pattern

The Pareto analysis of the star pattern assessment shows a very clearly advantage of the DLC surface over the chromium surface. All other factors of the DoE are much weaker than this factor (Figure 10a). According to the results of the test, the DLC cylinder produces clearly more homogeneous printed lines (Figure 10b) with an average grade of 1.9. Samples which were printed with the Chromium cylinder showed much worse results (average 3.7). Especially the thin vertical lines could not be reproduced in most cases. After the cylinder's surface, the next factors that influence the print are in order of proportionality the viscosity, the blade angle, and their combination. The best results are achieved with medium viscosity and medium blade angle. The doctor blade plays a minor role.

a)

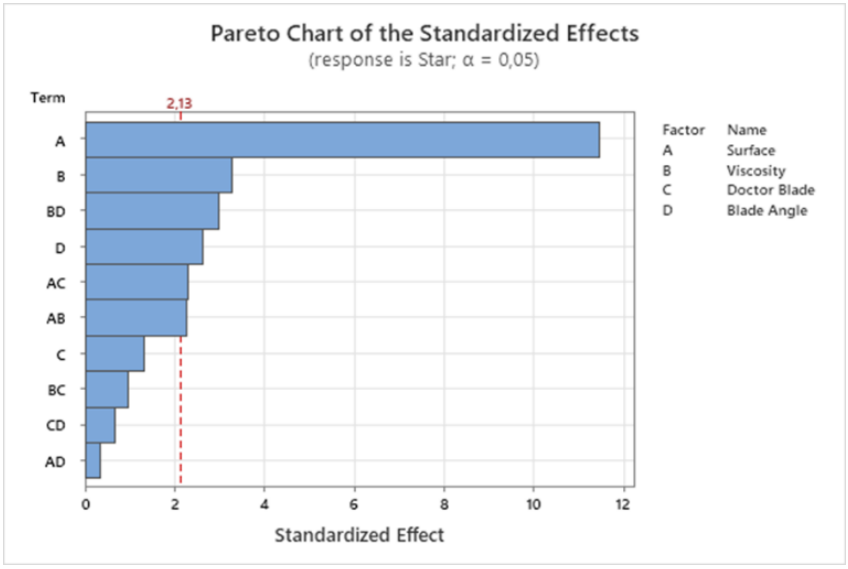

b)

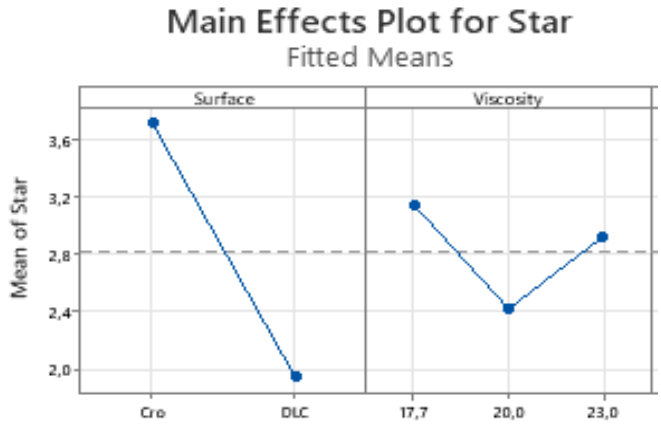

Figure 10: Pareto diagram of the standardized effects (a), and surface and viscosity plot (b) for the visual assessment of the star patterns

3.6 Surface energy

According to measurements by RotoHybrid the surface energy of the chromium plated cylinder's surface is in the range of 60 mN/m, while the surface energy of the DLC is in the range of 45 mN/m. Higher surface energies lead to a better wetting, i.e. filling of the cells. As organic solvents based gravure ink has typically a surface energy between 25 mN/m and 30 mN/m, which is significantly lower than these values, with both surface one can expect a good wetting. The ink release then is indeed an ink splitting. However, the point of splitting will lay the nearer to the surface the smaller the difference between the surface energies, therefore explaining at least part of the higher volume of ink transferred to the substrate with DLC.

Another factor is the thinner layer of DLC (4–5 µm compared to 5–7 µm for the chromium layer) which leads to a slightly larger cell volume of the DLC coated cells.

4. Conclusions and outlook

Practically each part of the print trial analysis has shown a crucial improvement in printing of micro structures and fine lines with DLC compared to traditional chromium plating. In every case of the DoE evalu-

ation the surface of the cylinder was the primary effect. In decreasing order, the viscosity, the blade type, and blade angle played a much smaller role in most cases. The smaller the structures the bigger the improvement. This indicates that the DLC surface has a significantly better ink releasing capability. This we postulate, as shown in the prior art, is due to a lower surface energy and a slightly thinner layer compared to the standard chromium surface. If microstructural properties of the surface play an additional role is to be shown in a future study.

Surely, this better performance together with the improved wear resistance is very interesting for high value applications like security printing and functional printing.

Acknowledgements

We kindly thank GRT (GRT GmbH, Hamm, Germany) for manufacturing of the gravure cylinder forms and the chrome plating of one of them and RotoHybrid (Roto-Hybrid Gravure Technologies, Wuppertal, Germany) for DLC coating the other as well as sharing the surface energy measurements.

References

Brumm, P., Weber, T.E., Sauer, H.M. and Dörsam, E., 2021a. Ink splitting in gravure printing: localization of the transition from dots to fingers. *Journal of Print and Media Technology Research*, 10(2), pp. 81–93. https://doi.org/10.14622/JPMTR-2016.

Brumm, P., Lindner, N., Weber, T. E., Sauer, H. M. and Dörsam, E., 2021b. A deep learning approach for the classification task of gravure printed patterns. In: C. Ridgway, ed. *Advances in Printing and Media Technology: Proceedings of the 47th International Research Conference of iarigai.* Athens, Greece, 19–23 September 2021. Darmstadt: iarigai, pp. 2–9. https://doi.org/10.14622/Advances_47_2021.

European Commission, 2022. *Periodic reporting for period 2 – green gravure (Roto-Hybrid Process® cylinders for green gravure printing)*. [online] Available at: <https://cordis.europa.eu/project/id/738010/reporting> [Accessed 25 March 2022].

Grau, G., Cen, J., Kang, H., Kitsomboonloha, R., Scheideler, W.J. and Subramanian, V., 2016. Gravure-printed electronics: recent progress in tooling development, understanding of printing physics, and realization of printed devices. *Flexible and Printed Electronics*, 1(2): 023002. https://doi.org/10.1088/2058-8585/1/2/023002.

Hübner, G., 1991. *Ein Beitrag zum Problem der Flüssigkeitsspaltung in der Drucktechnik.* Dr.-Ing. Dissertation. Technische Hochschule Darmstadt. https://doi.org/10.25534/tuprints-00013550.

Kumar, S., 2015. Liquid transfer in printing processes: liquid bridges with moving contact lines. *Annual Review of Fluid Mechanics*, 47(1), pp. 67–94. https://doi.org/10.1146/annurev-fluid-010814-014620.

Kunz, W., 1975. Ink transfer in gravure process. In: *TAGA Proceedings 1975: Annual meeting of the Technical Association of the Graphic Arts*. Toronto, Ontario, 1975. Rochester, NY, USA: TAGA, pp. 151–176.

Rosenberger, R.R., 2002. *Mottle measurement of wet trap, back trap and other motley images.* [pdf] VERITY IA. Available at: <https://www.verityia.com/_files/ugd/c4e5fa_efd8667d40f44c45a0187b99b2fb7559.pdf> [Accessed 25 March 2022].

Weichmann, A., 2015. *GravureQ: commercially available software for mottle and missing dots analysis*. Hochschule der Medien Stuttgart, Germany.

Weichmann, A., 2015. *Line analysis for printed Lines*. Hochschule der Medien Stuttgart, Germany.

DOI 10.14622/Advances_48_2022_21

Multivariate sensor dataset of an industrial rotogravure printing press (MSDIRPP)

Tobias Enk and Peter Urban

University of Wuppertal, School of Electrical, Information and Media Engineering,
Rainer-Gruenter-Straße 21, D-42119 Wuppertal
E-mails: toenk@uni-wuppertal.de; purban@uni-wuppertal.de

Short abstract

We present a multivariate sensor dataset for machine learning research in context of industrial print application. The dataset contains 7 608 rolls of pre-processed multivariate sensor data of a single production scale rotogravure printing press. The data volume corresponds to 43 181 km of printed cardboard and paper. For each roll, we provide high-resolution sampled inline sensor data, machine condition labels and several meta information. Besides basic information like machine speed the dataset contains web movement data such as web edge and web tension measurements, material measurement like web moisture and print quality data such as register measurements in cross and machine direction for 11 print units. We publish the dataset to provide data researchers a strong baseline dataset for several machine learning applications in industrial printing. The dataset is publicly available under Creative Common Licence CC BY 4.0 International.

Keywords: multivariate time series, industrial rotogravure printing, machine learning, web run, register quality

1. Introduction and background

A lack of access to industrial data is just one of many problems that stand in the way of successfully implementing machine-learning projects for industrial applications. The acquisition and processing of industrial data is a particularly time-consuming and tedious task for data scientists.

In the field of industrial printing, only a few major case studies from practice exist, where a larger amount of production data were gathered to investigate specific research questions. These datasets in most cases are not available to other researchers.

Examples of not publicly available datasets:
Alzghoul, et al. (2009) investigate web breaks and runnability with soft computing techniques using a dataset, which is divided into paper, winding and press related parameters.

Parola, et al. investigate the runnability and web widening in a larger dataset gathered in printing plants (Parola, et al., 2003; Paukku, Parola and Vuorinen, 2004).

Even fewer datasets are publicly accessible in an industrial printing related context, where other researchers can apply, test or develop existing or new machine learning approaches in this field.

Examples of publicly available datasets:
Bob Evans published the “Cylinder Band Data Set”, which is a multivariate categorical dataset for classification task in rotogravure printing application, focussing on banding effects (Evans, 1995).

Chitta Ranjan provides a multivariate time series dataset from a paper manufacturing process for data-driven web break analysis, which is very close to a printing industry (Ranjan, et al., 2018).

Pauline Brum provides a collection of digitized gravure printing samples as an image dataset from a lab-scale rotogravure press for the analysis of hydrodynamic pattern formation (Brumm, et al., 2021).

We provide a large public available multivariate inline measurement dataset collected from a single industrial rotogravure printing press for package printing over two years of production (Enk, 2022). It contains 7608 printed rolls of mainly cardboard material including rich annotations such as meta information and labels of the machine and sensor states. Sensor data were provided as machine speed independent, distance discrete multivariate datasets roll by roll.

The dataset can be used as a baseline dataset for various machine-learning approaches on the gravure printing domain, such as

- Rare event estimation
- Print quality estimation
- Cluster analysis
- Classification tasks
- Time series forecasting
- Feature extraction tasks
- Synthetic data generation
- Pre-training tasks

From a printing domain perspective, potential research topics could be

- Web runnability research
- Web movement research
- Register quality research
- Winding defect research
- Web tension dynamic research

2. Dataset structure

We provide the dataset in a simple structure containing a metadata file ‘metadata.csv’ with anonymized meta information for each roll and the printed job. The link to each signal file is the roll-id. Accordingly, we named the roll specific sensor files by their roll_id, exemplarily ‘10001.csv’ for roll_id 10001. Figure 1 demonstrates the dataset structure.

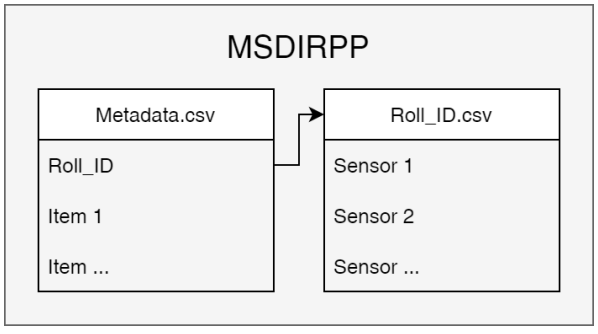

Figure 1: Dataset structure of the MSDIRPP dataset

A list of abbreviations used in MSDIRPP is shown in Table 1.

Table 1: Abbreviations used in MSDIRPP

Abbreviation	Name
CD	Cross Direction
MD	Machine Direction
OS	Operating Side
DS	Drive Side
UW	Unwinder
RW	Rewinder
IPU	Infeed Pull Unit
PU	Print Unit
EU	Embossing Unit
CC	Cross Cut Unit
WGS	Web Guiding System

An overview of columns in the metadata file and the signal files are given in Table 2 and Table 3. Missing values are marked as '−1' in metadata file. In the signal files missing values are marked as 'nan'.

Table 2: Metadata column description

Column name	Unit	Type	Valid within each	Data source	Values
Roll_ID	-	numerical	-	data recorder	[10001, (...), 17608]
SignalFile	-	textual	-	data recorder	[10001.csv, (...), 17608.csv]
TimeStamp	-	temporal	-	data recorder	[value]
Date	-	temporal	-	data recorder	[value]
Start_Time	-	temporal	-	data recorder	[value]
End_Time	-	temporal	-	data recorder	[value]
Roll_Nr	-	categorical	Batch_Nr	extern metadata	[−1, 1, 2, (...)]
Roll_CD_Position	-	categorical	Supplier	extern metadata	[−1, 1, 2, (...)]
Batch_Nr	-	categorical	-	extern metadata	[−1, 1, 2, (...), 246]
Material	-	categorical	-	extern metadata	[−1, C01, C02, C03, GC1, GC2, GZ1]
Web_Width_[mm]	mm	numerical	-	extern metadata	[−1, value]
Grammage_[g/qm]	g/m^2	numerical	-	extern metadata	[−1, value]
Factory	-	categorical	-	extern metadata	[−1, 1, 2, (...), 13]
Supplier	-	categorical	-	extern metadata	[−1, 1, 2, (...), 9]
Converting	-	categorical	-	extern metadata	[−1, 1(Sheet), 2(Roll)]
Order_Nr	-	categorical	-	extern metadata	[−1, 1, 2, (...), 634]
WebGuiding_Ref_Edge	-	categorical	-	extern metadata	[−1, 1(OS), 2(DS), 3(Center)]
Unwinding_Shaft	-	categorical	-	extern metadata	[−1, 1, 2]
Cylinder_ Circumference_[mm]	mm	numerical	-	signal files	[−1, value]
Roll_UW_Core_ Diameter_[mm]	mm	numerical	-	signal files	[−1, value]
Caliper_[mm]	mm	numerical	-	signal files	[−1, value]
Steady_State_Data_[m]	m	numerical	-	signal files	[−1, value]

Column name	Unit	Type	Valid within each	Data source	Values
Real_Run_Length_[m]	m	numerical	-	signal files	[−1, value]
State_Reg_PU02	-	logical	-	signal files	[−1, 0, 1]
State_Reg_PU03	-	logical	-	signal files	[−1, 0, 1]
State_Reg_PU04	-	logical	-	signal files	[−1, 0, 1]
State_Reg_PU05	-	logical	-	signal files	[−1, 0, 1]
State_Reg_PU06	-	logical	-	signal files	[−1, 0, 1]
State_Reg_PU07	-	logical	-	signal files	[−1, 0, 1]
State_Reg_PU08	-	logical	-	signal files	[−1, 0, 1]
State_Reg_PU09	-	logical	-	signal files	[−1, 0, 1]
State_Reg_PU10	-	logical	-	signal files	[−1, 0, 1]
State_Reg_PU11	-	logical	-	signal files	[−1, 0, 1]
State_Reg_PU12	-	logical	-	signal files	[−1, 0, 1]
State_Reg_EU01	-	logical	-	signal files	[−1, 0, 1]
State_Reg_EU02	-	logical	-	signal files	[−1, 0, 1]

Below are some additional descriptions of the column names:

- Roll_Nr: sequential number of produced roll (for each batch)
- Roll_CD_Position: CD position on original mother roll (supplier specific)
- Batch_Nr: categorical material batch number
- Converting: converting to sheets or roll after printing
- WebGuiding_Ref_Edge: reference edge using as input for web guiding
- Unwinding_Shaft: used shaft to unwind the roll
- Cylinder_Circumference_[mm]: printing cylinder circumference in mm
- Roll_UW_Core_Diameter_[mm]: diameter of roll core in mm
- Steady_State_Data_[m]: total length of steady state production
- Real_Run_Length_[m]: total unwound material length in m

Table 3: Signal file column description

Column name	x/y	Type	Unit	Description
Length	x	numerical	m	processed material length
[state_roll_inner_part]_L	y	logical	-	roll length minus first and last 200 m
[state_tension_UW]_L	y	logical	-	condition web tension at UW
[state_tension_IPU]_L	y	logical	-	condition web tension at IPU
[state_tension_PU7]_L	y	logical	-	condition web tension at PU7
[state_tension_PU12]_L	y	logical	-	condition web tension at PU12
[state_tension_EU1]_L	y	logical	-	condition web tension at EU1
[state_tension_CC]_L	y	logical	-	condition web tension at CC
[state_machine_speed]_L	y	logical	-	condition machine speed
[state_waste]_L	y	logical	-	unsaleble products marked by machine operator
[state_machine]_L	y	logical	-	steady state machie condition
[state_register_PU2]_L	y	logical	-	activity of register measurement at PU2
...	y	logical	-	activity of register measurement at PU3-12
[state_register_EU1]_L	y	logical	-	activity of register measurement at EU1

Column name	x/y	Type	Unit	Description
[state_register_EU2]_L	y	logical	-	activity of register measurement at EU2
[Web_Speed]_L	y	numerical	m/min	web speed
[WebGuiding_Motorposition]_L	y	numerical	-	current position of WGS
[WebGuiding_Center]_L	y	numerical	mm	center position of web
[WebGuiding_Edge1]_L	y	numerical	mm	web edge measured at WGS (OS)
[WebGuiding_Edge2]_L	y	numerical	mm	web edge measured at WGS (DS)
[Roll_UW_Rest]_L	y	numerical	m	rest material length on core at UW
[Roll_UW_Diameter]_L	y	numerical	mm	roll diameter at UW
[Caliper]_L	y	numerical	mm	material thickness/caliper
[Reg_PU2_CD]_L	y	numerical	mm	CD misregister at PU2
...	y	numerical	mm	CD misregister at PU3-12
[Reg_EU1_CD]_L	y	numerical	mm	CD misregister at EU1
[Reg_EU2_CD]_L	y	numerical	mm	CD misregister at EU2
[Reg_PU2_MD]_L	y	numerical	mm	MD misregister at PU2
...	y	numerical	mm	MD misregister at PU3-12
[Reg_EU1_MD]_L	y	numerical	mm	MD misregister at EU1
[Reg_EU2_MD]_L	y	numerical	mm	MD misregister at EU2
[WebEdge_UW]_L	y	numerical	mm	web edge measured at UW (DS)
[WebEdge_PU2]_L	y	numerical	mm	web edge measured at PU2 (DS)
[WebEdge_PU7]_L	y	numerical	mm	web edge measured at PU7 (DS)
[WebEdge_PU10]_L	y	numerical	mm	web edge measured at PU10 (DS)
[WebEdge_PU11]_L	y	numerical	mm	web edge measured at PU11 (DS)
[Dancer_UW]_L	y	numerical	%	dancer movement after UW
[Dancer_RW]_L	y	numerical	%	dancer movement before RW
[WebTension_UW]_L	y	numerical	N	web tension after UW
[WebTension_InfeedPullUnit]_L	y	numerical	N	web tension at IPU
[WebTension_PU7]_L	y	numerical	N	web tension at PU7
[WebTension_PU12]_L	y	numerical	N	web tension at PU12
[WebTension_EU1]_L	y	numerical	N	web tension at EU1
[WebTension_CC]_L	y	numerical	N	web tension at CC
[WebMoisture]_L	y	numerical	%	relative web moisture direct after UW

3. Materials and methods

3.1 Printing press

Our dataset was gathered from a 178 m long production scale roll-to-roll mechanical line shaft rotogravure press with 11 printing units (PU) and two embossing units (EU). The press consists of an unwinder (UW), a tension control system, a web guiding system (WGS) for compensation of lateral web displacements, followed by the infeed pull unit (IPU). In the 134 m long printing section are 11 equal PUs. The press can optionally convert printed web to roll or sheet. Solvent-based inks are thermal dried directly after each PU. Misregister is measured once per print length (once per printing cylinder turn) by observing printed triangle marks. The first printed colour is used as a reference for misregister calculation. These displacement

values are then used for register control, which is realised by adjusting the print cylinders in CD and changing the web length in MD before each PU. The press is equipped with several sensors see Figure 2.

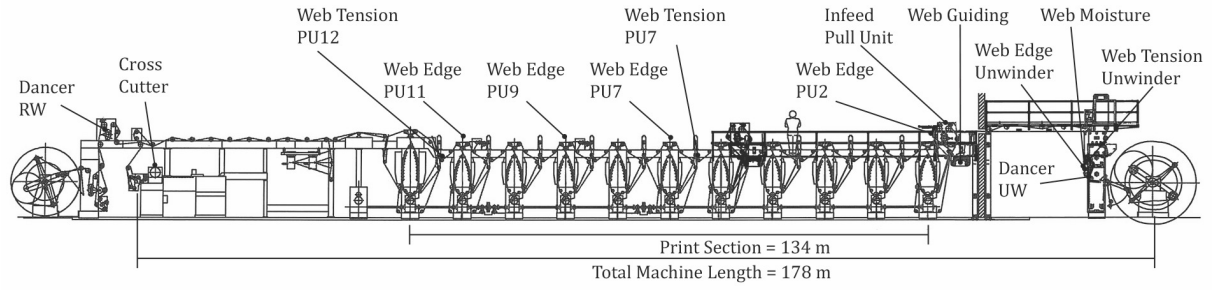

Figure 2: Production scale rotogravure printing press with some sensor positions

3.2 Data acquisition

All measurements are recorded by a process data acquisition system with a sampling rate of 100 Hz, independent of the real sensor specific sampling rate. Therefore, we fill missing values with the last recorded measurement value. Details of all inline measurements are given in Table 4.

Table 4: Inline measurement details

Nr	Measurement	Unit	MD Pos.	CD Pos.	Objective	Unit	Resolution	Sampling	Sensor
1	Web Moisture	UW	0 m	center	rel. moisture	%	-	> 100 Hz	infrared
2	Web Speed	Drive	0 m	-	speed	m/min	-	> 100 Hz	encoder
3	Roll Diameter	UW	0 m	center	distance	mm	-	> 100 Hz	laser distance
4	Web Tension	UW	2 m	CD	force	N	-	> 100 Hz	strain gauge
5	Web Tension	IPU	19 m	CD	force	N	-	> 100 Hz	strain gauge
6	Web Tension	PU7	78 m	CD	force	N	-	> 100 Hz	strain gauge
7	Web Tension	PU12	137 m	CD	force	N	-	> 100 Hz	strain gauge
8	Web Tension	EU	154 m	CD	force	N	-	> 100 Hz	strain gauge
9	Web Tension	CC	178 m	CD	force	N	-	> 100 Hz	strain gauge
10	Dancer Movement	UW	2 m	CD	movement	%	-	> 100 Hz	potentiometer
11	Dancer Movement	RW	170 m	CD	movement	%	-	> 100 Hz	potentiometer
12	Web Edge	UW	2 m	DS	position	mm	0.005 mm	500 Hz	CCD
13	Web Edge 1 + 2	WGS	18 m	OS + DS	position	mm	0.001 mm	500 Hz	infrared
14	Web Edge	PU2	20 m	DS	position	mm	0.005 mm	500 Hz	CCD
15	Web Edge	PU7	88 m	DS	position	mm	0.005 mm	500 Hz	CCD
16	Web Edge	PU10	112 m	DS	position	mm	0.005 mm	500 Hz	CCD
17	Web Edge	PU11	135 m	DS	position	mm	0.005 mm	500 Hz	CCD
18, 19	Register CD + MD	PU2	23 m	OS	misregister	mm	0.005 mm	1/cyl. turn	contrast
20, 21	Register CD + MD	PU3	35 m	OS	misregister	mm	0.005 mm	1/cyl. turn	contrast

Nr	Measurement	Unit	MD Pos.	CD Pos.	Objective	Unit	Resolution	Sampling	Sensor
22, 23	Register CD + MD	PU4	46 m	OS	misregister	mm	0.005 mm	1/cyl. turn	contrast
24, 25	Register CD + MD	PU5	59 m	OS	misregister	mm	0.005 mm	1/cyl. turn	contrast
26, 27	Register CD + MD	PU6	70 m	OS	misregister	mm	0.005 mm	1/cyl. turn	contrast
28, 29	Register CD + MD	PU7	81 m	OS	misregister	mm	0.005 mm	1/cyl. turn	contrast
30, 31	Register CD + MD	PU8	93 m	OS	misregister	mm	0.005 mm	1/cyl. turn	contrast
32, 33	Register CD + MD	PU9	105 m	OS	misregister	mm	0.005 mm	1/cyl. turn	contrast
34, 35	Register CD + MD	PU10	117 m	OS	misregister	mm	0.005 mm	1/cyl. turn	contrast
36, 37	Register CD + MD	PU11	129 m	OS	misregister	mm	0.005 mm	1/cyl. turn	contrast
38, 39	Register CD + MD	PU12	141 m	OS	misregister	mm	0.005 mm	1/cyl. turn	contrast
40, 41	Register CD + MD	EU1	157 m	OS	misregister	mm	0.005 mm	1/cyl. turn	contrast
42, 43	Register CD + MD	EU2	157 m	OS	misregister	mm	0.005 mm	1/cyl. turn	contrast

3.3 Pre-processing

Due to the special nature of sequentially ordered sub-processes in a web-processing system such as a printing press, process and quality measurement data are generated at different points in the press with different time stamps. To enable locally resolved analysis of all process and quality data over the web material independent of its original process speed, we pre-process the collected time series in three steps.

1. The continuous data stream coming from the data acquisition system is truncated, when a roll is changed at the unwinder and accumulated into a single multivariate time series raw data file containing all inline measurements for each roll.
2. For a web speed independent analysis, the signal data $x_i(t)$ of each sensor s_i were aligned via their specific time constant τ_i, according to the sensors position in the printing machine l_i relative to the unwinder (UW) and the web speed v (see Figure 3). Where $\hat{t}_i$ is the sensor specific aligned time axis. The individual web stretch is not considered.

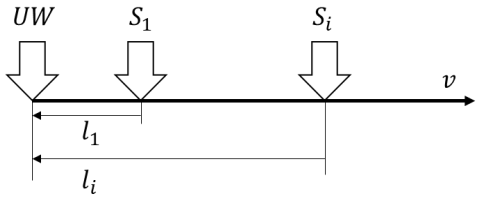

Figure 3: Time axis alignment relative to unwinder in printing machine

$$\tau_i = \frac{l_i}{v} \quad [1]$$

$$\hat{t}_i = t_i - \tau_i \quad [2]$$

3. Time series are resampled to a new uniform distance discrete base. We choose a sampling rate of 10 m^{-1} as a trade-off between data volume and resolution. By considering the Nyquist-Shannon sampling theorem, we think it is a sufficient value, because most relevant process fluctuations are considered to be slower than 5 m^{-1}, which corresponds to a wavelength of 0.2 m.

3.4 Machine condition labeling

For statistical evaluations, it can be useful to distinguish steady state machine condition data from unsteady production data. For this reason, we derive the boolean label signals 'state_machine' and 'state_register' from sensor signals. Where 'state_machine' marks steady state machine condition data and 'state_register' the activity of PUs. We use the web speed and web tension data as indicator signals to determine the machine condition. Both has to be in a specific value range, which indicates the machine runs in a stable and continuous production mode and not in a transient or setup mode. Further, we use standard deviation thresholds for indication of process parameter changes or sensor activity. In Table 5, all used thresholds are given to check machine condition or activity of indicator signals.

Table 5: Machine condition labelling thresholds

Activity	min value	max value	std dev threshold
check web speed steady state	50	800	10.00
check web tension steady state	100	3 000	100.00
check register activity	-	-	0.01

Condition state labels were calculated with a moving window of 200 m width and a movement of 0.1 m. To consider transition periods before and after a significant process change we keep the label centred over the signal by shifting the calculated label signal back in time with the half of the window width. Further the boolean indicator signal 'state_roll_inner_part' marks the entire roll except the first and last 200 m to ignore effects from a roll change. The final 'state_machine' label signal is the intersection of all indicator label signals. Steady state machine condition labelled data take account for approximately 87 % of the total dataset. The boolean 'state_waste' label is a manual signal, which is generated by the machine operator directly at the printing press to mark unsaleable products.

3.5 Data exploration

Our dataset contains 7 608 rolls of printed cardboard and paper, which corresponds to 43 181 km of printed web material. The dataset contains mainly multi-ply and coated cardboard materials in a grammage range of 210 g/m^2 – 240 g/m^2, next to some more lightweight materials, see Table 6.

Table 6: Material information

Material	Description	Rolls	Total run length [km]	Steady state [km]	Roll length median [m]	Grammage median [g/m^2]	Web width median [mm]	Caliper median [mm]
GC1	Coated FBB*, white back	3 879	20 458	18 065	5 352	220	743	0.316
GC2	Coated FBB*, bright back	44	228	201	5 218	210	705	0.330
GZ1	Coated SBB*	3 151	18 300	15 720	5 654	240	835	0.291
C01	Custom specific	12	172	165	14 290	70	757	0.052
C02	Custom specific	135	2 174	2 031	16 387	80	1 015	0.073
C03	Custom specific	29	222	208	7 707	−1	−1	0.148
−1	no information	358	1 627	1 328	4 933	−1	−1	0.336
Total		7 608	43 181	37 718				

* according to DIN 19303

The distributions of some dataset aspects are shown in the following plots. Figure 4 shows the dominance of some material suppliers. Figure 5 shows the preferred use of late PUs for jobs with less than 11 colors. There is no PU1 in the printing machine, so first possible printing unit is PU2. This means first register measurement can be made in PU3.

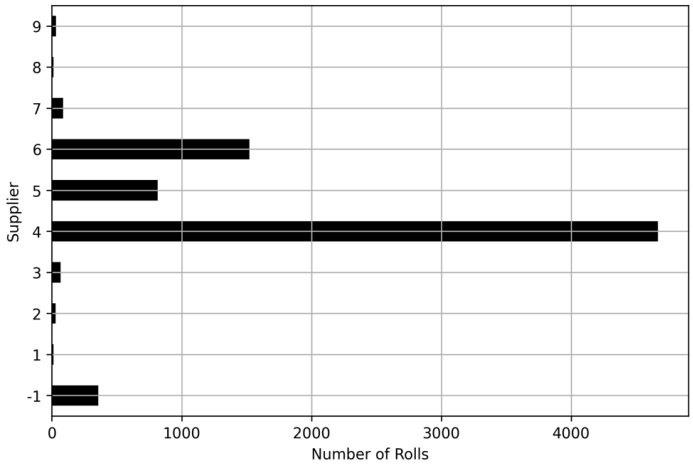

Figure 4: Number of rolls per suppliers

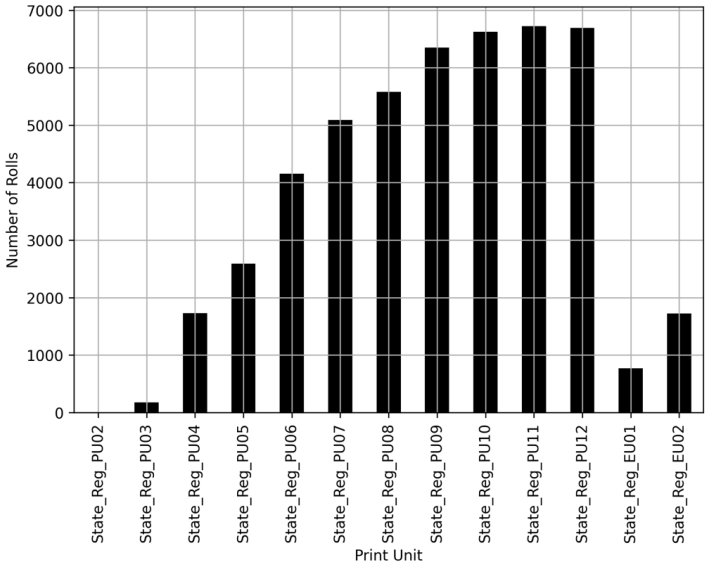

Figure 5: Frequency of active register measurements along the printing press

We would like to point out, that our dataset shows only a partial section of the entire complexity of the printing process of the studied rotogravure press. For example, we do not collect information about changes such as control, ink or dryer parameters that the press operator may have made. Further, one could gather many other potential interesting inline measurement data. However, our dataset provides a strong baseline dataset for various machine learning tasks in context of industrial print application.

4. License and accessibility

The dataset is available under Creative Commons public licence CC BY 4.0 International and can be accessed via DOI: https://doi.org/10.57899/4yjq-h434.

Acknowledgements

The author would like to express extraordinary gratitude to the anonymous industry partners for their great support of this research.

References

Alzghoul, A., Verikas, A., Hållander, M., Bacauskiene, M. and Gelzinis, A., 2009. Screening paper runnability in a web-offset pressroom by data mining. In: P. Perner, ed. *Advances in Data Mining: Applications and Theoretical Aspects: 9th Industrial Conference, ICDM 2009*. Leipzig, Germany, 20–22 July, 2009. Berlin, Heidelberg: Springer, pp. 161–175.

Brumm, P., Weber, T., Lindner, N., Sauer, H.M. and Doersam, E., 2021. *Collection of digitized gravure printed samples for the analysis of hydrodynamic pattern formation*. Technical University of Darmstadt. https://doi.org/10.48328/tudatalib-528.2.

Enk, T., 2022. *Multivariate sensor dataset of an industrial rotogravure printing press (MSDIRPP).* University of Wuppertal. https://doi.org/10.57899/4yjq-h434.

Evans, B., 1995. *Cylinder bands data set*. UCI Machine Learning Repository. [online] Available at: <https://archive.ics.uci.edu/ml/datasets/Cylinder+Bands> [Accessed 18 February 2022].

Parola, M., Kaljunen, T., Beletski, N. and Paukku, J., 2003. Analysing printing press runnability by data mining. In: *Proceedings of the 55th Annual Technology Conference of the Technical Association of the Graphic Arts.* Montreal, Canada, 6–9 April 2003. TAGA, pp. 59–60.

Paukku, J,. Parola, M. and Vuorinen, S., 2004. Web widening and lateral movements of paper web in a printing press. In: *International Printing and Graphic Arts Conference.* Vancouver, BC, Canada, October 2004. IPGAC Preprints, pp. 245–250.

Ranjan, C., Reddy, M., Mustonen, M., Paynabar, K. and Pourak, K., 2018. Dataset: rare event classification in multivariate time series. *arXiv.* [online] Available at: <https://arxiv.org/pdf/1809.10717> [Accessed February 2022].

DOI 10.14622/Advances_48_2022_02

Development and luminance measurements of a fully screen-printed multi-segmented electroluminescent clock

Thorsten Euler[1], Dawid Madzelan[1], Pauline Brumm[1,2], Edgar Dörsam[1,2] and Andreas Blaeser[3,4]

[1] Technical University of Darmstadt, Department of Mechanical Engineering, Institute of Printing Science and Technology, Magdalenenstr. 2, 64289 Darmstadt, Germany

[2] Collaborative Research Center (CRC) 1194 - Interaction between Transport and Wetting Processes, Project C01, Germany

[3] Technical University of Darmstadt, Department of Mechanical Engineering, Institute for BioMedical Printing Technology, Magdalenenstr. 2, 64289 Darmstadt, Germany

[4] Technical University of Darmstadt, Centre for Synthetic Biology, Schnittspahnstr. 10, 64287 Darmstadt, Germany

E-mails: euler@idd.tu-darmstadt.de; brumm@idd.tu-darmstadt.de; doersam@idd.tu-darmstadt.de; blaeser@idd.tu-darmstadt.de

Short abstract

Screen printing is a proven printing process for many graphic and functional applications such as printed electroluminescent (EL) panels. EL illumination technology is based on the light emission of a luminescent material exposed to an alternating electric field between two electrodes. Printed EL panels therefore generally consist of a stack of superimposed printed layers. We have developed and manufactured a new layout and flexible programmable control for a multi-segmented clock printed with screen printing based on EL technology. This setup is very well suited as a demonstrator for printed electronics. We have performed first measurements with the printed EL-clocks. This shows that the luminance increases linearly in the range of 7–105 cd/m^2 with increasing brightness level of the control. When several segments are operated in parallel, however, the luminance decreases significantly, so that there is still potential for optimization here. Further measurements will be carried out and more luminescent materials will be tested.

Keywords: printed electronics, screen printing, electroluminescent panel, multi-segmented EL panel, luminance

1. Introduction and background

Screen printing is a proven conventional printing process for many graphic and functional applications. Functional screen printing is used in many areas, e.g., automotive, architecture, life science, security features, textile printing or packaging (Bodenstein, et al, 2019; Hübner, 2018; Potts, et al., 2020). Printed electroluminescent (EL) panels are used in industry for e.g., lighting applications in the automotive industry, decorative elements in interior design or on flexible substrates (Janczak, 2019; Verboven and Deferme, 2021; Zao, et al, 2020). The EL lighting technology is based on the light emission of a luminescent material exposed to an alternating electric field between two electrodes (Hirmer, et al., 2019). EL panels therefore generally consist of a stack of layers printed on top of each other (see Figure 1). A luminescent layer, e.g., made from zinc sulfide (ZnS), and a dielectric insulator, e.g., barium titanate ($BaTiO_3$), are embedded between two electrodes. The luminescent layer emits light when a voltage is applied. Through printing technology, EL panels can be reproducibly fabricated in large quantities. Mostly EL panels are manufactured by screen printing or using coating techniques. Based on EL technology, clocks with 7-segment displays were also realized as applications. However, it turns out that the temporal behavior until full illumination and the decay of an illumination is unsatisfactory for the observer. This can be improved by an elaborate optimization (de Vos, et al., 2016).

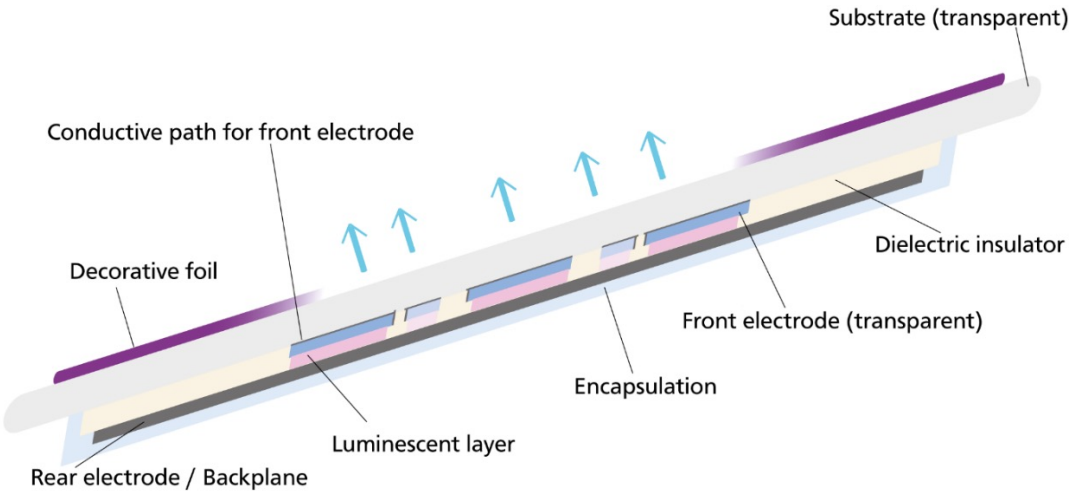

Figure 1: Schematic structure of an EL panel on a transparent substrate; between the rear electrode and the front electrode is the luminescent layer, surrounded by a dielectric layer; encapsulation is needed for protection from voltage, a decorative film provides sharp edges of the illuminated areas; printing of an EL panel usually starts on the transparent substrate

In this paper, we want to introduce a new way to design, print and electrically power a multi-segmented clock based on EL technology. This is accompanied by the following research question: Does the number of simultaneously illuminated segments with the same direct current (DC) input voltage of a screen-printed multi-segmented EL-clock influence the luminance and how can this be compensated?

2. Materials and methods

2.1 Printed components

2.1.1 Printing layout and positioning process

The printing layout consists of seven layers printed on top of each other, see Figure 2a. Between each printing step, the layers were dried at 70 °C for 10 or 60 minutes, see Table 1. On top of the printed layer stack, a decorative foil (ORACAL®751 C, ORAFOL®, Berlin, Germany) with 16 recessed elements such as lettering and clock times, was applied, see Figure 2b. The positioning of the printed layers relative to each other and relative to the contact pins of the circuit board was especially challenging. Therefore, a custom-made positioning system, i.e., a 3D printed frame, was added to the screen printing machine K15QSL, see Figure 3. First, the conductive paths for the front electrodes were printed with silver ink onto the protective film of a polylactic acid (PLA, PLEXIGLAS®XT, 3 mm, clear, Röhm GmbH, Darmstadt, Germany) panel (150 mm × 150 mm, with round edges with 42 mm radius). This step was repeated iteratively with an intermediate cleaning step, until the positioning of the contact pins of the circuit board relative to the conductive paths was satisfactory. Then, the protective foil was removed and the silver ink was printed directly onto the PLA panel. For the further inks, repositioning had to be performed manually by visual sight. The transparent poly (3,4-ethylenedioxythiophene) polystyrene sulfonate (PEDOT:PSS) was positioned according to the conductive paths. This step was followed by printing of the luminescent material, which was printed on top of the PEDOT:PSS. We used two types of luminescent materials (8150L LUXPRINT and 8152B LUXPRINT, see Table 1). After that, two cover layers of dielectric insulator ink were applied. The rear electrode was again printed with silver ink and finally the encapsulation was applied.

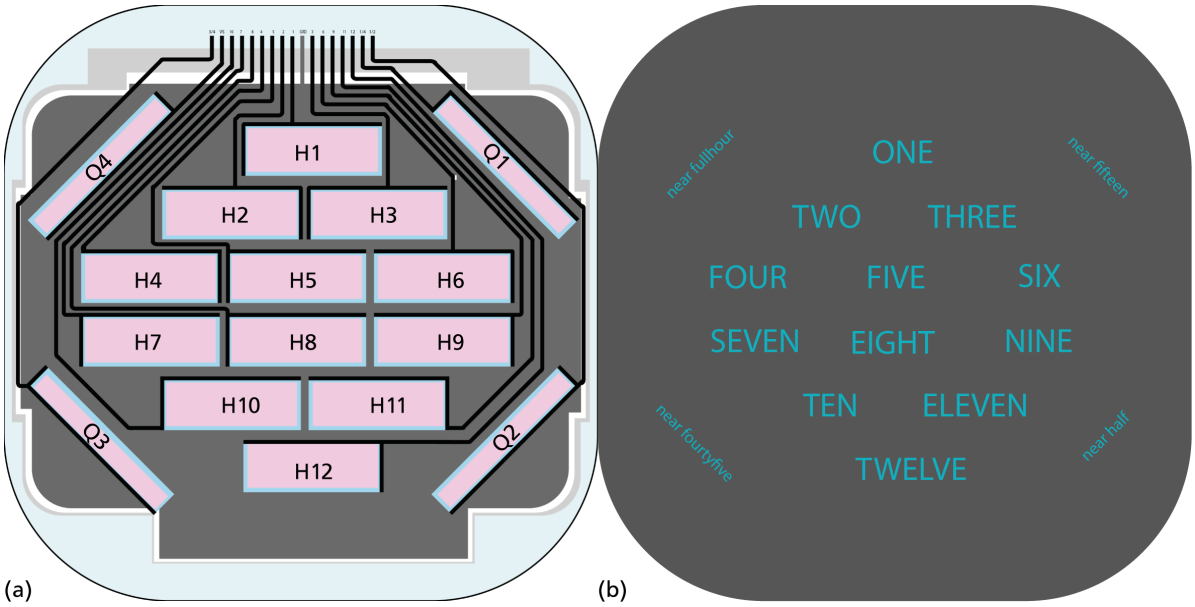

Figure 2: Design of the EL-clock; printed layer stack of seven layers with numbered segments (a) and decorative film with the design of the 16 elements to be displayed (b); the size of the clock is 150 mm × 150 mm with round edges

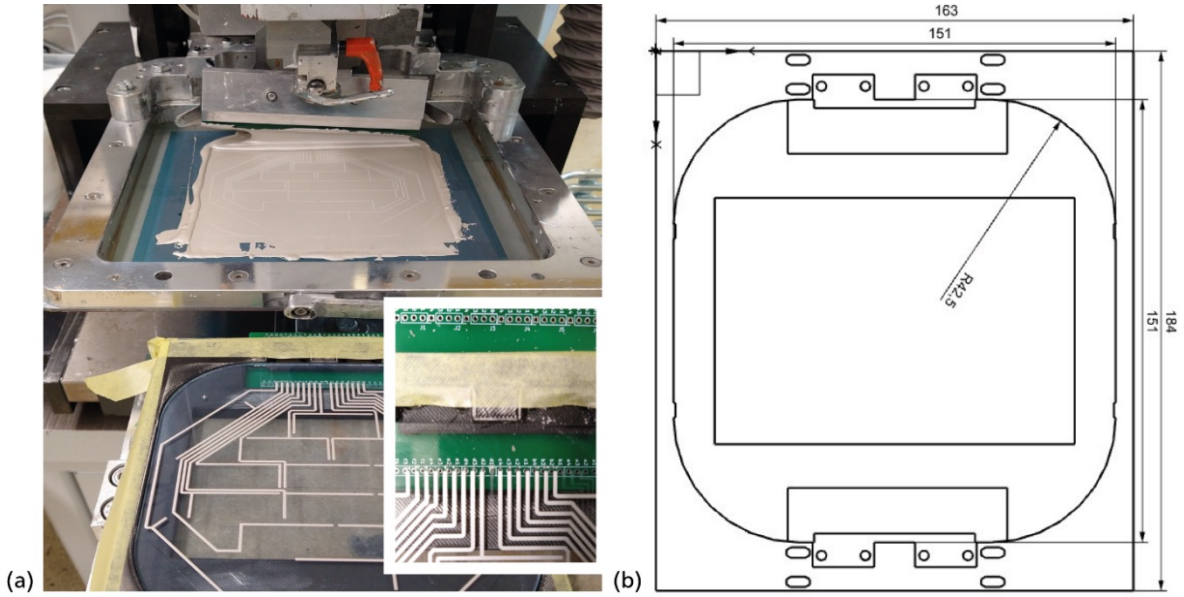

Figure 3: Screen printing machine K15Q SL and printed conductive paths on PLA panel (a) as well as technical drawing of 3D printed frame for positioning with dimensions given in millimeter (b)

2.1.2 Printing inks and printing parameters

All layers of the EL-clock were printed on a Kammann screen printing unit K15Q SL (Werner Kammann, Buende, Germany), (Griesheimer and Dörsam, 2011), see Figure 4a. Squeegee hardness was always 75° shore A. Inks from Heraeus (Heraeus Deutschland GmbH & Co. KG, Leverkusen, Germany) from Henkel (Henkel Nederland B.V., Nieuwegein, Netherlands) and from DuPont (DuPont, Bristol, UK) were used for the printing experiments. Meshes from Frintrup (Hans Frintrup GmbH, Bonn, Germany) were utilized. The choice of the printing parameters was influenced by the supplier information as well as industrial handbooks (Dupont, 2012) and was optimized iteratively, see Table 1.

Table 1: Printing inks and corresponding printing parameters

Layer #	Ink	Manu-facturer	Purpose, main material	Mesh name	Mesh material; mesh opening, and thread diameter both in µm	Printing velocity in m/s	Drying time at 70 °C in min
1	LOCTITE EDAG PF 050 E&C	Henkel	Conductive paths for front electrodes, silver ink	SD+ 63/36	Stainless steel; 63, 36	0.1	10
2	PEDOT:PSS SV4	Heraeus	Front electrodes, PEDOT:PSS	140-34 Y	Polyester; 31, 34	0.4	60
3	8150L LUXPRINT	DuPont	Luminescent material, ZnS	100-40 Y	Polyester; 57, 40	0.1	10
3	8152B LUXPRINT	DuPont	Luminescent material, ZnS	100-40 Y	Polyester; 57, 40	0.1	10
4–5	8153 LUXPRINT	DuPont	Dielectric insulator, $BaTiO_3$	61-64 Y	Polyester; 90, 64	0.1	10
6	LOCTITE EDAG PF 050 E&C	Henkel	Rear electrode, silver ink	SD+ 63/36	Stainless steel; 63, 36	0.1	10
7	7165 LUXPRINT	DuPont	Encapsulation, varnish	100-40 Y	Polyester; 57, 40	0.2	10

2.2 Main electrical components and source code

An alternating electric field is required to control the 16 illuminated fields (segments). We developed a circuit board layout as well as the source code to control our screen-printed multi-segmented electroluminescent clock. The main electrical components of the circuit board are a microcontroller (ATSAML21, Microchip Technology Inc., Chandler, AZ, USA), a high-voltage regulator (HV9150, Analog Devices Inc., Wilmington, MA, USA) and a 16-channel serial to parallel converter with backplane driver (short: '16-channel converter') (HV528, Microchip Technology Inc., Chandler, AZ, USA). One output of the 16-channel converter supplies the backplane electrode; the other 16 outputs control the 16 EL-clock segments. A simplified circuit diagram shows further electrical components that were used to operate the EL-clock, see Figure 4, but it is not a full overview of all used components. The microcontroller is accessed via a USB-C port that supplies a voltage of 5 V DC. A regulator decreases the input voltage to 3.3 V DC, which is required for the microcontroller. Using the Arduino integrated development environment (IDE) 1.8.19, we developed a source code in the programming language C which was transferred to the microcontroller in order to operate the printed EL-clock. A power supply sequencer is connected to the regulator and sequentially activates three further components which supply different voltages to the 16-channel converter. First, a switch is activated, which supplies 5 V DC to power the backplane electrode. Second, a bias supplies 5.5 V to 6.5 V DC to power the 16 individual segments of the EL-clock and third, a switch to generate a high voltage is activated. This switch forwards a high voltage of 50 to 220 V (DC), created by the high voltage regulator, to the 16-channel converter.

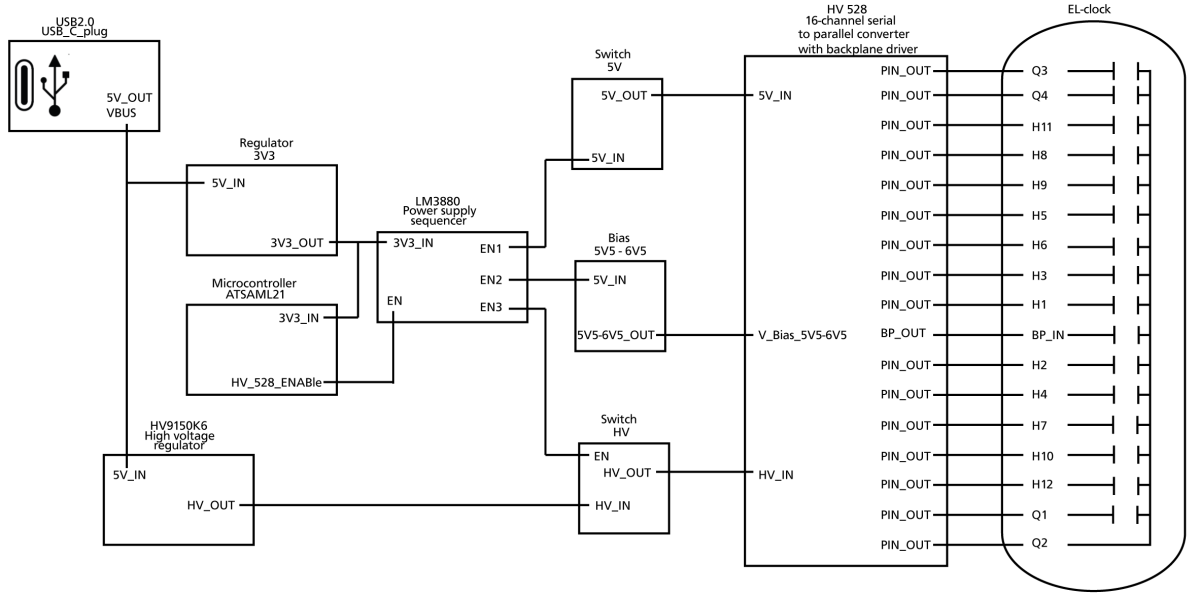

Figure 4: Circuit diagram for the screen-printed multi-segmented EL-clock

2.3 Measurements of luminance

For luminance measurements, the Gossen Mavo Monitor luminance meter (Gossen Foto und Lichtmesstechnik GmbH, Nuremberg, Germany) was used. This high-precision luminance meter for attachment measurement is classified in Class B according to DIN 5032-7, DIN EN 13032-1 Annex B and CIE 69 (Deutsches Institut für Normung, 2012; 2017; International Commision on Illumination, 1987). It measures the luminance of a luminous surface in candela per square meter (cd/m^2). Measurements were performed in a darkened room and were always taken at five different, equally spaced measuring points. An illuminated segment of size 34 mm × 12 mm, i.e., H1, without decorative foil, was measured at ten different brightness levels (10, 20, 30, 40, 50, 60, 70, 80, 90, 100 %). One segment (H1), two segments (H1, Q1) and five segments (H1, Q1, Q2, Q3, Q4) were illuminated simultaneously (see Figure 5). The excitation frequency is kept constant at 1 200 Hz and is a fraction of the microcontroller processor frequency, which is 12 MHz. This results in a constant light spectrum, in our case in a constant blue color. With increasing excitation frequency, the color changes from a greenish to a bluish tone. The maximum brightness level of 100 % was defined in the source code as ten consecutive light pulses at the given excitation frequency. Brightness level of Q1 to Q4 was always 100 %, brightness level of H1 varied from 10 % to 100 %. We restricted the number of simultaneously illuminated segments to five because the temperature of the 16-channel converter was measured over 70 °C with a FLIR One Pro infrared camera (Flir Systems, Wilsonville, OR, USA). A higher temperature could destroy the 16-channel converter.

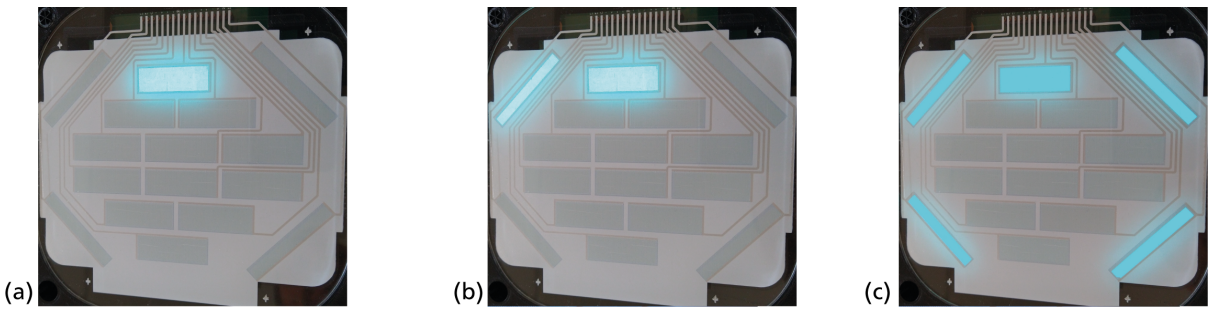

Figure 5: Illuminated measured segments H1 (a), H1, Q4 (b) and H1, Q1, Q2, Q3, Q4 (c)

3. Results and discussion

We were able to manufacture a fully functional, screen-printed multi-segmented EL-clock which can be used as a demonstrator for printed electronics. The EL-clock displays the current time in a modern design in the standard operating mode, i.e., one segment for the full hour from one to twelve and one of the four outer segments are illuminated which show quarter hours. In another operating mode, predefined lighting scenarios can be set independently of the time of day. This mode can be used for luminance measurements or to investigate further research questions. Initial measurements of luminance were made with the samples of the printed EL-clock. For the measurements, one segment was switched on and illuminated once, then two and five segments were switched in parallel and illuminated. The luminance was then measured at ten brightness levels as described in Section 2.3. During operation of the EL-clock, the voltage at the 16-channel converter was measured around 150 V. The results of the luminance measurements can be found in Figure 6. As shown, the luminance increases linearly with increasing brightness level regardless of the wiring type. It can also be seen that parallel operation of segments leads to a significant decrease in luminance. The differences between the two materials investigated are small. Further measurements, e.g., on the time dependence, are in progress.

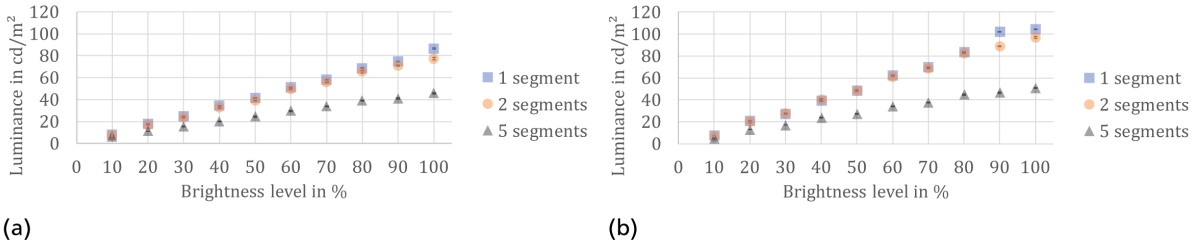

Figure 6: Luminance measurements over brightness level for luminescent materials 8150L LUXPRINT (a) and 8152B LUXPRINT (b)

In relation to our research question, we can conclude that the number of simultaneously illuminated segments influences the luminance significantly. This is an expected behaviour since an increasing number of segments leads to a voltage drop and thus to a luminance drop. Unexpectedly, the luminance drop between one and two illuminated segments was negligible whereas the luminance drop between two and five illuminated segments was significant.

4. Conclusions and outlook

We have developed and manufactured a new layout and flexible programmable control for a multi-segmented clock printed with screen printing based on EL technology. This setup is very well suited as a demonstrator for printed electronics. We have performed first measurements with the printed EL-clocks. This shows that the luminance increases linearly with increasing brightness level of the control. When several segments are operated in parallel, however, the luminance decreases significantly, so that there is still potential for optimization here. Further measurements will be carried out and more luminescent material will be tested. We also want to explore the technical limits of our EL-clock generator with regard to the maximum achievable voltage and the maximum brightness levels.

Acknowledgements

We kindly acknowledge the financial support by the Deutsche Forschungsgemeinschaft (DFG, German Research Foundation) – Project-ID 265191195 – SFB 1194 'Interaction between Transport and Wetting Processes', project C01. We kindly thank Heraeus and Acheson for providing printing inks.

References

Bodenstein, C., Sauer, H.M., Hirmer, K. and Dörsam, E., 2019. Printing process and characterization of fully pad printed electroluminescent panels on curved surfaces. *Journal of Coatings Technology and Research*, 16(6), pp. 1673–1681. https://doi.org/10.1007/s11998-019-00243-0.

Deutsches Institut für Normung, 2012. *DIN EN 13032-1: Light and lighting – Measurement and presentation of photometric data of lamps and luminaires - Part 1: Measurement and file format German version EN 13032-1:2004+A1:2012*. Berlin: DIN.

Deutsches Institut für Normung, 2017. *DIN 5032-7: Photometry – Part 7: Classification of illuminance meters and luminance meters*. Berlin: DIN.

Dupont, 2012. *Processing guide for DuPont Luxprint® electroluminescent inks*. Wilmington, DE, USA: Dupont.

Griesheimer, S. and Dörsam, E., 2011. Labormaschine für das funktionale Drucken im Siebdruckverfahren gemeinsam entwickelt. *Der Siebdruck*, 2011(9), pp. 12–13.

Hirmer, K., Bodenstein, C., Sauer, H. M., Dörsam, E. and Hofmann, K., 2019. Nonlinear behavior in electrical properties of fully screen printed electroluminescent panels. *Journal of Print and Media Technology Research*, 8(3), pp. 145–154. https://doi.org/10.14622/JPMTR-1905.

Hübner, G., 2018. Comparing inkjet with other printing processes and mainly screen printing. In: W. Zapka, ed., 2018. *Handbook of industrial inkjet printing*: a full system approach. Weinheim: Wiley-VCH. Vol. 2, Ch. 2. https://doi.org/10.1002/9783527687169.

International Commission on Illumination, 1987. *CIE 69: Methods of characterizing illuminance meters and luminance meters: performance, characteristics and specifications (E).* Vienna: CIE.

Janczak, D., Zych, M., Raczyński, T., Dybowska-Sarapuk, Ł., Pepłowski, A., Krzemiński, J., Sosna-Głębska, A., Znajdek, K., Sibiński, M. and Jakubowska, M., 2019. Stretchable and washable electroluminescent display screen-printed on textile. *Nanomaterials*, 9(9): 1276. https://doi.org/10.3390/nano9091276.

Potts, S.-J., Phillips, C., Jewell, E., Clifford, B., Lau, Y.C. and Claypole, T., 2020. High-speed imaging the effect of snap-off distance and squeegee speed on the ink transfer mechanism of screen-printed carbon pastes. *Journal of Coatings Technology and Research*, 17(2), pp. 447–459. https://doi.org/10.1007/s11998-019-00291-6.

Verboven, I. and Deferme, W., 2021. Printing of flexible light emitting devices: a review on different technologies and devices, printing technologies and state-of-the-art applications and future prospects. *Progress in Materials Science,* 118: 100760. https://doi.org/10.1016/j.pmatsci.2020.100760.

de Vos, M.; Torah, R.; Glanc-Gostkiewicz, M. and Tudor, J., 2016. A Complex multilayer screen-printed electroluminescent watch display on fabric. *Journal of Display Technology*, 12(12), pp. 1757–1763. https://doi.org/10.1109/JDT.2016.2613906.

Zhao, C., Zhou, Y., Gu, S., Cao, S., Wang, J., Zhang, M., Wu, Y. and Kong, D., 2020. Fully screen-printed, multicolor, and stretchable electroluminescent displays for epidermal electronics. *ACS Applied Materials & Interfaces*, 12(42), pp. 47902–47910. https://doi.org/10.1021/acsami.0c12415.

DOI 10.14622/Advances_48_2022_09

Exploring computer-to-screen applications for innovating a conventional screen-printing practicum

Carl Nelson Blue

Clemson University Department of Graphic Communications, South Carolina, USA
E-mail: cnblue@clemson.edu

Short abstract

This research explored and developed computer-to-screen (CTS) applications for innovating a conventional screen-printing practicum utilizing a MIMAKI UJF-6042 on-demand piezo head flatbed printer to image a stencil directly onto the mesh of a prepared screen. A test target was applied to standardize the imaging process and gauge the coverage that would sufficiently block out and hold a stencil to create an image. The project's goal was to develop a CTS system that would produce screens for spot color printing, replacing the make-ready consumables, shortening preparation time, and maintaining the quality accepted in comparable conventional screen imaging systems. A longer-term goal was to implement this innovative CTS procedure into the existing curriculum on a conventional cylindrical printing project for a practicum using an Innovative Machines Cylindrical Screen Press. This proposed CTS process would replace the traditional lab work of students creating digital single spot-color designs that are processed through a digital workflow into a TIFF file for outputting on a Kodak Trendsetter. The film positives are imaged onto a 230-mesh polyester screen prepared with Capillex-20 capillary film emulsion. The final steps include washing the exposed image, drying, blocking out, and redrying the prepared screen before setting up the press and printing on cylindrical glassware. Installation of the new CTS process predicts a reduction in consumables, shortening the preparation time and preferable alleviating mishaps observed in the conventional process.

Keywords: computer-to-screen, inkjet-to-screen, screen-printing, inkjet technologies

1. Introduction

Stenciling and screen-printing methods have much in common. The earliest form of human artistic expression, stenciling covers the walls of European caves. Stenciling applications existed over 40 000 years ago when early humans created hand stencils using various techniques for applying pigments onto the cave walls. Early forms of screen-printing appeared between 960 to 1279 AD in China. The Song Dynasty developed screen-printing – a technique that used silk mesh and ink-blocking methods developed from earlier stenciling practices. Japan took hold of the idea to incorporate stenciling on silk mesh and advanced the process for many years. (Lengwiler, 2013), and (ooshirts, n.d.).

Fast forward to modern applications and technologies, several U.S. patent applications and state-of-the-art inkjet technologies employ computer-to-screen (CTS) imaging systems for the preparation of print screens, as well as producing an image on a printing screen (Baxter, et al., 2006; Bourne, et al., 2006). There are predominantly three dissimilar technologies for exposing an UV photo-sensitive coated mesh used as a stencil in screen printing with an UV light source (Gmuender, 2017). First, film exposing, either directly mounted on the stencil, or indirectly imaged by using a projector. Second, direct exposing using Digital-Micromirror-Devices (DMD) or a UV laser beam, also called CTS. Third, Direct-to-Screen (DTS) where first the image is printed on the stencil by an ink jet printer and then in a second process is exposed by a UV lamp (Gmuender, 2017).

- In the 2006-Bourne patent, a specific formulated emulsion is mixed with a cross-linking agent to create a self-curing image (Bourne, et al., 2006).
- In the case of the Baxter patent, a photo activated emulsion is applied to a printing screen. The emulsion is using a laser as direct imaging technique to create an image in that emulsion. (Baxter, et al., 2006).
- In 2008, Berner developed an exposure device to produce screen print stencils (Berner, 2008). Berner's exposure system had a light source, and a lens system in an exposure head that yielded digital signals connected with the exposure system. Several laser diodes on the exposure unit controlled by the signals are guided to a raster plate in the exposure head. The light output of the raster plate is transferred to a focusing lens system in the exposure head (Berner, 2008).
- Nearly a decade later, a patent by Van Ness (2015), developed a screen-printing device and methodology for exposing an emulsion coated screen to light comprises an array of ultraviolet light emitting diodes (UV-LEDs). This system created a positive impression of the artwork to be printed; a flat transparent plate disposed between the array of UV-LEDs and the positive impression; a screen coated with a light-curable emulsion; the positive impression disposed on the side of the screen having the emulsion (Van Ness, 2015).
- More recently a patent by Oleson (2017), a mechanical system in which pre-stretched emulsion coated screens, digitally prints thereon, and exposes them before further processing and use in a screen-printing machine. Some of these patents have shown commercial value, as in the, "i-Image ST™ CTS Imaging System: from the M&R Companies (2022).

2. Materials and methods

In developing a CTS application, this research used an inkjet printer to print a stencil directly onto the mesh (ScreenPrinting, 2022) in a hybrid screen printing process. This research tested the functions of UV curable primer in a MIMAKI UJF-6042 (Mimaki, n.d.) on-demand piezo head flatbed inkjet printer (Figure 1) to prepare print screens. The project's goal was to develop a CTS system that would replace the need for emulsion and film for transferring an image to a tensioned mesh screen. The objective was to produce single-spot color screens for cylindrical printing on an Innovative Machines LP 400E Cylindrical Screen Press (Figure 2). Students create a digital single spot-color design for this specific cylindrical printing project. Once students create their digital file within the constraints and the desired specifications of the project, their files are converted into a TIFF file through ESKO's "Packedge/Automation-Engine" applications in a digital workflow process for outputting Kodak DITR film on a Kodak Trendsetter NX-Mid. These film positives are next imaged on a prepared 230-mesh polyester aluminum screen with Capillex-20 capillary film emulsion. The final steps include washing out the exposed image, drying, blocking out, and redrying the prepared screen before setting up the cylindrical screen press and printing on glassware.

Figure 1: MIMAKI UJF-6042 (Mark I Series) on-demand piezo head flatbed inkjet printer

Figure 2: Innovative Machines LP 400E Cylindrical Screen Press

2.1 Conventional process

The conventional system for preparing screen-printing frames for cylindrical printing is roughly a three to four-hour process if completed without any errors. Students complete this assignment individually and are presently allotted two to four labs (2 hours, and 45-minutes each) depending on the number of students enrolled in the lab. These labs are administered as rotating modules to better utilize space and equipment. Several of the steps are crucial in the process and mistakes can be made. If an error is made, then the process must be repeated to complete the project. The preparation of screens for this conventional process includes:

1. Processing digital files into film (30–60 minutes)
   a. This film also serves as a proof for checking the image quality on the glassware.
2. Cleaning, degreasing, and drying the mesh completely (30–45 minutes)
3. Application of capillary film and redrying the mesh thoroughly (50–60 minutes)
4. Imaging prepared screens correctly (5 minutes). If incorrectly, back to step 2.
5. Washing-out imaged capillary film (3–5 minutes). If incorrectly, a damaged stencil, back to step 2.
6. Drying the mesh, blocking out open mesh, and re-drying the block-out (45–60 minutes).
7. Prior to mounting the screens on the press, students prepare .025 pounds (11.34 ml) of ink, and .005 pounds (2.27ml) of catalyst mixed and allowed to bond for 20 minutes prior to printing. While waiting on the ink, their screen is mounted on the Innovative Machines LP 400E Cylindrical Screen Press (Figure 2). Students are encouraged to obtain a standard pint size glass with smooth flat sides in its profile (Figure 3).
8. Post-printing, remove ink, wash-out and reclaim screen for next student in the rotation.

Consumables: Kodak DITR film, Capillex-20 capillary film emulsion, Quick-dry Block-out, RE190 Thinner, ICC877 Degradant, ICC861 Degreaser.

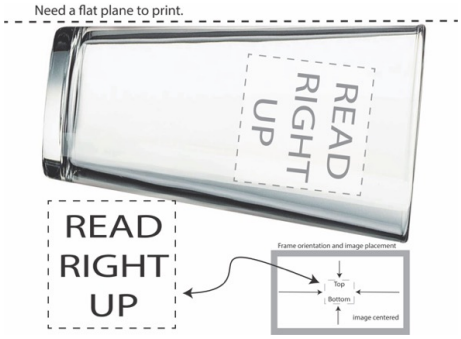

Figure 3: Standard pint size glass with smooth flat sides for printing

2.2 Hybrid inkjet stencil process

The proposed hybrid screen preparation process would include step 1, digital image preparation in the conventional system previously outlined, would eliminate steps 2 through 5 if the previous screen printer efficiently cleans the screen in their step 8. The new proposed hybrid inkjet stencil process includes:

1. Process digital files into single spot-color graphic as a TIF file. Upload to file server.
   a. Students are required to use this single spot-color graphic file to produce a proof on an alternate inkjet printer on transparent film prior to creating screen.
2. Load clean screen onto the platform of the MIMAKI printer (10 minutes)
3. Load prepared spot-color graphic into the printer's imaging software. (2–3 minutes)
4. Print two layers of primer @ 100 %, and a third layer of ink @ 100 %. (8–10 minutes)
5. Unload printed frame. Block-out the ink rest area mesh prior to cylindrical printing (20–30 minutes)
6. Preparation of ink… (30 minutes) (See Step 7 in Section 2.1]
7. Post-printing, remove ink, wash-out and reclaim screen for next student in the rotation

Consumables: UV Primer PR-200, UV ink LF140 White, Quick-dry Block-out, RE190 Thinner, ICC877Ink Degradant, ICC861 Degreaser.

2.3 Formulation and trials

The method and equipment for imaging a screen-printing screen utilized the capabilities of MIMAKI UJF-6042 on-demand piezo head flatbed printer to print a stencil on the exterior side of a print screen. The flat bed was able to adjust to the height of a standard 10" × 14" aluminum screen printing frame and self-adjusts the print heads so to print directly onto the various screen materials. Previous research on creating stencils for various mesh counts: 195, 230, and 420 found that a 230-mesh-count offered the best results in creating a durable and high coverage stencil (Blue, 2021). The test target (Figure 4) was developed to compare and seek to accomplish the capabilities of the capillary film. The priority was to test the inkjet-printed stencil's capacities to match the details achieved in capillary film as well as exceed the durability of a conventionally produce screen. Chemical properties of combination ink and added hardening catalyst require the use of caustic thinner and isopropyl alcohol for maintaining the fluidity of the ink and cleaning the stencil during longer printing applications. The inkjet-printed stencil needed to do as well as conventional systems.

The intent of this research was to print an adequate application of inkjet UV curable primer of a test target (Figure 4) to confirm the amount of coverage that would sufficiently block out the ink that passes through a screen. Based on previous research, and suggestions by the OEM to use primer instead of ink for creating the stencil. Primer provided better adhesion qualities for better results in creating an acceptable stencil (Blue, 2021). Previous trials involved testing a variety of applications of inks and primer on a range of mesh counts. Those initial formulations and process controls lead to the recommendation of applying two layers of primer to sufficiently create a stencil (Blue, 2021). Once the initial target was produced on the screen with two layers of primer, a third layer of white ink was printed onto the target stencil. This was done to counter the tackiness of the primer. This application of ink provided a smooth shell over the primer. The concern was the tackiness of the primer may affect the screen's contact with the glass substrate and attract unwanted ink deposits on the contact side of the screen. The prepared frame with print target stencil was setup on the cylindrical press, ink added, and trials commenced (Figure 5).

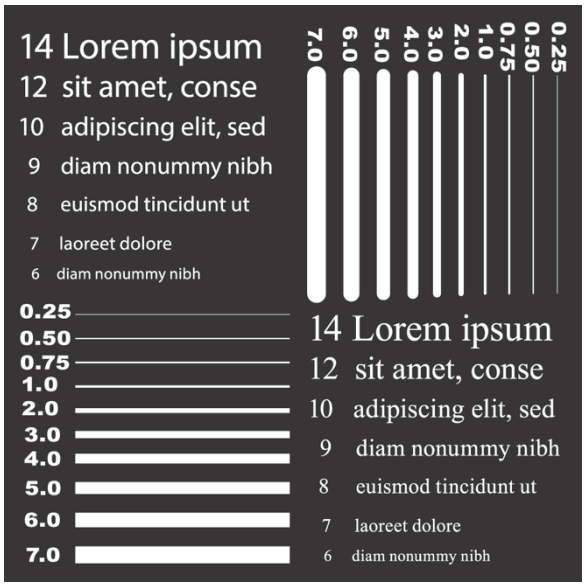

Figure 4: 3 × 3 inches (7.62 cm × 7.62 cm) test target for an inkjet-printed stencil for cylindrical printing

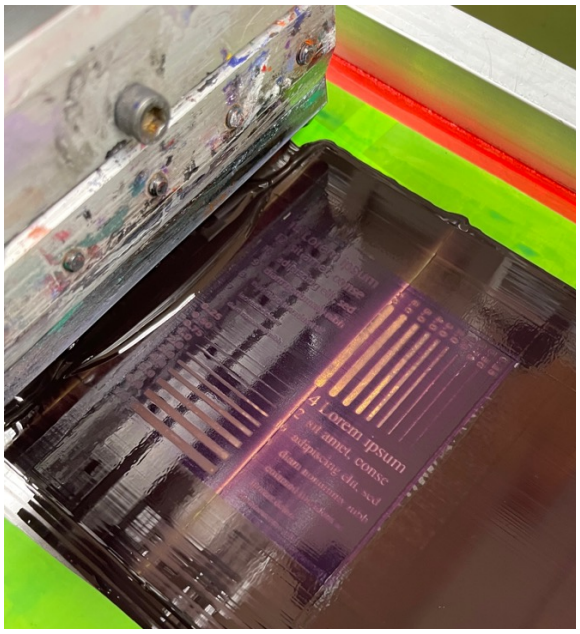

Figure 5: Printing the imaged stencil onto cylindrical substrate

3. Results and observations

The Mimaki UJF-6042 (Mark 1 Series) printer used in the project is an older model with limited profiles available. This model has the capacity to produce 1 800 × 1 800 dpi. However, the default profile on this machine produced a resolution of 720 × 900 VD. The VD stands for "variable dot" and there are three sizes produced. The smallest is stated as 4 pL, and the other sizes are approximated as 8 pL and 12 pL. The average droplet size would be 8 pL. Considering the limited access to control the resolution of profiles, for future testing for this type of stencil creation, a standardized dot size would be optimal.

In Figures 6 and 7 the results demonstrate the capabilities of the inkjet-printed stencil. The 0.25-point line showed the least desirable results, however in the project in which students would be designing graphics,

one of the constraints require students to limit any line art to 1.0-point. Regarding the font sizes, the stencil could reach a readable 6-point font for serif and sin-serif fonts. However, the project's design constraints for this project require any fonts used to be 12-point or larger. To ensure better visuals for the application of the primer, a Dino-lite™ Digital Microscope was used to take pictures of the primer/ink applications on the mesh. Figures 8 and 9 show the capabilities of the inkjet-printed stencil. Though the 0.25-point printed results were the least desirable, the outcomes exceeded the 1.0-point constraints.

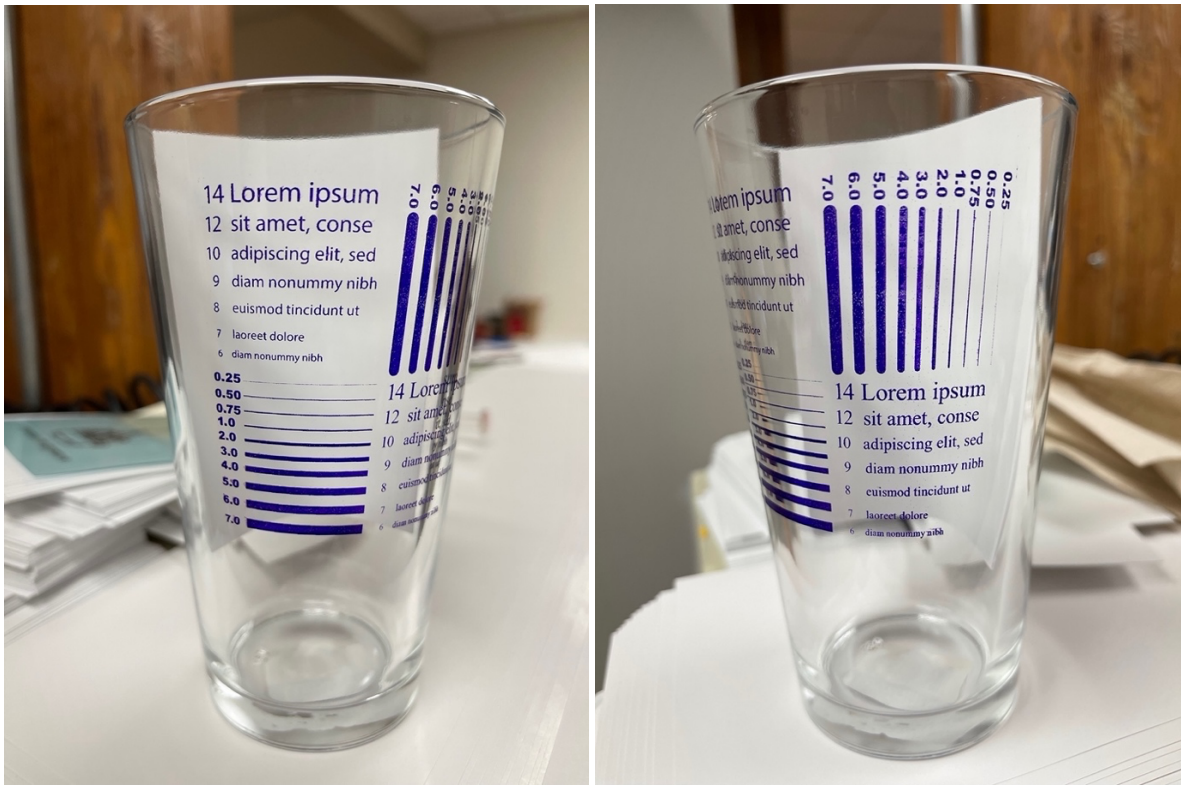

Figures 6 and 7: Printed glassware from inkjet-printed target trials

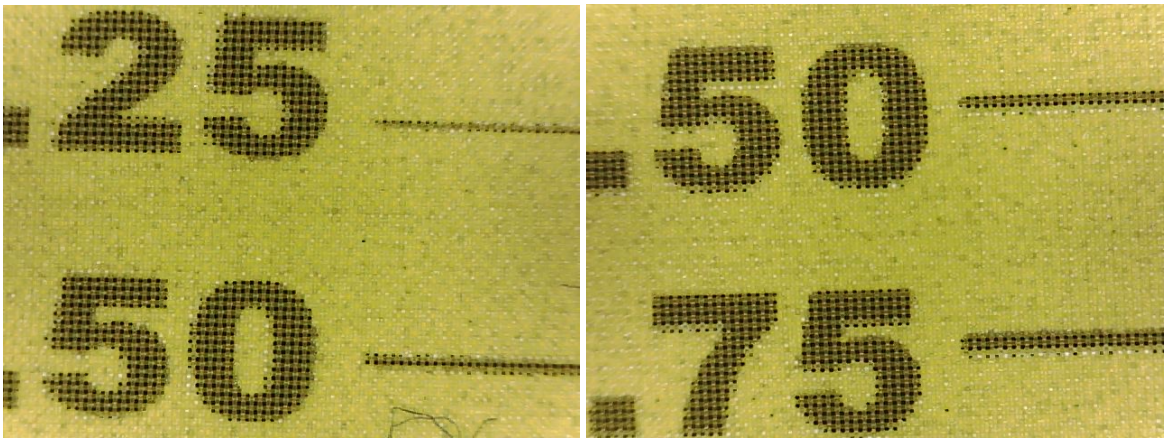

Figures 8 and 9: Enlargements of .25-point, .50 point, and .75-point lines

3.1 Updated process

1. Inkjet applications of one layer of primer, and a second layer of white ink of the (3 × 3 inch) Line art [in reverse] onto the outer surface of the 10 × 15 aluminum screen. (7 minutes)
2. Block-out remainder of screen with conventional block-out solution and/or masking taped the image edges.

3. Setup for the Innovative Machines LP 400E Cylindrical Screen Press for standard screens and tapered pint glassware.
4. Prepare epoxy ink with catalyst for glassware (20 to 30-minute prep-time)
5. Load imaged screen, load glassware, make necessary adjustments.
6. Introduce ink onto screen, began printing paper samples, make adjustment, print glassware.

3.2 Stencil durability, screen reclaim, and cleanup observations

Some of the early concerns in developing this CTS application for innovating a conventional screen-printing practicum in the classroom for students is one, the durability of the printed stencil, and secondarily, how easily the inkjet printer primer and ink could be removed, and the screen reclaimed for further use. In Figures 10 "*squeegee side of the mesh*" and 11 "*print side of the mesh*" demonstrate the durability of the inkjet-printed stencil. The ink has been removed using RE190 Thinner and ICC-871 Ink Degradant to remove the ink leaving the stencil and the block out. At this point the stencil is intact and showed no ware or degradation. The ink and ink thinner were left on the screen post-printing for over an hour to test the stencil's durability to the chemicals used. In a laboratory classroom setting the screens are clean immediately after printing.

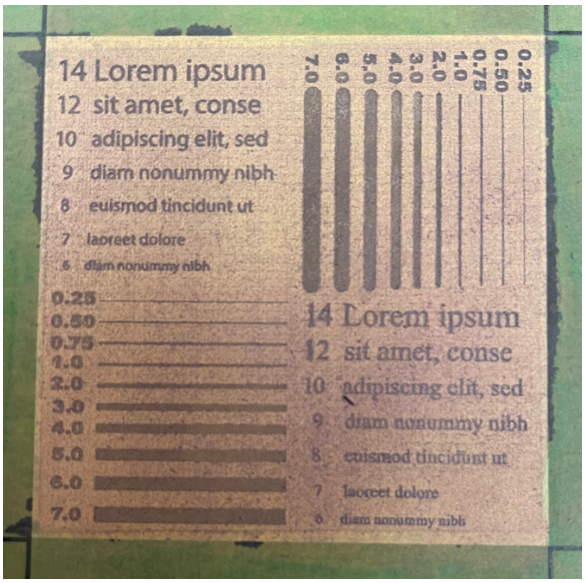

Figure 10: Squeegee side of the mesh

Figure 11: Print side of the mesh

In cleaning the screen's block-out, the green colored residue used for blocking out parts of the screen where there is no stencil, this was easily removed with water (Figures 12 and 13). At this point water without high pressure had little effect on the printed stencil. Some residue ink can be seen in the open spaces in the stencil. The next step will be to remove the printed stencil a high-pressure washer.

In cleaning the screen, there was some concern if the UV-cured inkjet-printed stencil would need specific products or processes to be removed from the mesh, however as noted in Figures 14 and 15, the stencil is easily removed by a pressure washer. In all previous research as in the case of this research, no chemical was needed to remove the stencil once the printing ink and block-out product were safely removed. The cleaning of the stencil took less than a minute to remove with no other chemicals, the residual ink cleaned up with some additional treatment. The finished clean screen, once dry is ready for re-use.

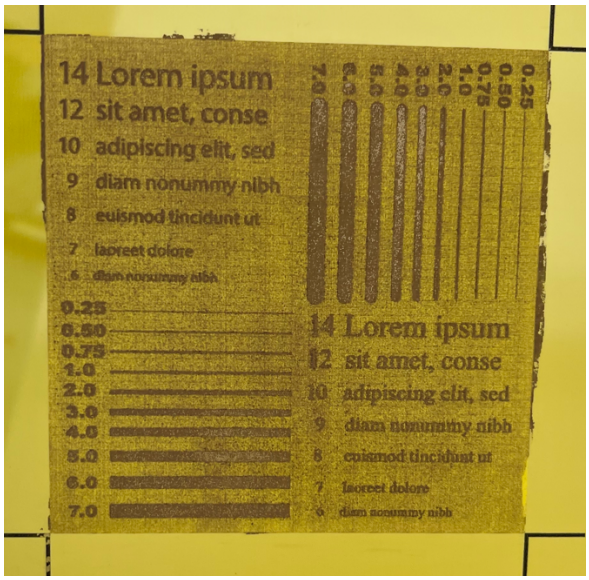

Figure 12: squeegee side of the mesh

Figure 13: print side of the mesh

Figure 14: Pressure washing 1

Figure 15: Pressure washing 2

4. Conclusion

The time spent preparing screens using the conventional system involved, 3 to 4 hours. The time spent on preparing screens in the CTS system took 1.5 to 2 hours. These achievements in utilizing a CTS process in a course practicum would shorten the preparation time, reduce costs in consumables, and alleviate possible mishaps in screen preparation. The CTS findings held up to the standards of conventional capillary film for single spot color reproduction. The shortened preparation time for processing screens provides opportunities for entertaining new design aspects beyond single-color applications to multiple spot color cylindrical printing, or several line-art graphics. These considerations allow greater experiences in learning and exposure to research.

Previous research in inkjet-printing stencils sought to develop CTS screens for four-color process printing (Blue, 2021). Attempts to create halftone and stochastic screens proved problematic yet a proof of

concept was achieved. Returning to that work is a goal for future research in CTS technologies. Much of the knowledge obtained in developing those four-color projects assisted in making this CTS single-color project viable. The variable-dot characteristics of these on-demand piezo printers can produce exceptional photo-like images in high detail (Figure 16). However, the varying dot sizes produced should be taken into consideration when limited profiles are available. Profile development and considerations for this type of stencil creation on mesh and a standardized dot size would be optimum. The opportunity to have students explore and develop a CTS system for innovating a conventional screen-printing practicum through discovery has encouraged positive outcomes.

Figure 16: Primer cylindrical printing with inkjet produced stencils

Acknowledgements

Thanks to Mr. Robert G Drago, Mimaki USA, Region Manager, Southeast Region, Suwanee, GA 30024, USA for their assistance and expertise on this project.

References

Baxter, G., Baxter, B., Kennedy, D., Wareberg, P.G., Wilson, S., Rayner, D. and Bourne, O., 2006. *Computer screen imaging system for the preparation of print screens.* U.S. Pat. 7,115,353 B2.

Berner, P., 2008. *Exposure device for the production of screen print stencils*. U.S. Pat. 2008/0047445 A1.

Blue, C.N., 2021. Developing a computer-to-screen (CTS) application using an inkjet printer to apply a stencil directly to the mesh in a hybrid screen printing processes. In: *Technical Association of the Graphic Arts (73rd annual technical conference)*. TAGA, pp. 161–171.

Bourne, O.L., Kennedy, D., Ingold, K., Wareberg, P.G., Girard, D., Baxter, G. and Baxter, B., 2006. *Method of producing an image on a printing screen*. PCT Pat. WO 2004/039586 A1.

Gmuender, T., 2017. Reaction of photochemical resists used in screen printing under the influence of digitally modulated ultraviolet light. In: *Proceedings Volume 10117: Emerging Digital Micromirror Device Based Systems and Applications IX*. San Francisco, CA, USA, 20 February 2017. SPIE. https://doi.org/10.1117/12.2247720.

Lengwiler, G., 2013. *A history of screen printing: how an art evolved into an industry*. Cincinnati, OH, USA: ST Media Group International.

Oleson, A.L., M&R Printing Equipment, Inc., 2017. *Method and apparatus for preparing a screen-printing screen.* U.S. Pat. 9,649.837 B2.

Van Ness, C.L., 2015. *Screen printing device and method.* U.S. Pat. 2015/0336372 A1.

ooshirts, n.d. *History of screen printing.* [online] Available at: <http://www.ooshirts.com/guides/History-of-Screen-Printing.html> [Accessed 3 April 2022].

M&R Companies, 2022. *i-Image ST™ Computer-to-Screen (CTS) imaging system.* [online] Available at: <www.mrprint.com/equipment/i-image-st-computer-to-screen-cts-imaging-system> [Accessed 3 April 2022].

ScreenPrinting, 2022. *Screen printing mesh.* [online] Available at: <https://www.screenprinting.com/collections/screen-printing-mesh> [Accessed 3 April 2022].

Mimaki, n.d. *UJF-6042.* [online] Available at: <mimaki.com/product/inkjet/i-flat/ujf-6042/specification.html> [Accessed 3 April 2022].

DOI 10.14622/Advances_48_2022_14

Printable electrolyte for printed batteries

Gunter Hübner, Michael Krebes, Laura Cirstea and Anna Kolesova

Innovative Applications of the Printing Technologies (IAD), Stuttgart Media University, Nobelstr. 10, 70569 Stuttgart, Germany
E-mails: huebner@hdm-stuttgart.de; krebes.michael@web.de; lc035@hdm-stuttgart.de; ak280@hdm-stuttgart.de

Short abstract

In this study, we focus on optimising the electrolyte layer of printed batteries. In the stack design of a printed battery, the electrolyte layer is located between the anode and cathode and is responsible for ion transport. However, the anode and cathode must not touch each other, so a material called a separator is usually used. This separator is an absorbent porous fleece-like material that is usually drenched with electrolyte. In the zinc/ manganese dioxide electrochemical system, the electrolyte is a salt dissolved in water, usually a zinc chloride solution. The solution is almost as liquid as water and therefore not printable in screen printing. In this research we used thickeners (gelling agents) to achieve printable fluid flow properties, added small rigid particles as spacers to the solution to get rid of the unnecessary fleece, and finally experimented with a mixture of ammonium chloride and zinc chloride to enhance the battery performance.

Keywords: printed batteries, screen printing, printable electrolyte, thickeners, spacers

1. Introduction and background

For a period of more than 15 years the research group Innovative Applications of the Printing Technologies (IAD) is working together the German battery manufacturer VARTA Microbattery GmbH. During this period very many different electrochemical systems have been investigated. However, the primary (non-rechargeable) system zinc/manganese dioxide aka zinc/carbon system is still of central importance. In the governmentally funded project OxiFlexIT (2022) this type of film batteries are employed for flexible skin patches to monitor physiological data such as blood oxygen levels. The batteries are used to drive the measurement setup and power broadcasting of data to a remote-control station. For hygienic reasons and ease of use, the batteries do not need to be rechargeable. However, the printed batteries need to be made as thin as possible to be flexible (total thickness <<1 mm). A rigid button cell (the competition) is markedly disadvantageous. Furthermore, there are serious indications and signs from industry partners that printed batteries based on this electrochemical system will be available on the mass market very soon. Therefore, the research shown here contributes significantly to improving the performance and manufacturability of thin film printed batteries. A quite similar project to OxiFlexIT, the EU funded research action called "BEWELL", also employs printed batteries (BEWELL, 2022). In a first version the same primary battery system was used and later expanded to rechargeable ones based on Li-ion technology.

The chemical systems zinc/ manganese dioxide, the printing technique, and mechanical properties used for these film batteries has been described earlier (Hübner, et.al., 2015; 2021). The design used here is the so-called stack design as shown in Figure 1.

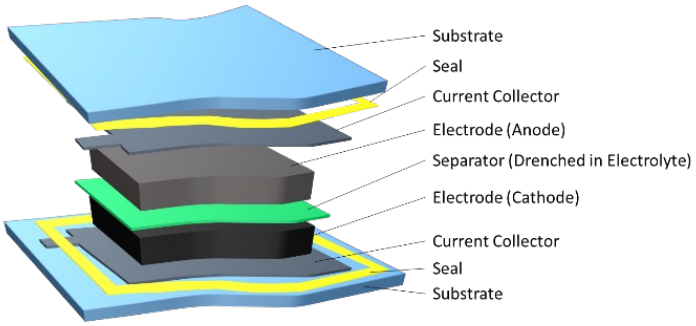

Figure 1: Basic design of the so-called stack design of printed batteries (Hübner, 2015)

The printing process that is the most suitable for this type of application is screen printing since the mass (layer thicknesses typically ~150 µm) of the active electrode materials determine the battery capacity and the particles used are quite coarse (10 µm to 25 µm). Nevertheless, with a total thickness of the printed cell of about 600 µm it remains bendable and can snuggle to the human skin.

In comparison to the alternative co-planar design, the stack can deliver much higher peak (burst) currents. These load peaks occur in the use case because high power demand for the measurement process and the transmission of the collected data regularly occurs in the use cycle after idle periods with low power consumption. The challenge of the stack design is that a direct contact between the anode and cathode must be avoided and therefore a separator is used. In classical setup, this separator is an absorbent porous fleece-like material that is usually drenched with electrolyte. For the zinc/manganese dioxide electrochemical system that is used here, the electrolyte is a salt dissolved in water, usually a zinc chloride solution. The solution is almost as liquid as water and therefore not printable in screen printing. In this research we used thickeners (gelling agents) to achieve printable fluid flow properties, added small rigid particles as spacers to the solution to get rid of the unnecessary fleece, and finally experimented with a mixture of ammonium chloride and zinc chloride.

The conventional battery is an electrochemical cell, in which redox reactions take place. In the Zn/MnO_2-cell, the following simplified chemical reactions take place (Wikipedia, 2019):

$$\text{at anode: } Zn \rightarrow Zn^{2+} + 2e^- \quad \text{and} \quad \text{at cathode: } 2MnO_2 + 2H_2O + 2e^- \rightarrow 2MnO(OH) + 2OH^- \qquad [1]$$

The nature of the electrolyte plays an important role in the development of the zinc/manganese dioxide cells (Wikipedia, 2022). In early times liquid ammonium chloride was used in the Leclanché cell, then in a thickened, immobilized form, the cell was called zinc-carbon cell. Later, zinc chloride was used, and the best performance shows the variant with a KOH-based electrolyte, which is called an alkaline battery. Here, the authors used either pure zinc chloride or a mixture of ammonium and zinc chloride. In other projects, a lot of experience was gained with KOH-based electrolytes, which showed that this solution creeps extremely and even attacks the seals. Therefore, the KOH-based types were not investigated here, because the usage will be on skin. Since the electrolyte must act as an ion transport system, it has to be kept moist during the whole lifetime of the battery. To prevent the battery from drying out, the cell must be tightly sealed. It is even advisable not to use substrates made of a single material through which water vapour can easily migrate, but to use composite films that enclose a barrier layer such as aluminium.

As the batteries are intended to become a mass product, some considerations about pricing and sustainability are appropriate. As discussed earlier elsewhere (Hübner, et al. 2021) the substrate plays an important role. If the tendency to dry out can be reduced by using a more hygroscopic electrolyte it could be possible to leave out the barrier layer in the substrate. Mixtures of ammonium and zinc chloride reduce

the tendency to dry out. Using mono-material foils could also be helpful regarding recyclability and in the present composition there are hardly any environmentally critical materials.

If the separator (fleece-type material), which has to be inserted into the battery either manually or by pick and place, can be avoided, a big step towards simple inline manufacturing has been taken. A printable electrolyte fulfilling the separator function by itself is a big cost saving factor.

2. Materials and methods

Measuring instruments and techniques are described below.

2.1 Rheology

A Physica MCR 300 rheometer was used to evaluate the flow behaviour of the printable electrolyte paste formulations. Typically, the pastes show a pronounced shear thinning behaviour. To compare different formulations, the viscosity value was recorded at a shear rate of 50 or 100 reciprocal seconds (s^{-1}). Because of the particles of up to 50 µm introduced into the pastes, a parallel plate geometry was used. The more accurate cone and plate geometry could not be used because the surfaces could be damaged by the abrasive effect of the particles in the small gap in the middle.

2.2 Conductivity and GEIS measurements

One of the performance-determining factors of batteries is the internal resistance. Obviously, the smaller the internal resistance of the ion transport system, the better the battery performance will be. Therefore, it is very important to determine the resistance – or better the impedance – of the electrolyte solution. The conductivity as the reciprocal of the impedance of the electrolyte solutions was measured with a setup shown in Figure 2.

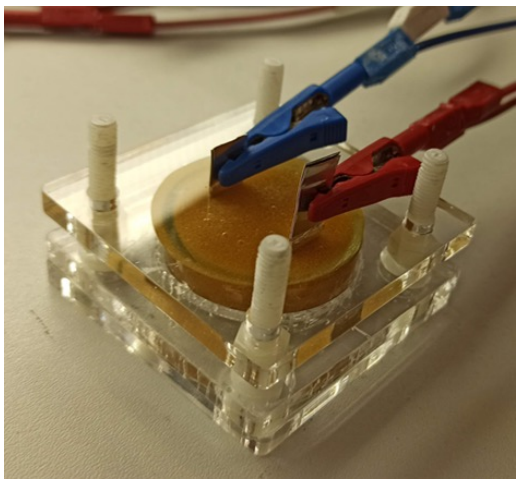

Figure 2: Conductivity measurement set-up

Two metal electrodes are immersed in the electrolyte, with the distance between the electrodes and the immersion depth being kept constant across all measurements. Nickel strips with a high corrosion resistance were used as electrodes and replaced after several measurements. The electrodes are connected by crocodile clips to the measurement device, a Bio-Logic SP-300 potentiostat (Biologic, 2022).

When the electrodes are immersed in the electrolyte, metal ions dissolve, leaving free electrons behind. This leads to the formation of an electrochemical double layer at the electrode/electrolyte phase boundary, which acts like a capacitor with capacitance *C*. The capacitor causes a frequency-dependent behaviour of the system. This is the reason why the conductivity of the electrolyte cannot be determined using a direct current (DC) measurement but must be determined using an alternating current (AC) impedance measurement. Figure 3 shows the (simplified) equivalent circuit diagram of the system. Detailed information on the corresponding measurement techniques and theory can be found in Knoblauch (2015), Gamry (2009), and Biologic (2022). The resistance parallel to the capacitor is called the polarization resistance R_P (Gamry, 2009). The resistance of the electrolyte which we are interested in is represented as resistance R_E. Both R_P and R_E can be regarded as frequency independent ohmic resistances.

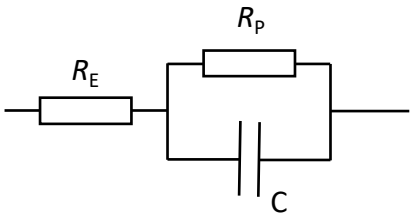

Figure 3: Equivalent circuit diagram

The capacitor C is characterised by the capacitive reactance X_C shown in Equation [2].

$$X_C = -\frac{1}{2\pi f C} \qquad [2]$$

To determine the R_E value, the impedance of the system is measured with a sinusoidal AC excitation at variable frequencies using the Galvanostatic Electrochemical Impedance Spectroscopy (GEIS) method (Biologic, 2022). In this work the GEIS measurements were performed with an alternating current of 200 µA amplitude and a frequency range from 1 Hz to 1 MHz.

Figure 4 shows an (idealized) result of a GEIS measurement of a system according to Figure 3 in the form of a Nyquist plot. The ohmic resistances R_E and R_P appear in the diagram at the points where the semicircle touches the *x*-axis, and the imaginary part of the impedance is 0. At those points the capacitive reactance is 0 (for $f \to \infty$) or approaching infinity (for $f \to 0$).

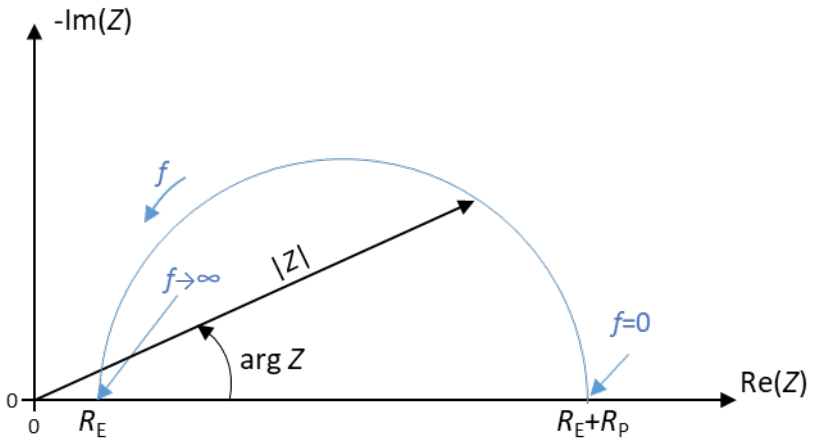

Figure 4: Sample Nyquist plot with impedance vector for a circuit according to Figure 3

To determine the conductivity of the electrolyte, the resistance R_E was taken from the Nyquist diagram.

2.3 Measurement conditions of the cell set-up

To calculate the conductivity, the cell constant K of the measurement set-up must be known. The cell constant K is primarily dependent on the geometric arrangement and can be determined using the procedure described above with a calibration solution with a known specific conductivity κ_{ref} in S cm^{-1}.

$$K = R_E \kappa_{ref} \quad [3]$$

After the cell constant is evaluated, the unknown specific conductivity of the electrolyte can be calculated from the measured impedance by using the same rearranged formula:

$$\kappa_{sample} = K \,/\, R_{Esample} \quad [4]$$

where K is the value obtained by the calibration and $R_{Esample}$ is the measured resistance value.

Since this measurement of the specific conductivity depends very much on the determination of the cell constant and other parameters the accuracy can be estimated at ±2 mS cm^{-1}.

2.4 Electrical characterisation of batteries

For characterization of the battery properties, the performance of the battery is characterized by the voltage U times the current I. The unit of electrical power P is Watt (W). The energy is power multiplied by the time the power is delivered, t.

$$E = P \cdot t = U \cdot I \cdot t \quad [5]$$

Another important characteristic is the energy capacity Q of the battery. Battery capacity is defined as the total amount of electricity generated due to electrochemical reactions in the battery and is expressed in ampere times hours. For example, if a battery has a capacity Q = 50 mAh, then a constant discharge current of 50 mA can be drawn out of the battery for 1 hour.

$$Q = I \cdot t \quad [6]$$

2.5 Printable electrolyte with separator function

In comprehensive preliminary experiments several thickener agents were tested to bring the zinc-chloride solution in a printable viscosity and appropriate flow behaviour range. It turned out that the best and most stable results could be achieved by using Agar-Agar. Agar-Agar belongs to the category of common gelling agents and is composed by 70 % agarose and 30 % agaropectin and it is extracted from the cell walls of different red algae (CarlRoth, 2022).

Agar-Agar should solely function as a thickener but should not play any performance influencing role in a battery. Thus, we used a laboratory grade. Maybe for a later mass production also other grades can be used.

Here, the highly pure BioScience Agar-Agar from vendor Carl Roth has been used. It is often employed in molecular- and microbiology.

2.5.1 Usage of spacers

Although the printable electrolyte shows quite high viscosity and thus high resistance to flow it does not have the capability to permanently separate anode from cathode. The idea adopted to overcome this problem is the addition of spacers into the solution. Just alike the usage of powder in the delivery of offset presses little bead-like particles should fulfil the purpose of spacing. Indeed, the first test was done with the starch-based particles used in the offset press. However, it turned out that these materials dissolve in the electrolytes and were not applicable.

Three different materials could be found from which appropriate beads could be sourced

- Phenolic resin – Figure 5
- Glass
- PMMA (Poly methyl methacrylate) – Figure 6

The phenolic resin beads that were found are hollow phenolic microspheres. Normally they are used as the performance enhancers for grinding wheels and are used as a filler material (Kremer, 2022). Their size ranges from 5 µm up to 127 µm and their relative density from 0.20 gcm^{-3} to 0.80 gcm^{-3}. They are an oligomeric reaction product of formaldehyde with phenol (CAS No. 9003-35-4; EINECS 2000052), purity ≥ 99.8 %. They are a red-brown granulate (Figure 5) provided by the company Kremer Pigmente GmbH & Co.

Figure 5: Phenol beads

Figure 6: PMMA beads

The glass beads that we found on the market for sandblasting did not have spherical shape. They showed irregularities and a wide distribution of particle sizes. Almost all preliminary tests showed short circuits. Thus, we did not investigate the glass material further.

The PMMA particles (Figure 6) are microspheres with the desirable spherical morphology. PMMA stands for Poly methyl methacrylate, also known as acrylic glass. The material is thermoplastic and transparent. Two sizes have been used for this work: 20 µm and 50 µm.

The goal is to find the optimum distance between anode and cathode. On the one hand a reliable separation must be assured on the other hand if the resistance is too high then the ions cannot move anymore between cathode and anode hindering the proper working of the battery. For that reason, the right number and size of the beads in the electrolyte must be evaluated.

To find out about the minimum separator function a simple short circuit test was carried out by putting different weights (mechanical loads) on the batteries. However, that was not a complete battery in this case. The test samples do not need to contain anode and cathode. The printable electrolyte was just sandwiched between the upper and the lower current collector making this a very harsh test since the thick-

ened electrolyte itself could contribute as well at least a bit to the separating function. During the loading with weights simply the ohmic resistance was measured using a multimeter.

2.5.2 Electrolyte composition and preparation

Both chemicals, $ZnCl_2$ and NH_4Cl, are white crystalline salts that are highly soluble in water. They both are commonly used as electrolytes as they have high ionic conductivity. Distilled water was used to create a solution with the Zinc Chloride and Ammonium Chloride as well as dissolve the Agar-Agar.

The electrolyte was prepared in a plastic laboratory jar. The substances were added in the following order: first the salts to form the solution with the water. Then the thickener Agar-Agar was added up in several steps, each time small amounts were added to the system until it reached the desired amount in the desired percentage. By adding the thickener, the electrolyte was constantly mixed up to avoid inhomogeneity. After the electrolyte was ready, it was manually mixed so that the Agar-Agar could dissolve in the liquid solution.

2.5.3 Printing process

A semi-automatic laboratory screen-printing machine Ekra E2 was used. The following specifications have been set up: the speed of the squeegee set to 100 mm/s; pressure of the squeegee 136 N; snap-off distance 2 mm. The screen used was a PET mesh with 21–140 (n-d i.e., mesh count in threads per cm – thread diameter in µm). This mesh has a nominal mesh opening of 340 µm. The rule of thumb that the mesh size should be at least 3 to 4 times the largest particle size (e.g., 50 µm PMMA beads) in the ink is thus easily fulfilled.

A two-stroke operation was used, meaning that the flood bar and the squeegee moved two times back and forth. Figure 7 shows the placement of the pre-printed current collectors onto the vacuum table of the press. Two copies with upper and lower current collectors fit on the layout. Later, the two halves are folded over each other along the previously made perforation in the middle.

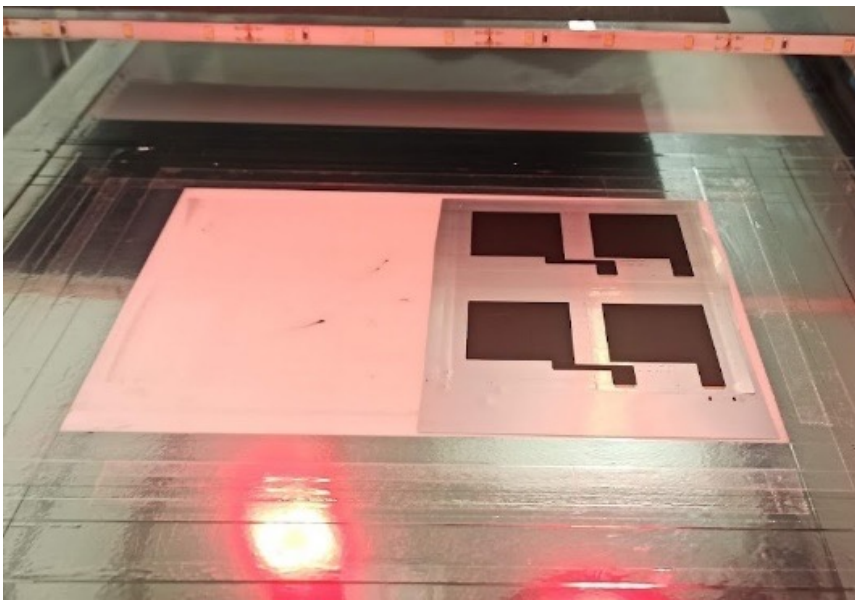

Figure 7: Pre-printed battery current collectors (two copies) placed on vacuum table of press

Figure 8 shows the simple, rectangular layout for the printing of the electrolyte. The electrolyte is printed on both the lower and the upper current collectors respectively electrodes. Since the left side of the screen was not used here it was taped with a silver blocking tape.

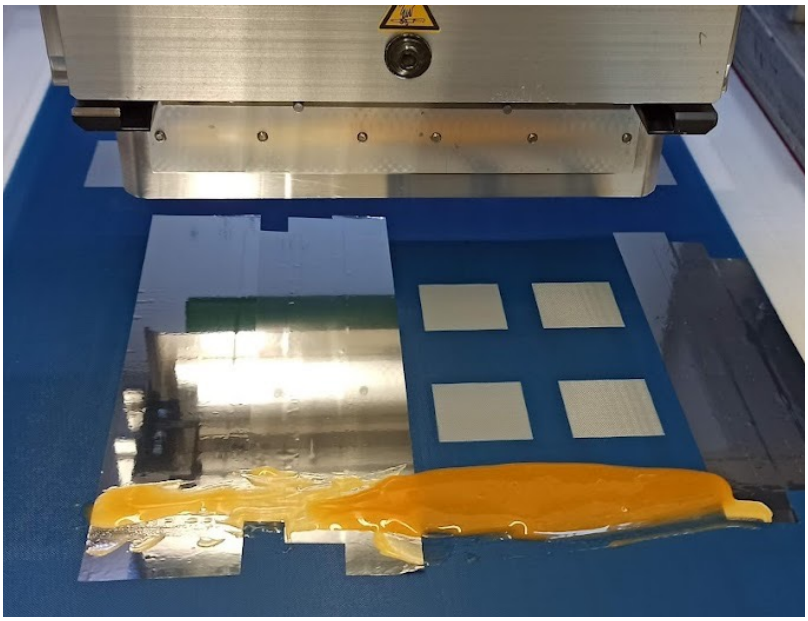

Figure 8: Ink (printable electrolyte) poured on the screen

3. Results

The standard electrolyte solution that was found to be optimal during previous preliminary tests was 40 wt.% of $ZnCl_2$. To this master solution different amounts of thickener (Agar-Agar) were added. Figure 9 shows the viscosity readings at a shear rate of 100 s^{-1}. The measurements were not repeated with a statistically significant numbers of test runs. However, the accuracy can be estimated at ± 2 Pas.

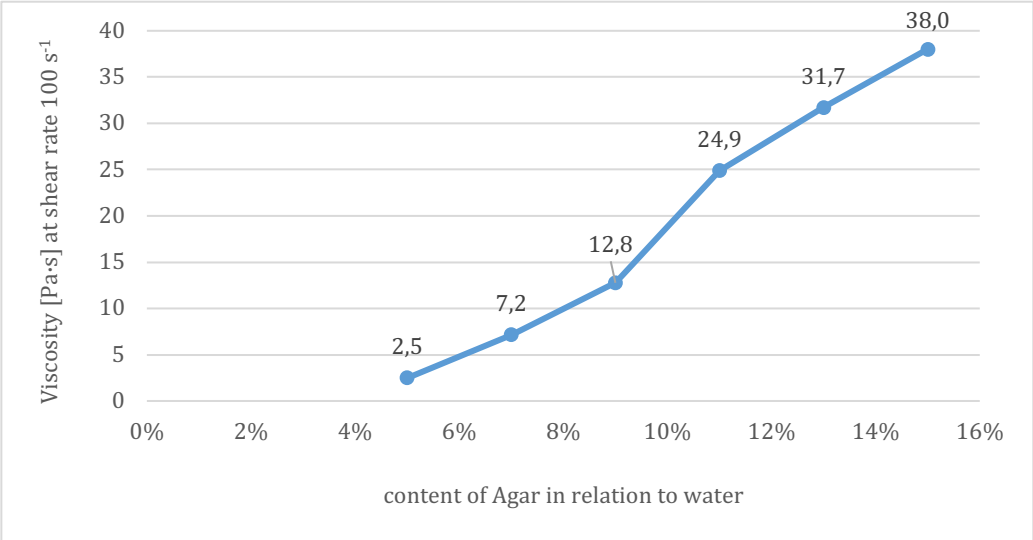

Figure 9: Viscosity of the electrolytes with six different percentages of Agar-Agar

The thickener has been added with regard to the amount of water in the solution. It is evident that the higher the amount of thickener is, the higher will be the viscosity. Since the printability of the tests was satisfactory beginning with an addition of 11 % thickener or higher, we continued all further experiments with a standard of 11 % (equivalent to 7 wt.% of the total solution).

With regard to battery performance, the influence of the addition of the thickener on the conductivity is important. From Figure 10 it can be seen that there is a clear influence. However, the assumption that the addition of the thickener reduces the amount of water and salt does not correspond to the extent of the decrease in conductivity. It could be that the addition of agar forms a gel network that impedes the movement of ions (including hydrate shells) through the electrolyte. These measurements were carried out in the test setup shown in Figure 2 and do not represent the final achievable battery performance. This is the subject of ongoing research.

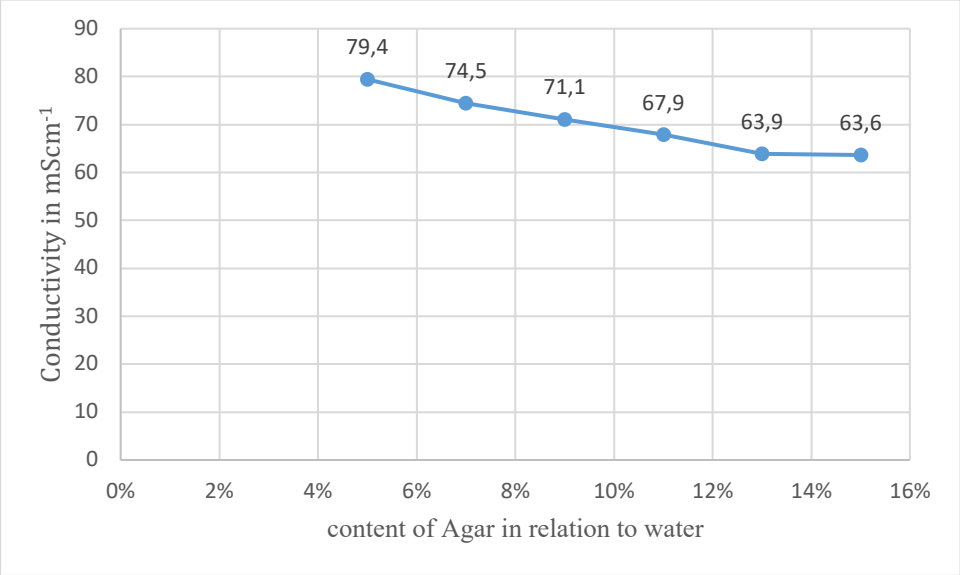

Figure 10: Conductivity measurements electrolyte solutions at frequency 1 MHz; the $ZnCl_2$ content was kept constant at 40 % with respect to water

3.1 Usage of spacers

Although results with the addition of phenolic resin beads to the standard formulation (40 % $ZnCl_2$ based on water content, 11 % Agar based also on water content) at the first glance looked promising

- Increase of viscosity (at 50 s^{-1}) from 35.5 Pas to 38.4 Pas
- Decrease of conductivity from 73.1 mS cm^{-1} to 71.5 mS cm^{-1}

the investigation was not continued because over time the properties changed significantly, and it is assumed that due the hollowness of the beads the electrolyte penetrates into the inner body and conversely that means that the resin somehow is softened or even dissolved. Further, a reaction could not to be excluded. As can be seen in Figure 11, the prints show a foam effect (trapped air escaping?) and a very inhomogeneous surface. The unevenness decreases a little over time, but too many imponderables remain, so this approach was not pursued further.

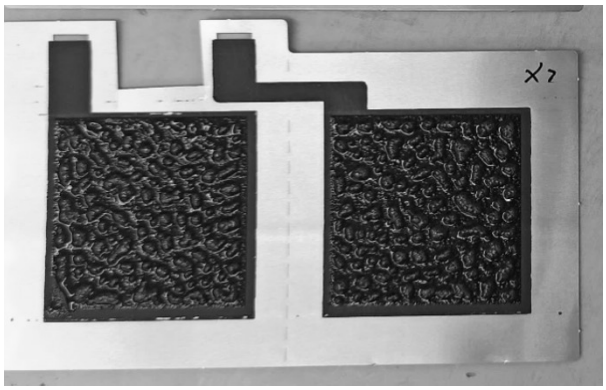

Figure 11: Inhomogeneous surface with foam like structures appeared after printing the standard electrolyte with phenolic resin hollow beads

The continuation of the experiments with PMMA beads turned out to be more successful. In Table 1 the results of the short circuit test (printable electrolyte with beads added sandwiched between lower and upper current collectors) are listed. Short circuit as a result means that there is no separation function achieved, infinite, however, is the desirable outcome.

Table 1: Results of the short circuit test with different weights (PMMA 20 µm beads)

PMMA 20 µm beads	Amount of beads					
	5 %	8 %	14 %	17 %	18 %	19 %
Weight 330 g	Short circuit	Short circuit	Short circuit	Short circuit	>600 kΩ	infinite
Weight 600 g					~300 Ω	
Weight 850 g					~70 Ω	
Weight 1 100 g					Short circuit	

The results of the short circuit test with the 50 µm PMMA beads summarized in Table 2 are much more promising.

Table 2: Results of the short circuit test with different weights (PMMA 50 µm beads)

PMMA 50 µm beads	Amount of beads			
	1 %	2 %	3 %	5 %
Weight 330 g	Short circuit	Short circuit	infinite	infinite
Weight 600 g			~70 Ω	
Weight 850 g			Short circuit	
Weight 1 100 g			Short circuit	

Based on this result for further testing PMMA 50 µm beads were used with 4 wt.% in the electrolyte formulation.

In parallel work was done on finding most promising mixtures of $ZnCl_2$ and NH_4Cl and further investigations focused on the optimum mixture of these two components. A series of measurements with different mixture ratios was carried out. Figure 12 shows the increase of conductivity measured with the different ratios. The components are abbreviated. "A" stands for NH_4Cl, and "Z" for $ZnCl_2$. The sum of the components was always kept at 40 %.

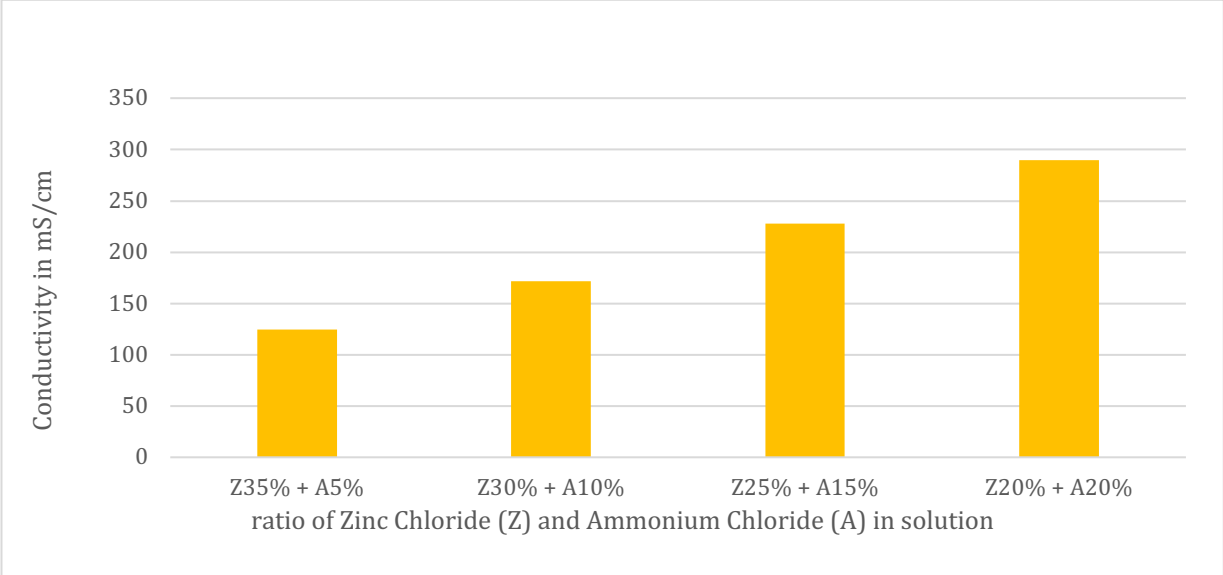

Figure 12: Conductivity of $ZnCl_2$ and NH_4Cl, solution mixtures

The rheological measurements with these different ratios showed no change in behaviour, at all.

To find out what is the optimum ratio between "A" and "Z" batteries were fully assembled and tested. Figure 13 shows the result in terms of energy.

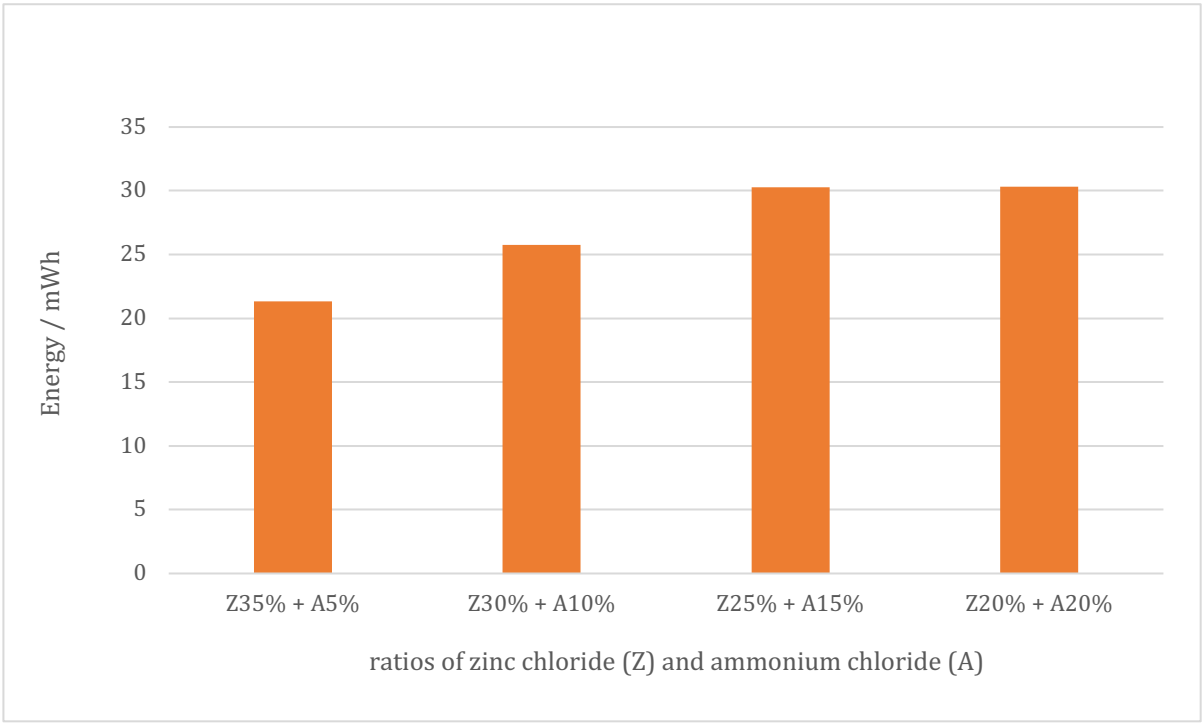

Figure 13: Performance of test cells with different $ZnCl_2$ / NH_4Cl mixtures

As a result from this test, the optimum ratio was assumed to be Z 25 % + A 15 %. In the further investigation this ratio is called "S".

Figure 14 shows a comparison of the measured conductivity between the new standard formulation "S" with different levels of Agar and the starting point "Z" 40 % + 11 % Agar. It is evident that the lowest amount of addition of any material is desirable.

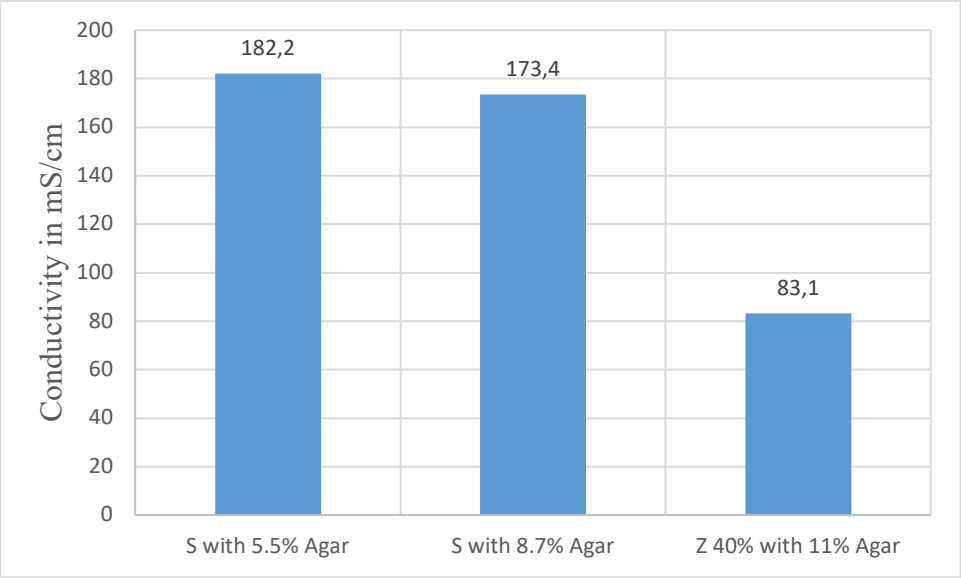

Figure 14: Conductivity of different electrolytes with 4 % PMMA 50 beads at f = 1 MHz

The addition of beads, however, changes the viscosity readings significantly. As can be seen in Figure 15 the values increase by factors between 25 and 4.

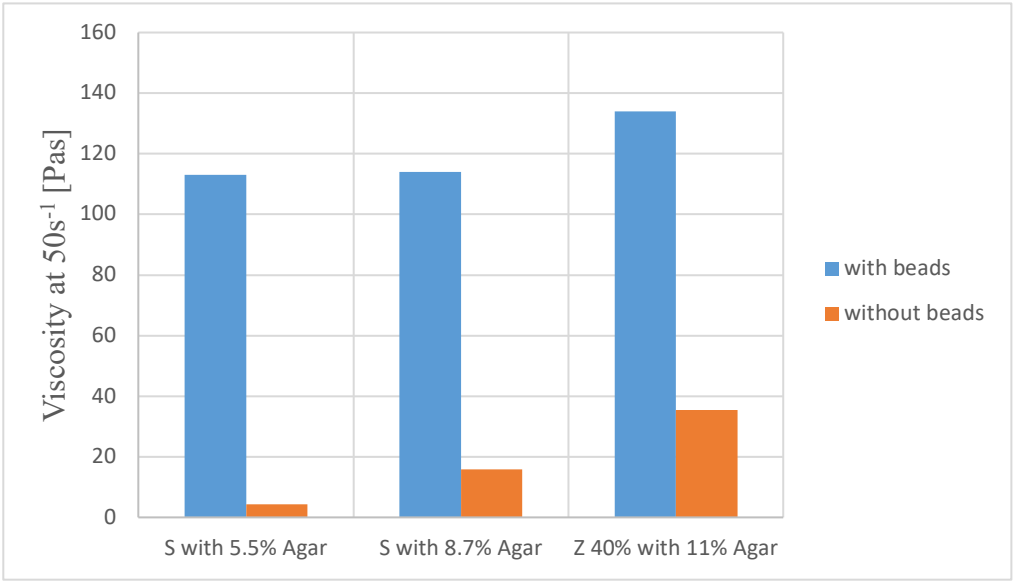

Figure 15: 2 viscosity of different electrolytes with and without 50 µm PMMA beads

Figure 16 shows some print results. The spacer functionality can be seen clearly. The $ZnCl_2$ electrolyte with the highest amount of Agar shows the smoothest surface. However, this might not be desirable since the electrolyte and the anode and cathode electrodes should have a high common surface to amplify the ease of ion transport.

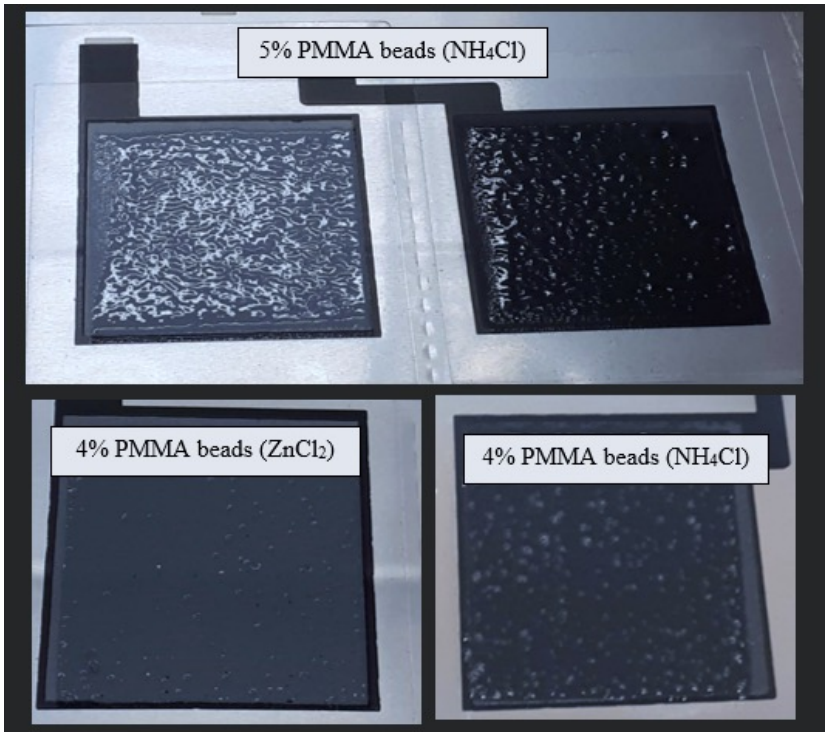

Figure 16: Printed samples with three different electrolytes and 5 % PMMA 50 µm beads

With these results in total six fully printed sample cells were assembled.

- 2 cells with 40 % $ZnCl_2$, 11 % Agar-Agar + 4 % PMMA 50 µm beads
- 2 cells with 25 % $ZnCl_2$ + 15 % NH_4Cl, 8.7 % Agar-Agar + 4 % PMMA 50 µm beads
- 2 cells with 25 % $ZnCl_2$ + 15 % NH_4Cl, 8.7 % Agar-Agar + 5 % PMMA 50 µm beads

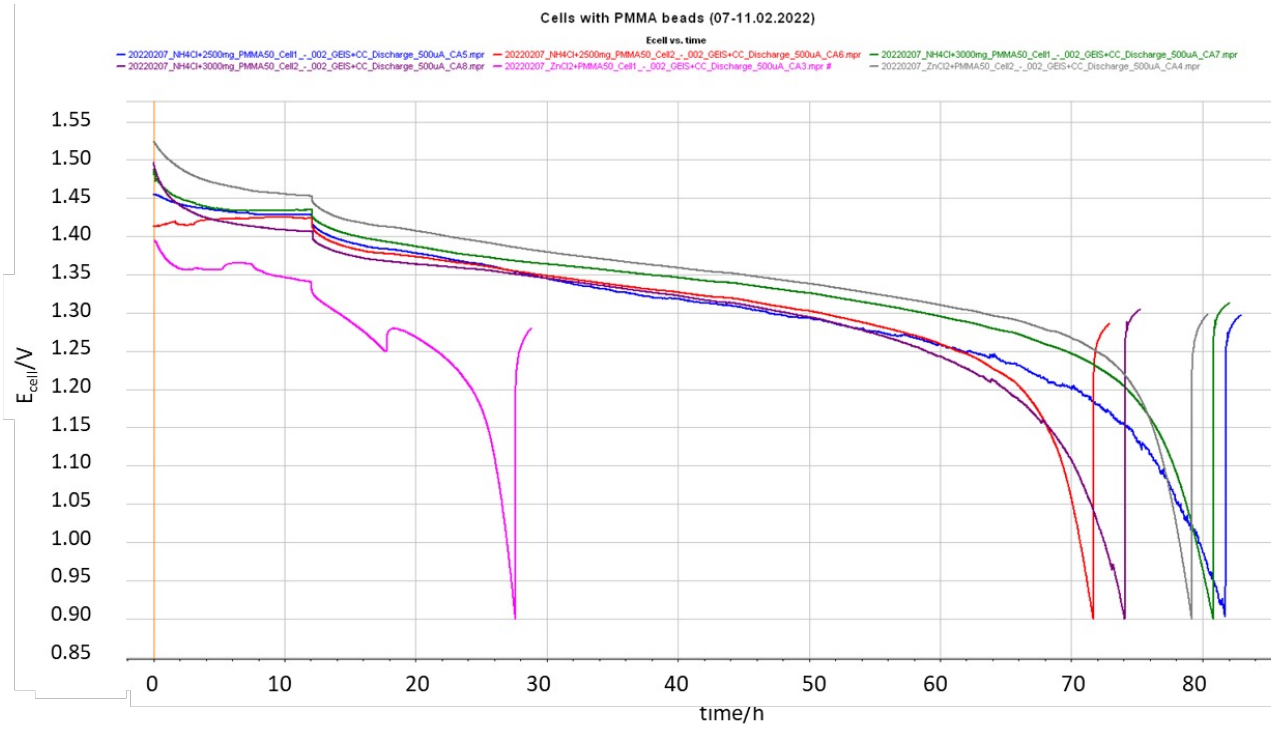

Figure 17: Discharge curves of the six assembled fully printed cells (the raise of the curves after the discharge voltage of 0.9 V has been reached is an artefact of the potentiostat which erroneously tries to recharge)

The discharge curves of the cells at a constant load of 0.5 mA are shown in Figure 17. One of the cells failed quite early. The reason is unknown, but all the others performed very well with a duration of up to 70 hours. In Figure 18 the corresponding performance results are shown. They are given in energy values mWh or, as usual for batteries, in terms of capacity in mAh. The area of the cells is approximately 13 cm^2. Thus, some cells show an – for printed zinc manganese dioxide cells – outstanding capacity of 2.7 mAh/cm^2.

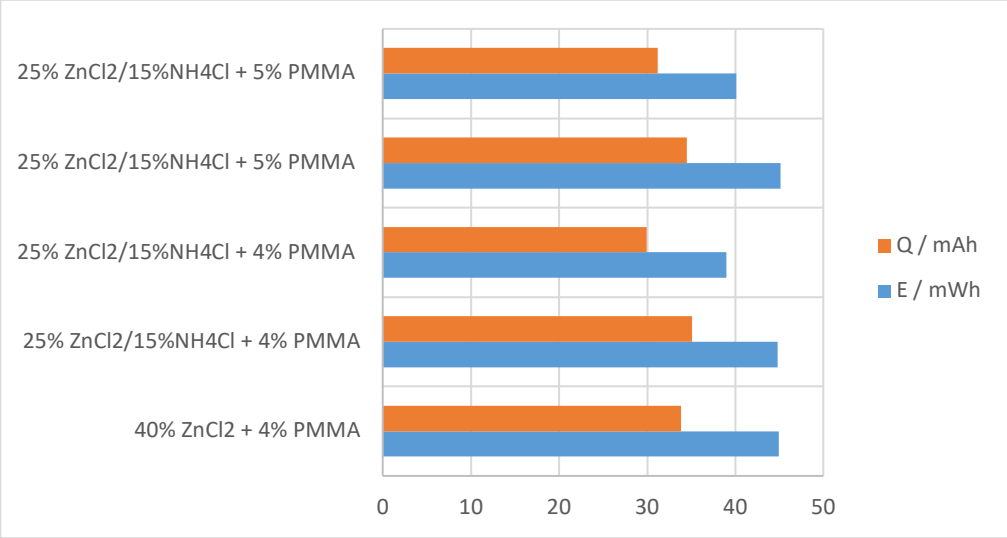

Figure 18: Energy and capacity of the cells (without the failed cell)

4. Conclusion

It could be shown that a printable electrolyte is possible by using a widely available and affordable ingredient Agar-Agar used as a thickener agent. By adding PMMA beads around 50 µm the separator function can be realized in printing techniques only by avoiding the disruptive process of inserting a fleece soaked with liquid electrolyte.

By using a mixture of ammonium chloride and zinc chloride the overall capacity of the battery could not be increased but the batteries perform much better if a pulsed load is applied.

Further optimizations need to be done regarding the size of the beads and shelf life stability.

Acknowledgements

Parts of the research was funded by the German Ministry of research and education in the scope of the project OxiFlexIT.

Some contributions stem from the project BEWELL that was funded under the EU program Horizon 2020. Thanks to all the partners in these projects, especially VARTA Microbattery GmbH.

References

BEWELL, 2022. *Wearable sensors and actuators*. [online] Available at: <https://h2020bewell.eu> [Accessed February 2022].

Biologic, 2022. *What is Electrochemical Impedance Spectroscopy (EIS)?* [online] Available at: <https://www.biologic.net/topics/what-is-eis/> [Accessed February 2022].

CarlRoth, 2022. *Agar-Agar, BioScience, granualted, 1 kg.* [online] Available at: <https://www.carlroth.com/de/en/agar/agar-agar-bioscience-granulated/p/1347.3> [Accessed February 2022].

Gamry, 2009. *Application note: basics of electrochemical impedance spectroscopy.* [pdf] Gamry Instruments. Available at: <https://www.gamry.com/assets/Application-Notes/Basics-of-EIS.pdf> [Accessed February 2022].

Hübner, G., Krebs, M., Rassek, P. and Willfahrt, A., 2015. Printed batteries, overview, status, recent developments, future perspectives. In: P. Gane, ed. *Advances in Printing and Media Technology: Proceedings of the 42nd International Research Conference of iarigai.* Helsinki, Finland, September 2015. Darmstadt: iarigai, pp. 183–193.

Hübner, G., Krebes, M., Etzel, F., Nußbaum, L. and Thamm, S., 2021. Printed batteries, properties of substrates and components, regarding bendability and barrier. In: C. Ridgway, ed. *Advances in Printing and Media Technology: Proceedings in of the 47th International Research Conference of iarigai.* Athens, Greece, 19–23 September 2021. Darmstadt: iarigai, pp. 29–42. https://doi.org/10.14622/Advances_47_2021.

Knoblauch, C., 2015. Impedanzspektroskopie – Ein Überblick von der Theorie bis zur Anwendung. *WOMag,* 4(9), pp. 31–39. https://doi.org/10.7395/2015/Knoblauch1.

Kremer, 2022. 59960 *Phenolic resin – hollow beads*. [pdf] Kremer Pigmente. Available at: <https://shop.kremerpigments.com/elements/resources/products/files/59960e.pdf> [Accessed February 2022].

OxiFlexIT, 2022. *OxiFlexIt – Mobiles Überwachungssystem für arteriosklerotische Gefäßerkrankungen*. [online] Available at: <https://oxiflexit.hdm-stuttgart.de> [Accessed February 2022].

Wikipedia, 2019. *Zinkchlorid-Zelle*. [online] Available at: <https://de.wikipedia.org/wiki/Zinkchlorid-Zelle> [Accessed February 2022].

Wikipedia, 2022. *Zink-Braunstein-Zelle*. [online] Available at: <https://de.wikipedia.org/wiki/Zink-Braunstein-Zelle> [Accessed February 2022].

DOI 10.14622/Advances_48_2022_04

Inks for Li-ion battery anodes printed by rotogravure

Jorge Vicco Mateo, Kevin Matthew, Alexandra Pekarovicova and Paul D. Fleming

Center for Printing and Coating Research, Western Michigan University, Kalamazoo, MI
E-mail: a.pekarovicova@wmich.edu

Short abstract

Inks for Li-ion battery anodes were formulated for printing with the rotogravure printing process. Graphite with different particle sizes were used as conductive materials along with nanoparticle carbon fillers. As polymer binders, polyvinylidenefluoride PVDF (commercial names Kureha 9100, Kureha 9300, Solef 5130) and polyvinyl pyrrolidone (PVP) were tested. Inks were printed using proprietary gravure engraving. Ink solid content of 30–70 % was examined. At 70 % solids, ink layers were 25–27 µm thick with mass loading of 2.1–2.5 mg/cm^2. Half cells were made using print with 1 000 µm holes or they were bar coated. Half cells were charged and discharged in order to measure irreversible capacity loss (ICL). Inks with mixed binders Kureha/PVP were performing better than sole polymers. Half-cell testing revealed that PVP should be mixed with PVDF for improved performance. ICL was lower when mixed PVDF/PVP binder was employed.

Keywords: printed batteries, anodes, rotogravure, ink formulation, half-cell, capacity, irreversible capacity loss

1. Introduction and background

Due to the increasing impact of oil pollution on the environment (CO_2 production and liquid spills), more automobile and many other industries have turned to electric item manufacturing. Therefore, the production of more energy-efficient and environmentally friendly batteries has become a hot topic at the moment. The traditional lead-acid battery is bulky and heavy, but the printed battery can print much thinner and lighter batteries through the printing process to provide power for wearable devices, flexible displays, smart labels among others (Costa, Gonçalves and Lanceros-Méndez, 2020; Khan, Lorenzelli and Dahiya, 2015). With the advent of printed electronics, flexible batteries have undergone rapid development in the past ten years. Currently, many researchers are focusing on screen printing of battery electrodes. This printing technology can use semi-liquid inks for printing, which allows them to have good coverage on substrates of different materials, such as paper, plastic, or foil, which are suitable for printing lithium metal battery electrodes (Khan, Lorenzelli and Dahiya, 2015). Based on the size required to print battery electrodes, the number of active materials, the roughness of the electrode layer, and the thickness of each layer of the battery can be modified. There have been many studies using printing methods such as gravure printing, flexographic printing, screen printing, extrusion printing, and inkjet printing to explore battery electrodes production (Søndergaard, Hösel and Krebs, 2013; Huebner, et al., 2015). Lithium metal powder-based inks, which include lithium metal powder, polymer binders, and other conductive materials, can be used in anode printing. In general, the advantages of printed batteries are based on mature printing technology, and the fact that they are light, flexible, low cost, can be mass-produced, customizable, and more environmentally friendly.

Research in the printed batteries based on gravure printing showed that the quality of the gravure printing layer mainly depends on several physical parameters such as ink, substrate, and process. To enable the mass production of batteries through gravure printing, the study was done using carbon coated $Zn_{0.9}Fe_{0.1}O$ (encapsulated in a thin film of carbon) as a reference alloying material (Bresser, et al., 2013). With the wa-

ter based electrode inks, 2-propanol can be used as a cosolvent to reduce the excessive surface tension of water-based inks, in combination with corona pretreatment of the substrate, for increased surface energy and thus ink adhesion (Biscay, Ghoufi and Malfreyt, 2011). Using the gravure printing process, multiple layers can be deposited, and the multilayer method applied is able to obtain the required mass loading (about 1.7 mg/cm^2) to achieve high homogeneity of the gravure printing layer, and its highly reproducible electrochemical performance up to 400 life cycles (Montanino, et al., 2021).

Printing inks for anode and cathode inks include active materials such as graphite, silicon, or active fillers such as nanocarbons, and resins or binders which were selected based on ink chemistry whether ink was solvent, or water based. Resins can include among others itigated polyacrylic acid, or polyvinylidene fluoride of different degree of polymerization. Printed layers should be thick, preferably up to 100 µm and therefore screen-printing is the process of choice (Rassek, et al., 2019). In this work, the aim was to formulate rotogravure printing inks for anodes and evaluate their printability in terms of print uniformity, thickness of the layers and ultimately, half-cell battery performance.

2. Materials and methods

A Thinky Mixer AR 100 (THINKY Co., Tokyo Japan) was used for mixing the inks. As the conductive graphite Philips 5 µm, 10 µm, 15 µm (Philips 66, Houston, Texas) and Mage 3 graphite (Hitachi Chemical, Sakuragawa, Japan), and conductive nanoparticle carbon filler (CB 4400 or C45) were used. Polyvinylidenefluoride (PVDF) (by Sigma Aldrich) with different degrees of polymerization and commercial names Kureha 9100, Kureha 9300 (Kureha Co., Japan) or Solef 5130 (Solvay Co.), with various molecular weights of 1×10^6 to 2.8×10^5 was dissolved in N-methyl-2-pyrrolidone (NMP) solvent and used as the vehicle. In some inks, a polyvinylidene/polyvinylpyrrolidone mix of binders (PVDF-PVP) was employed. Printing was done on Cu foil.

Rotogravure plate for RK gravure K-proofer was engraved in WRE /ColorTech (Greensboro, NC, USA) with proprietary engraving at 75 LPI. A plate was engraved with 1 000, 500, 250 and 125 µm hole shaped nonimage areas. Detail of 500 µm nonimage area is shown in Figure 1 and white light interferometry detail is shown at Figure 2, showing depth of cells at 75 µm and cell opening in one direction at 1 194 µm. Engraving was done by hybrid process of laser ablation and chemical etching.

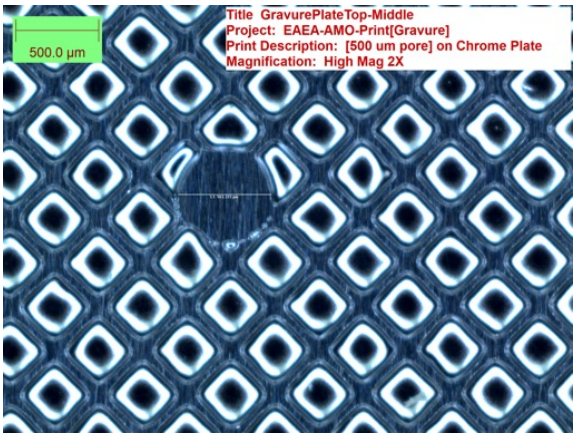

Figure 1: Detail of new gravure engraved plate (by WRE Color/Tech, Greensboro, NC, USA) with 500 µm nonimage area (round hole)

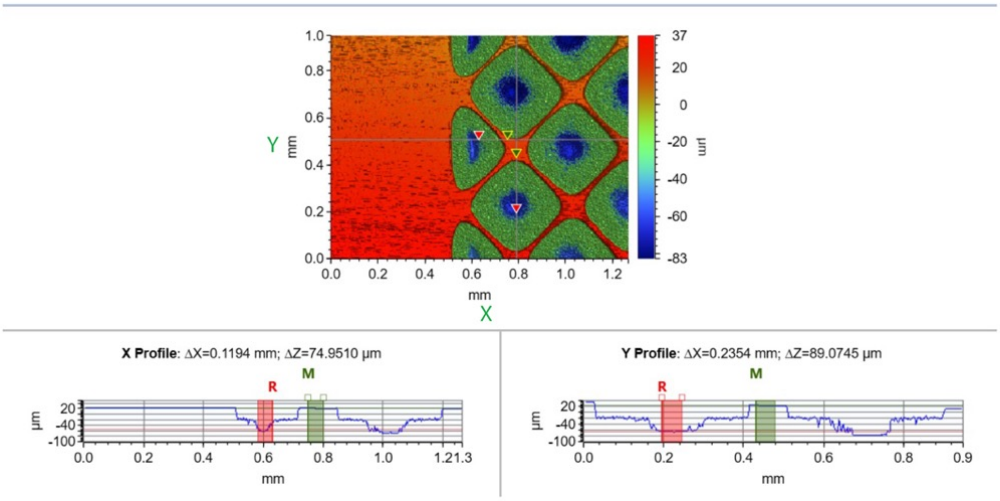

Figure 2: White light interferometry of gravure engraved plate

The profile of the plate and ink films was done on a Bruker white light interferometry instrument. Image analysis of printed ink films was done using Pax it 2 software.

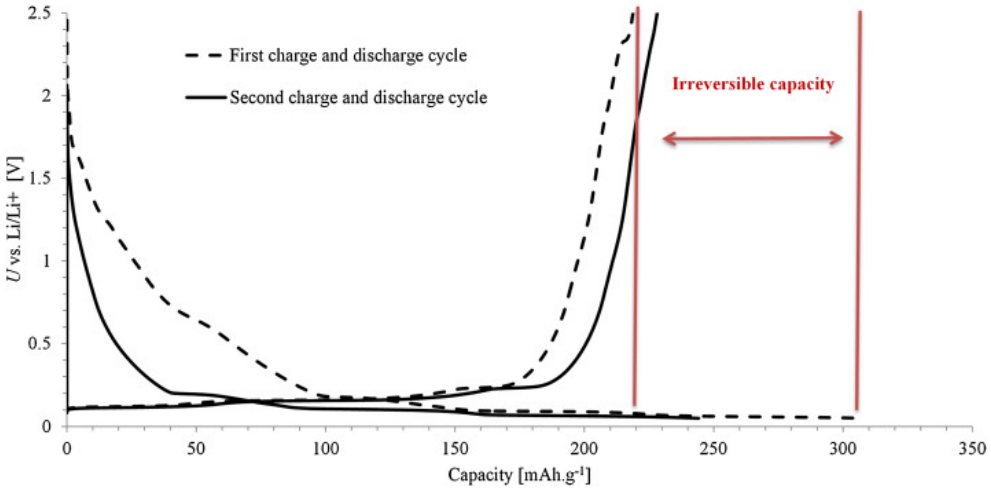

Figure 3: Illustration of irreversible capacity loss determination (Libich, et al., 2017)

Reversible/irreversible capacity and stability of the electrode can be obtained from the galvanostatic cycling technique (Figure 3). The galvanostatic cycling technique provides information about reversible/irreversible capacity and stability of the electrode. In order to test irreversible capacity loss of anodes, half coin cells were constructed (Figure 4).

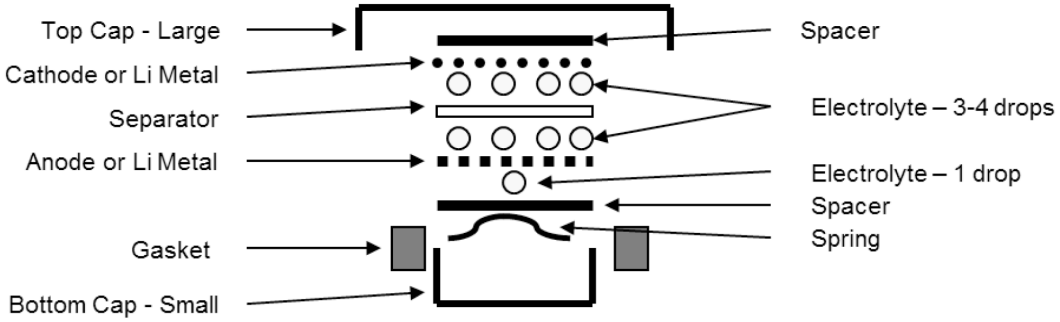

Figure 4: Schematic of half coin cell (Jansen, et al., 2018)

3. Results and discussion

A plate for rotogravure printing of anodes was engraved with 1 000, 500, 250 and 125 µm nonimage areas. Detail of engraving along with 500 µm nonimage area is shown in Figure 1 and white light interferometry detail of engraved plate is shown at Figure 2, showing depth of cells at 75 µm and cell opening in one direction 1 194 µm. Holes (non-image areas) in the electrode design are meant to improve access of electrolyte to electrodes in assembled battery. Anodes were printed with long chain polyvinylidenefluoride polymer inks such as Kureha 9300 or Solef 5130. As a solvent, with N-methylpyrrolidone (NMP) was employed. Inks were filled with graphite of different particle sizes. Gravure printing of these inks did not result in successful substrate coverage (data not shown). Because of ink's high viscosity, it most likely could not enter and exit gravure cells.

A new resin polyvinylpyrrolidone (PVP) at 10 000 molecular weight was used to disperse graphite and nanocarbon active materials. Inks with 30–72 % solids were made. Inks were formulated with Graphite from Philips (P5) with size of 5 microns, and conductive filler CB 4400 with the ratio of ingredients: Philips P5/CB 4400/PVP (80:5:15). As a solvent, ethanol or NMP were used. Ethanol was evaporating too fast, thus N-methylpyrrolidone (NMP) was chosen as a more suitable solvent. The average surface tension of NMP ink with 70 % solids was 39.4 mN/m and average contact angle with copper surface was 40.8° (data not shown). At 70 % solids, ink layers were 25–27 µm thick with mass loading of 2.1–2.5 mg/cm^2 (data not shown). Half cells were made using print with 1 000 µm holes or they were bar coated. Gravure prints with N-methylpyrrolidone (NMP) as a solvent were easier to work with than using inks with water or ethanol as a solvent. Designed holes with diameter 1 000 µm were resulting in printed 846 ± 20 µm in diameter, while 500 µm holes were printed with 219 ± 11 µm diameter (data not shown).

Printed ink films on copper foil were used to construct half coin cells according to Figure 4. Half cells were used to assess reversible/irreversible capacity and stability of printed anodes. Irreversible capacity loss of half coin cells made with PVP inks was too high and half cells did not have sufficient electrical performance. Thus, in the next step PVP was mixed with PVDF – Kureha 9100 or Kureha 9300 and half cells were made again. First attempts showed that mixing Kureha and PVP resins is possible, so far 2:1 ratio was tested, and inks exhibited uniform prints. Their performance in terms of irreversible capacity loss (ICL) was tested again (Figure 5). Inks were bar coated, not gravure printed to ensure higher thickness of layers than what was possible to achieve with gravure printing.

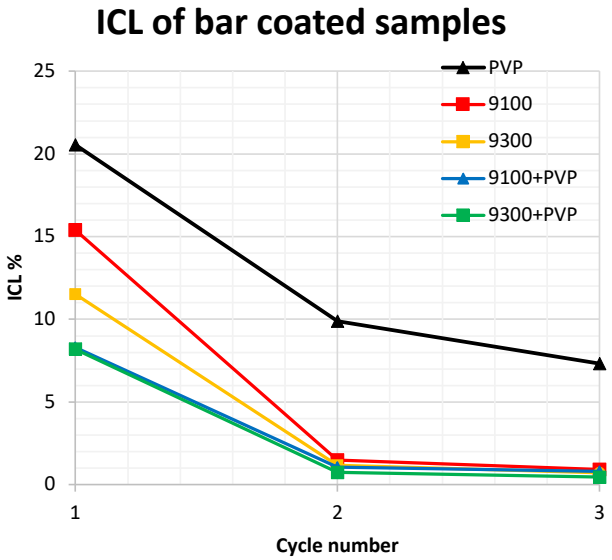

Figure 5: Comparison of half-cell battery performance (as ICL) with resins: sole PVP, sole PVDF or combination PVP/PVDF

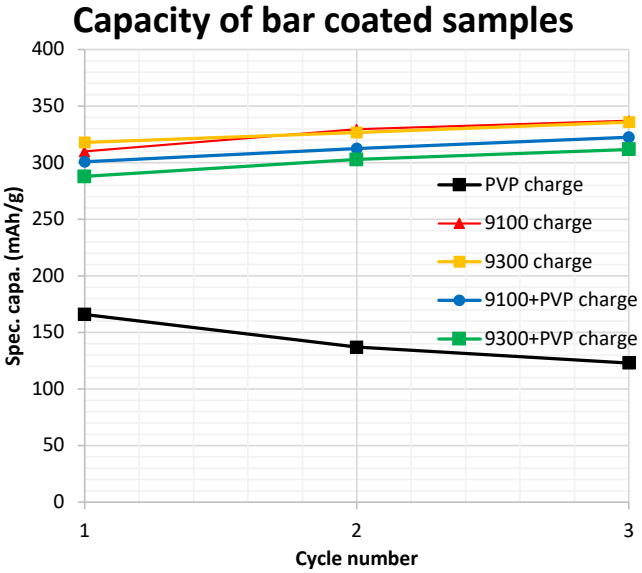

Figure 6: Capacity of bar coated samples; test conditions: formation: 0.01–1.5 V; +/– 0.1 C

From Figures 5 and 6 it can be seen that performance of mixed PVP/PVDF inks was greatly improved, and mixed PVP/PVDF achieved actually slightly better performance and suffered from less ICL than inks made with sole Kureha 9100 or 9300.

4. Conclusions

Gravure inks for battery anodes were formulated and printed on a laboratory K-proofer with proprietary engraving. It was found that polyvinylpyrrolidone (PVP) inks showed good printability but poor battery performance. Using mixed PVP/PVDF 9300 or PVP/PVDF 9100 binder combination could effectively improve battery performance without significantly sacrificing the printability. From several graphites having particle sizes between 5 µm to 15 µm, graphite with 5 µm particle size was the most suitable for gravure printing. Polyvinylidenefluoride (PVDF) inks under commercial name Kureha 9100 or 9300 with N-methylpyrrolidone (NMP) solvent showed best specific capacity during three charging/discharging cycles, and irreversible capacity loss was even lower when these PVDF polymers were mixed with polyvinylpyrrolidone.

References

Biscay, F., Ghoufi, A. and Malfreyt, P., 2011. Surface tension of water–alcohol mixtures from Monte Carlo simulations. *The Journal of Chemical Physics,* 134(4): 044709. https://doi.org/10.1063/1.3544926.

Bresser, D., Mueller, F., Fiedler, M., Krueger, S., Kloepsch, R., Baither, D., Winter, M., Paillard, E. and Passerini, S., 2013. Transition-metal-doped zinc oxide nanoparticles as a new lithium-ion anode material. *Chemistry of Materials,* 25(24), pp. 4977–4985. https://doi.org/10.1021/cm403443t.

Costa, C.M., Gonçalves, R. and Lanceros-Méndez, S., 2020. Recent advances and future challenges in printed batteries. *Energy Storage Materials*, 28, pp. 216–234. https://doi.org/10.1016/j.ensm.2020.03.012.

Huebner, G., Krebs, M., Rassek, P. and Willfahrt, A., 2015. Printed batteries overview, status, recent developments, future perspectives. In: P. Gane, ed. *Advances in Printing and Media Technology: Proceedings of the 42nd International Research Conference of iarigai.* Helsinki, Finland, 6–9 September 2015. Darmstadt: iarigai.

Jansen, A., Dunlop A., Polzin, B. and Trask, S., 2018. *CAMP facility electrode and cell development for fast charge applications*. [pdf] Washington, DC: US DOE, Vehicle technologies office, 2018 Annual Merit review. Available at: <https://www.energy.gov/sites/default/files/2018/06/f52/bat371_Jansen_2018_o.pdf> [Accessed: February 2022].

Khan, S., Lorenzelli, L. and Dahiya, R.S., 2015. Technologies for printing sensors and electronics over large flexible substrates: a review. *IEEE Sensors Journal,* 15(6), pp. 3164–3185. https://doi.org/10.1109/JSEN.2014.2375203.

Libich, J., Máca, J., Vondrák, J., Cech, O. and Sedlaríková, M., 2017. Irreversible capacity and rate-capability properties of lithium-ion negative electrode based on natural graphite, *Journal of Energy Storage*, 14(3), pp. 383–390. https://doi.org/10.1016/j.est.2017.03.017.

Montanino, M., Sico, G., De Girolamo Del Mauro, A., Asenbauer, J., Binder, J.R., Bresser D. and Passerini, S., 2021. Gravure-printed conversion/alloying anodes for lithium-ion batteries. *Energy Technology,* 9(9): 2100315. https://doi.org/10.1002/ente.202100315.

Rassek, P., Steiner, E., Herrenbauer, M. and Claypole, T.C., 2019. The effect of electrode calendering on the performance of fully printed Zn|MnO_2 batteries. *Flexible and Printed Electronics,* 4(3): 035003. https://doi.org/10.1088/2058-8585/ab38e2.

Søndergaard, R.R., Hösel, M. and Krebs, F.C. 2013. Roll-to-roll fabrication of large area functional organic materials. *Journal of Polymer Science Part B: Polymer Physics,* 51(1): pp. 16–34. https://doi.org/10.1002/polb.23192.

DOI 10.14622/Advances_48_2022_19

Generation of a paper embossing preview using 3D scanning and Fourier analysis

Jakob Feldmann[1], *Felix Braig*[1], *Dieter Spiehl*[1], *Edgar Dörsam*[1] *and Andreas Blaeser*[2,3]

[1] Technical University of Darmstadt, Department of Mechanical Engineering, Institute of Printing Science and Technology, Magdalenenstr. 2, 64289 Darmstadt, Germany

[2] Technical University of Darmstadt, Department of Mechanical and Process Engineering, Institute for BioMedical Printing Technology, Magdalenenstr. 2, 64289 Darmstadt, Germany

[3] Technical University of Darmstadt, Centre for Synthetic Biology, Schnittspahnstr. 10, 64287 Darmstadt, Germany

E-mails:feldmann@idd.tu-darmstadt.de;spiehl@idd.tu-darmstadt.de;doersam@idd.tu-darmstadt.de;blaeser@idd.tu-darmstadt.de

Short abstract

The design and manufacture of embossing tools is a strong bottleneck in the development of new embossed paper and cardboard products. In the previous conventional process, a new embossing tool often has to go through several iteration loops until a satisfactory embossing result is achieved with it in trial embossings. This not only causes considerable cost and time expenditure, but also delays the market launch of new products. In order to provide the possibility of a preliminary evaluation and preview of the embossing result, a method was developed to determine the embossing behavior in the desired substrate. For this purpose, a universal test tool is used to emboss the substrate to be embossed. The embossing result is then scanned in three dimensions. The two data sets, original heightmap and fitted 3D scan relief data, are then transformed into the frequency domain utilizing a fast Fourier transformation (FFT). With a comparison it can be determined which frequency ranges deviate by which amount between the original data and the real embossing result. This allows conclusions to be drawn about the embossing capability of details and embossing features, as well as the creation of a preview of future embossing reliefs for this substrate. The results of this approach are presented and their significance for the future design process of new embossing tools is discussed.

Keywords: embossing, 3D printing, additive manufacturing, heightmaps, Fourier transformation, structured light scanning

1. Introduction and background

In addition to graphic print, raised elements and embellishments on packaging are an important way of attracting the attention and recognition of a product for the end consumer market (Hartmann and Haupt, 2016). Next to a visual enhancement of features such as letters and logos, raised elements add a haptic component to the perception of packages. With increasing environmental awareness, more and more packaging that previously used plastic is being replaced by ones made of paper and cardboard (Burger, et al., 2021). While plastic blister packs can be vacuum formed into almost any shape, making it easy to create these elements, embossing must be used for raised features in paper packaging. Embossments in paper are also used for finishing of a wide range of other paper products, such as cards, advertising materials or as copy protection in documents (Werblow, 2009). In addition to purely decorative purposes, embossing can also serve to add functional elements, such as closure flaps, adhesive surfaces or hazard labels for the visually impaired (Wilken, 2013). Conventionally, a two-part embossing tool, consisting of a female die and a male die is used, which represent inversions of each other, to deform the substrate under the application of compressive force. In the process, the substrate is pressed by the male die into the cavity of the female die and conforms to its surface. After removal of the force the plastic deformation of the paper remains, leaving a permanent impression of the desired relief geometry on the substrate (Wilken, 2013).

Embossing tools used for paper embossing are commonly manufactured from metal blanks which are processed using CNC milling or even manual engraving (Fachverband deutscher Stanzformhersteller e.V., n.d.), which can be very time consuming and can take up to a full business day. The manufacturer of the embossing tool and the printshop that carries out the embossing are often two different entities. Hence, shipping and communication between companies prolong overall lead times further. In addition, an evaluation of the embossing relief is only possible after the production has been completed. Often, defects that need to be corrected and unsatisfactorily formed regions are discovered in the embossing result during initial embossing tests, so that the embossing tool has to be reworked or completely remanufactured. These, often necessary iterative design changes and long manufacturing duration per tool iteration result in lead times of up to several weeks from initial layout to the final embossing tool. Therefore, in contrast to digital graphical print, the preparation of a new embossment poses as an immense bottleneck in the conceptual design of a new packaging or other cardboard product. In addition, multiple iteration loops in the design of new embossing tools lead to a significant additional environmental impact. Each iteration consumes further resources, but most significantly requires transportation between manufacturer of the tool and the printshop. Feldmann, Spiehl and Dörsam (2021) presented a method to fabricate embossing dies directly from relief data using stereolithography additive manufacturing and presents a comparison of lead times between conventional and additive manufacturing. Although this approach enables production duration of approximately 2.5 hours per set of dies and therefore reducing the overall lead times and costs for a new embossing tool conception, the necessity for possible multiple iteration loops to match a desired embossing layout still remains. It becomes evident, that the reduction or elimination of necessary iteration steps would have an even larger impact on the reduction of the duration, cost and environmental impact of the whole process chain than only shortening production times per step.

We developed a basic method with which substrates can be characterized for embossing and a preview of the embossing result can be estimated. This allows visualization of the expected embossing result already during the initial design of the planned relief design, i.e. even before the production of the tool has started. The purpose of this work is to reduce the number of iterations required by identifying undesirable embossing results early in the embossing relief design process. Also, the preview could be used for communication, as one can get an idea of the intended result before the first test embossing.

2. Technology and methods

As a basic concept we designed a universal embossing test tool, which can be used to characterize substrates intended for embossments. Using this universal test tool, embossments are created which are then digitized using a structured-light 3D scanner. By comparing original data with the obtained 3D scan data of the embossing result, it can be determined which features of the relief design are attenuated by which amount through the embossing process. This is done by fast Fourier analysis (FFT) of the original and the scanned data, allowing the calculation of a comparing characteristic transfer function (CTF). The CTF describes the relative amount each frequency in the original embossing relief layout is altered due to the embossing process and can therefore be used to characterize the substrate and predict embossing results of future designs. The process steps are described in detail below.

2.1 Design of universal embossing test tool

The design of the universal embossing test tool has to fulfill several requirements in order to cover a wide range of possible embossing features and to be significant for an analysis in the Fourier representation. Ideally, the test relief contains features which result in a constant signal for every possible frequency in the Fourier transform, hence it should contain fine details which result in higher frequencies up to broader sections representing lower frequencies. Further, we want to analyze the anisotropic embossing feedback

of the substrate which can be achieved by orienting the lines and features in a circular shape. This also allows for a smooth transition of high frequency details from the center towards lower frequency details at the edge of the relief geometry, which facilitates avoidance of undesired spectral leakage by tapering the relief height at the edge towards zero. In addition to the elements that are used in the Fourier analysis, an individual marker is also placed at each of the four corners of the tool. These markers are imprinted during the embossing process onto the substrate and help to align the original data and 3D scan data with each other by means of feature detection and image matching (see section 2.4). The markers were designed to be as diverse as possible and to contain a variety of detectable features such as radii, edges and cusps, following suggestions discussed by Košťák and Slabý (2021) as well as to be well suited for embossing into a wide range of possible substrates. Also, their positioning in the corners of the tool and thus at maximum distance from each other ensure that the transformation following image matching via homography (Hartley and Zisserman, 2004) can be as accurate as possible. Larger distances between markers ensure that only negligible angular error is induced for small lateral deviations when matching features. Figure 1 shows an 8-bit heightmap representation of the relief geometry of the universal embossing test tool of 2 000 × 2 000 pixels, as it was also used to create the test tool using additive manufacturing, as well as a rendered relief derived from it. Heightmaps represent the elevation of each point of the surface by the brightness of each pixel.

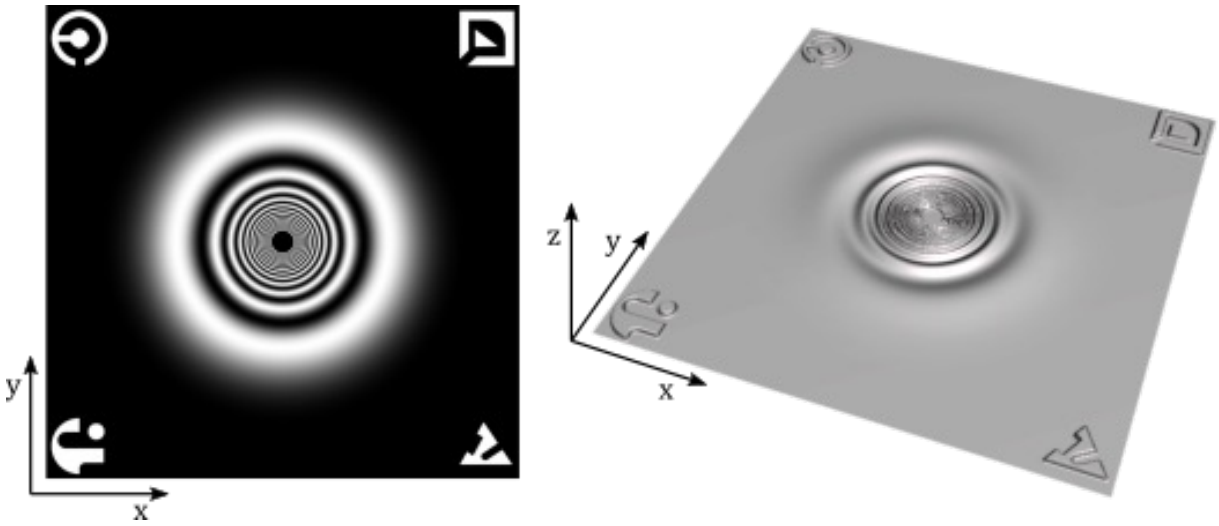

Figure 1: 8-bit heightmap of the universal test tool relief design on the left and derived rendered surface of it on the right; concentric rings with features that become narrower towards the center ensure the greatest possible coverage of the frequency spectrum, the ring-shaped arrangement also allows for analysis of embossing features in all possible orientations, and the four elements in the corners of the relief serve as markers for later feature detection and homographic matching between original data and 3D scanned data

2.2 Additive manufacturing of universal embossing test tool

Following the workflow presented by Feldmann, Spiehl and Dörsam (2021), a masked stereolithography (MSLA) additive manufacturing system (*Sharebot Viking*, Sharebot, Italy) was used for the fabrication of all embossing tools. The MSLA machine features a liquid crystal display with a resolution of 2 560 × 1 600 pixels and with a screen size of 182 mm × 120 mm, resulting in a lateral pixel resolution of 75 µm. The layer height was set to 25 µm, which is the minimum the machine can achieve. All embossing tools were fabricated with commercially available resin (*Azure Blue Tough Resin*, Prusa Research, Czech Republic). Adhesion to the build platform was increased by printing the first 8 layers of each tool with higher exposure time of 55 seconds per layer. All other layers were exposed for 5.5 seconds to UV-light during the fabrication process. After printing all tools were rinsed in isopropyl alcohol for at least 15 minutes to remove uncured resin residue, dried and post-treated in an UV-curing chamber (*Form Cure*, Formlabs, USA) for 15 minutes

at 40 °C. The tool is set to be of a size of 55 × 55 mm with a maximum embossing depth of 0.5 mm and a tool gap of 0.1 mm between fully closed female and male die. For the male embossing die the relief was printed via MSLA directly onto a bi-directional reinforced fiberglass composite sheet of a thickness of 0.5 mm, which was attached on the printing platform using adhesive tape. A fiberglass panel was chosen, which is made with epoxy resin to favor the best possible bond between it and the chemically similar additive manufacturing resin. This allows for the male die to be very thin, thus application on a wide range of embossing machines can be realized, even where space for male dies is limited. Both tool dies of the universal embossing tool are shown in Figure 2.

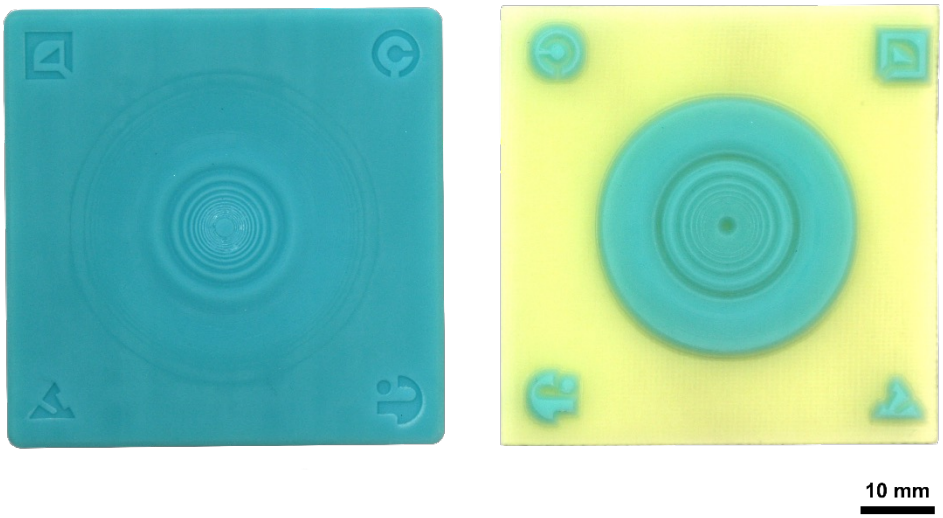

Figure 2: Photograph of the universal embossing test tool, the female die is displayed on the left and the male die on the right; while the female die was entirely additively manufactured using MSLA stereolithography, the embossing relief of the male die was printed via MSLA onto a sheet of fiberglass

2.3 Embossing and 3D scan examination

For the creation of embossments for examination via 3D scanning, a cotton substrate was selected that is common for embossing products (*Gmund Cotton* 450 g/m^2, Büttenpapierfabrik Gmund GmbH & Co. KG, Germany), which was embossed on an embossing press (*Geba 6*, Baier, Germany) under a load of 10 kN. Samples were then cut to approximate size and scanned using an optical 3D profilometer (*Keyence VR 5200*, Keyence, Japan), which achieves a lateral resolution of 23.53 µm using 12× optical magnification. The 3D scanning system is based on structured light, in which a known light pattern is projected onto the 3D object. Based on the deformation of the light pattern, which is recorded by a camera, the 3D surface of the object can then be reconstructed (Bartol, et al., 2021).

2.4 Data processing and analysis

The 3D scan is output in the form of two-dimensional data arrays, which contain the respective height of the embossment as a value in a grid with a lateral resolution of 23.53 µm. This results in a 2D data array of approximately 2 300 × 2 300 data points for the relevant area of the embossing relief, which has a size of 55 mm × 55 mm (see section 2.2). In a first step, the 3D scan data is transformed using a homography transformation to align as closely as possible to the original heightmap. To accomplish this, the scan data itself is first converted into an 8-bit grayscale heightmap representation. Utilizing the Scale Invariant Feature Transform “SIFT” feature detection (Lowe, 2004) built into OpenCV 3.4.2 (Bradski, 2000), possible relevant features in the original heightmap and the 3D scan data are identified and collected. Image features are then compared between the original and the scan heightmaps and closest matches are listed employing the Fast Library for Approximate Nearest Neighbors “FLANN” (OpenCV team, 2022). These

feature matches can then be used to find a homography transformation matrix (Hartley and Zisserman, 2004), which aligns the 3D scan onto the original heightmap, and therefore fits its resolution, orientation, distortion and lateral position. Although four feature matches are already sufficient for a fitting attempt, we found that applying the 10 closest feature matches gave the best results. The markers incorporated in the embossment design proved to be very beneficial for the performed image matching. Figure 3 shows a comparison between the original heightmap and the scan which was converted to a heightmap. Relevant features detected are highlighted in red, while the matches used for the homography transformation are shown as green lines between the two images.

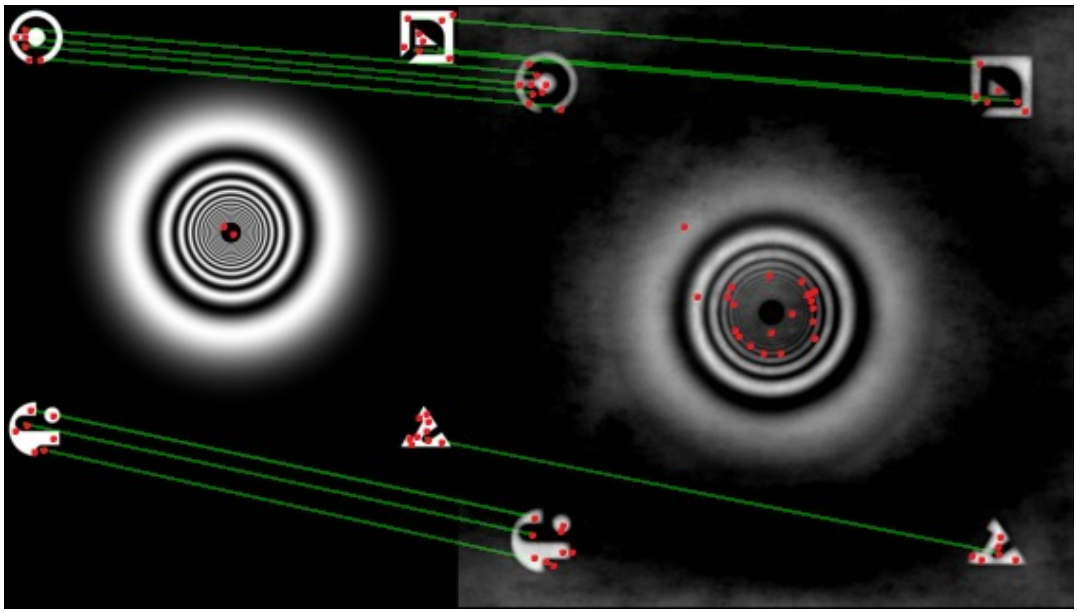

Figure 3: Visualization of found feature matches between the original heightmap used for the production of the embossing tool (left) and the 3D scanned and heightmap converted embossment (right); detected relevant features are shown as red dots, while the 10 most relevant matches are shown as green lines between the two images, note the importance of the matching markers in the corners of the embossing relief, which facilitate feature detection and matching

In a secondary step, the markers are cropped out, as they are no longer needed for the analysis once the two images are matched. The two data sets, original heightmap and fitted 3D scan relief data, are then transformed into the frequency domain utilizing a fast Fourier transformation (FFT). By comparing both transformed datasets we can obtain information about the embossment and the amount of alteration of features and their details depending on their size and orientation. For this, we calculate the characteristic transfer function (CTF) as the quotient for each data point *i,j* by dividing the Fourier transform of the 3D scanned data set $\mathcal{F}(HM_{\text{scan},i,j})$ by the Fourier transform of the original heightmap $\mathcal{F}(HM_{\text{original},i,j})$:

$$CTF_{i,j} = \frac{\mathcal{F}(HM_{\text{scan},i,j})}{\mathcal{F}(HM_{\text{original},i,j})} \quad [1]$$

We may now use this CTF to obtain an approximate preview of a future embossment, by elementwise multiplying the CTF to a Fourier transform of a new relief heightmap, provided that the new embossment is supposed to be done with the same compression force, a similar embossing depth and onto the same substrate.

$$\mathcal{F}\left(HM_{\text{preview},i,j}\right) = \mathcal{F}\left(HM_{\text{new},i,j}\right) \cdot CTF_{i,j} \quad [2]$$

Finally, we can view an estimated embossment preview by calculating an inverse Fourier transformation of the result of Equation [2].

2.5 Verification of the plausibility of the embossing preview

For verification of the here proposed model for approximation of embossments, another embossing tool was fabricated. In the same workflow as described in section 2.2 an embossing tool resembling a logo was created. This logo stands as an example of an embellishment, how it could be found on a cardboard box or other paper products. The heightmap depicting the logo used for the fabrication of this tool as well as the finished tool is shown in Figure 4. We took care to create it from a heightmap with the same resolution as the one used for the universal embossing test tool as well as setting its embossing depth to 0.5 mm and its tool gap to 0.1 mm, as it was done with the test tool. Also, the same embossing press, substrate and compression force was used. The physical embossment could then be 3D scanned and compared to the preview, obtained through the process outlined earlier.

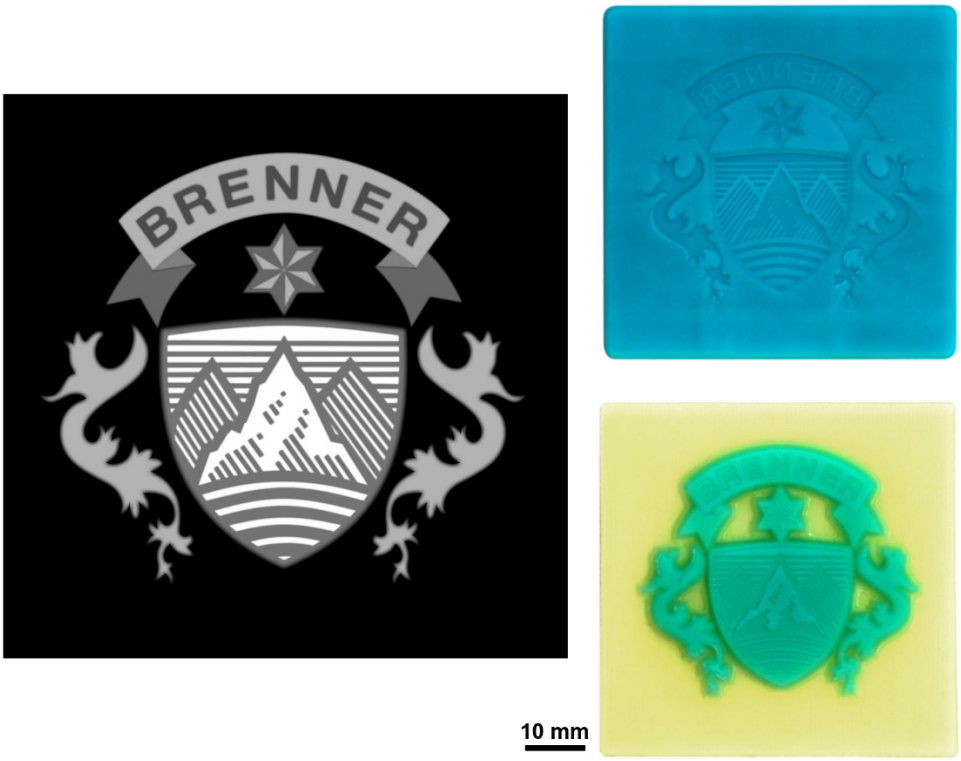

Figure 4: View of the 8-bit heightmap, on which the embossing tool to evaluate the plausibility of the embossing prediction is based (left) and an image of the embossing tool derived from it, consisting of a female die (top right) and a male die (bottom right)

3. Results and discussion

In initial tests of the algorithm, it could be shown that a comparison between the Fourier analysis of the original heightmap and the 3D scanned embossing result can indeed provide a rough indication of the characteristics of an embossing substrate and by which degree details are altered in the embossing process. An intuitive assessment of the attenuation of details by the embossing process is given by a polar display (Jähne, 2005) of the CTF, this is shown in Figure 5. Here, the transfer ratio for each orientation is displayed for each frequency. The recognizable wave structure of the CTF can possibly be explained by the finite resolution of the underlying data or the physical embossing tool. Likewise, the low number of quantification levels of an 8-bit heightmap may have an impact on the CTF's appearance. The influence of these factors or a combination of these are subject of future research.

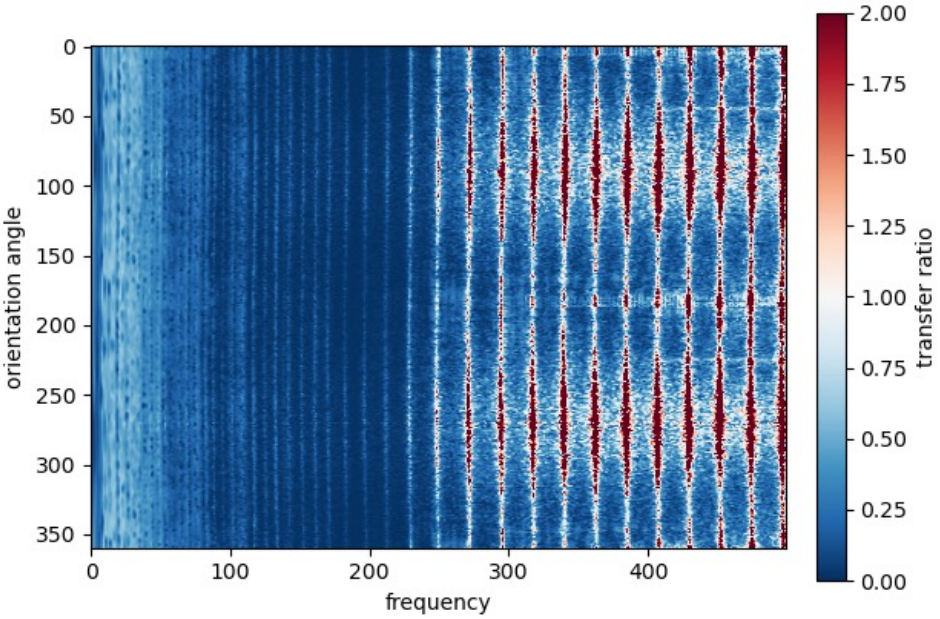

Figure 5: Representation of the characteristic transfer function (CTF) of the test embossment in polar coordinates (polar display); on the ordinate the angular orientation of the analyzed frequencies is plotted, while the frequency itself is displayed along the abscissa, the transfer ratio for each orientation and frequency is shown as either varying shades of blue for domains which are attenuated or red for domains, where the transfer ratio is greater than one, thus where an enhancement of the respective frequencies was found

To provide better access to the data shown in Figure 5, the transfer ratio can be averaged over all angles to show only the influence of the frequency on the transfer behavior. Thus, Figure 6 shows the average transfer ratio over all angles versus the frequency. For better visualization, the moving average was added in red, as well as a constant at a transfer ratio with the value one, representing the theoretical ideal embossment, where all details are fully transferred onto the substrate. It becomes apparent, that the amount of transfer changes depending on the frequency. Meaning, that the amount of transfer ratio (i.e. clarity or contrast of the embossment) changes according to the structure and details of the embossing relief. Since the physical feature size of these details can be calculated from the frequency if the size of the embossed image is known, a direct statement can be made about the transfer of individual features of the relief. Figure 7 therefore shows the transfer ratio versus the feature size of the embossing relief, which is equal to the inverse of the frequency, scaled according to the image size. Again, a constant at the transfer ratio with the value one was added, to visualize the theoretical ideal embossment transfer. For coarser embossing features, of 3 mm to 8 mm, the average transfer ratio reaches values of about 0.5, but shows significant reduction for smaller details. Below a feature size of approximately 0.5 mm the average transfer ratio rises significantly. This can be explained by the increased influence of the paper structure and paper fibers, which are in the domain of the 3D scan for small features, but are not included in the heightmap original.

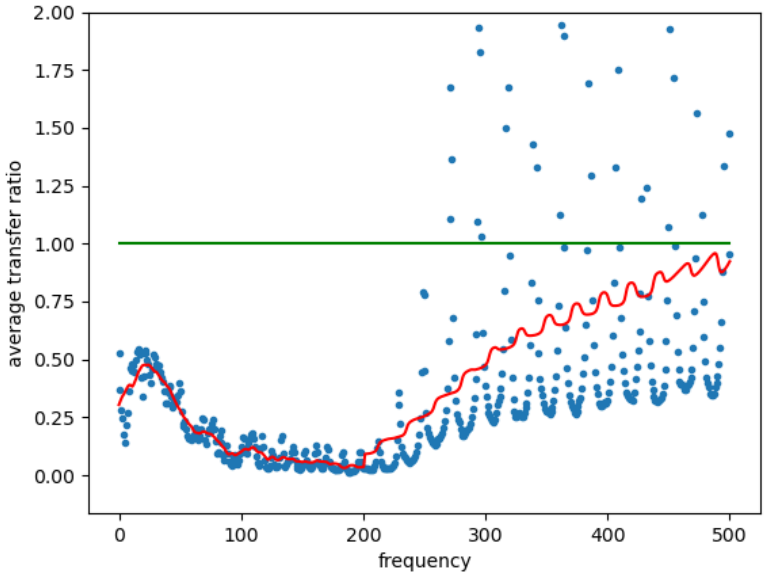

Figure 6: Representation of the average transfer ratio across all orientation angles; the red line represents the moving average of the frequency dependent transfer ratio, the green line visualizes the theoretical ideal transfer ratio with a constant value of one, if all details were impressed onto the substrate without deviation, note that larger frequency domains represent the transfer of smaller details and vice versa

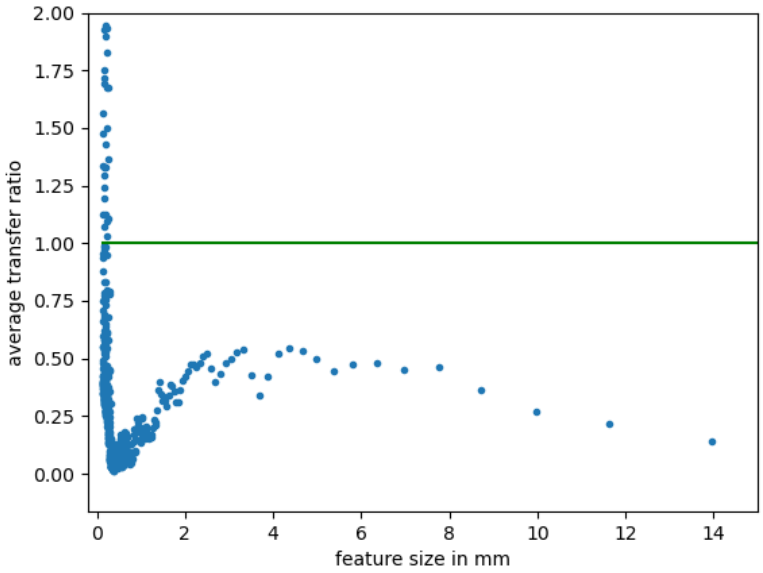

Figure 7: Representation of the average transfer ratio across all orientation angles plotted against the respective feature size of the transferred details, the green line visualizes the theoretical ideal transfer ratio with a constant value of one, if all details were impressed onto the substrate without deviation

Plotting the average transfer ratio per orientation angle and across all frequencies provides information about the dependence of the transfer of details and embossing features on their orientation in the embossing relief. In Figure 8, the average transfer ratio is plotted over all frequencies up to 250. The moving average is shown as a red line. It thus shows the angle-dependent transfer of details before the increase of the CTF, which is induced by the paper structure. It can be seen that the transfer of embossing details in the horizontal direction (90° or 270°) is higher than in the vertical direction (0° or 180°), which correlates with the cross direction (CD) of the substrate, which is also horizontal to the observer. These differences could have their origin in different mechanical properties of the substrate in machine and cross direction, which result in orthotropic embossing behavior (Kirwan, 2013) and the ductility of paper in CD is often significantly greater than in machine direction (MD) (Wilken, 2013).

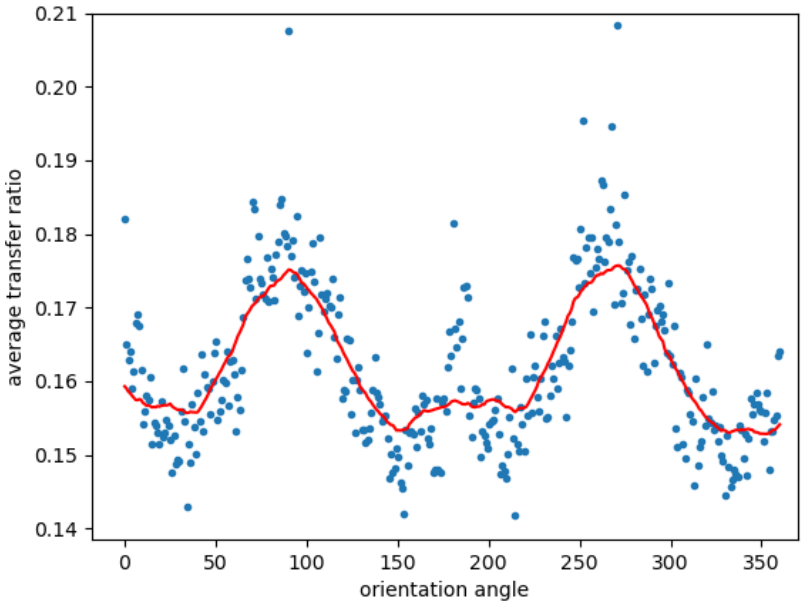

Figure 8: Plot of the average transfer ratio across all frequencies, thus visualizing alteration in transfer of details depending on orientation angle, an orthotropic behavior of the transfer can be identified, with larger transfer ratios along the 90° – 270° axis

The embossment preview obtained following Equation [2] shows satisfactory results. It delivers an estimation of the embossing result which can be expected by washing out details and attenuating sharp edges and corners of the relief design shown in Figure 4. Further, the impression of paper structure is added to the heightmap preview by increasing the grain of the image. Comparison between the preview and the 3D scan of the actual embossment, as shown in Figure 9, shows how close the outcome of the process described here matches the true embossing result.

Figure 9: Direct comparison of the estimated heightmap of the embossing preview and an actual 3D scanned embossment in cotton paper with a grammage of 450 g/m²

Figure 10 shows a representation of an embossing in white substrate, which was rendered on the basis of the preview heightmap, as well as a photograph of the real embossing in cotton paper with a grammage of 450 g/mm². Even though no perfect prediction is possible yet, the comparison demonstrates the potential of the approach to simulate and evaluate planned embossments in advance.

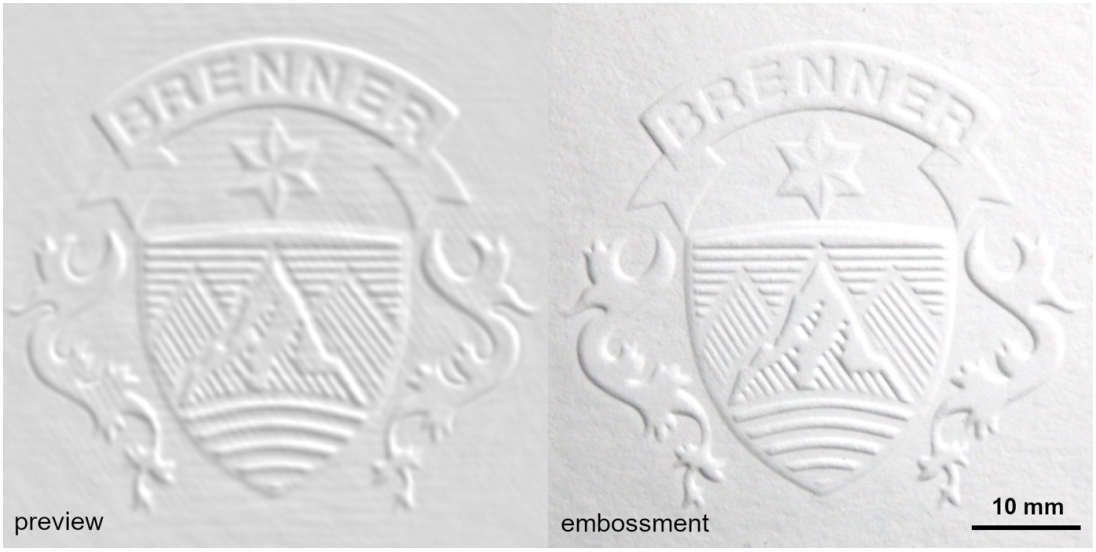

Figure 10: Comparison between a rendered visualization of the embossing preview, based on the heightmap shown in Figure 8 (left) and a photograph of the actual embossment, created with an embossing tool fabricated according to the same data under similar lighting conditions

4. Conclusions

The method presented in this text for characterizing embossing substrates, as well as the embossing previews generated by it, show potential to shorten the process chain and reducing the environmental impact of creating new embossing designs. It also forms a good basis for enabling further visualizations, for example for communication between designer, customer and manufacturer, which were previously only possible through time consuming and costly test embossing. Here, we have shown that the method is suitable for examining the entire process chain of creating a new embossment. Alternatively, it is conceivable to examine each intermediate step of the production process separately, which would reveal which sub process leads to which attenuations in the finished embossed image, e.g. which deviations are caused by the fabrication of the embossing tool and which by the embossing process itself. The algorithm forms the basis for an evaluation of the embossing behavior of different substrates, under different load conditions and environmental influences. Here, the workflow for a single substrate type was demonstrated. However, the test tool and algorithm can form a foundation for the creation of a database of various substrates. For systematic analyses, it can further be used as a tool for determining the influence of embossing parameters on the embossing result, so that in future more precise statements can be made in advance about the probable outcome of an embossing. Thus, not only the embossing relief design can be fit to the needs of the substrate, but also the right embossing parameters, such as compression force and humidity can be chosen accordingly. The generated analysis and preview so far shows the detail size-dependent deviation of the embossment, assuming that the embossing is in principle error-free. However, a frequent cause of necessary iteration loops in the design of new embossing tools are also artifacts and defects, such as tears, punch-outs or areas that were not completely impressed into the substrate. The object of future research is therefore the detection and evaluation of such defects, so that strategies can be developed to exclude or at least reduce them even before the first actual embossing is done. In addition, the approach shown here will be further developed and made into a generally applicable tool for characterizing embossing substrates. With its help embossing response of commonly used substrates will be collected and influences of different parameters on the embossment result will be analyzed.

References

Bartol, K., Bojanić, D., Petković, T. and Pribanić, T., 2021. A review of body measurement using 3D scanning. *IEEE Access*, 9, pp. 67281–67301. http://doi.org/10.1109/ACCESS.2021.3076595.

Bradski, G., 2000. The OpenCV library. *Dr. Dobb's Journal*, 25(11), pp. 120–126.

Burger, A., Cayé, N., Jaegermann, C. and Schuler, K., 2021. *Aufkommen und Verwertung von Verpackungsabfällen in Deutschland im Jahr 2019: Abschlussbericht*. Mainz: GVM Gesellschaft für Verpackungsmarkforschung mbH, im Auftrag des Umwelt Bundesamt.

Fachverband deutscher Stanzformhersteller e.V., n.d. Esupedia: *Stanzwerkzeuge für die Karton- und Wellpappenverarbeitung.* Meerbusch, Germany: Europäische Stanzform Union e.V.

Feldmann, J., Spiehl, D., and Dörsam, E., 2021. Paper embossing tools: a fast fabrication workflow using image processing and stereolithography additive manufacturing. In: C. Ridgway, ed. *Advances in Printing and Media Technology: Proceedings of the 47th International Research Conference of iarigai*. Athens, Greece, 19–23 September 2021. Damstadt: iarigai, pp. 146–154. http://dx.doi.org/10.14622/Advances_47_2021.

Hartley, R. and Zisserman, A., 2004. *Multiple view geometry in computer vision*. 2nd ed. Cambridge: Cambridge University Press.

Hartmann, O. and Haupt, S., 2016. *Touch!: Der Haptik-Effekt im multisensorischen Marketing*. 2nd ed. Freiburg, München, Stuttgart: Haufe Gruppe.

Jähne, B., 2005. *Digital image processing*. 6th ed. Berlin, Heidelberg, New York: Springer.

Kirwan, M.J. ed., 2013. *Handbook of paper and paperboard packaging technology*. 2nd ed. Chichester, West Sussex: Wiley-Blackwell.

Košťák, M. and Slabý, A., 2021. Designing a simple fiducial marker for localization in spatial scenes using neural networks. *Sensors*, 21(16): 5407. http://doi.org/DOI: 10.3390/s21165407.

Lowe, D., 2004. Distinctive image features from scale-invariant keypoints. *International Journal of Computer Vision*, 60(2), pp. 91–110. https://doi.org/10.1023/B:VISI.0000029664.99615.94.

OpenCV team, 2022. *FLANN: Fast library for approximate nearest neighbors.* [online] Available from: <https://docs.opencv.org/3.4.2/dc/de2/classcv_1_1FlannBasedMatcher.html> [Accessed 18 April 2022].

Werblow, S., 2009. Anti-counterfeiting packaging. In: K.L. Yam, ed. *The Wiley encyclopedia of packaging technology*. 3rd ed. Hoboken: John Wiley & Sons, pp. 46–48.

Wilken, R., 2013. Verfahren der Papierbearbeitung. In: J. Blechschmidt, ed. *Papierverarbeitungstechnik*. München: Fachbuchverl. München: Carl Hanser Verlag, pp. 130–241.

DOI 10.14622/Advances_48_2022_03

Wetting and adhesion phenomena of surface-treated float glass

Sarah Patejdl, Ulrich Jung and Katharina Freieck

Bergische Universität Wuppertal, Gaußstraße 20, 42119 Wuppertal, Germany
E-mails: patejdl@uni-wuppertal.de; ujung@uni-wuppertal.de

Short abstract

Float glass is a commonly used substrate for automotive-, architecture-, decorating- and functional industries. The two-sidedness of float glass can form different adhesive forces depending on glass surface properties, like wettability. A significant example is the binding or bonding of organic UV radiation-curable fluid systems to the very smooth inorganic float glass surface which can result in insufficient adhesion. The main reason for this phenomenon is a well-known incompatibility of fluid/substrate combinations. Current research works on binding organic fluids to inorganic silica surfaces proved the reasonable use of silane-based self-assembling monolayers (SAMs), like hexamethyldisilazane (HMDS), to improve the adhesion. This work investigated the influence of cleaning methods with an alkaline solution of the float glass surface with an overall increasing wettability of air- and tin side and especially achieve a nearly equalised wettability behaviour. This hydrophilic behaviour is used to define an initial state for a following HMDS surface functionalising. The functionalisation methods lead to different hydrophobic wettability behaviours of the float glass surface, but do not lead to a strong improvement of adhesion, measured with the 90° peel test. This fact shows a significant missing link between wetting and adhesion properties of modified glass substrates.

Keywords: float glass, glass cleaning, contact angle, wetting, adhesion, peel test, HMDS, hydrophobic, hydrophilic, ultraviolet radiation curable coatings

1. Introduction and background

Combinations of mechanical, physical and chemical pre-treatments of surfaces are wildly used to modifier surfaces, e.g. polymers, metals or glass, to bind or bond coatings, inks and adhesives on surfaces or materials together to reach a defined adhesion behaviour depending on the application purpose. Theories of adhesion mechanisms are detailed described (da Silva, Öchsner and Adams, 2011). Especially the adhesive bind- and bonding of e.g. ultraviolet radiation curable coatings, inks, adhesives and metal oxide coating on float glass prefer only one side of the glass for application, but not even the same (Silvestru, et al., 2018; Saint-Gobain, 2018). The two-sidedness of float glass results from the Pilkington manufacturing process, which revolutionised the worldwide industrial production of flat glass (Pilkington, 1969; Persson, 1969) and is the predominant method for manufacturing soda-lime-silica (SLS) flat glass (Krohn, et al., 2005). By processing, the approx. 1 000 °C glass melt flows on a 232 °C molten tin bath (Haldimann, Luible and Overend, 2008) with building a smooth surface, roughness 1–2 nm (Silvestru, et al., 2018), and leads to the diffusion of tin ions up to 40 µm into the surface, with the highest tin concentration in the top of 100–200 nm (Goodman and Derby, 2011), depending on named process parameters (Tamglass Ltd Oy, 1997; Krohn, et al., 2005). This side, called the tin side, fluoresces milky white by using a tin detector ($\lambda \approx 254$ nm). The other side, called the air side, is surrounded by a protective gas atmosphere of N_2/H_2 to avoid the formation of tin oxide while the floating process (Zhang, Chen and Li, 2011; Fernández Oro, et al., 2008). In summary, the air- and tin side differ in their surface properties and wetting tests with water show after surface preparation methods in the majority still no levelling between the air- and tin sides (Lazauskas and Grigaliūnas, 2012). The influence of tin can only be removed by material removal (Neroth

and Vollenschaar, 2011). Current research is concerned with self-assembling monolayer (SAM) pretreatment of glass with organosilicon compounds as an adhesion promoter (Wang, et al., 2021), coupling agents or primer (Wypych, 2018), e.g. hexamethyldisilazane (HMDS) (Fiorillo, et al., 2017), to form a covalent network between surface and silane molecules (Herzer, Hoeppener and Schubert, 2010) to improve adhesion of inorganic- with organic materials. HMDS should give silica surfaces hydrophobic wetting properties and should serve as an adhesion promoter.

This research aims to equalise the two-sidedness of float glass with homogeneous hydrophilic wetting properties to define an initial state for HMDS-functionalisation of the float glass surface. The HMDS-functionalisation was practised in two different ways to get deviating wetting properties on float glass surfaces. Peel tests on the different modified glass surfaces, printed with UV varnishes, should allow the gaining of further insights into the adhesion behaviour of UV varnishes.

2. Materials and methods

2.1 Instruments

A contact angle measuring device (OCA 50, Dataphysics) is used to measure the static contact angle (sessile drop method) with test fluids according to DIN EN ISO 19403-7 (Deutsche Institut für Normung, 2020a) to get quantitative data about the wetting properties of the cleaned and functionalised float glass surface.

A flexo- and gravure pressure device (IGT, F1) is used for the application of UV varnishes with a 24 ml/cm^2 anilox roller in the flexographic procedure.

An adhesion tester (Kyowa, VPA-H100) is used to measure the adhesion of hardened UV varnishes on cleaned and functionalised float glass samples with the pull-off angle of 90° and defined pressure application of tape (type: 4204, width: 25 mm, tesa).

2.2 Materials

In Table 1 are all materials listed, which were used for this research work.

Table 1: Material used

Substrate	Float glass, clear, seamed edge
UV varnishes (radically hardening)	GSB-Wahl: PR9410, PR9415, PR9291 Weilburger: 360027 Hi-Tech Coatings: U8730, U888
Cleaning agents	Laboratory dishwasher cleaner (LDC), Neodisher Labo GK, Dr. Weigert Ethanol absolute 99.9 % (Chemsolute), CAS-no.: 64-17-5
Silylating agent	Hexamethyldisilazane, Carl Roth, CAS no.: 999-97-3
Contact angle (CA) test fluids	Water, Aqua Dest., Wittig Umweltchemie, CAS-no.:7732-18-5 Diiodomethane, 99 %, stab., Alfa Aesar, CAS-no.: 75-11-6 Benzyl alcohol, 99 %, Alfa Aesar, CAS-no.: 100-51-6 Glycerol, 99+ %, Alfa Aesar, CAS-no.: 56-81-5

2.3 Cleaning methods

Three cleaning methods were performed on float glass (batch of 34) and quantified by water contact angle (WCA) measurements. After cleaning, samples are stored dust-tight in sample boxes at room temperature for 24 h. In the first cleaning method (clear rinsing method = CRM) float glass is rinsed clear with distilled water in a mini-dishwashing machine (MD 37004, Medion) using programme P2 (wash: 50 °C, rinse: 65 °C, dry: 1h) to remove coarse organic/inorganic contaminants and to provide a basis for comparing the cleaning methods of their cleaning effect. The second method (room temperature method = RTM) involves cleaning the float glass in a ≈ 21.4 °C mildly alkaline cleaning bath with a concentration of 4 g/l laboratory dishwasher cleaner (LDC) in 4.3 l tap water for 1h, followed by rinsing with CRM. In the third cleaning method (enhanced method = EM), float glass is cleaned in a ≈60 °C cleaning bath with the same conditions as RTM. The product information sheet gives a pH value (20°C) of 10.8–11.9 by a concentration of 2–5 g/l LDC. For each cleaning method, 10 WCA on 10 samples (G1–G10) were measured, with the use of distilled water instead of tap water 10 WCA on 3 samples (G1–G3) on the front- and backside was measured.

2.4 Contact angle methodology

The contact angle measurement of lying drops is described in DIN EN ISO 19403-2:2020-4 (Deutsche Institut für Normung, 2020b) and recommends for evaluation of contact angles (CA) < 20° the circle fit (CF) method and >20° the ellipse fit method (EF), but not an evaluation time point for the determination of the fitting method and contact angle. The used test fluids show, because of their different disperse and polar components, a wide range of contact angles and spreading behaviours on different cleaned and functionalised float glass surfaces. To compare the contact angles, rules for evaluation of fitting method and evaluation time point of contact angle were defined as followed.

The placement of liquid drops (drop volume: 2 µl) on the cleaned and functionalised float glass surfaces was recorded by video (frame rate: 22.39 fps) and allows a defined assignment of CF- and EF-method. The data fit of the first complete and sharply contoured lying drop on the surface (t_1) is fitted with EF and decides first the final fit for evaluation. CA ≥ 20° receives the ellipse fit and CA < 20° receives the circle fit. The ellipse-fitted contact angle (CA) was evaluated after 10.0 s. (frame 224) to reach approximate a three-phase equilibrium. The circle fitted CA usually spreads so quickly, that the forwarded flat contact angle could not be detected by the Dataphysics software. Contact angle evaluation at time point 1.6 s (frame 35) after drop placement leads to stable detectable contact angles.

2.5 Surface energy methodology

The surface energy of room temperature-, enhanced cleaned and functionalised float glass surfaces were determined by using sessile drop data (Chapter 2.4) of test fluids water, diiodomethane, benzyl alcohol and glycerol (20 drops each on air- and tin side). The test fluid contact angles are abbreviated like followed:

- Water contact angle (WCA)
- Diiodomethane contact angle (DICA)
- Benzyl alcohol contact angle (BACA)
- Glycerol contact angle (GLCA)

For reference water [Ström, et al.], diiodomethane [Ström, et al.], benzyl alcohol [Rabel] and glycerol [Ström, et al.] was used and evaluated with Owens, Wendt, Rabel and Kaelble-method (OWRK). The references were chosen in accordance with DIN EN ISO 19403-7:2020-04.

2.6 Functionalisation methodology

EM-cleaned and one-week conditioned float glass are used to get hydrophobic behaviour of glass surfaces in two ways in batches of 8 float glass.

1. Hydrophobic method (HM1): Retention time of 1 h in HDMS at room temperature.
2. Hydrophobic method (HM2): Retention time of 1 h with 80 °C heated HDMS.

After functionalisation, the float glass is cleaned with a cleanroom cloth (Vipers PC 68) surrounded by a plastic squeegee with ≈3 ml ethanol with two repetitions and was stored for 1 h under vacuum in a desiccator with silica gel and is then clear rinsed (CRM). The hydrophobic wetting behaviour was determined with OCA 50 using two samples (G1, G2). On the front- and backside, 15 water-, diiodo-methane-, benzyl alcohol- and glycerol contact angles were applied and evaluated.

2.7 Peel test methodology

EM cleaned and functionalised (HM1/HM2) float glass was printed with 6 UV varnishes on air- and tin sides (five samples each) and hardened with a UV-belt dryer (Actiprint Mini/e 18-1, Technigraf, λ: 190 nm to 400 nm, speed: 3 m/min, 120 W/cm). Peel data (speed: 300 mm/min.) were evaluated with the mean value from peel length 40 to 100 mm. Approximately 15 min. elapsed between the tape application and the peel test. Measured peel forces ≤ 0.50N were counted as having no adhesion behaviour, because of delaminating and weak bounding adhesion forces.

2.8 Methodological overview

Figure 1 describes the methodological overview of practised tests on cleaned and functionalised float glass surfaces.

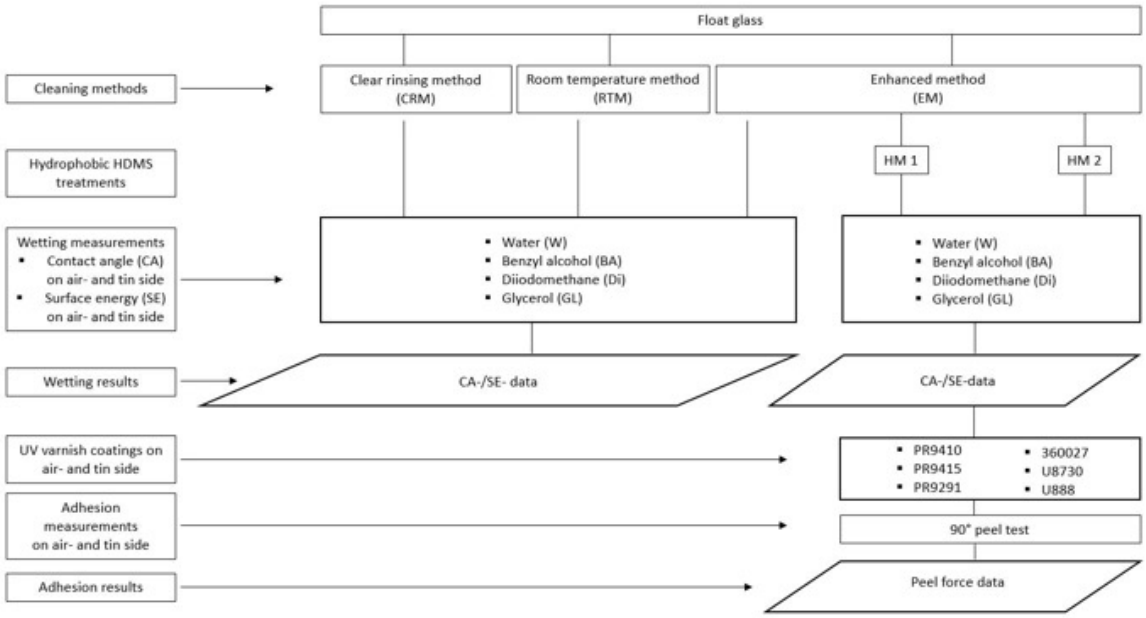

Figure 1: Methodological overview of practised tests on cleaned and functionalised float glass surfaces

3. Results and discussion

3.1 Contact angle measurements (cleaning methods)

Water contact angle results (G1–G10) of CRM-, RTM- and EM cleaned float glass were tested with software OriginPro2020 for normal distribution using Shapiro-Wilk-Test and afterwards normally distributed data pairs (air- vs. tin side contact angle of a sample) were tested on significance using the pair sample *t*-test.

Clear rinsed float glass shows 197 ellipses fitted WCA of 200 measured contact angles in a range of 12.9° to 45.4°. At time point t_1, 9 (4.5 %) of 200 measured WCA have less than 20° and have to be circle fitted, but to compare the WCA-data they were additionally ellipse fitted with the Dataphysics software SCA 20. 3 out of 9 WCA measurements could not be ellipse fitted. Only 4 out of 8 normally distributed WCA data pairs show strong significance and did not allow reliable identification of the air- and tin side.

Room temperature cleaned float glass shows 181 ellipses fitted WCA of 200 measured contact angles in a range of 6.7° to 60.0° (Figure 2a). At time point t_1, 47 (23.5 %) of 200 measured WCA have less than 20° and have to be circle fitted. To compare the WCA data they were additionally ellipse fitted with the Dataphysics software. 19 out of 47 WCA measurements could not be ellipse fitted and reduced the number of evaluable data in measurement series G1 to G10. Contact angle series G2, G3, G8 and G10 were not evaluated, because due to too less ellipse fitted data (DF <7) and not normally distributed contact angle data. 6 out of 6 normally distributed contact angle data pairs enable clearly differentiable wetting effects from the front- to the backside of the float glass with $p \leq .001$ (Figure 2, Table 3).

Enhanced cleaned float glass shows WCA (CF) between 4.2° and 8.1° (Figure 2b); recognise the adjustment of the *y*-axis. The significance test shows by only 3 out of 7 normally distributed contact angle data pairs weak significant results (Table 4). Even if wetting differences between float glass sides are not visible, the tin detector shows still the existence of tin in the glass matrix. The enhanced method causes an equalising homogeneous interfacial layer on both sides of the float glass surface with hydrophilic wetting properties based on WCA data. The hydrophilic effect of glass storage in alkaline solution is well known (Schreithofer, Laskowski and Heiskanen, 2010) and the influence on the surface roughness of alkaline solutions, like NaOH, too (Hüppauff and Lengeler, 1994). EM cleaned float glass showed visible partial milky effects, looks like corrosion, and not like decreasing roughness in visible moderation. Additionally, the hydrophilic cleaning effect is slowly reversible and after 5 weeks verifiable with WCA.

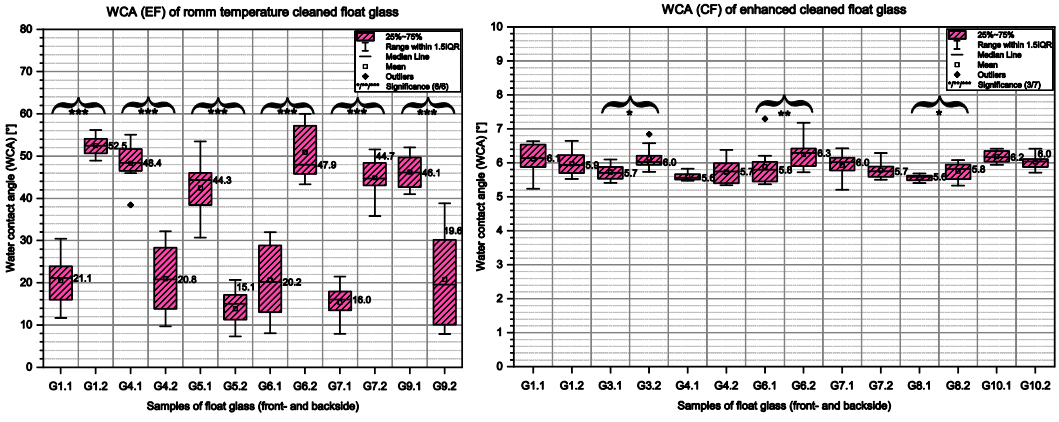

a) *b)*

Figure 2: Ellipse fitted water contact angle on front- and backside of room temperature cleaned float glass (a) and enhanced cleaned float glass (b); the significance test for RTM shows clearly the reinforced two-sidedness of the float glass and the significance test for EM shows no differences between air- and tin side with homogenous hydrophilic surface properties

Subsequent investigations, by using distilled water in the cleaning procedure instead of tap water, and using a tin detector, confirm the results in tap water cleaned float glass (Table 2). In contrast to CRM, the air- and tin side of RTM cleaned float glass could be identified with the tin detector with a water contact angle range of 17.4° to 55.8° and 4.9° to 31.0°. Furthermore, the measured WCA-data shows on the "same" float glass sides different inhomogeneous CA-data. It is assumed that these different wetting effects can results in an unsaturated RTM cleaning effect or are caused by varying process parameters of the float glass manufacturing process. Organic- and inorganic contaminants were not visible on the cleaned float glass surface.

Table 2: WCA of float glass cleaning methods using distilled water

Cleaning methods		WCA Air side	WCA Tin side
CRM	min. – max. [°]	18.5 – 42.0	11.7 – 43.6
RTM	min. – max. [°]	17.4 – 55.8	6.3 – 31.0
EM	min. – max. [°]	4.0 – 6.4	– 6.9

Table 3: Significance results of room temperature cleaned (RTM) float glass

Samples RTM	*t*-statistics	Prob. > |*t*|	$p \leq .001$	Mean	SD	SEM	Median
G1.1 DF (7) G1.2	−13.947	.000	***	20.518 52.451	6.210 2.432	2.195 0.860	21.141 52.487
G4.1 DF (7) G4.2	6.983	.000	***	48.320 20.983	4.992 8.486	1.765 3.000	48.389 20.826
G5.1 DF (8) G5.2	11.201	.000	***	42.456 13.863	6.723 4.668	2.241 1.556	44.344 15.053
G6.1 DF (8) G6.2	−12.170	.000	***	20.658 50.939	9.527 6.431	3.176 2.144	20.170 47.933
G7.1DF (8) G7.2	−15.425	.000	***	15.371 44.859	3.979 4.830	1.326 1.610	16.050 44.699
G9.1 DF (7) G9.2	5.771	.000	***	46.232 20.787	4.139 11.596	1.463 4.100	46.086 19.551

Table 4: Significance results of enhanced cleaned (EM) float glass

Samples EM, DF(9)	*t*-statistics	Prob. >|*t*|	$p \leq .05$	$p \leq .01$	$p \leq .001$	Mean	SD	SEM	Median
G1.1 G1.2	0.941	.372	-	-	-	6.110 5.973	.435 .336	.138 .106	6.142 5.937
G3.1 G3.2	−2.599	.029	*	-	-	5.726 6.134	.235 .333	.074 .105	5.703 6.021
G4.1 G4.2	−0.993	.347	-	-	-	5.602 5.729	.127 .341	.040 .108	5.562 5.747
G6.1 G6.2	−3.733	.005	*	**	-	5.892 6.246	.571 .428	.180 .135	5.795 6.289
G7.1 G7.2	0.797	.446	-	-	-	6.925 5.784	.382 .241	.121 .076	6.013 5.750
G8.1 G8.2	−2.930	.017	*	-	-	5.560 5.748	.097 .260	.031 .082	5.590 5.818
G9.1 G9.2	1.761	.112	-	-	-	6.186 6.026	.174 .214	.055 .068	6.166 6.037

3.2 Surface energy measurement (cleaning methods)

Surface energy measurement of RTM- and EM cleaned float glass was carried out with test fluids water, diiodomethane, benzyl alcohol and glycerol (20 drops on each float glass side, one sample for each test fluid). The measured contact angles are shown in boxplots (Figure 3). Because of the strong spreading behaviour of water on enhanced cleaned float glass surface a WCA (EF) of 3° was assumed and used for surface energy evaluation. The wetting envelopes of air- and tin side are shown in Figures 4 to 7.

Water-, diiodomethane-, benzyl alcohol- and glycerol show clearly contact angle differences dependent on the float glass side for the room temperature- and enhanced cleaned float glass are shown in Figure 3. The contact angle range of used test fluids is listed in Table 5.

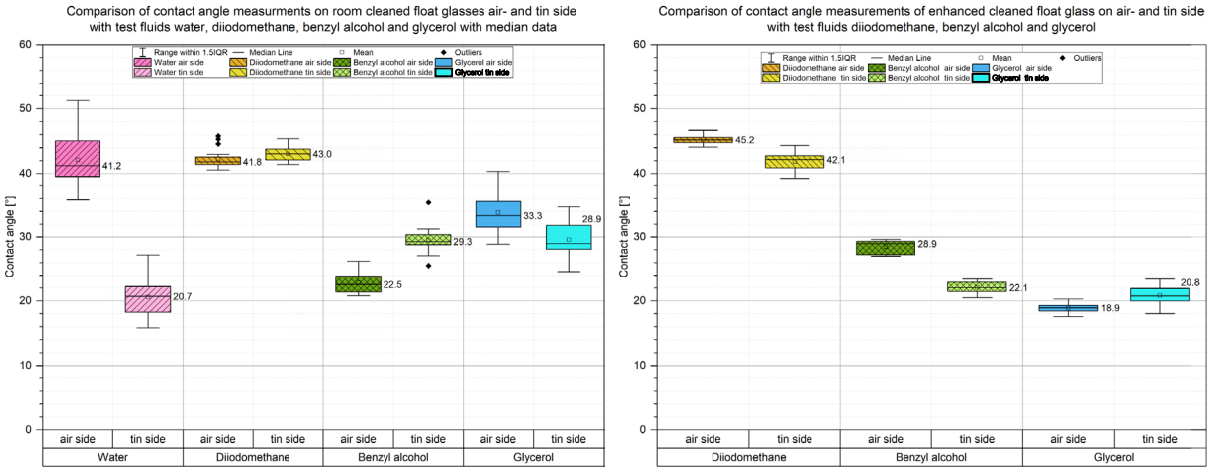

a) *b)*

Figure 3: Comparison of contact angle boxplots of test fluids water, diiodomethane, benzyl alcohol and glycerol on air- and tin side of room temperature cleaned (RTM) float glass (a) and of enhanced cleaned (EM) float glass (b); because of the hydrophilic behaviour with circle fitted contact angle water was not listed in the (b) figure, for comparison of RTM- and EM surface energies, for EM an ellipse fitted contact angle of 3.0° was assumed

Table 5: Contact angle range of RTM- and EM cleaned float glass with test fluids water, diiodomethane, benzyl alcohol and glycerol

Cleaning methods	Water		Diiodomethane		Benzyl alcohol		Glycerol	
	air	tin	air	tin	air	tin	air	tin
RTM min. – max. [°]	35.8 – 51.3	15.8 – 27.2	40.5 – 43.0	41.4 – 45.4	20.8 – 26.2	27.1 – 31.3	28.9 – 40.3	24.6 – 34.7
EM min. – max. [°]	3.0 – 3.0	3.0 – 3.0	44.1 – 46.7	39.3 – 44.4	27.0 – 29.6	20.5 – 23.4	17.6 – 20.3	18.0 – 23.4

The evaluated contact angles of the EM cleaned float glass sides show interestingly the opposite tendencies in comparison to the contact angles of the RTM cleaned float glass and describe clearly the different surface properties caused by cleaning methods, which differences results of the cleaning bath temperature. Furthermore, the WCA of EM cleaned float glass sides show a hydrophilic spreading behaviour with no detectable differences, but the test fluids diiodomethane, benzyl alcohol and glycerol show still the two-sidedness, which shows still the presence of surface wetting differences, resulting from the tin diffusion.

RTM cleaned float glass shows on the air side surface energy of 53.6 mN/m with the dispersive component of 27.7 mN/m and the polar component of 26.0 mN/m without outliers (Figure 4). The tin side shows

higher surface energy of 61.7 mN/m with the dispersive component of 25.07 mN/m and the polar component of 36.6 mN/m without outliers (Figure 5). The wetting envelopes show additionally clearly the two-sidedness of room temperature cleaned float glass.

Surface energy measurement of EM cleaned float glass leads on the air side to surface energy of 51.8 mN/m with the dispersive component of 30.4 mN/m and the polar component of 21.5 mN/m (Figure 6). The tin side shows a little bit higher surface energy of 52.1 mN/m with the dispersive component of 32.3 mN/m and the polar component of 19.8 mN/m (Figure 7).

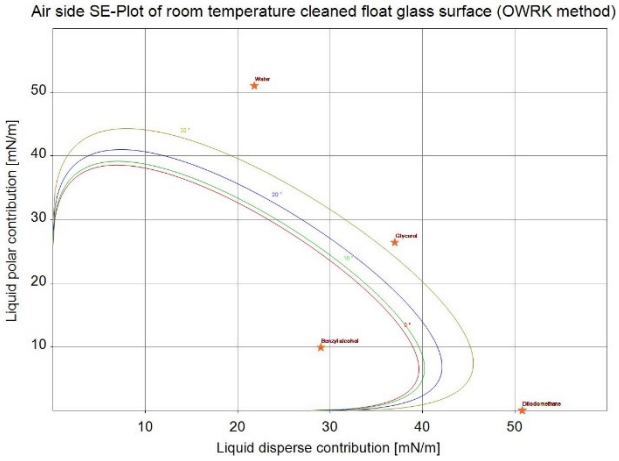

Figure 4: Wetting envelope, consisting of sessile drop measurement of test fluids water, diiodo-methane, benzyl alcohol and glycerol, on air side of RTM cleaned float glass; surface energy: 53.6 mN/m, disperse: 27.7 mN/m, polar: 26.0 mN/m, RQ: 0.8778, sChi: 11.71

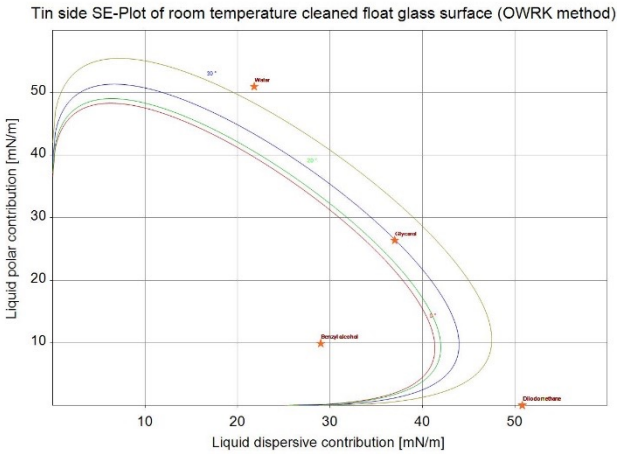

Figure 5: Wetting envelope, consisting of sessile drop measurement of test fluids water, diiodo-methane, benzyl alcohol and glycerol, on tin side of RTM cleaned float glass; surface energy: 61.7 mN/m, disperse: 25.1 mN/m, polar: 36.6 mN/m, RQ: 0.8623, sChi: 15.61

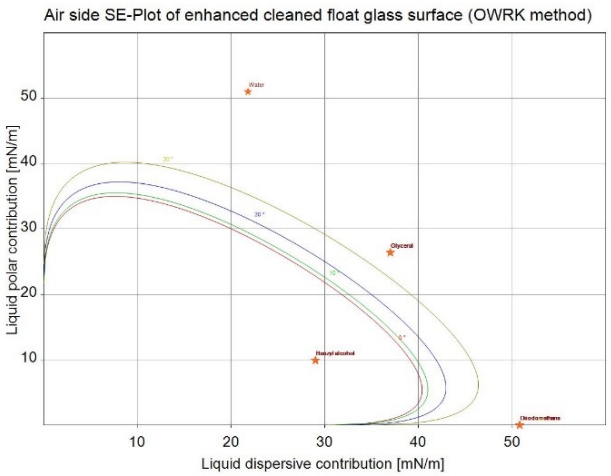

Figure 6: Wetting envelope, consisting of sessile drop measurement of test fluids water, diiodo-methane, benzyl alcohol and glycerol, on air side of EM cleaned float glass; surface energy: 51.8 mN/m, disperse: 30.4 mN/m, polar: 21.5 mN/m, RQ: 0.8478, sChi: 12.52

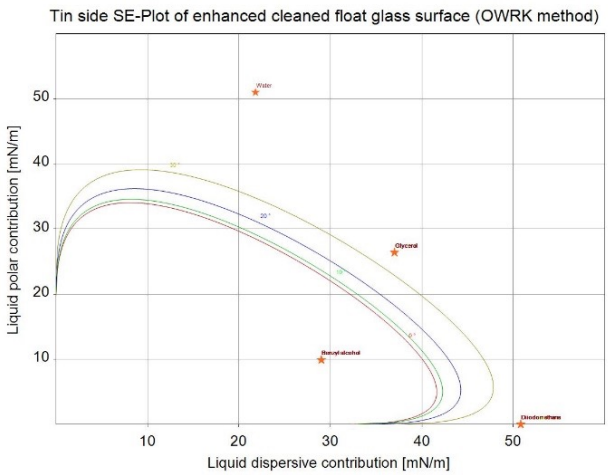

Figure 7: Wetting envelope, consisting of sessile drop measurement of test fluids water, diiodo-methane, benzyl alcohol and glycerol, on tin side of EM cleaned float glass; surface energy: 52.1 mN/m, disperse: 32.3 mN/m, polar: 19.8 mN/m, RQ: 0.8519, sChi: 11.62

3.3 Adhesion of hydrophilic surface (EM)

Following, peel forces on EM cleaned hydrophilic surfaces, air- and tin side, printed with UV varnishes (Table 1), were measured. Each combination, air- and tin side with UV varnishes, will be counted as one measurement series. In summary, 12 measurement series (❶...⓬) with 5 peel tests for each combination were analyzed (Table 6).

Table 6: Overview of peel forces from UV varnishes on enhanced cleaned float glass

Measurement series and their peel forces				
UV varnish	Measurement series	Air side peel force measurements	Measurement series	Tin side peel force measurements
PR9410	❶	0.50, -, -, -, -	❷	0.16, 0.12, 0.11, 0.08, -
PR9415	❸	3.22, -, -, -, -	❹	3.52, 3.96, 3.87, 4.01, -
PR9291	❺	0.01, 0.01, 6.85, 6.70, -	❻	4.06, -, -, -, -
360027	❼	3.60, 3.52, 3.53, -, -	❽	3.35, 3.48, 3.49, 3.49, 3.47
U8730	❾	4.96, 5.62, 5.39, 5.40, -	❿	4.57, 5.05, 0.50, 5.30, -
U888	⓫	5.38, 5.42, 5.97, 5.77, -	⓬	5.33, 5.23, 5.49, -

25 peel force measurements, red marked, out of 60, on hydrophilic surface show peel forces ≤ 0.50 N. Without peel forces ≤ 0.50 N, 5 out of 12 measurement series (❶, ❷, ❸, ❺, ❻) have less than 3/5 evaluable peel trials (grey-filled cells). The reached adhesion forces with ≥ 3/5 peel trials, blue marked, are between 3.35 N and 5.97 N (Table 7, Figure 8 to 13).

The evaluated mean value of min. and max. reached peel forces of each measurement series could be an indication of peel force differences between the air- and tin side (Table 7). A deviation of ± 0.3 N is set as the basis for assessing the adhesion force differences of the glass sides. Differences between the glass sides can be recognised by 4 out of 6 UV varnishes (blue-filled cells, Table 7).

In summary, the hydrophilic behaviour of the surface seems to be not only sufficient for the formation of adhesion of UV varnishes. Differences between air- and tin side of adhesion behaviour need more evaluable peel trials, but actually performed peel tests indicate first an influence of air- and tin side on the adhesion behaviour of UV varnishes.

Table 7: Peel forces and their trials on hardened UV varnishes on EM cleaned float glass surface

Cleaning method	UV varnish	PR9410		PR9415		PR9291		360027		U8730		U888	
		air	tin	air	tin	air	tin	air	tin	air	tin	air	tin
EM	min. [N]	-	-	3.22	3.52	6.70	4.06	3.52	3.35	4.96	4.57	5.38	5.23
	max. [N]	-	-	3.22	4.01	6.85	4.06	3.60	3.49	5.62	5.30	5.97	5.49
$\bar{x}$ [min./max.]	[N]	0.00	0.00	3.22	3.77	6.78	4.06	3.56	3.42	5.29	4.94	5.68	5.36

Legend of peel trials	0/5	1/5	2/5	3/5	4/5	5/5

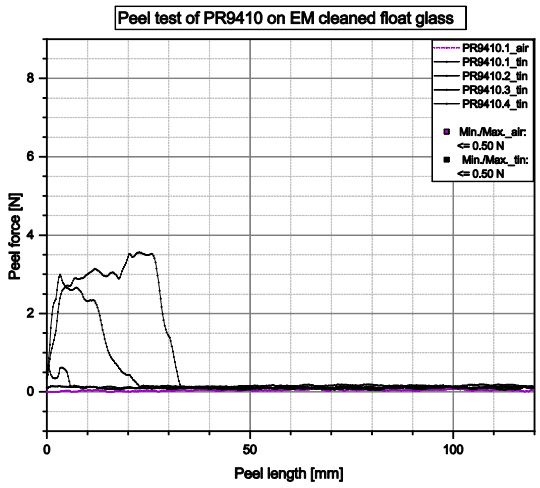

Figure 8: Peel test of PR9410 on EM cleaned float glass

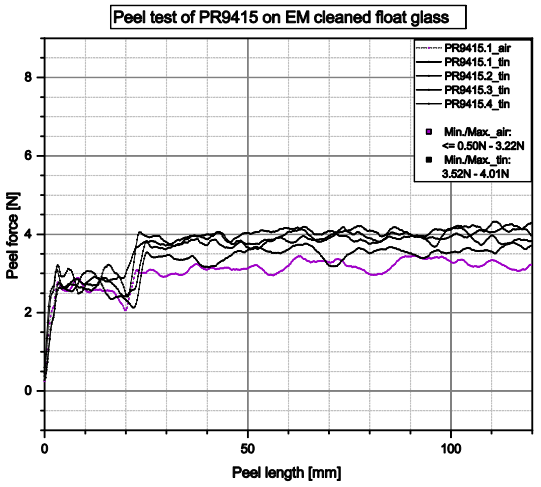

Figure 9: Peel test of PR9415 on EM cleaned float glass

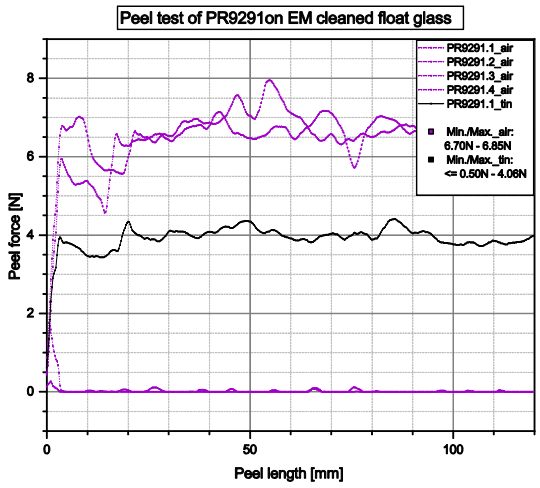

Figure 10: Peel test of PR9291 on EM cleaned float glass

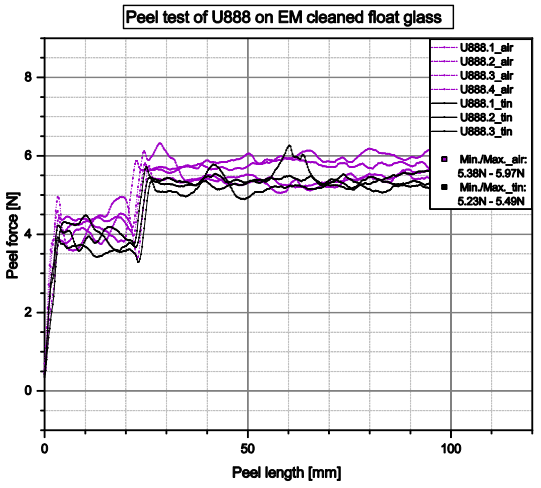

Figure 11: Peel test of 360027 on EM cleaned float glass

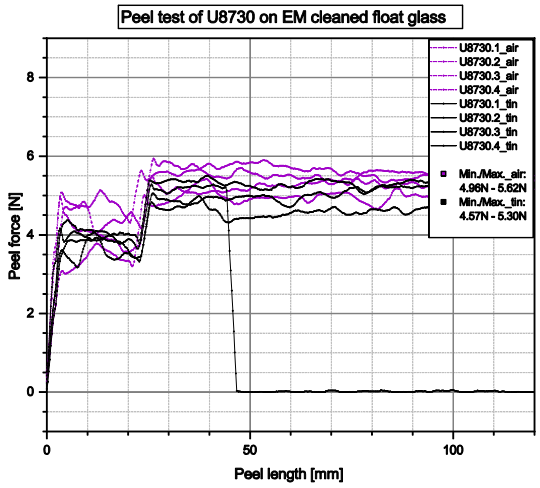

Figure 12: Peel test of U8730 on EM cleaned float glass

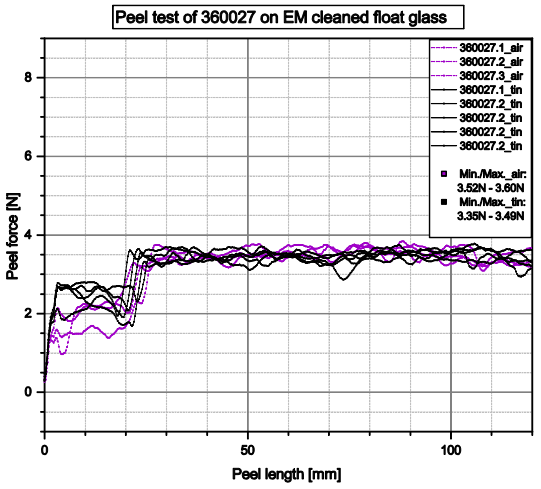

Figure 13: Peel test of U888 on EM cleaned float glass

3.3 Contact angle measurements on hydrophobic surfaces (HM1)

HM1 functionalising leads to a significant deviation of wetting behaviour in contrast to EM cleaned float glass, tested on samples G1 and G2. Figure 14 shows an example of the measured contact angles of sample G1 with test fluids water-, diiodomethane-, benzyl alcohol- and glycerol and their median data. The contact angle range of G1/G2 and their deviation are shown in Table 10 and the significances of functionalised samples in Table 8.

Benzyl alcohol and glycerol indicate a strong significant difference between the air- and tin side. Water and diiodomethane show no to only weak significance.

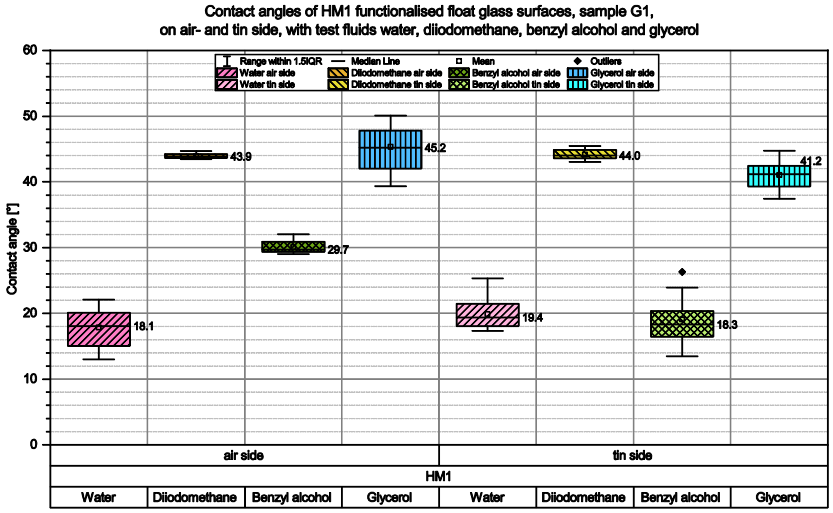

Figure 14: Comparison of contact angle boxplots of test fluids water, diiodomethane, benzyl alcohol and glycerol on air- and tin side of HM1 functionalised float glass (Sample G1)

Table 8: Significance results of WCA, DICA, BACA and GLCA of HM1 functionalised float glass

Samples G1, HM1, (DF 14)	*t*-statistics	Prob. > |*t*|	$p \leq .05$	$p \leq .01$	$p \leq .001$	Mean	SD	SEM	Median
HM1_WCA	−2.521	.024	*	-	-	17.871 19.871	2.848 2.275	.735 .587	18.070 19.375
HM1_DICA	−.719	.484	-	-	-	43.949 44.129	.350 .762	.090 .197	43.862 44.009
HM1_BACA	11.062	.000	*	**	***	30.101 19.094	.903 3.471	.233 .896	29.727 18.307
HM1_GLCA	4.012	.001	*	**	***	45.335 41.060	3.290 1.929	.850 .498	45.210 41.186

3.4 Contact angle measurements on hydrophobic surfaces (HM2)

HM2 functionalising leads to significant deviation of wetting behaviour, exemplarily of sample G1 with water-, diiodomethane-, benzyl alcohol- and glycerol-CA and median data (Figure 16), in contrast to HM1 (Figure 15). The contact angle range of G1/G2 and their deviation are shown in Table 10 and the significance of functionalised samples in Table 9.

Water and diiodomethane indicate a strong significant difference between the air- and tin side. Benzyl alcohol and glycerol show no to only weak significance.

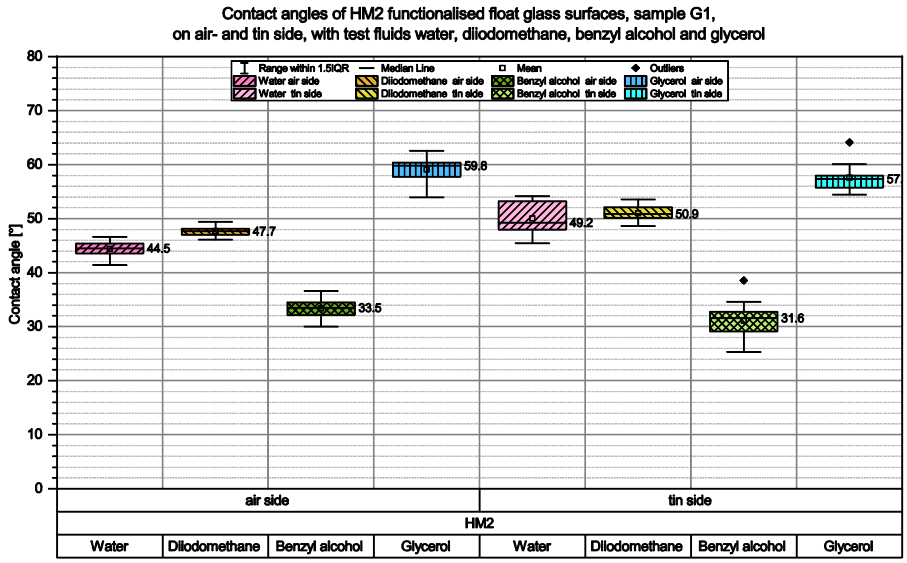

Figure 15: Comparison of contact angle boxplots of test fluids water, diiodomethane, benzyl alcohol and glycerol on air- and tin side of HM2 functionalised float glass (Sample G1)

Table 9: Significance results of WCA, DICA, BACA and GLCA of HM2 functionalised float glass

Samples G1, HM2, (DF 14)	*t*-statistics	Prob. > |*t*|	$p \leq .05$	$p \leq .01$	$p \leq .001$	Mean	SD	SEM	Median
HM2_WCA	−6.141	.000	*	**	***	44.373 50.036	1.338 2.799	.345 .723	44.488 49.240
HM2_DICA	−8.488	.000	*	**	***	47.667 50.969	.862 1.345	.223 .347	47.663 50.872
HM2_BACA	2.447	.028	*	-	-	33.376 31.089	1.860 3.303	.480 .853	33.507 31.609
HM2_GLCA	1.619	.128	-	-	-	59.105 57.573	2.381 2.429	.615 .627	59.819 57.341

Table 10: Contact angle range of samples G1/G2 of WCA, DICA, BACA and GLCA with functionalisation HM1/HM2 and mean values with deviation without outliers

Sample G1/G2	HM1		HM2	
	air side	tin side	air side	tin side
	min. – max.	min. – max.	min. – max.	min. – max.
Test fluids	[°]	[°]	[°]	[°]
Water	13.0 – 24.5	17.3 – 28.6	41.4 – 55.0	45.4 – 55.5
Deviation	18.8 ± 5.8	23.0 ± 5.7	48.2 ± 6.8	50.5 ± 5.1
Diiodomethane	43.3 – 45.5	42.5 – 45.5	45.7 – 49.5	47.2 – 53.5
Deviation	44.4 ± 1.1	44.0 ± 1.5	47.6 ± 1.9	50.4 ± 3.2
Benzyl alcohol	25.6 – 32.8	13.5 – 23.9	30.0 – 36.6	21.4 – 35.6
Deviation	29.2 ± 3.6	18.7 ± 5.2	33.3 ± 3.3	28.5 ± 7.1
Glycerol	32.4 – 50.1	31.1 – 44.7	49.0 – 62.6	50.5 – 65.5
Deviation	41.3 ± 8.9	37.9 ± 6.8	55.8 ± 6.8	58.0 ± 7.5

3.5 Surface energy measurement (functionalisation methods)

Surface energy measurements of HM1- and HM2 functionalised float glass surfaces were carried out with test fluids water, diiodomethane, benzyl alcohol and glycerol (20 drops on each float glass side, one sample for each test fluid). The wetting envelopes of air- and tin side are shown in Figures 16 to 19.

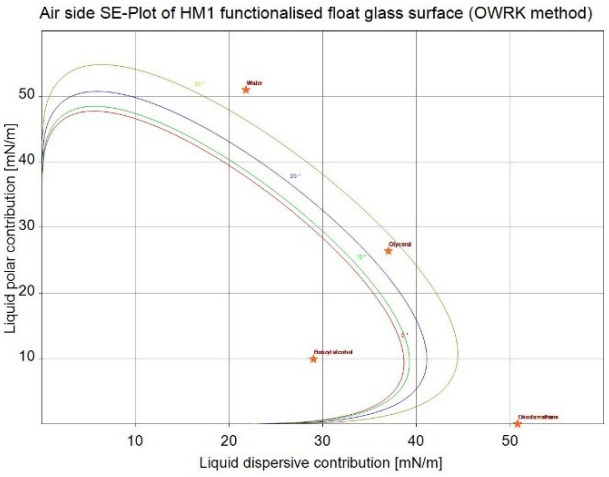

Figure 16: Wetting envelope of sample G1, consisting of sessile drop measurements of test fluids water, diiodomethane, benzyl alcohol and glycerol, on air side of HM1 cleaned float glass; surface energy: 59.6 mN/m, disperse: 22.3 mN/m, polar: 37.3 mN/m, RQ: 0.8056, sChi: 16.53

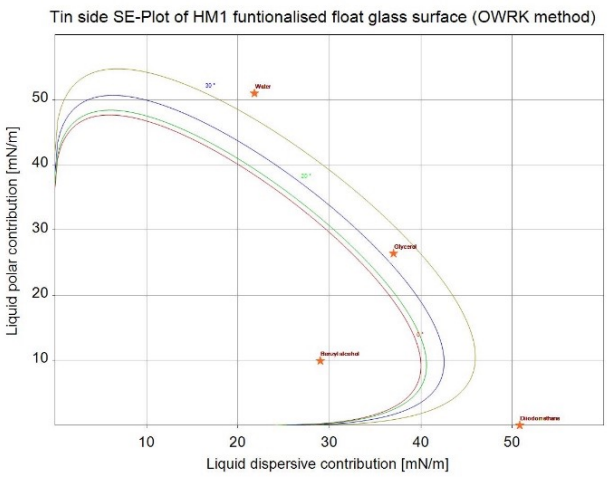

Figure 17: Wetting envelope of sample G1, consisting of sessile drop measurements of test fluids water, diiodomethane, benzyl alcohol and glycerol, on tin side of HM1 cleaned float glass; surface energy: 60.5 mN/m, disperse: 24.2 mN/m, polar: 36.3 mN/m, RQ: 0.8440, sChi: 14.50

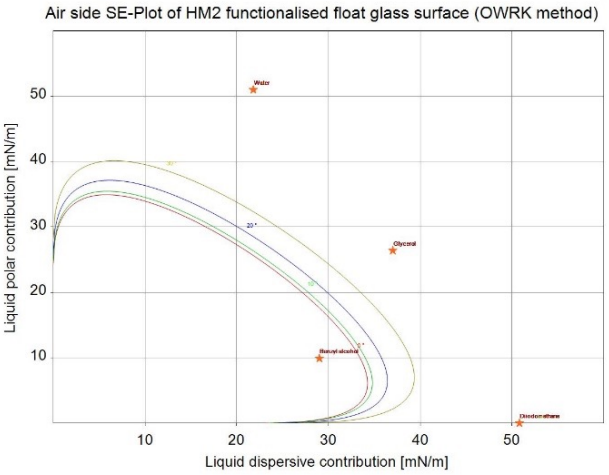

Figure 18: Wetting envelope of sample G1, consisting of sessile drop measurements of test fluids water, diiodomethane, benzyl alcohol and glycerol, on air side of HM2 cleaned float glass; surface energy: 47.5 mN/m, disperse: 23.2 mN/m, polar: 24.3 mN/m, RQ: 0.7524, sChi: 13.15

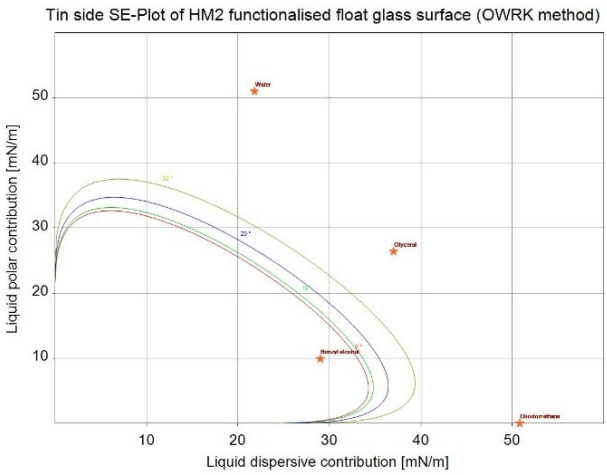

Figure 19: Wetting envelope of sample G1, consisting of sessile drop measurements of test fluids water, diiodomethane, benzyl alcohol and glycerol, on tin side of HM2 cleaned float glass; surface energy: 45.9 mN/m, disperse: 24.3 mN/m, polar: 21.6 mN/m, RQ: 0.8212, sChi: 10.54

HM1 functionalised float glass surface show on the air side surface energy of 59.6 mN/m with the dispersive component of 22.3 mN/m and the polar component of 27.3 mN/m without outliers (Figure 16). The tin side shows similar surface energy of 60.5 mN/m with the dispersive component of 24.2 mN/m and the polar component of 36.3 mN/m without outliers (Figure 17).

Surface energy measurement of HM2 functionalised float glass lead on the air side to surface energy of 47.5 mN/m with the dispersive component of 23.2 mN/m and the polar component of 24.3 mN/m (Figure 18). The tin side shows similar surface energy of 45.9 mN/m with the dispersive component of 24.3 mN/m and the polar component of 21.6 mN/m (Figure 19). The wetting envelopes and evaluated surface energies show not clearly the two-sidedness of HM1- and HM2 functionalised float glass, but the increasing hydrophobic wetting effect can be seen in smaller wetting envelopes of HM2 in comparison to HM1.

3.6 Adhesion on hydrophobic surfaces (HM1)

Following, peel forces on HM1 functionalised hydrophobic surfaces (air- and tin side) printed with UV varnishes were measured (Table 11). Each combination, air- and tin side with UV varnishes, will be counted as one measurement series. In summary, 12 measurement series with 5 peel tests for each combination were analyzed.

Table 11: Overview of peel forces from UV varnishes on HM1 functionalised float glass

Measurement series and their peel forces				
UV varnish	Measurement series	Air side peel force measurements	Measurement series	Tin side peel force measurements
PR9410	❶	4.89, 4.79, 3.85, 4.31, 3.66	❷	3.86, 4.27, 4.43, 4.36, -
PR9415	❸	3.69, 3.76, 3.72, 4.13, 3.90	❹	3.41, 3.53, 3.86, 3.68, 3.68
PR9291	❺	6.63, 6.79, 7.36, 6.92, 6.55	❻	6.76, 6.58, 6.96, 0.12, 0.12
360027	❼	3.90, 2.57, 2.79, -, -	❽	0.06, 1.74, 0.08, 2.26, 2.52
U8730	❾	4.57, 4.79, 5.31, 5.31, -	❿	4.92, 4.69, 5.33, 5.16, -
U888	⓫	5.68, 5.64, -, -, -	⓬	4.58, 4.71, 5.02, -, -

14 peel force measurements, red marked, out of 60, on HM1 functionalised surface show peel forces ≤ 0.50 N (❻, ❼, ❽, ❾, ❿, ⓫, ⓬). Without peel forces ≤ 0.50 N, 1 (⓫) out of 12 measurement series have less than 3/5 evaluable peel trials (grey-filled cell) with clear adhesion results and forces between 1.74 N and 7.36 N (blue marked).

Peel force tendencies show the changing of peel force from EM cleaned- to HM1 functionalised float glass surfaces printed with UV varnishes (Table 12). UV varnish PR9410, PR9415 and PR9291 show strong increasing adhesion forces in comparison to EM cleaned float glass surface. The other UV varnishes show similar to decreasing adhesion forces. UV varnish 360027 and U888 tend to show differences between air- and tin side (blue-filled cells).

Table 12: Peel forces and their trials on hardened UV varnishes on HM1 functionalised float glass

Method	UV varnish	PR9410		PR9415		PR9291		360027		U8730		U888	
		air	tin	air	tin	air	tin	air	tin	air	tin	air	tin
HM1	min. [N]	3.66	3.86	3.69	3.41	6.63	6.58	2.57	1.74	4.57	4.69	5.64	4.58
	max. [N]	4.89	4.43	4.13	3.86	7.36	6.96	3.90	2.52	5.31	5.33	5.68	5.02
$\bar{x}$ [min./max.]	[N]	4.28	4.15	3.91	3.64	7.00	6.77	3.24	2.13	4.94	5.01	5.66	4.80
Peel force tendency: EM to HM1		⇧	⇧	⇧	▬	⇧	⇧	⇩	⇩	⇩	▬	▬	⇩

Legend of peel trials and peel force tendencies	0/5	1/5	2/5	3/5	4/5	5/5
	⇧		Increasing peel force			
	⇩		Decreasing peel force			
	▬		Similar peel force			

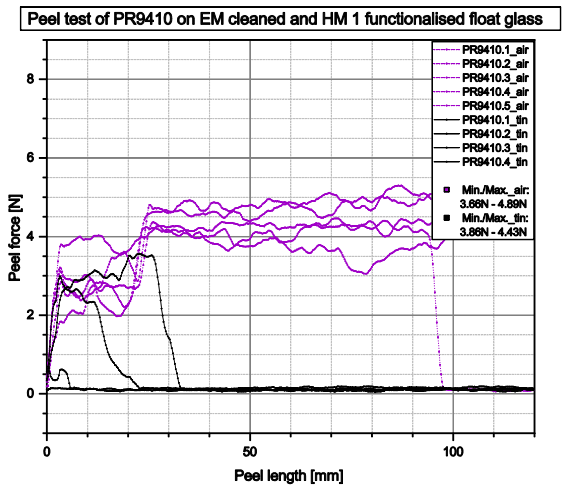

Figure 20: Peel test of PR9410 on EM cleaned and HM1 functionalised float glass

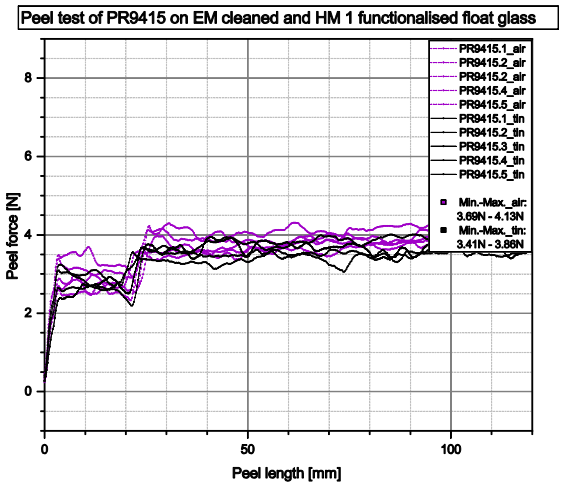

Figure 21: Peel test of PR9415 on EM cleaned and HM1 functionalised float glass float glass printed with PR9415

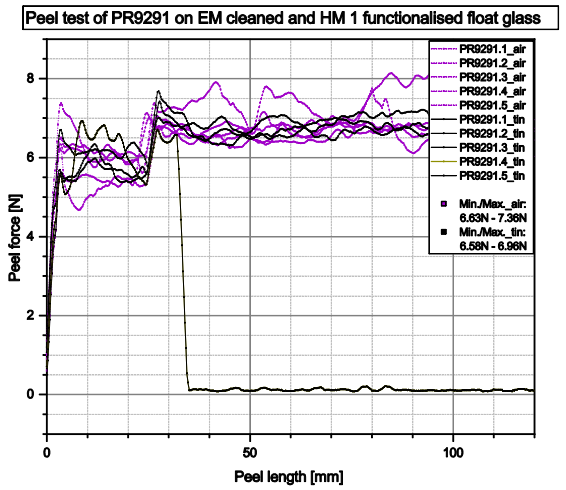

Figure 22: Peel test of PR9291 on EM cleaned and HM1 functionalised float glass

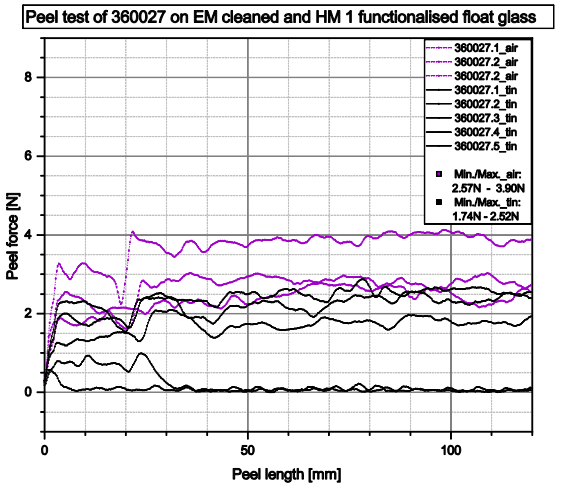

Figure 23: Peel test of 360027 on EM cleaned and HM1 functionalised float glass float glass printed with PR9415

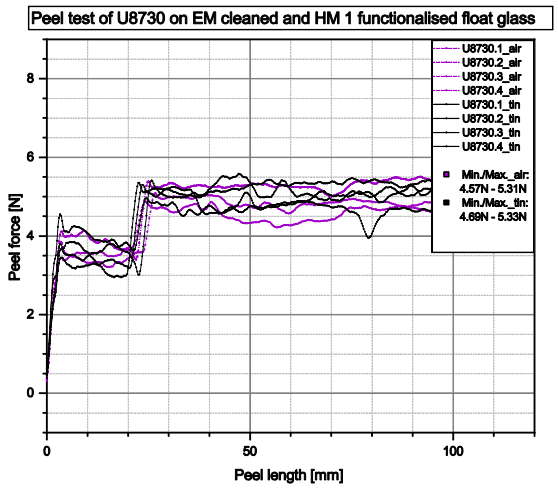

Figure 24: Peel test of U8730 on EM cleaned and HM1 functionalised float glass float glass printed with PR9415

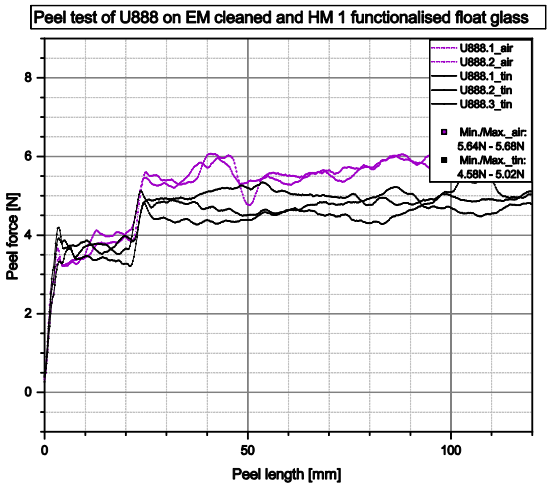

Figure 25: Peel test of U888 on EM cleaned and HM1 functionalised float glass float glass printed with PR9415

3.7 Adhesion on hydrophobic surfaces (HM2)

Following, peel forces on HM2 functionalised hydrophobic surfaces (air- and tin side) printed with UV varnishes were measured (Table 13). Each combination, air- and tin side, printed with UV varnishes will be counted as one measurement series. In summary, 12 measurement series with 5 peel tests for each combination were analyzed.

Table 13: Overview of peel forces from UV varnishes on HM2 functionalised float glass

Measurement series and their peel forces				
UV varnish	Measurement series	Air side peel force measurements	Measurement series	Tin side peel force measurements
PR9410	❶	4.08, 0.12, 4.35, 4.09, 3.83	❷	4.00, 3.23, 3.88, 3.96, 4.03
PR9415	❸	2.88, 3.10, 3.02, 3.12, -	❹	2.57, 2.75, 2.63, -, -
PR9291	❺	6.66, 6.75, 6.23, -, -	❻	5.69, -, -, -, -
360027	❼	3.31, 3.10, 2.66, 3.19, 3.53	❽	2.36, 2.84, 2.99, 3.12, 3.30
U8730	❾	5.32, 5.17, 4.93, -, -	❿	4.99, 5.09, 5.06, -, -
U888	⓫	4.82, 0.05, 5.37, -, -	⓬	4.44, 4.50, 5.11, 5.07, -

18 peel force measurements, red marked, out of 60, on HM2 functionalised float glass surface show peel forces ≤ 0.50 N (❶, ❸, ❹, ❺, ❻, ❾, ❿, ⓫, ⓬). Without peel forces ≤ 0.50 N, 2 out of 12 (❻, ⓫) measurement series (Figure 14) have less than 3/5 evaluable peel trials (grey marked cells) with clear adhesion results and forces between 2.36 N and 6.75 N (blue marked).

In the majority, the measured adhesion forces slightly decrease with increasing WCA in comparison to HM1. 4 of 6 UV varnishes show adhesion differences between air- and tin side.

Table 14: Peel forces and their trials on hardened UV varnishes on HM2 functionalised surface.

Method	UV varnish	PR9410		PR9415		PR9291		360027		U8730		U888	
		air	tin	air	tin	air	tin	air	tin	air	tin	air	tin
HM2	min. [N]	3.83	3.23	2.88	2.57	6.23	5.69	2.66	2.36	4.93	4.99	4.82	4.44
	max. [N]	4.35	4.03	3.12	2.75	6.75	5.69	3.53	3.30	5.32	5.09	5.37	5.11
$\bar{x}$ [min./max.]	[N]	4.09	3.63	3.00	2.66	6.49	5.69	3.09	2.83	5.13	5.04	5.10	4.78
Peel force tendency: HM1 to HM2		▬	⇩	⇩	⇩	⇩	⇩	▬	⇧	⇧	▬		▬

Legend of peel trials and peel force tendencies	0/5	1/5	2/5	3/5	4/5	5/5
	⇧		Increasing peel force			
	⇩		Decreasing peel force			
	▬		Similar peel force			

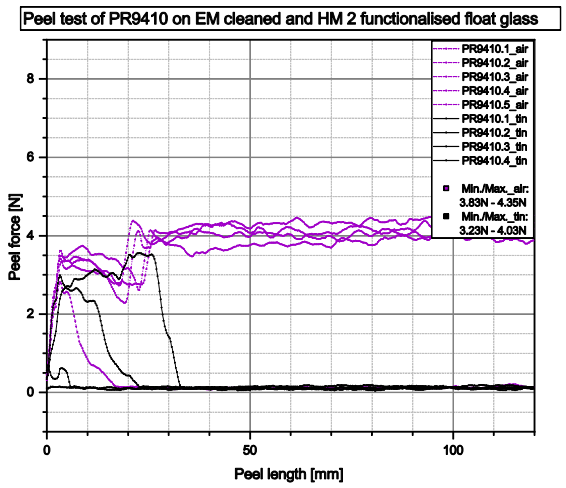

Figure 26: Peel test of PR9410 on EM cleaned and HM2 functionalised float glass

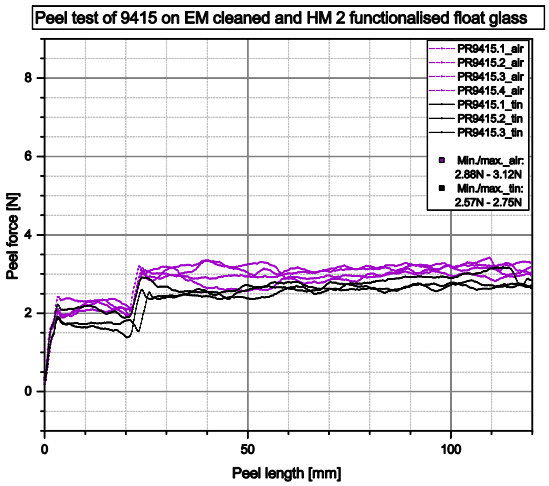

Figure 27: Peel test of PR9415 on EM cleaned and HM2 functionalised float glass

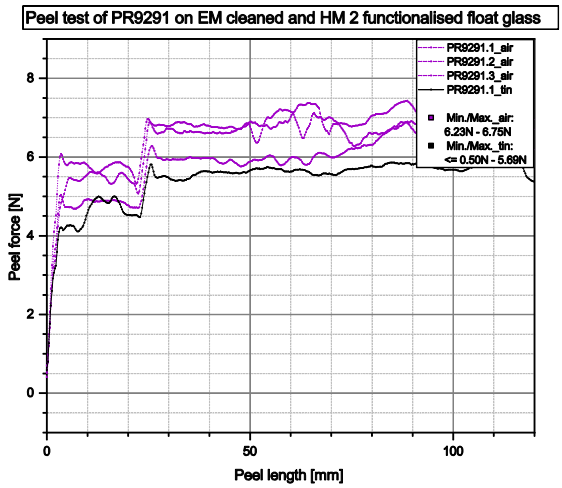

Figure 28: Peel test of PR9291 on EM cleaned and HM2 functionalised float glass

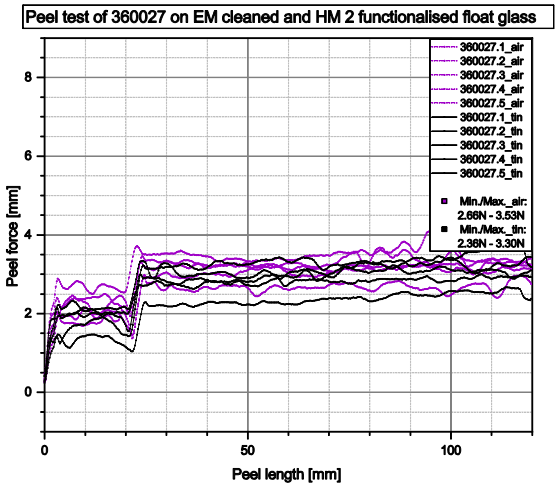

Figure 29: Peel test of 360027 on EM cleaned and HM2 functionalised float glass

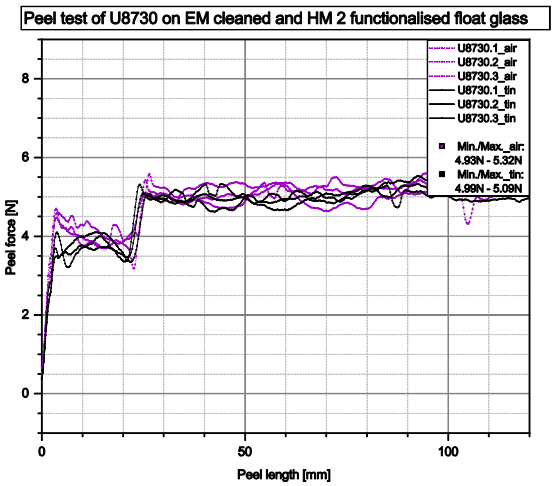

Figure 30: Peel test of U8730 on EM cleaned and HM2 functionalised float glass

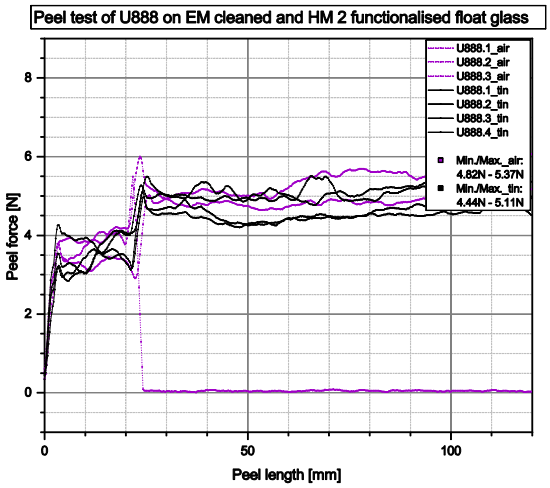

Figure 31: Peel test of U888 on EM cleaned and HM2 functionalised float glass

4. Conclusion

4.1 Wetting results

The wetting properties of float glass can be influenced by cleaning methods RTM and EM by using a mildly alkaline cleaning bath with different adjustments of temperature. RTM reinforces significant the two-sidedness of the float glass with WCA (air/tin): 17.4° to 55.8°/6.3° to 31.0°. The enhanced cleaning method, in contrast, equalises the two-sidedness with WCA (air/tin): 4.0° to 6.9° and gives the float glass surface a very hydrophilic and homogeneous wetting behaviour.

RTM cleaned float glass shows on the air side surface energy of 53.6 mN/m and on the tin side 61.7 mN/m. The two-sidedness is clearly differential in water contact angle and surface energy. In contrast to RTM, EM cleaned float glass shows on the air side surface energy of 51.8 mN/m and on the tin side 52.1 mN/m. The surface energy of the air- and tin side are relatively similar, but contact angle measurement with test fluids diiodomethane, benzyl alcohol and glycerol show still the expected influence of tin doping.

In summary, the EM cleaned float glass cares for a very homogenous and hydrophilic float glass surface, that was used as preliminary cleaning method and initial state for a following HMDS surface functionalising, to reach a homogeneity hydrophobic wetting behaviour with used functionalisation methods HM1 and HM2. Furthermore, the surfactant-free laboratory dishwasher cleaner is a harmless, easy to handle and cost-effective alternative in comparison to the mainly used Piranha cleaning.

The functionalisation of float glass surface with HM1 and HM2 cares for two clearly differentiable hydrophobic wetting behaviour in contrast to EM. Contact angles of test fluids water, diiodomethane, benzyl alcohol and glycerol were measured and evaluated. The homogeneity of contact angles decreased, in contrast to EM, but is comparable with the research of Wang, et al. (2021) and Prístavok (2006) and confirms the implementation of the functionalisation methods. The results were listed in Table 10. Significance test of normally distributed contact angle data pairs of HM1 functionalised float glass surface shows a strong significance difference between air- and tin side by using test fluids benzyl alcohol and glycerol. In contrast to HM1, HM2 shows a strong significance between air- and tin side, and so sensibility to the two-sidedness of the float glass, with test fluids water and diiodomethane.

HM1 functionalised float glass show on the air side surface energy of 59.6 mN/m and on the tin side 60.5 mN/m. HM2 functionalised float glass show on the air side surface energy of 47.5 mN/m and on the tin side 45.9 mN/m**.** The evaluated polar components decreased with increasing functionalisation (HM1 to HM2) and changed the sensibility of the test fluids in relation to the functionalisation method.

4.2 Adhesion results

The adhesion results of used UV varnishes on EM cleaned, HM1- and HM2 functionalised float glass surfaces are characterised by incomplete peel force measurement series. The adhesion measurement failures were not attributable to a specific UV varnish, so might be, the reason for failure could be a too-low contact pressure of the defined applied tape to the hardened UV varnishes surface and/or a too-short duration time of the tape on the hardened UV varnishes between application and peel force testing and/or an adhesive inhomogeneity of the used tape. Next investigations should include more peel trails and an optimisation of the tape application to reduce this source of deviation.

The evaluation of the peel tests with ≥3/5 trials and without peel forces ≤ 0.50 N show for applicated UV varnishes on EM cleaned float glass surface peel forces between 3.35 N and 5.97 N, for applicated UV varnishes on HM1 functionalised float glass surfaces between 1.74 N and 7.36 N and for HM2 functionalised float glass surfaces peel forces between 2.36 N and 6.75 N. The peel force overview (Table 15) gives an impression of the peel force deviation depending of the applied 6 UV varnishes from the air- to tin side and between the 3 different surface modifications.

Table 15: Overview of measured peel forces on, printed with UV varnishes, EM cleaned and HM1- and HM2 functionalised float glass with marked peel force tendencies in relation to the surface modifications

Peel forces	PR9410		PR9415		PR9291		360027		U8730		U888	
	air	tin	air	tin	air	tin	air	tin	air	tin	air	tin
EM x̄ [min./max]	0.00	0.00	3.22	3.77	6.78	4.06	3.56	3.42	5.29	4.94	5.68	5.36
HM1 x̄ [min./max]	⇧ 4.28	⇧ 4.15	⇧ 3.91	▬ 3.64	⇧ 7.00	⇧ 6.77	⇩ 3.24	⇩ 2.13	⇩ 4.94	▬ 5.01	▬ 5.66	⇩ 4.80
HM2 x̄ [min./max]	▬ 4.09	⇩ 3.63	⇩ 3.00	⇩ 2.66	⇩ 6.49	⇩ 5.69	▬ 3.09	⇧ 2.83	⇧ 5.13	▬ 5.04	⇩ 5.10	▬ 4.78

Legend of peel force tendencies		
	⇧	Increasing adhesion
	⇩	Decreasing adhesion
	▬	Similar adhesion

Hydrophilic wetting properties seem not to be only sufficient for the formation of "good" adhesion of UV varnishes, although good wetting of a surface is considered a prerequisite for good adhesion between applied fluid and substrate. The "good" adhesion behaviour is not clear defined, because it depends on the application purpose. The pre- tested solvent based 2K screen printing ink ZGM with hardener SVC/H, especially for glass printing, is used in this report as reference for the evaluation of the determined adhesion forces. The screen printing ink showed an average adhesion force of 4.40 N on EM cleaned float glass surface. In comparison, the applied and hardened UV varnishes show adhesion values between 0.00 N and 6.78 N and show of the in-/compatibility of UV varnishes to the very hydrophilic float glass surface.

The peel force investigations show with increasing water contact angle, EM to HM1, by 5 measurement series an unexpected slight increase of peel force, e.g. the UV varnish PR9410, 3 measurement series show similar peel force and 4 measurement series show a decreasing peel force. So, a higher water contact angle

in a range of 13.0° to 28.5° can improve the adhesion behaviour in comparison to EM cleaned and printed float glass samples (WCA ≈ 3°). The authors suspect an increasing formation of covalent bonds on the float glass surface which result to higher peel forces. The other UV varnishes show no interaction with the HMDS functionalisation (HM1).

The influence of the two-sidedness of the float glass is better detectable on EM cleaned float glass as on HM1 functionalised float glass. Further investigations with customised UV formulations and extended peel trials will provide information about these phenomena.

The peel force investigations show with increasing water contact angle, HM1 to HM2, by only 2 measurement series an increasing peel force (U8730 and U888), 4 measurement series show similar peel force and 6 measurement series show a decreasing peel force. So, a higher water contact angle in a range of 41.4° to 55.5° can reduce the adhesion properties in comparison to HM1 functionalised and printed float glass samples. The increase in temperature results in decreasing wetting behaviour, but in the majority not to increasing peel forces.

The two-sidedness of the float glass is better detectable on HM2 functionalised float glass as on HM1 functionalised float glass. Further investigations with known UV formulations and more peel trials can provide information about these phenomenas. The lowest influence of the air- and tin sides seems to be on the HM1 functionalised float glass surfaces.

The printing industry preferred the printing on the air side of the float glass. By viewing the measured peel forces in Table 15, it seems like, the tin side has lower peel forces as on the air side, if a deviation of ± 0.3 N is assumed. Exceptions occurred with UV varnish PR9415 (EM) and U8730 (HM1). It might be one of the reasons why in printing industry application often prefer the air side of the float glass.

The research of adhesion behaviour in comparison of wetting properties on modified float glass show this interdependancy as a worthwhile goal although there are used mature and stable industrial applications. Peel results showed different peel forces depending on glass cleaning/-functionalisation/-side and applied UV varnishes with different reactive diluents, binding agents and photoinitiators. Future investigations of peel tests with known UV formulations and different silanes are meaningful to allow gaining further insights into the adhesion of UV varnishes and different wetting states on functionalised float glass surfaces.

References

Deutsche Institut für Normung, 2020a. *EN ISO 19403-7:2020: Paints and varnishes - Wettability - Part 7: Measurement of the contact angle on a tilt stage (roll-off angle).* Berlin: DIN.

Deutsche Institut für Normung, 2020b. *DIN EN ISO 19403-2:2020-04: Beschichtungsstoffe - Benetzbarkeit - Teil 2: Bestimmung der freien Oberflächenenergie fester Oberflächen durch Messung des Kontaktwinkels (ISO 19403-2:2017)*. Berlin: DIN.

Fernández Oro, J.M., Argüelles Díaz, K.M., Santolaria Morros, C., Cobo Hedilla, A. F. and Lemaille, M., 2008. Multiphase modelling of pouring glass over the spout lip of an industrial float in the flat glass forming process. *International Journal for Numerical Methods in Fluids,* 58(10), pp. 1147–1177. https://doi.org/10.1002/fld.1793.

Fiorillo, M.R., Liguori, R., Diletto, C., Bezzeccheri, E., Tassini, P., Maglione, M., Maddalena, P., Minarini, C. and Rubino, A., 2017. Analysis of HMDS self-assembled monolayer effect on trap density in PC70BM n-type thin film transistors through admittance studies. *Materials Today: Proceedings,* 4(4), pp. 5053–5059. https://doi.org/10.1016/J.MATPR.2017.04.113.

Goodman, O. and Derby, B., 2011. The mechanical properties of float glass surfaces measured by nanoindentation and acoustic microscopy. *Acta Materialia,* 59(4), pp. 1790–1799. https://doi.org/10.1016/j.actamat.2010.11.045.

Haldimann, M., Luible, A. and Overend, M., 2008. *Structural use of glass*. Zürich: International Association for Bridge and Structural Engineering (IABSE). https://doi.org/10.2749/sed010.

Herzer, N., Hoeppener, S. and Schubert, U.S., 2010. Fabrication of patterned silane based self-assembled monolayers by photolithography and surface reactions on silicon-oxide substrates. *Chemical communications,* 46(31), pp. 5634–5652. https://doi.org/10.1039/C0CC00674B.

Hüppauff, M. and Lengeler, B., 1994. Surface analysis of floatglass by means of x-ray absorption, reflection, and fluorescence analysis. *Journal of Applied Physics,* 75(2), pp. 785–791. https://doi.org/10.1063/1.356430.

Krohn, M.H., Hellmann, J.R., Mahieu, B. and Pantano, C.G., 2005. Effect of tin-oxide on the physical properties of soda-lime-silica glass. *Journal of Non-Crystalline Solids,* 351(6-7), pp. 455–465. https://doi.org/10.1016/j.jnoncrysol.2005.01.050.

Lazauskas, A. and Grigaliūnas, V., 2012. Float glass surface preparation methods for improved chromium film adhesive bonding. *Materials Science,* 18(2), pp 181–186. http://dx.doi.org/10.5755/j01.ms.18.2.1924.

Neroth, G. and Vollenschaar, D. eds., 2011. *Wendehorst Baustoffkunde: Grundlagen – Baustoffe – Oberflächenschutz*. 27th ed. Wiesbaden: Vieweg + Teubner (Praxis).

Persson, R., 1969. *Flat glass technology*. Boston, MA: Springer US.

Pilkington, L.A.B., 1969. Review lecture: the float glass process. *Proceedings of the Royal Society A,* 314(1516), pp. 1–25. https://doi.org/10.1098/rspa.1969.0212.

Prístavok, R., 2006. *Analyse und Modellierung der Haftungsmechanismen bei der Beschichtung und Verklebung von Papierwerkstoffen*. Dr.-Ing. Dissertation. Technischen Universität Bergakademie Freiberg.

Saint-Gobain, 2018. *CSP_Broschuere_TIMELESS_A4_01115_CSP_04_2018_001_RZ*. [pdf] Available at: <https://climaplus-securit.com/xde-content/uploads/2018/04/CSP-Brosch%C3%BCre-TIMELESS-A4-01115-CSP-04-2018-001-RZ.pdf> [Accessed 2018].

Schreithofer, N., Laskowski, J.S. and Heiskanen, K., 2010. Changes of methylated silica surfaces on ageing. *Adsorption,* 16(4–5), pp. 271–277. https://doi.org/10.1007/s10450-010-9226-1.

da Silva, L.F.M., Öchsner, A. and Adams, R.D. eds., 2011. *Handbook of adhesion technology.* Berlin, Heidelberg, Cham: Springer.

Silvestru, V.A., Drass, M., Englhardt, O. and Schneider, J., 2018. Performance of a structural acrylic adhesive for linear glass-metal connections under shear and tensile loading. *International Journal of Adhesion and Adhesives*, 85, pp. 322–336. https://doi.org/10.1016/j.ijadhadh.2018.07.006.

Tamglass Ltd Oy, 1997. Glass processing days. In: *The Fifth International Conference on Architectural and Automotive Glass [now and in the future]*. Tampere, Finland, 13–15 September 1997. Tampere: Tamglass Engineering Oy.

Wang, Y., Hansen, C.J., Wu, C.-C., Robinette, E.J. and Peterson, A.M., 2021. Effect of surface wettability on the interfacial adhesion of a thermosetting elastomer on glass. *RSC Advances,* 11(49), pp. 31142–31151. https://doi.org/10.1039/D1RA05667K.

Wypych, G., 2018. *Handbook of adhesion promoters*. Toronto, Ontario: ChemTec Publishing.

Zhang, Q., Chen, Z. and Li, Z., 2011. Simulation of tin penetration in the float glass process (float glass tin penetration). *Applied Thermal Engineering* 31 (6–7), pp. 1272–1278. https://doi.org/10.1016/j.applthermaleng.2010.12.030.

Index of authors